THÈSE

En vue de l'obtention du
DOCTORAT DE L'UNIVERSITÉ DE TOULOUSE

Délivré par l'Université Toulouse 3 - Paul Sabatier

Présentée et soutenue par

Tianqi CANG

Le 29 novembre 2021

MODÉLISATION DE L'ACTIVITÉ DES ÉTOILES FROIDES A PARTIR DE DONNÉES PHOTOMÉTRIQUES ET SPECTROPOLARIMÉTRIQUES

Ecole doctorale : **SDU2E - Sciences de l'Univers, de l'Environnement et de l'Espace**

Spécialité : **Astrophysique, Sciences de l'Espace, Planétologie**

Unité de recherche :
IRAP - Institut de Recherche en Astrophysique et Planetologie

Thèse dirigée par
Pascal PETIT et Jean-François DONATI

Jury

Mme Gaitee HUSSAIN, Rapporteure
M. Shenghong GU, Rapporteur
M. Jianning FU, Examinateur
Mme Catherine DOUGADOS, Examinatrice
M. Pascal PETIT, Directeur de thèse
M. Jean-François DONATI, Co-directeur de thèse
M. Arturo LOPEZ ARISTE, Président

Detecting activity of late-type stars with spectropolarimetry and photometry

Tianqi CANG (苍天启)

15 Sep 2020

Abstract

The various active phenomena observed in solar-type stars are a consequence of their internal magnetism. Stellar rotation is responsible for the efficient amplification of internal magnetic fields through a global dynamo. However, magnetic activity seems to reach an upper limit for stars with sufficiently large rotation rates, although the exact rotation threshold for saturation depends on the magnetic tracer taken into account. This so-called saturation phenomenon is still lacking an in-depth exploration. While a number of classical activity tracers unveil the presence of magnetic fields in the atmosphere of cool stars, their direct measurement has long been very difficult. During the last three decades, the spectacular progress in our capacity to measure and model the Zeeman effect has increased dramatically our knowledge of stellar magnetism.

A fine understanding of stellar activity is also critical to model the planetary environment of close-in planets. Most M-dwarfs display high activity levels, and these stars dominate the stellar population in the solar neighborhood. For M-dwarfs, the low stellar mass results in a close-in habitable zone, where stable liquid water can exist on the planetary surface. Close-in giant planets around young Suns are also attractive to investigate, as they reflect the early evolution of planetary systems, and provide a key insight into the migration pathways creating hot Jupiters. Photometric monitoring is one of the most efficient methods to characterize transiting exoplanets and activity-induced brightness variations of the host stars. We proposed to build a near-infrared CubeSat-type photometer named MARSU. This compact space telescope is low-cost and flexible to schedule observations. As a dedicated infrared space photometer with an 8.5cm diameter, MARSU is expected to detect transiting Earth-like planets in the habitable zone of M dwarfs, while characterizing the activity of the host star. It will achieve continuous photometric monitoring in the near-infrared for stars up to an H magnitude of 11, at a precision better than one mmag over continuous periods of up to 3 months.

In the first study of this thesis, we investigated the magnetic activity of the prototypical, zero-age main sequence, rapid rotator V530 Per. Time-resolved spectropolarimetric observations at two epochs (2006 and 2018) were gathered with ESPaDOnS, enabling us to explore the surface distribution of brightness and magnetic fields, the latitudinal differential rotation, and the prominence system by using tomography tools. The brightness map is dominated by a large, dark spot near the pole, accompanied by a complex distribution of bright and dark features at lower latitudes. Most of the large-scale magnetic field energy is stored in the toroidal field component. Both brightness and magnetic field maps of V530 Per are sheared by solar-like differential rotation. The prominence system is organized in a ring at the approximate location of the co-rotation radius and displays significant short-term evolution within a few days.

The second part of the thesis was a feasibility assessment for the detection of exoplanets around active stars with MARSU. We developed an end-to-end numerical simulator of MARSU observations. This simulates all stages, from the light generated by the planetary system to the image acquisition and the extraction of light curves. A number of tests were made to evaluate the performance of the payload and confirmed that MARSU can detect habitable Earth-like exoplanets around M-dwarfs and close-in giant planets

around young solar-like stars.

Resumé

Les divers phénomènes actifs observés dans les étoiles de type solaire sont une conséquence de leur magnétisme interne. La rotation stellaire est responsable de l'amplification des champs magnétiques internes à travers une dynamo globale. Cependant, l'activité magnétique semble atteindre une limite supérieure pour les étoiles avec des vitesses de rotation suffisamment grandes, bien que le seuil de rotation exact pour la saturation dépende du traceur magnétique pris en compte. Le régime saturé de la dynamo stellaire n'a pas encore bénéficié d'une exploration approfondie. Si nombre de traceurs d'activité classiques révèlent la présence de champs magnétiques dans l'atmosphère des étoiles froides, leur mesure directe a longtemps été très difficile. Au cours des trois dernières décennies, les progrès spectaculaires de notre capacité à mesurer et à modéliser l'effet Zeeman ont considérablement augmenté nos connaissances sur le magnétisme stellaire.

Une compréhension fine de l'activité stellaire est également essentielle pour modéliser l'environnement planétaire des planètes proches. La plupart des naines M affichent des niveaux d'activité élevés, et ces étoiles dominent la population stellaire dans le voisinage solaire. Pour les naines M, la faible masse stellaire se traduit par une zone habitable rapprochée, où de l'eau liquide stable peut exister à la surface de la planète. Les planètes géantes proches des jeunes Soleils sont également importantes à étudier, car elles reflètent l'évolution précoce des systèmes planétaires et fournissent un aperçu clé des canaux de migration à l'origine des Jupiters chauds. Le suivi photométrique est l'une des méthodes les plus efficaces pour caractériser les exoplanètes en transit et les variations de luminosité induites par l'activité des étoiles hôtes. Nous avons proposé de construire un photomètre de type CubeSat proche infrarouge nommé MARSU. Ce télescope spatial compact est peu coûteux et de programmation flexible. En tant que photomètre spatial infrarouge dédié, d'un diamètre de 8,5 cm, MARSU va détecter les planètes semblables à la Terre en transit dans la zone habitable des naines M, tout en caractérisant l'activité de l'étoile hôte. Il réalisera une surveillance photométrique continue dans le proche infrarouge pour les cibles jusqu'à une magnitude H de 11, avec une précision meilleure qu'une mmag, sur des périodes continues allant jusqu'à 3 mois.

Dans le premier volet de cette thèse, nous avons étudié l'activité magnétique d'un prototype d'objet à l'âge zéro de la séquence principale : le rotateur rapide V530 Per. Des observations spectropolarimétriques sur deux époques (2006 et 2018) ont été obtenues avec ESPaDOnS, nous permettant de reconstruire la distribution de surface de la luminosité et des champs magnétiques, la rotation différentielle latitudinale et le système de protubérances en utilisant des méthodes tomographiques. La carte de luminosité est dominée par une grande tache sombre près du pôle, accompagnée d'une distribution complexe de régions brillantes et sombres aux latitudes inférieures. La majeure partie de l'énergie du champ magnétique à grande échelle est stockée dans la composante du toroïdale. Les cartes de brillance et de champ magnétique de V530 Per sont cisaillées par une rotation différentielle de type solaire. Le système de protubérances est organisé en anneau à l'emplacement approximatif du rayon de co-rotation et affiche une évolution significative à court terme, sur quelques jours.

La deuxième partie de la thèse était une évaluation de faisabilité de la détection

d'exoplanètes autour d'étoiles actives avec MARSU. Nous avons développé un simulateur numérique de bout en bout des observations MARSU. Celui-ci simule les étapes allant de la lumière générée par le système planétaire à l'acquisition d'images et à l'extraction des courbes de lumière. Un certain nombre de tests ont été effectués pour évaluer les performances de la charge utile et ont confirmé que MARSU peut détecter des exoplanètes habitables semblables à la Terre autour des naines M, ainsi que des planètes géantes chaudes autour de jeunes étoiles semblables au soleil.

Acknowledgements

1.10.2017 - 29.11.2021, the four years of my Ph.D career working at IRAP/OMP have been a precious growth experience for me. My work involved two different projects, many of which were new and challenging for me. In addition, living in a foreign country and the sudden emergence of the new crown epidemic added some bumps to the journey. I was fortunate to meet many lovely people and receive irreplaceable help and encouragement during this process.

Firstly, of course, I'd like to express my gratitude to my supervisor Pascal Petit. It was my luck to be your student for this 4 years. Thanks for your great patience, encouragement and kindness, for the huge amount of communication and discussions. You have taught me knowledge and imparted the wisdom of scientific research. Without your support, this thesis would not have been possible. I am also very grateful to my co-supervisor, Jean-François Donati, for your patient guidance and discussions, and for your constructive comments on my work.

I thank the two reviewers, Gaitte Hussain and Shenghong Gu Institute, for taking the time to read my paper and provide corrections, and for many valuable suggestions to improve the thesis manuscript. Thanks to the jury members, Arturo Lopez Ariste and Catherine Dougados, for their support during the thesis defense process. Special thanks to Jianning Fu, for his support and assistance in my follow-up work.

Thanks to my thesis committee members Sylvie Vauclair and Santerne Alexandre for their advice and help in the completion of the thesis

I thank my collaborators Colin Folsom, Moira Jardine, Carolina Villarreal D'Angelo, Aline Vidotto, Stephen Marsden and Florian Gallet for their comments and suggestions during the work on V530 Per. for their comments and suggestions. Thanks to Driss Kouach for his support and assistance in the work of MARSU.

Thanks to my friends and colleagues in IRAP for their kindness and help: Bonnie, Anthony, Louise, Baptiste, Florian, Bastien, Stefano, Paul, Gang, Wenchao and all other members in PS2E and IRAP/OMP. Special thanks to Gérard Vauclair, the gentleman in the next office, for his constant kindness and support.

Thanks to Philippe Mathias and Agnès Lèbre who helped me during the observations on Pic du Midi .

Special thanks to Weikai Zong, for his help when I first arrived in Toulouse and for helping me to integrate more quickly into my new life.

Finally, I would like to thank my parents, who are always there to support me. They are the warm, unfailing light in my heart.

Contents

List of astronomical constants

Name	Notion	Value	Unit
Astronomical unit	au	$1.495978707 \times 10^{11}$	m
Boltzmann constant	k_B	$1.38064852 \times 10^{-23}$	m^2 kg s^{-2} K^{-1}
Bohr magneton	$\mu_B = \frac{e\hbar}{2m_e}$	$9.274009994 \times 10^{24}$	J/ T
Electron mass	m_e	$9.10938356 \times 10^{-31}$	kg
Electron charge	e	$1.602176634 \times 10^{19}$	C
Gravitational constant	G	6.67408×10^{11}	m^3 kg^{-1} s^{-2}
Parsec	pc	$3.085677581 \times 10^{16}$	m
Plank constant	h	$6.62607004 \times 10^{-34}$	J·s
Reduced Planck constant	$\hbar = \frac{h}{2\pi}$	$1.054571817 \times 10^{-34}$	J·s
Solar radius	$R_\odot$	6.9634×10^8	m
Solar mass	$M_\odot$	1.98847×10^{30}	kg
Speed of light	c	2.99792458×10^8	m/s

Foreword

One thing that never changes in the universe is change and there is no exception for stars. In Sun-like stars, the main driver of short-term variability is stellar activity. This is a collective name for a series of variable phenomena that originate in the atmosphere of the star (e.g., Reiners 2012). The human record of stellar activity dates back to the observation of sunspots by ancient Chinese in 800 BC (Mossman, 1989). However, it was not until 400 years ago, when Galileo Galilei pointed his telescope at the Sun, that people began to understand the active phenomena occurring on a star. The knowledge of the activity on the Sun, which is the nearest star to us, has been accumulated since that date, and information collected about solar activity now spans the entirety of the electromagnetic spectrum. For stars other than the Sun, however, it is hard to observe the manifestations of stellar activity with a spatial resolution as high as the one achievable for the Sun (e.g., O'Gorman et al. 2017). Moreover, although we know that stellar activity is intrinsically linked to the magnetism since George Ellery Hale detected the Zeeman effect in observations of a solar spot (Hale, 1908), the elusiveness of magnetic fields set huge difficulty to the observation. A possible approach to interpreting the active behavior observed on other stars is to analogize from the knowledge obtained from solar observations. In return, the variety of the manifestations of activity observed on other stars will improve our understanding of the Sun itself.

Over the last two decades, techniques for observing and modeling the stellar activity have undergone spectacular progress (e.g.,Berdyugina 2005; Charbonneau 2005; Brown et al. 2010). On the observational side, stellar spectropolarimetry has become able to reveal the distribution of magnetic fields on cool stars, through the Zeeman-Doppler Imaging technique (ZDI, an extension of the temperature and abundance mapping of stellar surfaces, which can reveal the magnetic topology of active stars; Donati et al. 1999, 2006b). Modeling the activity of young, late-type stars is a key to better understand the early evolution of solar analogs and their planets. A large fraction of young Suns close to the early main sequence experience very large rotation rates, as they still possess most of the angular momentum acquired during the stellar formation process (Bouvier 2013). For stars with sufficiently rapid rotation, magnetic activity seems to reach an upper limit, although the exact rotation threshold for dynamo saturation is still a matter of debate (Pallavicini et al., 1981; Prosser et al., 1996; Wright et al., 2011). Attempts to model this saturated state in global numerical simulations of G-K stars remain scarce (e.g., Augustson 2017; Guerrero et al. 2019). Fast rotators are also original laboratories for studying stellar prominences and their impact on angular momentum evolution in young stars. Prominences, along with stellar winds, remove angular momentum from stars and, therefore, contribute to the early evolution of active solar analogs (Aarnio et al., 2012; Jardine et al., 2020). For rapidly rotating stars, prominence systems become much more massive and extended than on the Sun (Collier Cameron, 1999). Following the first detection by Collier Cameron & Robinson (1989a), prominence systems have been reported in a small number of young Suns (Donati et al., 2000; Dunstone et al., 2006a).

Since stellar activity has a crucial influence on the stellar environment, including on

the formation and early evolution of their orbiting planets, it is also critical to investigate the potential presence of close-in planets orbiting young stars, and the relative frequency of various classes of young planets with respect to those of mature Sun-like stars. A detailed understanding of stellar activity is also a prerequisite for exoplanet detection through indirect methods that rely on the efficient filtering of the activity noise. Photometric monitoring is a widely used method for characterizing stars with variable brightness, such as active stars, young accreting stars, and for the detection of transiting exoplanets. Space telescopes are ideal tools to carry out continuous observations of variable stars since they can avoid some critical drawbacks of ground-based observations, like day/night alternation and atmospheric variations (e.g., variable cloud cover, turbulence). Currently, several photometric space observatories are dedicated to the detection of exoplanetary transits and to stellar physics (e.g., TESS, CHEOPS). However, large missions have very limited flexibility (if any) in their observing program, while a number of science cases would benefit from customized observations of specific targets. Tiny space telescopes based on the CubeSat concept, which consists in stacking standard cubic units (1U) with 10 cm of width, offer a flexible and low-cost opportunity for the monitoring of bright targets, as demonstrated by the ASTERIA (Knapp et al., 2020) proof of concept in the optical domain.

The MARSU project proposes to build a near-infrared CubeSat-type space photometer, aimed at (i) searching for Earth-like planets in the habitable zone of low-mass stars, and (ii) studying the formation of low-mass stars and planets in the presence of magnetic fields. This project will work in parallel with SPIRou (Donati et al., 2020) and SPIP, two twin ground-based nIR spectropolarimeters & velocimeters for the Canada-France-Hawaii Telescope (CFHT, Maunakea Observatory, Hawaii) and the Télescope Bernard Lyot (TBL, Observatoire du Pic du Midi, France), respectively.

This thesis includes two main works: (i) The investigation of magnetic fields and activity tracers of the young, solar-like, rapid rotator V530 Per with a mass of $\sim 1 M_{\odot}$, and rotational period of $\sim$ 0.32d. Spectropolarimetric time series were obtained at two epochs, with a 12-year gap. Tomographic inversion, especially ZDI, was applied to model the surface brightness, magnetic field, and prominences of the star. (ii) A numerical simulator is developed to test the feasibility of the MARSU CubeSat and establish the near-infrared detectability of planets using its compact payload.

The first chapter (Ch. 1) briefly introduces the background knowledge and historical information connected with the main objectives in this thesis, including (i) Stellar structure and early evolution of late-type dwarfs; (ii) Stellar activity in young, late-type stars. The second chapter (Ch. 2) details the methodology for modeling the stellar activity from spectroscopic and spectropolarimetric data. The application of these techniques to V530 Per is documented in the third chapter (Ch. 3), with investigations of the long- and short-term variations of several magnetic phenomena. The fourth part (Ch. 4) describes the MARSU project, and numerical tests for the feasibility to achieve the science goals, especially Earth-like planet detection around M-dwarfs. Finally, the last chapter (Ch. 4.5) summarizes the results obtained in this thesis, places them in a broader scientific picture, and provides perspectives for future work.

Avant-propos

Dans les étoiles semblables au Soleil, le principal moteur de la variabilité à court terme est l'activité stellaire. Sous cette appellation générique, apparaît une série de phénomènes variables qui affectent l'atmosphère de l'étoile (par exemple, Reiners 2012). Les relevés humains de l'activité stellaire remontent à l'observation des taches solaires par les Chinois, en 800 avant notre ère (Mossman, 1989). Cependant, ce n'est qu'il y a 400 ans, lorsque Galilée a pointé son télescope vers le Soleil, que notre connaissance des phénomènes actifs se produisant sur une étoile a vraiment décollé. L'observation systématique de l'activité du Soleil, qui est l'étoile la plus proche de nous, s'est accumulée depuis cette date, et les informations recueillies sur l'activité solaire couvrent désormais l'intégralité du spectre électromagnétique. Pour les étoiles autres que le Soleil, cependant, il est difficile d'observer les manifestations de l'activité avec une résolution spatiale aussi élevée que celle réalisable pour le Soleil (par exemple, O'Gorman et al. 2017). De plus, bien que nous sachions que l'activité stellaire est intrinsèquement liée au magnétisme depuis que George Ellery Hale a détecté l'effet Zeeman sur la tache solaire (Hale, 1908), l'invisibilité du champ magnétique a posé d'énormes difficultés à l'observation. Une approche possible pour interpréter le comportement actif observé sur d'autres étoiles est de transposer les connaissances obtenues à partir des observations solaires. En retour, la variété des manifestations d'activité observées sur d'autres étoiles améliorera notre compréhension du Soleil lui-même.

Au cours des deux dernières décennies, les techniques d'observation et de modélisation de l'activité stellaire ont connu des progrès spectaculaires (Berdyugina 2005; Charbonneau 2005; Brown et al. 2010). Du côté des observations, la spectropolarimétrie stellaire est devenue capable de révéler la distribution des champs magnétiques sur les étoiles froides, grâce à la technique d'imagerie Zeeman-Doppler (ZDI, une extension de la cartographie de température et d'abondance des surfaces stellaires, qui peut révéler la topologie magnétique des étoiles actives Donati et al. 1999, 2006b). La modélisation de l'activité des jeunes étoiles froides est une clé pour mieux comprendre l'évolution précoce des analogues solaires et de leurs planètes. Une grande partie des jeunes Soleils proches du début de la séquence principale connaît des taux de rotation très élevés, car ils possèdent encore la majeure partie du moment cinétique acquis pendant le processus de formation stellaire (Bouvier 2013). Pour les étoiles à rotation suffisamment rapide, l'activité magnétique semble atteindre une limite supérieure, bien que le seuil de rotation exact pour la saturation de la dynamo soit encore un sujet de débat (Pallavicini et al., 1981; Prosser et al., 1996; Wright et al., 2011). Les tentatives de modélisation de cet état saturé dans les simulations numériques globales des étoiles G-K restent rares (par exemple, Augustson 2017; Guerrero et al. 2019). Les rotateurs rapides sont également des laboratoires originaux pour étudier les protubérances stellaires et leur impact sur l'évolution du moment angulaire dans les étoiles jeunes. Les protubérances, ainsi que les vents stellaires, extrait le moment cinétique des étoiles et, par conséquent, contribuent à l'évolution précoce des analogues solaires actifs (Aarnio et al., 2012; Jardine et al., 2020). Pour les étoiles en rotation rapide, les systèmes de protubérance deviennent beaucoup plus massifs et étendus que sur le Soleil (Collier Cameron, 1999). Suite à une première

détection par Collier Cameron & Robinson (1989a), des systèmes de protubérance ont été documentés dans un petit nombre de jeunes Soleils (Donati et al., 2000; Dunstone et al., 2006a).

Étant donné que l'activité stellaire a une influence cruciale sur l'environnement stellaire, y compris sur la formation et l'évolution précoce de leurs planètes, il est également essentiel d'étudier la présence potentielle de planètes chaudes autour de jeunes étoiles, et la fréquence relative de diverses classes de jeunes planètes par rapport à celles des étoiles matures semblables au Soleil. Une compréhension détaillée de l'activité stellaire est également une condition préalable à la détection d'exoplanètes grâce à des méthodes indirectes qui reposent sur le filtrage efficace du bruit d'activité. La surveillance photométrique est une méthode largement utilisée pour caractériser les étoiles à luminosité variable, telles que les étoiles actives, les jeunes étoiles en accumulation, et pour la détection des exoplanètes en transit. Les télescopes spatiaux sont des outils idéaux pour effectuer des observations continues d'étoiles variables car ils peuvent éviter certains inconvénients des observations au sol, comme l'alternance jour/nuit et les variations atmosphériques (par exemple, couverture nuageuse variable, turbulence). Actuellement, plusieurs observatoires spatiaux photométriques sont dédiés à la détection des transits exoplanétaires et à la physique stellaire (e.g., TESS, CHEOPS). Cependant, les grandes missions ont une flexibilité très limitée dans la programmation de leurs observations, alors qu'un certain nombre de cas scientifiques bénéficieraient d'observations flexibles de cibles spécifiques. De très petits télescopes spatiaux peuvent se baser sur le concept de CubeSat, qui consiste à empiler des unités cubiques standard (1U) avec 10 cm de largeur. Ils offrent une option flexible et peu coûteuse pour le suivi de cibles brillantes, comme illustré par le démonstrateur ASTERIA (Knapp et al., 2020) dans le domaine optique.

Le projet MARSU propose de construire un photomètre spatial proche infrarouge de type CubeSat, visant à (i) rechercher des planètes semblables à la Terre dans la zone habitable des étoiles de faible masse, et (ii) étudier la formation d'étoiles de faible masse et de planètes en présence de champs magnétiques. Ce projet fonctionnera en parallèle avec SPIRou (Donati et al., 2020) et SPIP, deux spectropolarimètres jumeaux et vélocimètres pour le Télescope Canada-France-Hawaii (CFHT, Observatoire du Maunakea, Hawaï) et le Télescope Bernard Lyot (TBL, Observatoire du Pic du Midi, France), respectivement.

Cette thèse comprend deux travaux principaux : (i) L'étude des champs magnétiques et des traceurs d'activité du jeune rotateur rapide de type solaire V530 Per, avec une masse de $\sim 1 M_{\odot}$ et une période de rotation de ~ 0.32d. Des séries temporelles spectropolarimétriques ont été obtenues à deux époques, avec un écart de 12 ans. L'inversion tomographique, en particulier via ZDI, a été appliquée pour modéliser la luminosité de la surface, le champ magnétique et la distribution spatiale des protubérances. (ii) Un simulateur numérique est développé pour tester la faisabilité de MARSU et établir la détectabilité des planètes par sa charge utile très compacte.

Le premier chapitre (Ch. 1) présente brièvement les connaissances de base et les informations historiques liées aux principaux objectifs de cette thèse, notamment (i) la structure stellaire et l'évolution précoce des étoiles froides; (ii) l'activité stellaire

chez les jeunes étoiles froides. Le deuxième chapitre (Ch. 2) détaille la méthodologie adoptée pour la modélisation de l'activité stellaire à partir de données spectroscopiques et spectropolarimétriques. L'application de ces techniques à V530 Per est documentée dans le troisième chapitre (Ch. 3), avec une étude des variations à long et à court terme de plusieurs phénomènes magnétiques. La quatrième partie (Ch. 4) décrit le projet MARSU et les tests numériques de faisabilité pour atteindre les objectifs scientifiques, en particulier la détection de planètes semblables à la Terre autour des naines rouges. Enfin, le dernier chapitre (Ch. 4.5) résume les résultats obtenus dans cette thèse, les replace dans un cadre scientifique plus large, et ouvre des perspectives de travaux futurs.

Chapter 1

Introduction to the late-type stars

1.1 Brief introduction to stellar structure and evolution

1.1.1 Spectral classification of stars

The life of a star is so much longer than any observations of human beings that it is impossible to record the history of a star from birth to the end. Studies of stellar structure and evolution are essentially based on the observation of a large sample of stars. Thus, each star can provide some information on its evolutionary stage. One can plot the stellar luminosity (or absolute magnitude) as a function of the effective temperature $T_{\rm eff}$ (or spectral type), and get the famous Hertzsprung-Russell (HR) diagram (e.g., Fig 1.1.1). Redder stars have a lower $T_{\rm eff}$, and populate the right of the diagram. On the contrary, bluer stars settle on the left.

Note that the majority of the stars lie on a strip across the HR diagram from the red, faint stars (right bottom corner) to the blue, bright stars (left top corner). This strip is the so-called main sequence (MS). The color of stars is thus commonly used for the stellar classification. For most stars ($\geq 99\%$), the spectral type can be classified under the Morgan–Keenan (MK, or Harvard) system using the letters O (hot), B, A, F, G, K, and M (cold)[1]. Each spectral type can be subdivided into the numbers 0 to 9 (e.g., the Sun is classified as G2V, where V stands for the luminosity class of a MS star). For historical reasons, O, B, A-type stars are usually referred to as *early*-type stars, while K, M, and sometimes G-types stars are referred to as *late*-type. Late-type dwarfs with mass close or less than the Sun (e.g., F-K dwarfs) is occupied the most of population in the nearby space.

Most MS stars, including the Sun, are also called dwarf stars with relatively small mass and low surface temperature. The distribution of stars on the MS is related to the stellar mass and radius, and the mass–luminosity relation is empirically determined by

[1] **Oh Be A Fine Girl, Kiss Me!** is always used to assist students in remembering, suggested by Henry Norris Russell

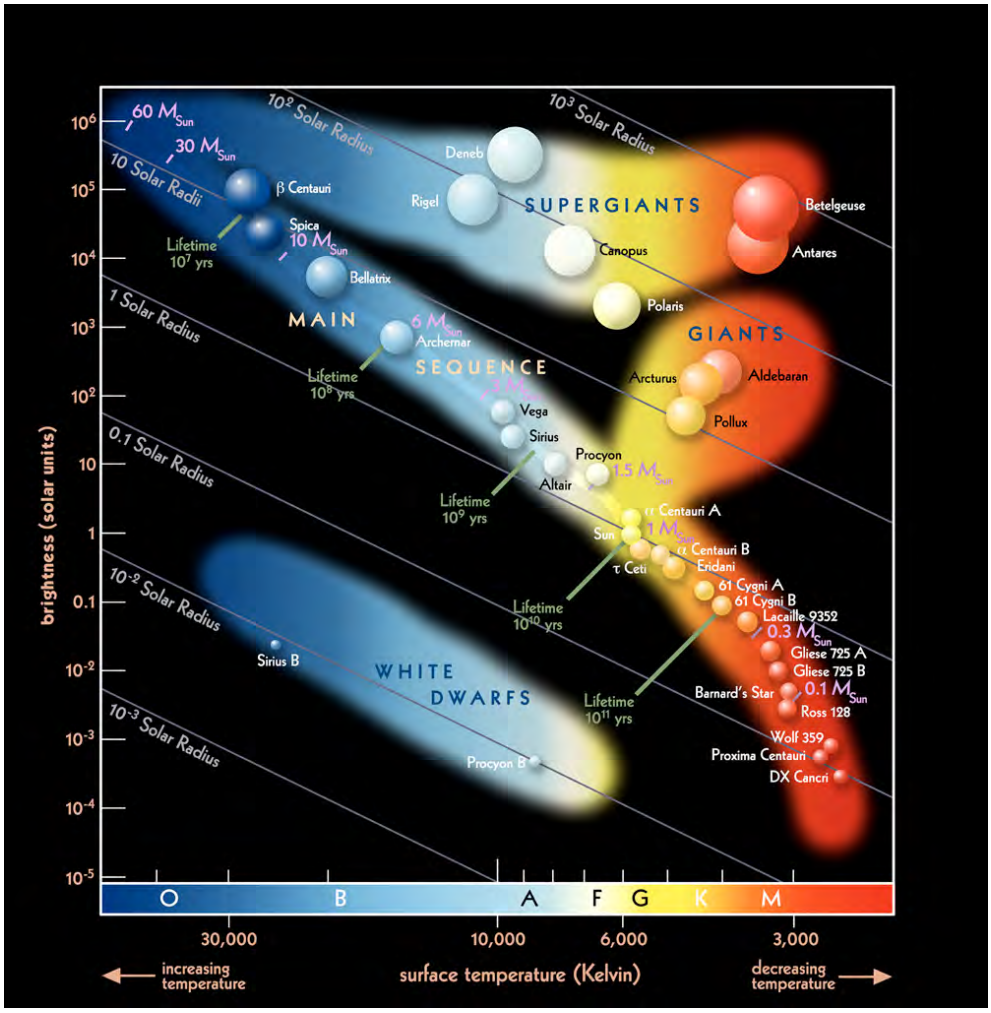

Figure 1.1.1: Hertzsprung-Russell diagram. Image Credit: ESO, source from https://www.eso.org/public/images/eso0728c/

(first noted by Kuiper 1938):

$$\frac{L_*}{L_\odot} \approx (\frac{M_*}{M_\odot})^a, \tag{1.1.1}$$

where the value of the exponent a is typically between 1 to 6, depending on the evolutionary stage and mass of the star (e.g., Henry et al. 1999; Malkov 2007).

1.1.2 Early evolution of late-type stars

The most widely accepted theory of star formation is based on the Nebula Hypothesis, proposed by Emanuel Swedenborg in 1734. It suggested that the Sun and the solar system were formed by a rotating cloud of gas, which collapsed under gravity, forming a disk centered on the Sun, at the origin of planets.

As a starting point, it is generally accepted that stars form from huge molecular

Figure 1.1.2: Pillars of Creation - molecular clouds within the Eagle Nebula(Credit: NASA)

clouds. They are typically more than 10 thousand times the mass of the Sun (Fukui & Kawamura, 2010). Fig. 1.1.2 shows Pillars of Creation, one of the most famous pictures of molecular clouds taken by Hubble telescope. Observations show that giant molecular clouds are primarily in a roughly equilibrium state, where the thermal motion counteracts the gravitational forces produced by the cloud itself. Owing to the onset of a gravitational instability, molecular clouds collapse and get fragmented, forming local nuclei with increased density. The surrounding gas keeps falling into the cloud nucleus, so that the mass of the core continues to rise, while the temperature and density of its center also increase. When the pressure in the center of the cloud nucleus rises to the same level as the gravitational pressure, and begins to establish the hydrostatic equilibrium, a protostar begins to develop. After this step, the surrounding gas continues to be accreted, so that the mass of the protostar continues to increase until it becomes a pre-main sequence star (PMS). Finally, its central temperature reaches the ignition temperature of hydrogen fusion. From then on, the protostar enters the zero-age main sequence (ZAMS), and starts its life cycle as a star.

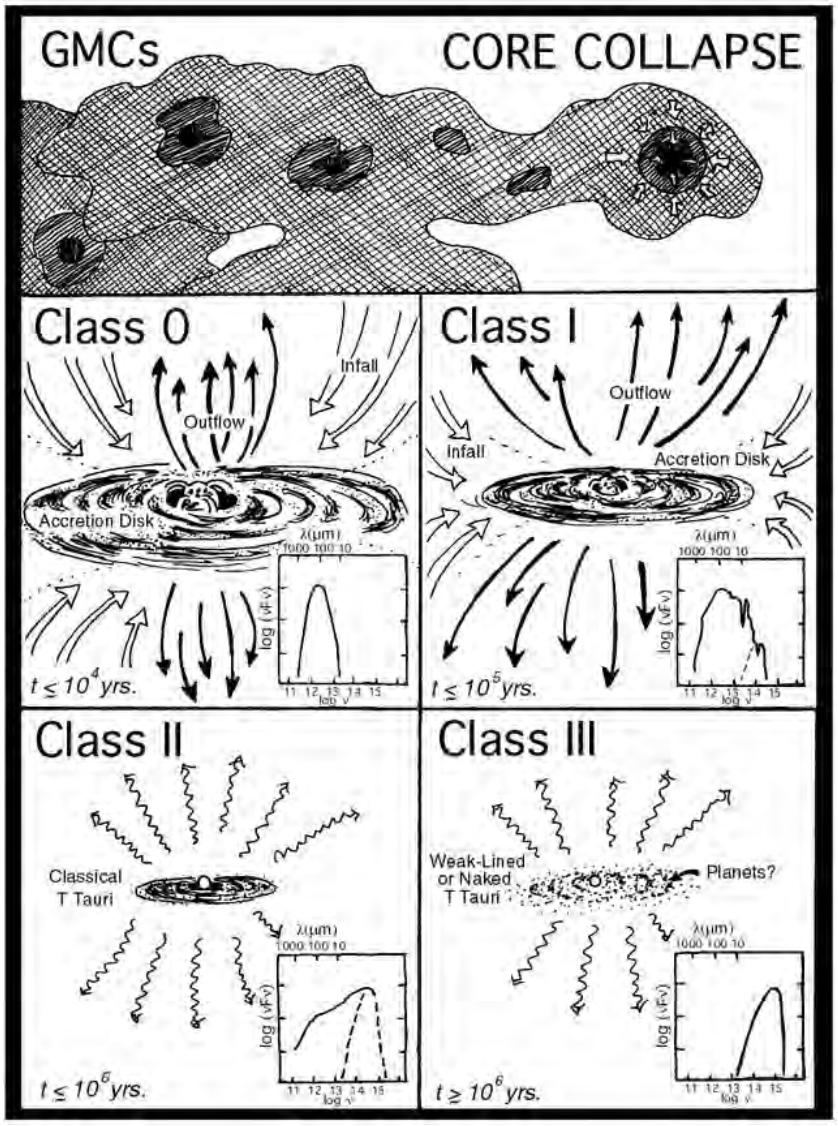

Figure 1.1.3: Schematic diagrams showing some of the key characteristics typical of different phases of low mass star formation. There is usually an overlap between in time between each of these phases. Figure from Yu (2000)

1.1.3 Low-mass star formation

In order to describe the instability of a MC, the Jeans mass M_J, named after James Jeans(Jeans, 1902), is used to determine the upper limit of the mass of the MC:

$$M_J = \frac{\pi}{6} \frac{c_s^3}{G^{\frac{2}{3}} \rho^{\frac{1}{2}}}, \tag{1.1.2}$$

where c_s is the sound speed in the gas, ρ the average density, and G is the gravitational constant. In other words, gas clouds will gravitationally collapse if their mass exceeds the local Jeans mass, until a prestellar core is generated.

Once a prestellar core has been formed, the subsequent evolutionary steps of the infant star are divided into four classes (e.g., Oswalt & Barstow (2013)). In general, Class 0 and I are called protostars, and Class II and III are PMS. A sketch of the process is illustrated in Fig. 1.1.3, taken from Yu (2000). The corresponding evolution of the spectral energy distribution (SED) of young stellar objects (YSOs) through the class 0 to class III of star formation in the figure shows the spectroscopic observational signatures of each class (e.g., Lada & Kylafis 1999; Andre et al. 2002).

- **Class 0 -** The protostar in this very early stage is formed by the free-fall collapse of the prestellar core. The majority of the mass of the core is in the envelope where the protostar is embedded. The heavy envelope makes the protostar almost invisible in the optical domain, so that it looks like an infrared point source with a blackbody emission. During this phase, jets and outflows can be visible, resulting from the strong magnetic field. The class 0 protostar keeps accreting material from the envelope and develops a massive disk, over a duration $\leq 10^4$yrs.

- **Class I -** The protostar enters the class I phase once around half of the initial core mass has been accreted. The star is still invisible in the optical domain, but the stellar radiation starts contributing to the SED. This stage is over in $\leq 10^5$yrs.

- **Class II/Classical T Tauri -** The YSO in this stage is also called Classical T Tauri stars (CTTs), and becomes a PMS. Most of the evelope has been accreted onto the star, and the star becomes visible. The dominant contributor to the SED is radiation directly from the stellar photosphere. The accretion disk, as well as outflows, still exist in CTTs, and strong Hα and X-ray emission are observed. This phase lasts for a few 10^6 yrs.

- **Class III/Weak-Lined T Tauri -** Once the disk is depleted of its gas content, the strong signatures of accretion and outflow that characterize the CTT phase also disappear. In the weak-lined T Tauri (wTT) phase, only very weak spectral signatures and a slight infrared excess from the disk remain. This phase is observationally difficult to distinguish from a main sequence star except that the star is rather over-luminous for its color as it has a larger radius than a main sequence star of the same mass as it is still contracting. During this phase the rest of the gas on the disk dissipates (leaving only a debris disk in some cases). Depending on the mass of the star this phase can take a few 10^7 years.

1.1.4 Internal structure of late-type dwarfs

The main chemical composition of a star is typically 70-75% hydrogen (in mass), $\sim 25\%$ helium, and a small amount of heavy elements. The energy source of a MS star is mainly fusion reactions from hydrogen to helium, which happens in the core of the star. For late-type MS stars, there are two main types of conversion: the proton–proton chain (p-p chain) and the carbon–nitrogen–oxygen cycle (CNO cycle). Both of these possible channels were established by Hans Albrecht Bethe in late 1930s, as part of

his work in stellar nucleosynthesis, which won the Nobel Prize in Physics in 1967. MS stars with masses $M_* \geq 1.5M_\odot$, which possess higher-temperature cores, have their nuclear reactions dominated by the CNO cycle, while stars with lower masses ($M_* \leq 1.3M_\odot$) host a predominent p-p chain (Salaris & Cassisi, 2005). Outside of the core, the temperatures and pressures are not high enough to ignite nuclear fusion. The heat transfer dominates the remaining structure of the star, and is generally determined by the possible predominance of two processes: radiation and convection. In the radiation zone, the effect of the internal plasma on the radiation is manifested by the absorption, emission, and scattering processes. This region is stable compared to the convection zone, with bulk buoyant motions (typically loops) of plasma driven by a steep radial temperature gradient.

The actual structure depends on the mass of the stars. The CNO cycle is highly sensitive to the local temperature, with $\epsilon_{\rm CNO} \propto T^{20}$, where $\epsilon_{\rm CNO}$ is the energy generation rate (i.e., energy generated by mass and time units), and T is the local temperature. The p-p chain is less dependent on temperature, with $\epsilon_{\rm pp} \propto T^4$. For stars with $M_* \geq 1.5M_\odot$, the CNO cycle dominates and the core is convective because of the steep temperature gradient, while radiation transports the heat throughout the outer envelope. For stars with masses between 0.5 and 1.5 $M_\odot$ (e.g., F-G-K dwarfs), the hydrogen is converted to helium predominantly via the p-p chain. The core temperature gradient is less steep, so that they have a radiation zone in the central portion of the star. Since the outer layers of these intermediate mass stars is cool enough, they have a convective envelope. The very low mass MS stars (e.g., M dwarfs) with $M_* \leq 0.5M_\odot$ have small or no radiation zones, resulting in an almost fully convective interior (Hansen et al., 2004).

In part of our work, we focus on a solar analogue with a convective envelope, which just settles on ZAMS. Nuclear fusion just started to become the dominant energy source of these stars, while the contraction is nearly but not over. It would be particular interesting to explore the evolution state of this kind of young stars.

1.2 Stellar activity in late-type star

1.2.1 Magnetic activity and the global dynamo

The atmosphere of late-type stars can host strong and complex magnetic fields, responsible for the non-radiative heating of the corona (e.g., Kuperus 1969). In some cases, stellar magnetic activity can be similar to that observed on the Sun, but very different manifestations are also observed. The physical mechanisms believed to drive stellar magnetic activity are grouped in a so-called a *dynamo* (see Brun & Browning 2017 for a review), which is based on the coexistence of the convection zone under the stellar surface and the large-scale shear generated by the internal differential rotation (e.g., Fig. 1.2.1 for surface differential rotational in solar case). For solar-like stars with a radiative core and a convective envelope, it is widely accepted that the $\alpha - \Omega$ dynamo type (e.g., Krause & Raedler 1980; Spiegel & Zahn 1992) dominates the global amplification of the magnetic field. The differential rotation contributes to transforming the initially poloidal field

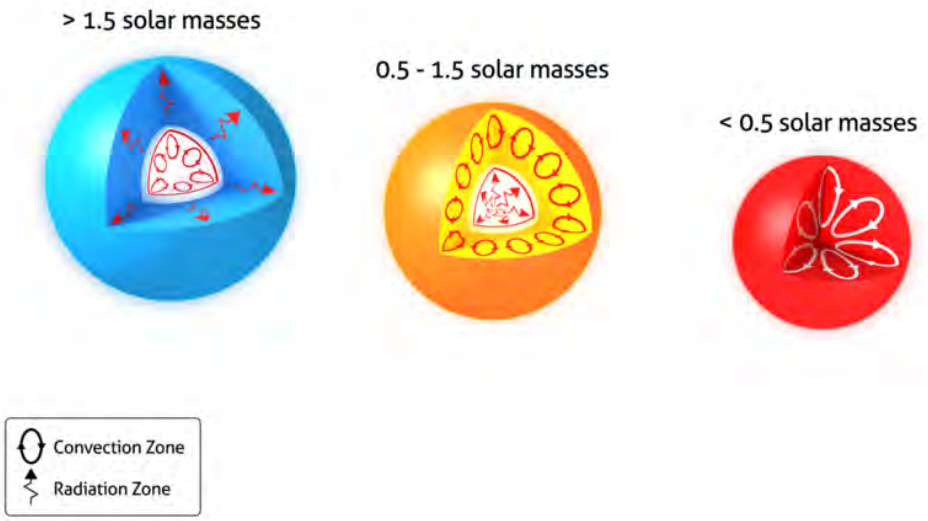

Figure 1.1.4: Types of heat transfer for different mass regimes. Credit: Sun.org

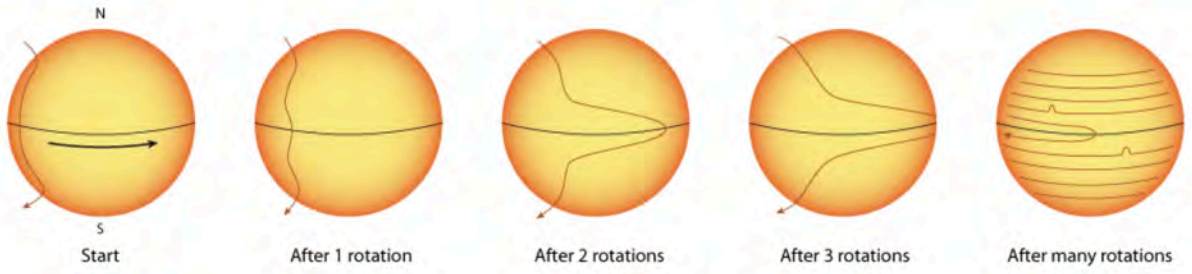

Figure 1.2.1: Conversion of a poloidal magnetic field into a toroidal field through differential rotation.

into a toroidal component (the Ω effect). The interplay between turbulent convection and rotation twists the toroidal field lines, regenerating the poloidal component (the so-called α effect). The coupling of these two effects succeed to continuously amplify the magnetic field and contribute to the variability observed as magnetic activity.

For fully convective stars like M-dwarfs, the $\alpha - \Omega$ dynamo paradigm cannot explain the observed activity, due to the absence of a radiative-convective interface. Different types of dynamos (e.g., α^2 dynamo Chabrier & Küker 2006) were proposed to explain the presence of magnetic activity in these very low-mass stars. It is likely that such an alternate dynamo can co-exist with an $\alpha - \Omega$ dynamo in the most active Sun-like stars, for which evidence is accumulating of an efficient dynamo action in the bulk of the convection zone (Donati et al., 2003b). Since, in many cases, current dynamo theories are not enough to fit the vast diversity of the observed active phenomena (e.g., the solar cycle itself), additional dynamo mechanisms are regularly invoked (e.g., Babcock 1961) to improve the situation, without any consensus up to now about the exact physical ingredients entering this complex mechanism.

Gathering observational constraints on stellar magnetism can obviously enrich the testing of dynamo models (primarily developed for the Sun), since a wide parameter space can be explored with stars in the solar neighbourhood. Beside the origin of stellar magnetic fields, stellar observations can also improve our understanding of the impact of the dynamo on the outer stellar atmospheres (i.e., the photosphere, the chromosphere, the transition region, and the corona). The magnetic flux tubes produced by the dynamo in the convection zone (e.g., Caligari et al. 1995) result in prominent phenomena at the photospheric level, such as starspots and faculae (see Sec. 1.2.2). The stellar magnetic field is also the primary source of activity in the outermost layers (the chromosphere, the corona, and the stellar wind) of a star (see recent reviews of Hall 2008 and Vidotto 2021). A typical manifestation of magnetism above the photosphere are the local gas accumulations called prominences featuring a chromospheric temperature, supported by magnetic loops, and plunging into the stellar corona.

1.2.2 Surface activity

In the photosphere, darker regions with a local temperature lower than the effective stellar temperature are called "starspots". On the contrary, the bright patches with a temperature higher than the quiet photosphere are called "faculae", with chromospheric counterparts called "plages". Both starspots and faculae are transitory regions created by strong local magnetic fields. Fig. 1.2.2 illustrates a typical distribution of active regions on the solar surface. Their spectroscopic signatures have been observed in a number of active stars, sometimes with a surface coverage much higher than observed on the Sun (Strassmeier, 2009).

Information on surface magnetic activity is mainly obtained from the following methods:

- **Direct Imaging and interferometry -** Getting a direct image of a stellar surface, or obtaining a surface view through interferometry, has been possible for a

small number of evolved stars close to the Sun (See Sec. 2.1.1). However, for the vast majority of late-type stars, current technology does not allow us to obtain a high spatial resolution image directly.

- **Photometric lightcurves -** Broad-band photometric monitoring gives access to brightness variations created by the rotational modulation of active regions or by activity cycles (e.g., Eaton & Hall 1979; Rodono et al. 1995; Lanza et al. 2003, 2004). High-precision space photometers (e.g., *COROT*, *MOST*, *Kepler*) can provide continuous lightcurves that reveal the rotational properties of large samples of stars. Photometric time series can be inverted to reconstruct a distribution of spots and facula, but because of the mutual cancellation of spots and faculae, simple models including a limited number of circular spots are not suitable to obtain a fair description of the complex brightness distribution of an actual active star (Vogt et al., 1999).

- **Doppler Imaging (DI) -** Thanks to the rapid rotation rates of some active stars, spots located at different longitudes have different relative velocities with respect to the observer depending on their position on the projected stellar disk. This results in Doppler shifts in spectral line profiles, and this additional information can be used to reconstruct the surface location of brightness inhomogeneities. Using a time series of spectra collected at different rotational phases, DI is an indirect method reconstructing the 2-D image of the surface brightness distribution. A detailed description of this approach will be documented in Sec. 2.2.

- **Zeeman Doppler Imaging (ZDI) -** Is similar to DI in its principle, but ZDI introduces the Zeeman effect into the model and uses spectropolarimetric observations. ZDI is able to reconstruct the large-scale magnetic field geometry, in addition to the brightness. A detailed description can be found in Sec. 2.3.

All these methods suffer from a limited spatial resolution, and accurately reconstructing spots as small as those observed on the solar surface is out of reach as of today. For the most active stars, however, spotted areas can cover up to 20% of the entire stellar surface, versus about 0.1% for the Sun (Kővári et al., 2007; Strassmeier, 2009), with large individual spots. Maps of temperature or brightness can be reconstructed by DI (e.g., Berdyugina 2005 for a review). The typical temperature difference between spots and the quiet photosphere ranges from about 2000K in Sun-like stars to 200K in M dwarfs (see Schrijver & Zwaan 2000 for more details). Polar spots are found in more than half of stars with available Doppler maps (Pagano, 2013), unveiling brightness distributions very different from the Sun. Large-scale magnetic fields mapped by ZDI also show features never observed in the solar case e.g., strong toroidal fields (Donati et al., 2003a, 2014, 2016). Evolutionary time scales of starspots is typically tens of days, with longer lifetimes from months to years also reported for the largest structures like polar spots (see Hussain 2002 for a review). Starspots can create spectroscopic signatures similar in their timescale and amplitude to the Doppler shifts generated by exoplanets around the

star, resulting in an activity noise that must be mitigated to detect exoplanets detection around the most active stars (Hatzes, 2002; Dumusque et al., 2017).

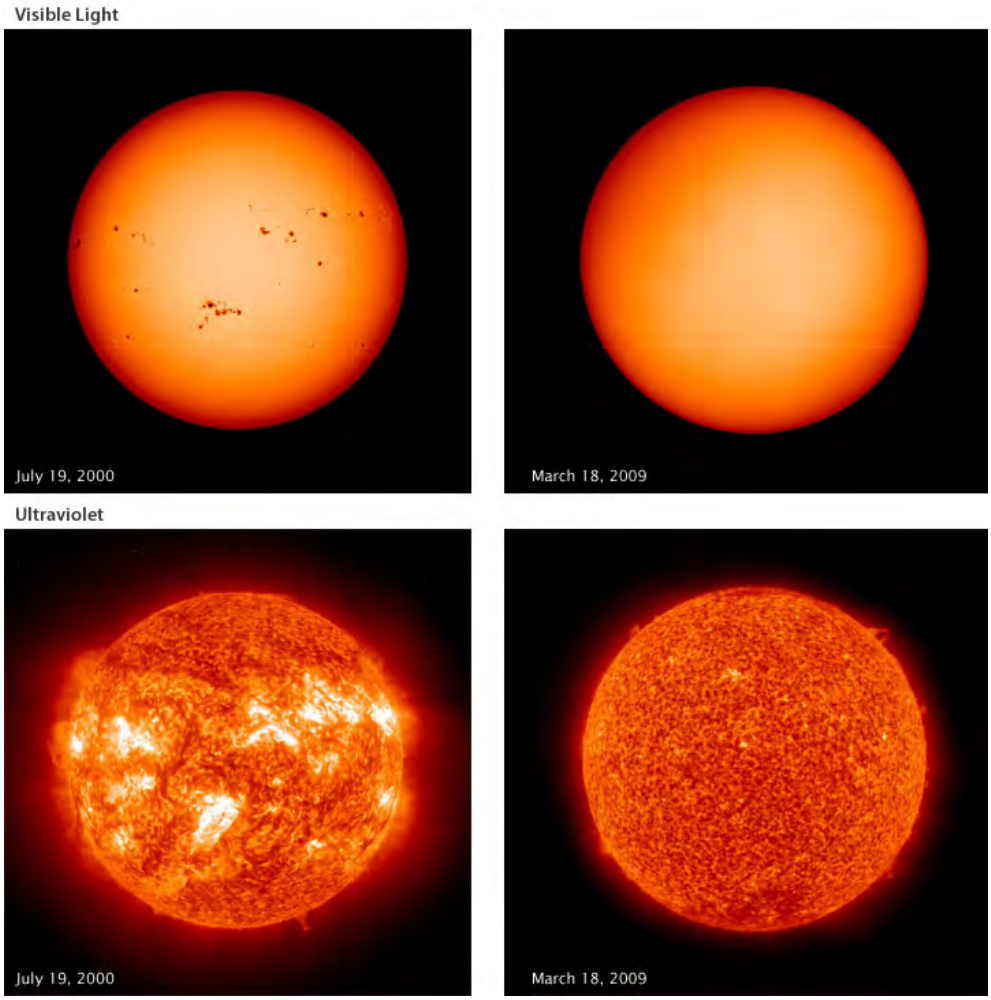

Figure 1.2.2: The Solar surface in different wavelength domains, as observed by the Solar and Heliospheric Observatory (SOHO) spacecraft, during a period of high solar activity (left), and low activity (right). Top pairs are taken in visible wavelengths, where solar spots can be well seen. Bottom pairs are obtained in the extreme ultraviolet. The very bright patches are associated with plages. Image courtesy SOHO, EIT Consortium, and the MDI Team.

1.2.3 Prominences and Stellar wind

In the solar case, prominences always appear as bright arcade-like structures on or above the solar limb, with temperatures at chromospheric level ($7 \times 10^3 \leq T \leq 2 \times 10^4$ K, Stix 2004). As a consequence of the low temperature (compared to the surrounding corona at $\sim$ 1MK), the prominence core is partially-ionized. Subsequently, prominences

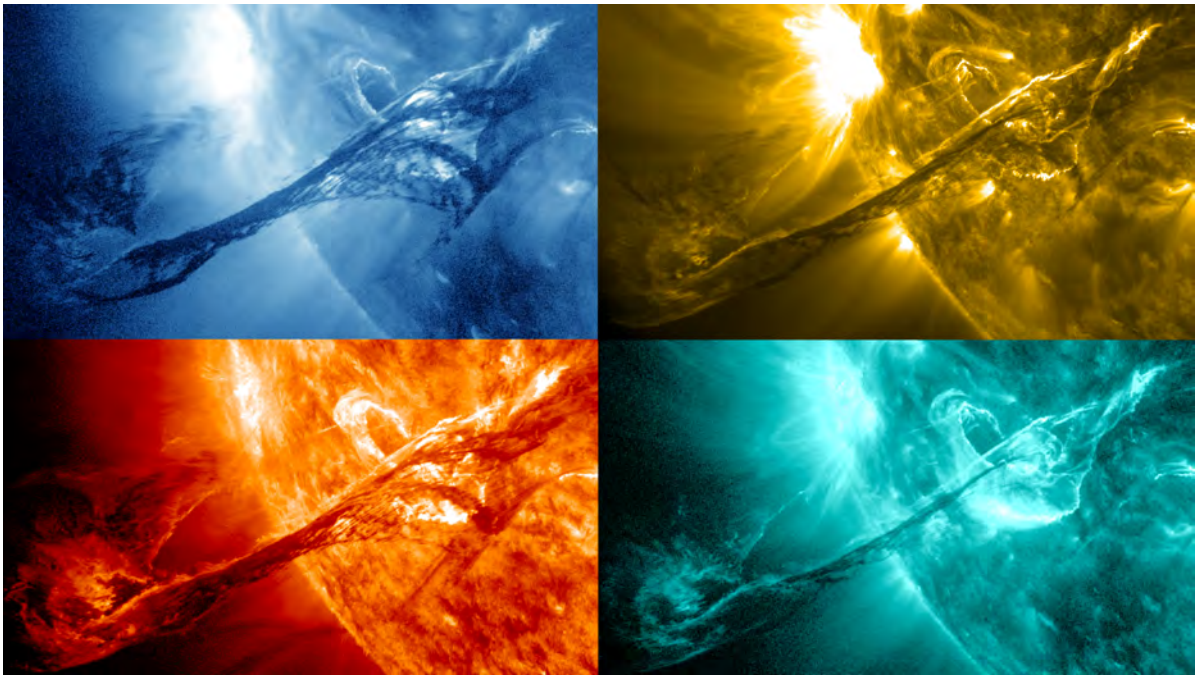

Figure 1.2.3: Four images of a filament on the sun observed on August 31, 2012. The panels show various radiation wavelengths, as captured by NASA' s Solar Dynamics Observatory (SDO). Starting from the upper left and going clockwise they represent wavelengths of: 335, 171, 131 and 304 Angstrom. Credit: NASA/SDO/AIA/GSFC

are optically thick to certain chromospheric lines (e.g., most of the hydrogen and helium lines). On the disk, they appears as dark, thin curves, and historically so-called *filaments*. Fig. 1.2.3 shows a picture of a large prominence arc (filament) in different wavelengths. The typical length of filaments varies from 3×10^4 to 1.1×10^5 km, and they can last from days to weeks (e.g., see the recent review on solar prominences from Parenti 2014).

The very first observational evidence of cool prominences was reported for binary stars through the pencil-beam method (i.e., the eclipse detection of prominences, e.g., Schroeder 1983; Jensen et al. 1986). Evidence was also collected for prominences in a small number of active G and K stars (Donati et al., 2000; Dunstone et al., 2006a), M-dwarfs (Byrne et al., 1996; Eibe, 1998), and PMS stars (Skelly et al., 2008, 2009). The spectral signatures of these condensations are usually extracted from Balmer lines, and around rapidly rotating stars the centrifugal force takes an active part in the equilibrium and evolution of the prominence clouds, which are dubbed *slingshot prominences* (see the review of Collier Cameron 1999). The typical mass of the slingshot prominence systems is between 10^{17} and 10^{20} g, with a lifetime of individual structures of the order of few days (Villarreal D'Angelo et al., 2019). When spectral signatures are seen in emission (i.e., mainly if the line-of-sight inclination of the stellar rotation axis is small), the spatial distribution of prominences can be reconstructed through tomographic models inspired from the observation of cataclysmic variables (Donati et al. 2000; Barnes et al. 2001, see Sec. 2.4).

Slingshot prominences contribute to the stellar winds, remove mass and angular momentum from stars (see review of Vidotto 2021). They, therefore, contribute to the early evolution of active stars as well (Aarnio et al., 2012; Jardine et al., 2020). As suggested by Jardine & Collier Cameron (2019), prominences in active stars are mainly observed at an altitude comprised between the sonic point and the Alfvén radius. One can thus estimate the mass-loss rate through stellar winds from the mass and dynamics of the prominence system. For young sun-like stars, the mass-loss rates estimated through this method can be hundreds to thousands of times larger than in the solar case (e.g., Donati et al. 2000; Dunstone et al. 2006b; Cang et al. 2020).

1.2.4 Rotation-Activity relationship

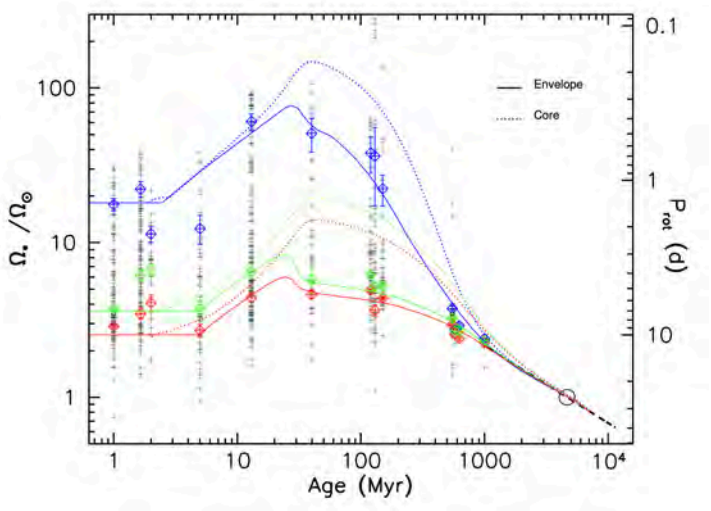

Figure 1.2.4: The rotational evolution of solar-type stars. Black crosses mark solar-type stars in known associations and young open clusters. The associated red, green, and blue diamonds represent the 25, 50, and 90th percentiles of the observed rotational distributions. The Sun lies at the right-bottom corner (black circle). Theoretical models are made for the convective envelope (solid line) and the radiative core (dashed lines). Rotator models of slow (red), median (green), and fast (blue) rotators have initial periods of 10.0, 7.0, and 1.4 days, respectively. The dashed black line shows the asymptotic Skumanich's relationship (Skumanich, 1972), $\Omega \propto t^{-0.5}$. Figure extracted from Gallet & Bouvier (2013)

. .

Stellar rotation is the main driver of the activity of Sun-like stars, through the onset of a global dynamo. This parameter evolves a lot during stellar evolution, with important consequences on stellar properties throughout the lifetime of the star (e.g., Ekström et al. 2012). Fig. 1.2.4, extracted from Gallet & Bouvier (2013), shows the rotational evolution of young solar-type stars. After the age of $\sim$ 1 Gyr, the rotational rate Ω roughly follows $\Omega \propto t^{-0.5}$, in agreement with the early work of Skumanich (1972). In the

early stage of evolution, however, angular momentum from stellar birth, combined with stellar contraction, produces a population of very rapidly rotating stars characterized by an intense magnetism.

The consequence of rapid rotation on the dynamo can be observed through a number of indirect activity tracers. This is the case, for example, in Ca II H&K emission (Noyes et al., 1984), X-ray flux (Wright et al., 2011), or photometric variability due to spots (Walkowicz & Basri, 2013) and flares (Davenport, 2016). However, for stars with sufficiently large rotation rates (typically $P < 0.3$d), magnetic activity seems to reach an upper limit. The exact rotation threshold for saturation depends on the magnetic tracer taken into account. X-ray observations clearly highlight this so-called saturation phenomenon (Pallavicini et al., 1981; Prosser et al., 1996; Wright et al., 2011), as well as Zeeman broadening measurements (Reiners, 2012) or large-scale magnetic field measurements (Vidotto et al., 2014; See et al., 2019). When the rotational rate is even larger, coronal activity decreases again, as shown in Fig. 1.2.5 adopted from Randich (2000). Supersaturation is not found in M dwarfs Jeffries et al. (2011), which may be a result of the fully convective interior.

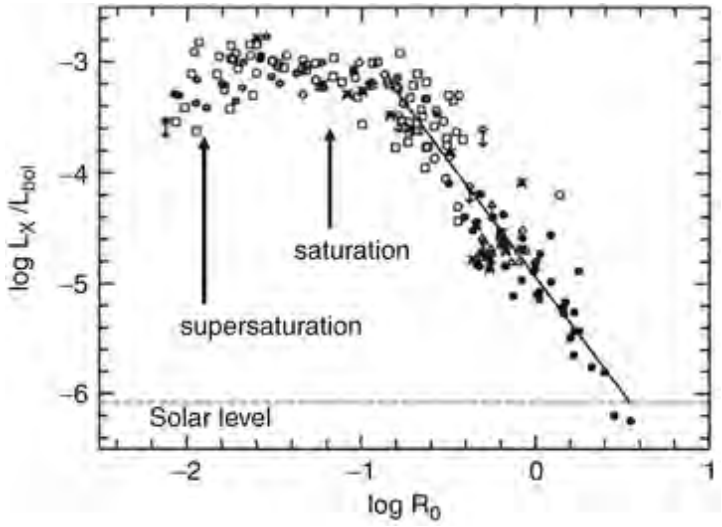

Figure 1.2.5: X-ray activity level (given as the ratio of X-ray emission to the bolometric luminosity) as function of the Rossby number $R_0 = P_{\rm rot}/\tau_c$ (where $P_{\rm rot}$ is the stellar rotation period and τ_c is the convective turnover time). Taken from Fig. 10-20 of Oswalt & Barstow (2013)

Chapter 2

Modeling the stellar activity and magnetic fields with tomography

2.1 Image reconstruction

2.1.1 Basic principle of tomography

The diffraction limit of telescopes does not allow us to obtain a detailed image for a distant star directly. As shown in Fig. 2.1.1, one of the most precise stellar image was taken through submillimeter interferometry observations of Betelgeuse with ALMA (O'Gorman et al., 2017).

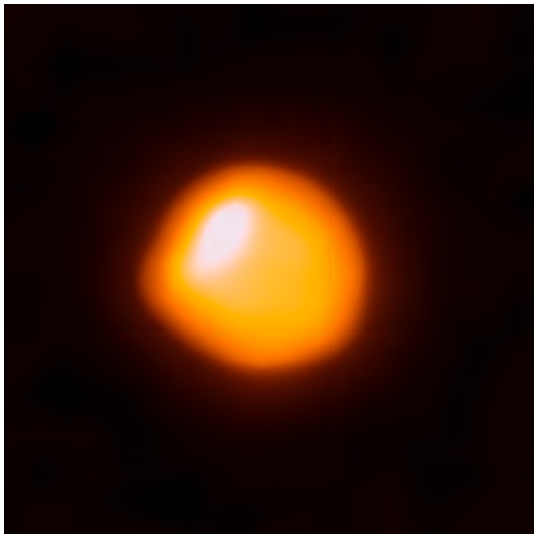

Figure 2.1.1: ALMA image of Betelgeuse, which shows the inhomogeneous atmosphere. Image taken from O'Gorman et al. (2017).

Another recent result, using long-baseline infrared interferometry, provided us with brightness images of the rapid rotating giant star ζ Andromedae (Roettenbacher et al., 2016), and shown clear polar dark spots (Fig.2.1.2).

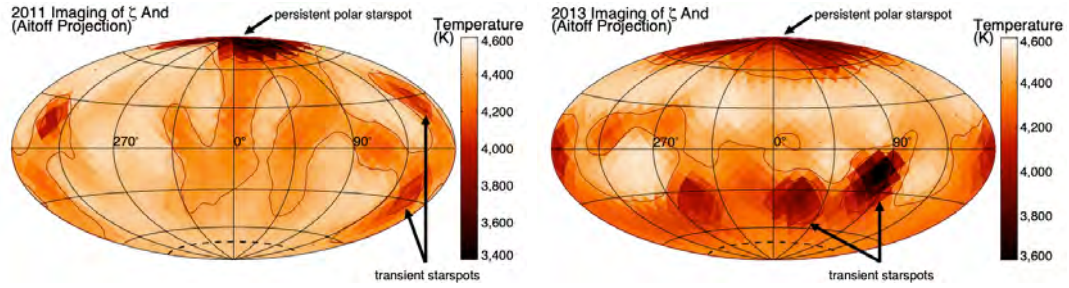

Figure 2.1.2: Long-baseline infrared interferometry images of ζ Andromedae in the year 2011 (left) and 2013 (right). Long lived, large dark spots are observed on the polar region, while smaller dark spots, seen at lower latitudes, come and go. Images taken from Roettenbacher et al. (2016).

The stellar size and brightness of our main target in this work (the G dwarf V530 Per, $\sim$ 168pc) is too small to resolve the surface structure by direct imaging. Taking advantage of the rotation of the star, we can obtain information at different rotational phases. Assuming that the stellar surface brightness is stable and nonuniform, observations at different phases (e.g., spectra) can be used to recover the brightness distribution. This indirect imaging process can be expressed in the general framework of a linear inverse problem:

$$D = IR + e. \tag{2.1.1}$$

where D is the observational data D with noise e, the known operator (model) R, and the unknown actual image I. In practice, we will discuss the noiseless linear inverse problem ($e = 0$) for focusing on the key features. We can reconstruct an indirect image of a star by solving this inverse problem. The process is also called *tomography*, to make an analogy with industrial tomography (e.g., tomography scan as a medical imaging technique).

2.1.2 Maximum entropy image reconstruction

Most inverse problems, including tomography, are ill-posed (or improperly-posed), which means that the solution of the model to describe a system is generally not unique, and the inverse operator R^{-1} is not continuous. For tomography, in order to get an approximate solution, numerical methods are widely applied. In this thesis, we used the maximum entropy method (MEM) as an optimal technique for image reconstruction, based on the implementation of Skilling & Bryan (1984).

An image can be divided into a grid of pixels with a positive quantity f_j being attributed to the jth pixel. The entropy S of image is defined by:

$$S = -\sum p_j \log(p_j), \qquad p_j = f_j / \sum f. \tag{2.1.2}$$

The selected image, which maximizes the entropy among all possible images, will feature minimized spatial information and the least contrast between the features and

background (e.g., spots versus the quiet stellar photosphere). Note that MEM is the *least arbitrary* selection of a solution for the image reconstruction (Shore & Johnson, 1980; Skilling & Bryan, 1984). To further constrain the model fitting, the algorithm introduces a χ^2 to describe the misfit between the observational data D_k with uncertainty σ_k and the corresponding solution given by the model F_k (Gull & Daniell, 1978):

$$\chi^2 = \sum_j (F_k - D_k)^2 / \sigma_k^2. \tag{2.1.3}$$

Working iteratively through a conjugate gradients approach, the MEM can efficiently approach a solution by seeking a maximum of $Q = S - \lambda\chi^2$, where λ is the Lagrange multiplier. The resulting solution is unique.

2.2 Doppler Imaging

2.2.1 Spectral line profile of a spotted star

Doppler imaging (DI) is a powerful technique for mapping stellar surface structures, by reconstructing spatial information from high-resolution, time-resolved spectral line profiles. The idea was first expressed by Deutsch (1958), mapping the magnetic field of periodic spectrum variables. The first successful application of Doppler imaging for a spotted star was achieved for the RS CVn-type star HD 1099 by Vogt & Penrod (1983). The line profile shape of a rapidly rotating star is dominated by the rotational Doppler broadening, so that each point on the profile can be attributed to a region of the stellar surface with the same radial velocity (e.g., Fig. 2.2.1). As first described by Vogt et al. (1987) (Fig. 2.2.2), DI is more powerful to reconstruct surface brightness on the star by applying the MEM. So far, the applications of DI reveal the brightness structure, especilly the polar spot, of a number of cool stars (e.g., LQ Lup, AB Dor, EK Dra, AP 193, He 520, He 699, Donati et al. 2000; Donati & Collier Cameron 1997; Donati et al. 2003a; Strassmeier & Rice 1998; Waite et al. 2017; Järvinen et al. 2018; Barnes et al. 2001). Further more, filtering the information of inhomogeneous brightness can help to detect minor signal from the star (e.g., detecting exoplanets around active stars, Donati et al. 2016).

Our implementation of DI to model the stellar surface brightness is based on time-resolved spectroscopic (Stokes I) observation. The surface of the star is divided into a grid of pixels whose edges lie along lines of latitude and longitude with the area of each pixel being roughly the same, as described by, e.g., Vogt et al. (1987). An example is shown in Fig. 2.2.4. Each pixel is linked to a corresponding local line profile and radial velocity. Here, a simple Gaussian function, with a central wavelength that is set to the equal wavelength of the LSD profile (See Sec. 2.3.2 for details) was used to produce local line profiles. In addition to a projection factor depending on the limb angle, and a scaling following the brightness map, the continuum is re-scaled to follow a linear limb darkening law of the following form (e.g., Gray, 2005):

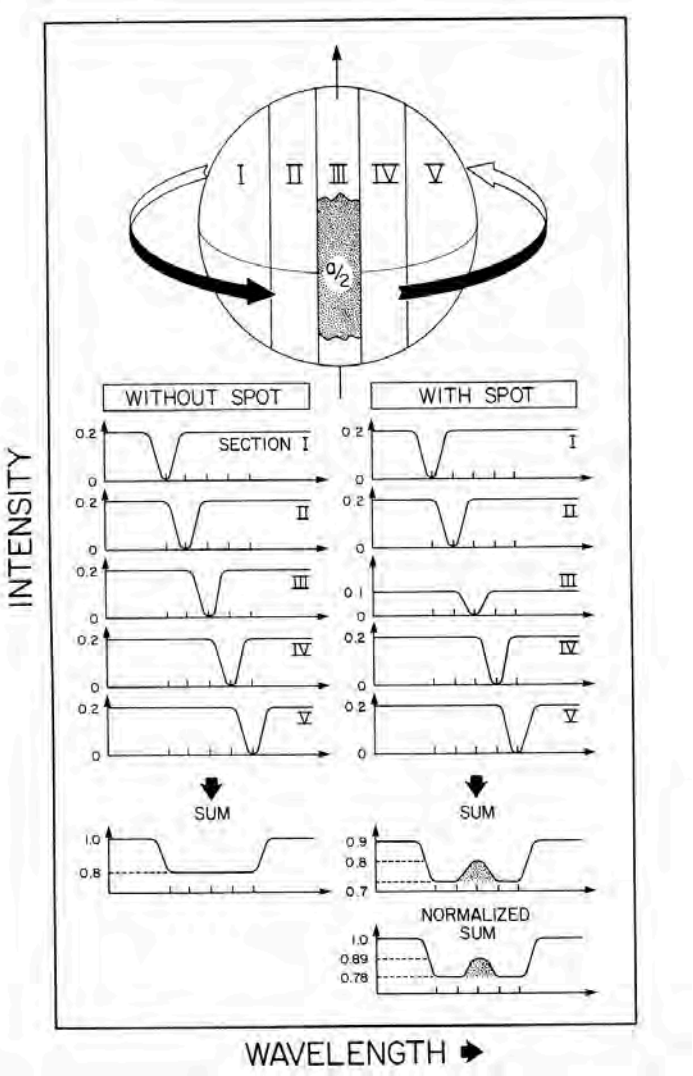

Figure 2.2.1: Illustration of the formation of positive bumps in the absorption lines of a rapidly rotating, spotted star. Image taken from Vogt & Penrod (1983).

$$I_c/I_c^0 = 1 - \eta + \eta\cos(\Phi) \tag{2.2.1}$$

where η is the limb darkening coefficient, Φ is the angle from disk center, and I_c/I_c^0 is the ratio between local brightness (I_c) and the central brightness (I_c^0) at the limb angle Φ. Variations in local line depth relative to the local continuum as a function of the limb angle are neglected. The final line profile is a sum of all visible surface elements (Fig. 2.2.3).

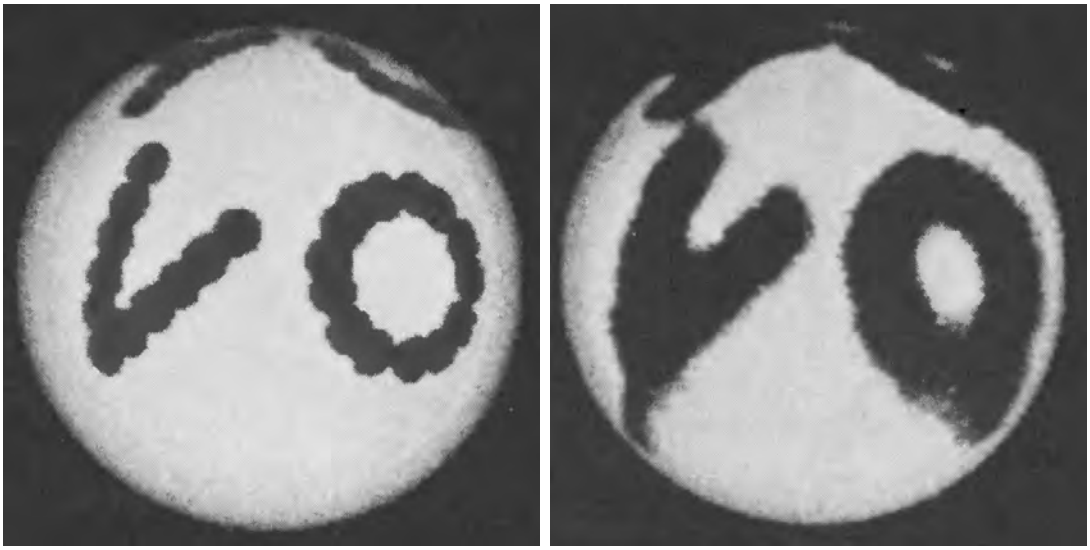

Figure 2.2.2: Artificial spotted star and reconstructed structures by Doppler imaging. Extracted from Vogt et al. (1987)

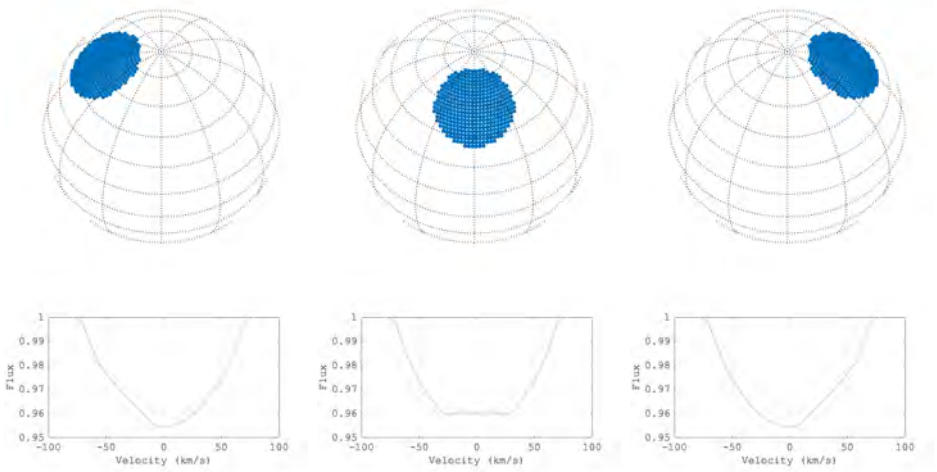

Figure 2.2.3: Samples of line profile variations due to a dark spot. The inclination of the stellar spin axis is taken equal to 40°, the spot brightness is equal to 60% of the unspotted brightness.

2.2.2 Oblate stellar shape

The shape of rapidly rotating stars is oblate. In this situation, the surface brightness varies with the latitude due to gravity darkening (von Zeipel, 1924). On the equator of star, a lower effective gravity is linked to a lower brightness, compared to the poles. Fig. 2.2.5 shows recent high angular resolution observations of rapid rotators, all featuring an oblate shape (Monnier et al., 2007; Zhao et al., 2009; Che et al., 2011).

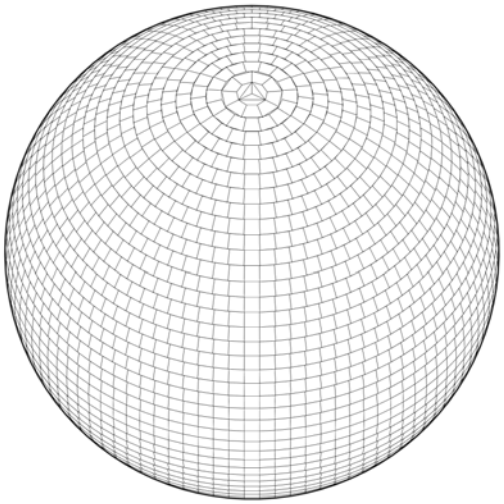

Figure 2.2.4: Example of surface grid division. The surface is divided up into 50 latitude rings. At this inclination of 40°, a total of 3186 zones are required to cover the visible portion of the star.

In most published DI studies, the stellar surface is assumed to be spherical, implying that the rotational oblateness is neglected. Considering for simplicity the hydrostatic equilibrium in an incompressible, uniform-density star, we obtain to first order (see Tatebe et al. 2007):

$$\frac{R_p}{R_e} \approx 1 - \frac{3\Omega^2}{8G\pi\rho} \tag{2.2.2}$$

where R_p and R_e stand for the polar and equatorial radii, Ω for the rotational rate, G for the gravitational constant and ρ for the density. This rough approach can provide us with an order of magnitude of the oblateness for V530 Per, for which we obtain $R_p/R_e q \approx 0.92$. Since the oblateness cannot be neglected in such a rapid rotator, we modified the local velocities assuming that the stellar surface shape can be described by a Roche model (named after Edouard Albert Roche) (Tassoul, 1978), in which the equipotentials $\Phi(R_*, \theta)$ include a centrifugal term:

$$\Phi(R_*, \theta) = -\frac{GM_*}{R_*} - \frac{1}{2}\Omega^2 R_*^2 \sin^2\theta \tag{2.2.3}$$

where R_* is the stellar radius at colatitude θ. Since the whole stellar surface belongs to the same equipotential, the potential of each point should be the same as the potential of the pole ($\theta = 0$):

$$-\frac{GM_*}{R_p} = -\frac{GM_*}{R_*} - \frac{1}{2}\Omega^2 R_*^2 \sin^2\theta \tag{2.2.4}$$

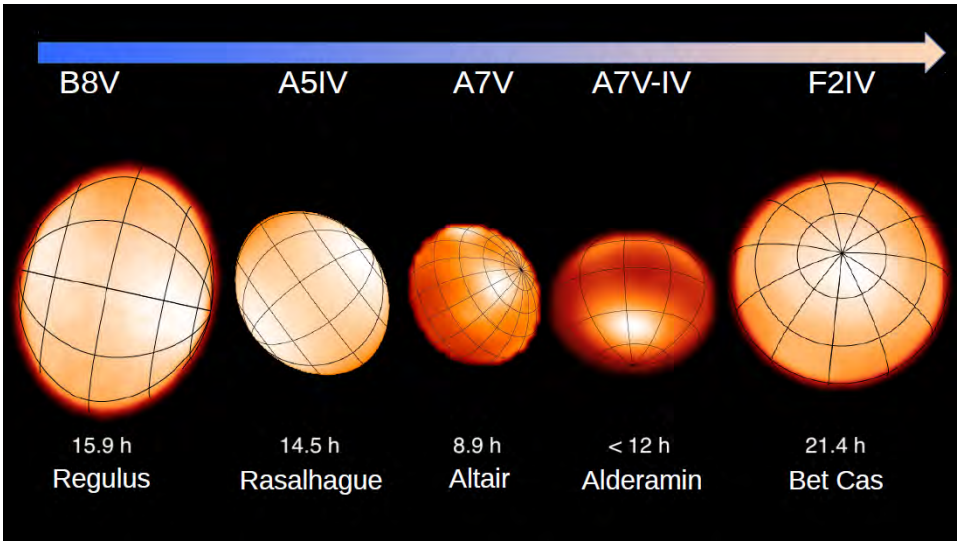

Figure 2.2.5: Images of rapid rotators by infrared interferometry. They all feature a clear oblate shape. Credit: CHARA array.

where R_p is the polar radius of the star. The break-up angular velocity Ω_c is reached when the centrifugal force at the equator ($R_* = R_{eq}$) is equal to the gravitational force:

$$\frac{GM_*}{R_{eq}^2} = \Omega_c^2 R_{eq}. \tag{2.2.5}$$

By substituting Ω_c into Eq. 2.2.4, we obtain the maximal value of $R_{eq} = R_*(\pi/2)$, equal to $R_{eq} = 3/2R_p$. Defining the fractional angular velocity $\omega = \Omega/\Omega_c$, Ω can be expressed as:

$$\Omega = \omega\sqrt{\frac{8GM_*}{27R_p^3}} \qquad 0 \leq \omega \leq 1. \tag{2.2.6}$$

Taking $x = x(\omega, \theta) = R_*(\theta)/R_p$, Eq. 2.2.4 can be expressed by:

$$\frac{4}{27}\omega^2 x^3 \sin^2\theta - x + 1 = 0, \tag{2.2.7}$$

the first trigonometric solution of this cubic equation describes the surface shape: (Collins, 1965; Collins & Harrington, 1966; Cranmer, 1996):

$$x(\omega, \theta) = \frac{3}{\omega \sin\theta} \cos[\frac{\pi + \cos^{-1}(\omega \sin\theta)}{3}]. \tag{2.2.8}$$

Fig. 2.2.6 displays surface shapes calculated by Eq. 2.2.8 for different values of ω. Taking $\theta = \pi/2$, the oblateness obtained for V530 Per is $R_p/R_e \approx 0.91$, in agreement with our first approach. One can then define the effective gravity $\mathcal{G}$, as well as its radial (g_r) and latitudinal (g_θ) components:

$$g_r = -\frac{\partial\Phi}{\partial r} = \frac{GM_*}{R_p^2}(-\frac{1}{x^2} + \frac{8}{27}x\omega^2\sin^2\theta), \tag{2.2.9}$$

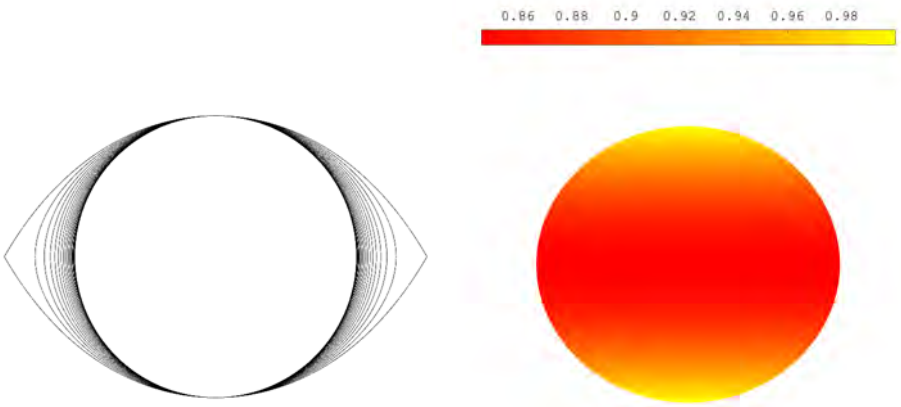

Figure 2.2.6: (left) Meridional cross sections of surface shapes obtained from a Roche model, for ω between 0 and 1 with increments of 0.05. (right) gravity darkening of V530 Per with $b = 0.1$.

$$g_\theta = -\frac{1}{r}\frac{\partial \Phi}{\partial \theta} = \frac{GM_*}{R_p^2}(\frac{8}{27}x\omega^2 \sin\theta\cos\theta), \tag{2.2.10}$$

with $\mathcal{G}^2 = g_r^2 + g_\theta^2$. The non-uniform $\mathcal{G}$ is linked to a non-uniform brightness distribution, the so-called gravity darkening. Following the prescription of Lucy (1967), the brightness is therefore assumed to vary as g^{4b}, where g is the normalized effective gravity with $g = 1$ at $\theta = 0$, and b is the gravity darkening coefficient. The exact value that should be used for b is still a matter of debate today (see van Belle 2012 for a review). Lucy (1967) presented a rough approach for the cool stars (for convective envelopes) of $\beta = 4b = 0.32$. Claret (1998) developed more smooth method to calculate β, and different value can be applied for particular stellar parameters. In our work for the young Sun V530 Per (Sec. 3.4.1), we applied here a different value $\beta = 0.46$, which is interpolated from the table of Claret & Bloemen (2011) according to the fundamental parameters of the star, and results in an equatorial brightness equal to $\sim$ 83% of the polar one. Note that, β coefficient has little actual impact on the resulting map from the variation between $\beta = 0.32$ and 0.46.

2.2.3 Differential rotation

A cross-correlation test between maps can be applied to characterize the potential latitudinal differential rotation of the star (Fig. 2.2.7, see Donati & Collier Cameron 1997 for details of method), and has been used in a number of more recent papers (e.g., Barnes et al. 2017; Kriskovics et al. 2019; Kővári et al. 2019). In the stellar grid we used for the model, the pixel shape is identical for all pixels in a specific latitudinal ring. The cross-correlation value $f \star g$ at the $n_{\rm th}$ pixel is:

$$(f \star g)[n] = \sum_{m=1}^{N} f[m]g[m+n] \tag{2.2.11}$$

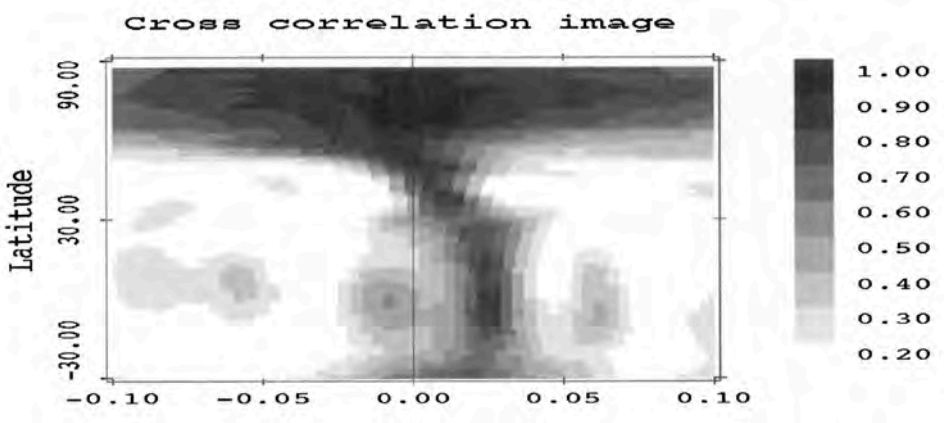

Figure 2.2.7: Cross-correlation images obtained by cross-correlating each latitude belt. Extract from Donati & Collier Cameron (1997).

where f, g is the finite discrete functions of brightness model at the the same latitude.

The *sheared image* method presented by Donati et al. (2000) and assessed by Petit et al. (2002) is applied to model the latitudinal differential rotation on the stellar surface. This technique incorporates a built-in latitudinal shear of the stellar surface into the DI or ZDI model, taking the advantage of the surface grid described above, and provides robust results even for sparse data sets (Petit et al., 2002; Donati et al., 2003a). In our model, the rotation rate Ω is assumed to vary with the latitude θ, following a simple solar-like dependence:

$$\Omega(\theta) = \Omega_{\rm eq} - d\Omega \sin^2 \theta \tag{2.2.12}$$

where $\Omega_{\rm eq}$ is the rotation rate of the equator and $d\Omega$ the pole to equator gradient in rotation rate. Fig. 2.2.8 shows an example of the The diagram shown reduced χ^2 between data and observation at constant spot coverage as a function of $\Omega_{\rm eq}$ and $d\Omega$.

2.3 Zeeman Doppler Imaging

Early attempts of detecting the large-scale magnetic field of stars other than the Sun by traditional polarization observation had limited success (e.g., Brown & Landstreet 1981; Leroy & Le Borgne 1989). The main reason is attributed to the highly complex structure of the magnetic field, which results in the cancellation of the polarimetry signal as well as the relatively weaker magnetic field strength compared to e.g. Ap stars. Inspired from Doppler imaging (DI), Zeeman-Doppler imaging (ZDI hereafter) was develop to reconstructed large-scale magnetic field structure with time-resolved spectropolarimetric observation (e.g., Brown et al., 1991; Donati et al., 1992; Donati & Collier Cameron, 1997; Donati et al., 1997). As the name implies, ZDI accounts for the Zeeman effect in the tomography using information contained in polarized spectra data (Stokes Q, U, V). Although the signal in a single spectral line is typically weak, the least-Squares Deconvo-

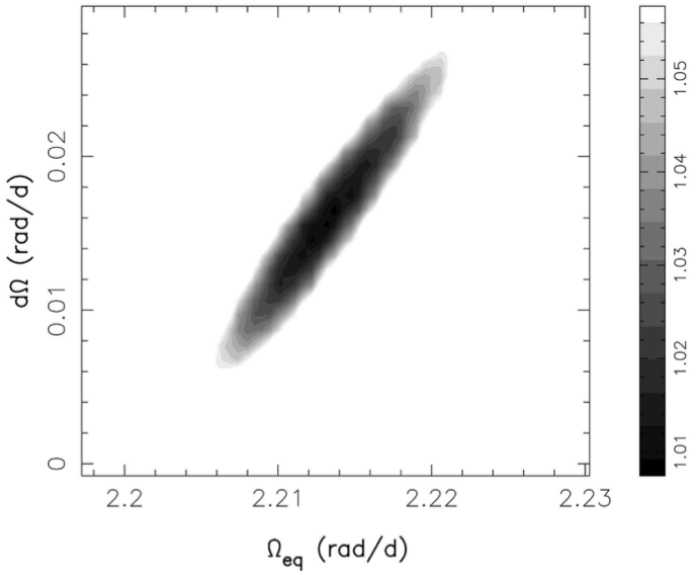

Figure 2.2.8: Simulation results for sheared image by Petit et al. (2002).

lution method can significantly improve the S/N of Zeeman signal. In the last 30 years, ZDI has been applied to several dozens of cool active stars on the main sequence (e.g., Petit et al. 2008 for solar analogs, Morin et al. 2008 for M dwarfs, or See et al. 2019 for a global study).

2.3.1 Zeeman Effect

When the external magnetic field B is much smaller than the atomic internal magnetic field, or is not strong enough to destroy the $L-S$ coupling, the spin S and orbital angular momenta L of the electron couple together and form a total angular momentum J. The atomic magnetic moments $\vec{\mu_J}$ can be expressed as:

$$\vec{\mu_J} = -g_J \frac{\mu_B}{\hbar} \vec{J}, \tag{2.3.1}$$

where g_J is the Landé splitting factor:

$$g_J = 1 + \frac{J(J+1) + S(S+1) - L(L+1)}{2(J(J+1))}, \tag{2.3.2}$$

and μ_B is Bohr magneton. The Zeeman effect is an essential consequence of the interaction between $\vec{\mu_J}$ and B, resulting in the splitting of atomic energy levels and their corresponding spectral lines, named after Pieter Zeeman (Zeeman, 1897). For the system with $\vec{\mu_J}$ in the field B, the potential energy $U = -\vec{\mu_J} \cdot B = M g_J \mu_B B$, where M is the magnetic quantum number. The energy difference ΔE between two energy levels E_{J_1} and E_{J_2} is given by:

$$\Delta E = h\nu^{'} = h\nu_0 + (M_2 g_2 - M_1 g_1)\mu_B B, \tag{2.3.3}$$

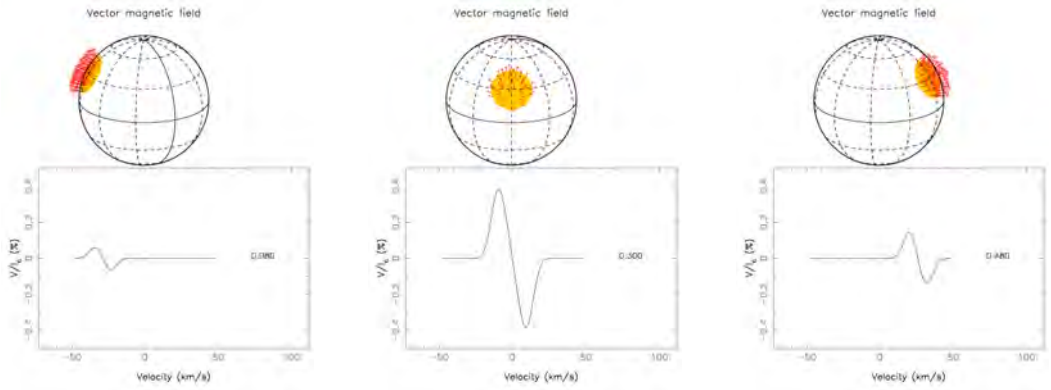

Figure 2.3.1: Samples of Stokes V (circular polarisation) line profile variations due to a magnetic spot. Credit: Jean-François Donati, extracted from http://www.ast.obs-mip.fr/article.php3?id_article=457.

where ν_0 gives the non-split frequency. According to the selection rule, $\Delta M = M_2 - M_1 = -1, 0, +1$, resulting in three components of spectral lines: $-\sigma, \pi, +\sigma$, respectively. in the case of a classical Zeeman triplet, as shown in Fig. 2.3.2, the so-called effective Landé factor g is often used:

$$g = \frac{1}{2}(g_2 + g_1) + \frac{1}{4}(J_2 - J_1)(g_2 - g_1)(J_2 + J_1 + 1). \tag{2.3.4}$$

For $\sigma^{\pm}$ components, the photon has an angular momentum $\pm\hbar$, parallel to $\vec{B}$. When the line of sight is parallel to $\vec{B}$, $\sigma^{\pm}$ can be observed with circular polarization. When the line of sight is perpendicular to $\vec{B}$, $\sigma^{\pm}$ components are linearly polarized. For the π component, the angular momentum of light is perpendicular to $\vec{B}$. Since $\Delta M = 0$, it is always linearly polarized and the light can not be observed if the line of sight is parallel to $\vec{B}$.

Stokes parameters are usually used to characterize the polarized light, and defined by:

$$\begin{aligned} I &= I \\ Q &= I\cos 2\beta \cos 2\chi \\ U &= I\cos 2\beta \sin 2\chi \\ V &= I\sin 2\beta \end{aligned} \tag{2.3.5}$$

where the intensity I, the ellipticity angle χ and the orientation angle β describe all polarized features of an elliptically polarized light. Stokes I is unpolarized light, V is circular polariztion, and (Q, U) are two directions of linear polarization. Stokes parameters

In practice, the measurement of polarization is determine I as a function of artificial

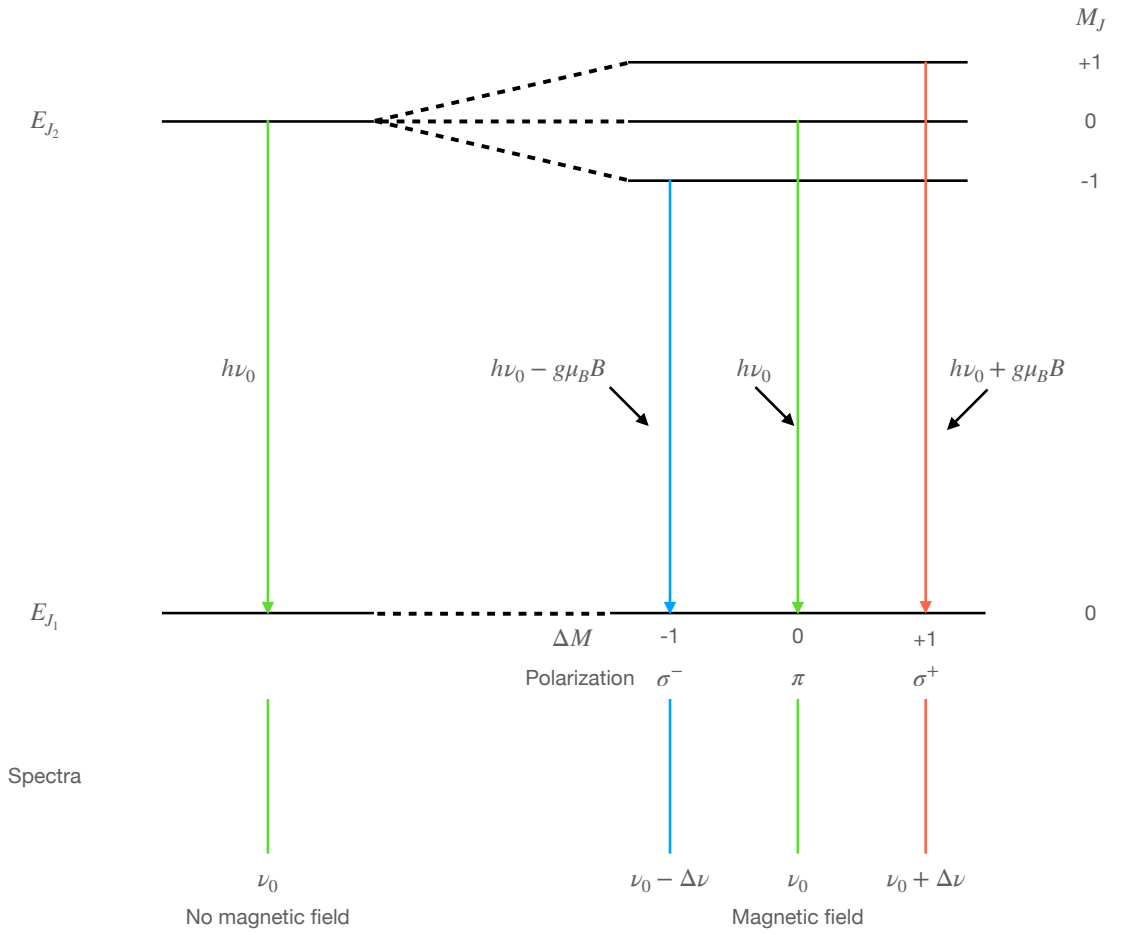

Figure 2.3.2: Zeeman splitting for a spectral line with frequency ν_0.

introduced orientation angle ψ and phase shift η:

$$I(\psi,\eta) = \frac{1}{2}[I + Q\cos 2\psi + (U\cos\eta - V\sin\eta)\sin 2\psi]. \tag{2.3.6}$$

In this case, At least 4 different ψ with $\eta \neq 0$ are required to determine Stokes parameters (I, Q, U, V), then the polarized state can be derived. A detailed introduction of astronomical polarimetry was presented by Tinbergen (1996).

2.3.2 Least Squares Deconvolution

Detecting Zeeman signatures with a high S/N is critical for the reconstruction of a magnetic map through the tomographic procedure. In the application of ZDI, the available signal in the polarized spectra can be extremely small. Increasing the exposure time and combining the spectral can help a little, but may lead to loss of phase information (i.e., smear effect). However, one can take advantage here of the fact that all photospheric

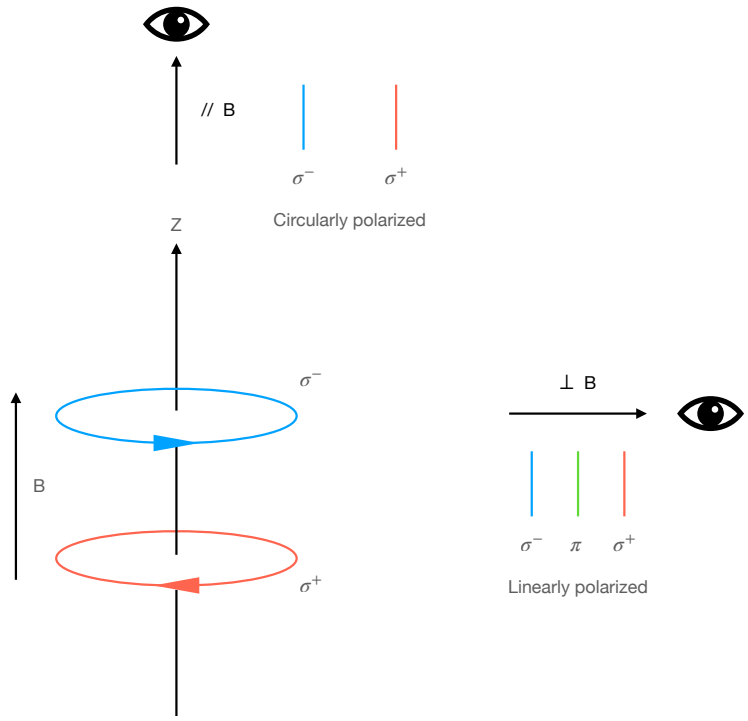

Figure 2.3.3: Polarization of Zeeman components

lines mostly display the same shape, with differences from line to line originating from the line depth (in Stokes I), or from a combination of the line depth, Landé factor and wavelength (in Stokes V). A multi-line approach is therefore a great help to increase the S/N and get rid of the blending issue. Least-Squares Deconvolution method (LSD, see Donati et al., 1997; Kochukhov et al., 2010) is a widely employed method to compute an average pseudo-line profile from a list of photospheric spectral lines in the spectra. The selection of lines follows a line pattern function or line mask matrix $\mathbf{M}$:

$$M(\nu) = \sum_i w_i \delta(\nu - \nu_i), \tag{2.3.7}$$

where ν_i is the position in velocity space and w_i is the weight of each spectral line. Then the polarized spectrum $\mathbf{V}$ can be written as a convolution expression ($\mathbf{V} = \mathbf{M} * \mathbf{Z}$), where $\mathbf{Z}$ is the mean line profile. The problem then converts to minimize the χ^2 function:

$$\chi^2 = (\mathbf{V} - \mathbf{M} \cdot \mathbf{Z})^T \cdot \mathbf{S}^2 \cdot (\mathbf{V} - \mathbf{M} \cdot \mathbf{Z}^T), \tag{2.3.8}$$

where $\mathbf{S}$ is a square diagonal matrix, with element S_{jj} containing the inverse uncertainty $1/\sigma_j$, of each pixel j in the observational spectra. The least-squares solution of $\mathbf{Z}$ is:

$$\mathbf{Z} = (\mathbf{M}^T \cdot \mathbf{S}^2 \cdot \mathbf{M})^{-1} \cdot \mathbf{M}^T \cdot \mathbf{S}^2 \cdot \mathbf{V}. \tag{2.3.9}$$

In practice, the line mask is a theoretical list of photospheric spectral lines from the VALD database (getting rid of spectral ranges plagued by telluric or chromospheric

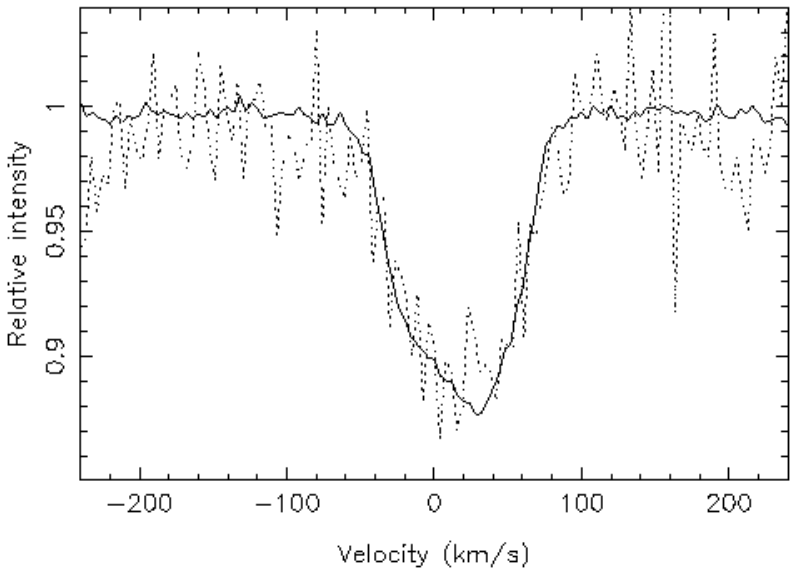

Figure 2.3.4: Performance of Least Squares Deconvolution on the Stokes I profile of classical T Tauri star SU Aur. Credit: Jean-François Donati. http://www.ast.obs-mip.fr/users/donati/multi.html

lines), using the nearest line list in a grid computed by Marsden et al. (2014). It was noticed by Folsom et al. (2016) that LSD profiles obtained from spectra with S/N below about 70 are sometimes affected by spurious polarized signatures that show up in the polarized line profile and in the Null profile (which is a control parameter that is expected to display only noise). This effect is much less prominent (but sometimes spotted as well) with S/N values between 100 and 150. Given that our observations of V530 Per fall within this second S/N range, we checked that our set of Null LSD profiles were free from any detectable spurious signal, and that the same conclusion was reached after averaging all available data together.

2.3.3 Spherical harmonics decomposition of the magnetic field

The magnetic model is computed under the weak field approximation (Stokes V is assumed to be proportional to the derivative of Stokes I), which is a valid approach over the range of field values encountered hereafter (i.e., a few hundred Gauss, e.g., Kochukhov et al. 2010). To express the magnetic field geometry, the model uses a spherical harmonics decomposition of the field based on Donati et al. (2006b) (see also Vidotto, 2016, for more discussion) by following the set of equations below:

$$B_r(\theta,\phi) = \sum_{\ell=1}^{L} \sum_{m=0}^{\ell} \mathrm{Re}[\alpha_{\ell m} Y_{\ell m}(\theta,\phi)] \tag{2.3.10}$$

$$B_\theta(\theta,\phi) = -\sum_{\ell=1}^{L}\sum_{m=0}^{\ell} \mathrm{Re}[\beta_{\ell m} Z_{\ell m}(\theta,\phi) + \gamma_{\ell m} X_{\ell m}(\theta,\phi)] \tag{2.3.11}$$

$$B_\phi(\theta,\phi) = -\sum_{\ell=1}^{L}\sum_{m=0}^{\ell} \mathrm{Re}[\beta_{\ell m} X_{\ell m}(\theta,\phi) - \gamma_{\ell m} Z_{\ell m}(\theta,\phi)] \tag{2.3.12}$$

where:

$$Y_{\ell m} = c_{\ell m} P_{\ell m}(\cos\theta) e^{im\phi} \tag{2.3.13}$$

$$X_{\ell m}(\theta,\phi) = \frac{c_{\ell m}}{\ell+1}\frac{im}{\sin\theta} P_{\ell m}(\cos\theta) e^{im\phi} \tag{2.3.14}$$

$$Z_{\ell m}(\theta,\phi) = \frac{c_{\ell m}}{\ell+1}\frac{\partial P_{\ell m}(\cos\theta)}{\partial\theta} e^{im\phi} \tag{2.3.15}$$

and

$$c_{\ell m} = \sqrt{\frac{2\ell+1}{4\pi}\frac{(\ell-m)!}{(\ell+m)!}} \tag{2.3.16}$$

Here (θ, ϕ) are the colatitude and longitude on the stellar surface, P_{lm} is the associated Legendre polynomial with ℓ and m giving the degree and order of the spherical harmonics mode. In practice, the model is described by a series of three complex coefficients: $\alpha_{\ell m}$ corresponding to the radial poloidal field, $\beta_{\ell m}$ the tangential poloidal field and $\gamma_{\ell m}$ the toroidal field component. We note that the spherical harmonics decomposition is used for both the spherical and oblate stellar geometries described above (although is it, strictly speaking, only valid for a sphere). This field decomposition is convenient to calculate various magnetic parameters from the ZDI model, to further characterize the magnetic field structure of the star. The calculation of different energy components from the spherical harmonics decomposition is detailed in Sec. A.3. In our work, only circular polarization sequences (Stokes Vparameter) were collected as part of our program, as Zeeman signatures are much larger in this polarization state for a cool star (a factor of ∼10 stronger than Q & U, e.g., Landi Degl'Innocenti 1992; Wade et al. 2000; Kochukhov et al. 2011).

In our work, the acquisition of polarimetric spectra used ESPaDOnS spectropolarimeter (Donati et al., 2006a), which started working in 2004, and is mounted at the Cassegrain focus of the Telescope Canada-France-Hawaii (CFHT, 3.58m) on Maunakea at Hawai'i. Under its spectropolarimetric mode, ESPaDOnS acquires a complete optical spectrum from 370nm to 1,050nm, in a single exposure with a resolving power of about 68000. The density of the grating is 79 gr/mm, the full spectrum spans 40 grating orders. A 2k×4.5k CCD detector is used to collect spectra. Fig. 2.3.5 shows a picture of CFHT and a close view of ESPaDOnS. In 2006, NARVAL, a twin instrument of ESPaDOnS, was mounted on Telescope Bernard Lyot (2m) in Observatory Midi-Pyrénées, Pic du Midi, France. In 2021, NARVAL was updated to Neo-NARVAL, to increase the suitability and support the research of magnetic field of exoplanet host stars. Recently, nIR spectropolarimeters & velocimeters SPIRouDonati et al. (2020) is in operation at CFHT since 2018.

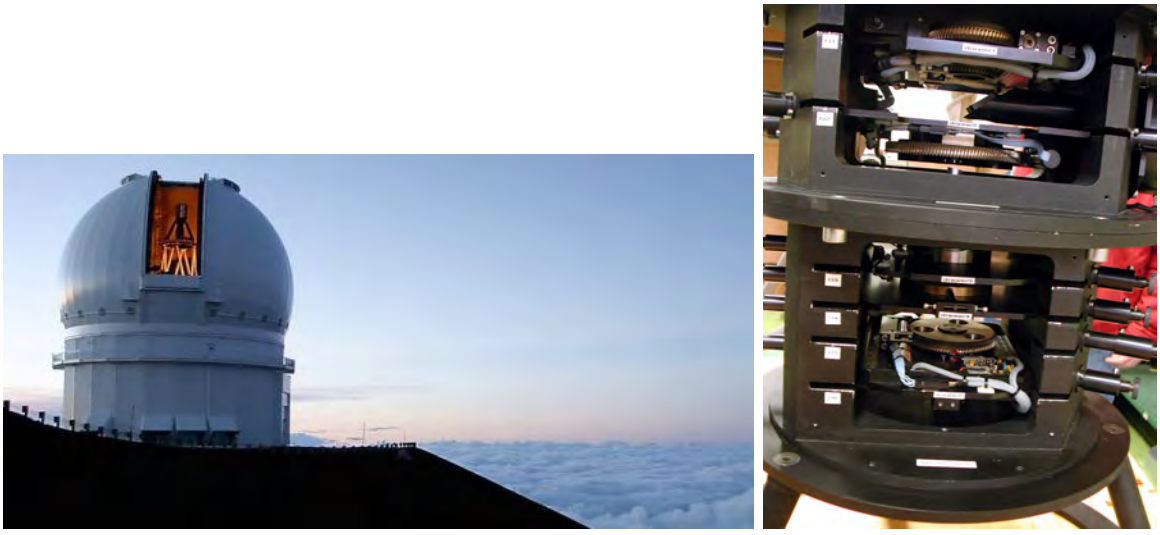

Figure 2.3.5: Pictures for Telescope Canada-France-Hawaii and a close view of ESPaDOnS. Credit: CFHT

2.4 Velocity map reconstruction of prominences

Prominences structures co-rotating with a star are located at a height above the stellar surface. When Balmer lines are purely in emission, a simple model is used to visualize the spatial distribution with a maximum entropy tomographic code developed by Donati et al. (2000), which is inspired from an algorithm initially developed for cataclysmic variables by Marsh & Horne (1988). Through this model, each emitting spot is attributed to a set of 2D Doppler velocities (V_x, V_y) in a Keplerian velocity field. In a spectral time-series, a spot of emission then traces out a sinusoidal radial velocity curve of:

$$V(\phi) = \gamma - V_x \sin 2\pi\phi + V_y \cos 2\pi\phi \tag{2.4.1}$$

where ϕ is the orbital phase, γ is the systemic radial velocity of the system. In practice, a Keplerian velocity field is divided by a number of equal areas of square pixels, each pixel is assigned a local line profile. Fig. 2.4.1 shows a sketch map for the spots on the velocity map and corresponding trace, and Fig. 2.4.2 shown an example for the application. Since the velocity coordinate is not exactly the same as a spatial coordinate and this method does not model the third dimension, it is hard to determine whether a spot is eclipsed by the star at a certain observation. A simplified approach is the assumption that the emitting material is optically thin (Donati et al., 2000) or far enough from the star to be visible in all observations (Watson et al., 2019). We note that the outcome of the model is mostly unsensitive to the exact value of the local width of line profile. In the case of corotating material, the velocity distribution is a straightforward illustration of the spatial distribution. Here, the emission is modeled above the continuum (without subtraction of any reference profile). The reconstructed equivalent widths should therefore not be considered physically meaningful, the main objective of this simple model being to locate the emitting material in the velocity

space and highlight its possible short term evolution. This method has been applied to detection of prominences in V530 Per (Barnes et al., 2001), LQ Lup (Donati et al., 2000) and CC Eri Budding et al. (2006). It is also a potential tool for detecting exoplanet atmospheres (Watson et al., 2019).

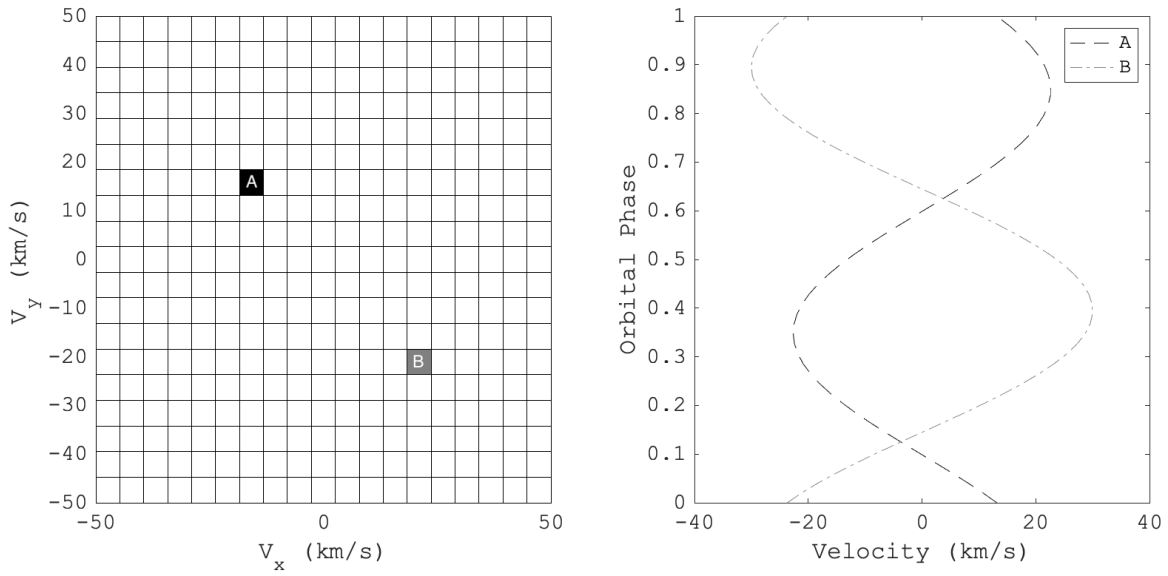

Figure 2.4.1: Spots on the Keplerian velocity field (left) and corresponding trace (right)

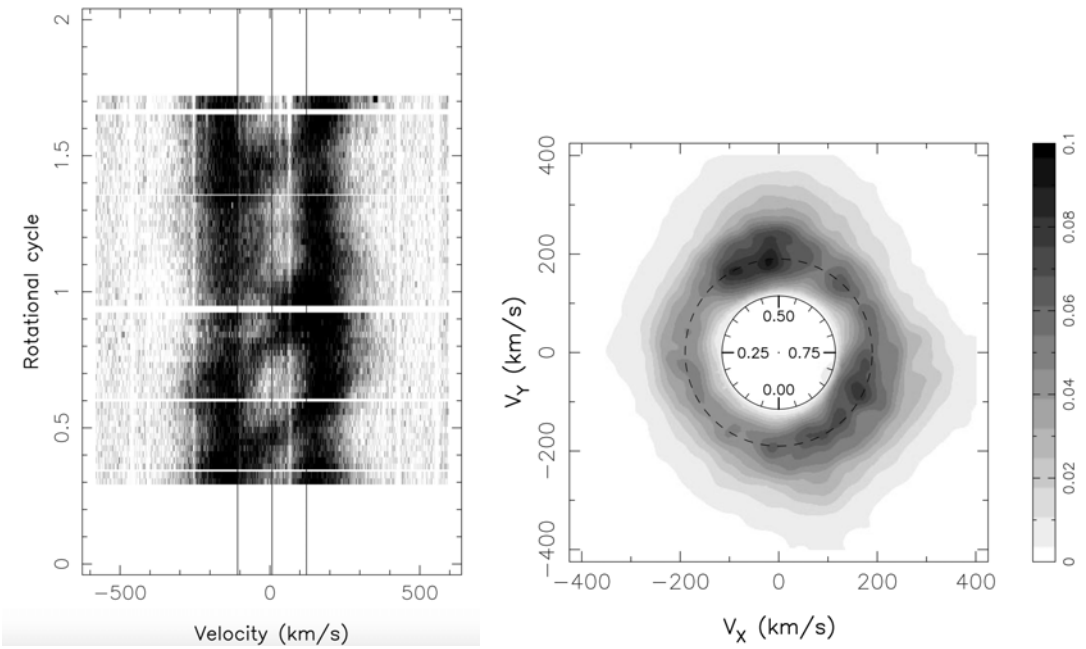

Figure 2.4.2: Prominences distribution reconstructed from Hα spectra for the post T Tauri star LQ Lup. Extracted from Donati et al. (2000).

Chapter 3

The stellar activity of a young sun: V530 Per

3.1 Background information

A fraction of young solar analogues in open clusters possess short rotation periods, a puzzling observation indicating that the magnetic braking supposed to act during pre-main sequence evolution was less efficient than expected on these objects, compared to slow rotators observed at the same age. In the most extreme cases, these rapidly rotating stars reach the so-called *saturated* dynamo regime, and sometimes the *supersaturated* regime (Pallavicini et al. 1981; Prosser et al. 1996; Wright et al. 2011, see Sec. 1.2.4 for more information). We propose here to characterize the magnetic field and related phenomena (e.g., active regions, prominences) of a prototypical saturated star.

Tomographic mapping is a powerful approach to characterize the large-scale surface magnetic fields and stellar prominences of rapid rotators. Although the first cool ZDI targets were saturated stars (Donati et al., 1992) as their Zeeman signatures are easier to detect, recent observing projects dealing with G-K dwarfs have mainly concentrated on objects in the unsaturated regime. As a consequence, while the unsaturated dynamo regime is now well explored by the ZDI models available so far, we are still left with few G-K dwarfs in the saturated regime, which remains mostly populated by M dwarfs in ZDI surveys. Our observations of V530 Per are aimed at enlarging the sample of fast rotators studied with ZDI.

Stellar prominences can be used as a proxy to estimate the loss of mass and angular momentum through the stellar wind (e.g., Villarreal D'Angelo et al. 2019; Jardine & Collier Cameron 2019; Vidotto 2021), which is of prime importance in our understanding of the early evolution of cool active stars (Aarnio et al., 2012; Jardine et al., 2020). For rapidly rotating stars, prominence systems become much more massive and extended than on the Sun (see the review by Collier Cameron, 1999). Although the knowledge we get from the Sun can provide rich information to understand the physics of prominences in a stellar context, available observations of prominence systems in other stars remain scarce as of today, so that the precise loss of mass and angular momentum through

ejected prominence material is still uncertain. For rapidly rotating objects, the centrifugal force becomes involved in the equilibrium and dynamics of the so-called slingshot prominences (e.g. Collier Cameron & Robinson 1989a,b; Donati et al. 1999). They were witnessed in co-rotation with a few, young solar-like objects (e.g., Donati et al. 2000; Dunstone et al. 2006b; Cang et al. 2020; Zaire et al. 2021), and were shown to evolve over time scales as short as a few days.

Here, we investigated the large-scale photospheric magnetic field and prominence system of V530 Per (also named AP 149), which is a cool, rapidly rotating member of the young open cluster α Persei (Prosser, 1992). Combining its X-ray flux and projected rotational velocity, V530 Per was proposed to be a saturated (O'dell et al., 1994) or even super-saturated (Prosser et al., 1996) star, making it an interesting object for ZDI studies lacking G-K stars in this extreme magnetic regime. Its sustained magnetic activity is also responsible for regular photometric variations attributed to a $\sim$8 hr rotation period (O'dell & Collier Cameron, 1993). Doppler mapping performed by Barnes et al. (2001) revealed the presence of a large, dark spot near the visible rotation pole. They also recovered a first prominence map from their Hα time series, unveiling large prominences extending up to several stellar radii.

In this work, we present a time-series of spectropolarimetric observations of V530 Per (Sec. 3.2). We first refine and discuss its fundamental parameters (Sec. 3.3) and then reconstruct its brightness and magnetic field map (Sec. 3.4). We also modeled the latitudinal differential rotation of V530 Per (Sec. 3.5) and present prominence maps reconstructed from individual nights, in order to highloight the short-term variation of the prominence structures (Sec. 3.6).

3.2 Observations

Two time-series of spectropolarimetric data of V530 Per were collected for two epochs with a 12-year gap (2006 & 2018, E06 & E18 hereafter). All of the observations were carried out at Maunakea observatory by the ESPaDOnS spectropolarimeter (Donati et al., 2006a), mounted at the Cassegrain focus of the Canada-France-Hawaii Telescope (CFHT), which has a usable aperture diameter of 3.58m. We used the polarimetric mode of this instrument, delivering a spectral resolution of about 65,000 and simultaneous coverage of the wavelength domain between 0.37 and 1.05 μm. Circular polarization sequences (Stokes V parameter) were collected as part of our program, as Zeeman signatures are much larger in this polarization state (a factor of $\sim$10 stronger than Q & U, e.g., Landi Degl'Innocenti 1992; Wade et al. 2000; Kochukhov et al. 2011). Every polarization sequence consists of four subexposures with a fixed integration time of 600s, and different angles of the two half-wave rotatable Fresnel rhombs in the polarimetric module, following a procedure designed to remove spurious polarization signatures at first order (Semel et al., 1993). Normalized, reduced Stokes I and V spectra are extracted from the raw ESPaDOnS images using the `Libre-ESpRIT` automatic pipeline tool (Donati et al., 1997, 2006a). The typical peak signal-to-noise ratio (S/N) of our Stokes V spectra is slightly above 100, while Stokes I spectra corresponding to single

subexposures have a peak S/N of about 50. In the rest of this study, all tasks involving Stokes I spectra alone make use of the subexposures, as they offer a denser temporal sampling. All reduced spectra analyzed here are available through the PolarBase archive (Petit et al., 2014).

The observations of E06 were secured over two nights separated by a 6-day gap (November 29 and December 05). We obtained an equal number of observations during both nights, leading to a total of 14 Stokes V spectra and 56 Stokes I spectra. In E18, observations span over four close nights (17, 18, 22, and 23 October). For this second epoch, we obtained in total 34 Stokes V spectra, and 136 Stokes I spectra (see Tab. 3.2.2).

To assign a rotational phase (E) to every observation, we used the ephemeris:

$$\begin{aligned} HJD_{\rm obs} &= HJD_0 + P_{\rm eq} \times E \\ &= 2454072.0 + 0.3205E, \end{aligned} \tag{3.2.1}$$

where $P_{\rm eq} = 0.3205$d is the rotational period of the equator, taken from our differential rotation measurement for E06 (see Sec. 3.5), and the initial Heliocentric Julian date $HJD_0 = 2454072.0$ is arbitrarily selected in the middle of E06. Note that, in any case, the ability to compare phases between two observing runs separated by 12 years is hampered by the propagation of the uncertainty on the rotation period. The resulting phases, reported in Table 3.2.1 and Table 3.2.2, show that successive Stokes V spectra are separated by about 10% of a rotation cycle (about $\sim 2\%$ for Stokes I subexposures). The phase smearing during the collection of a Stokes V sequence, which is of the same order, may be responsible for a reduced amplitude of polarized signatures generated by low latitude features (experiencing the largest Doppler shifts).

Our observations for E06 in each individual night were able to cover about 60% of one rotation cycle. The rotational phase reached at the end of the first night was within 10% of the phase observed at the beginning of the second night. We therefore end up with a complete phase coverage of the target, and with redundant observations between phases 0.85 and 0.15. For E18, we see that the rotation coverage in each individual night was always over 50%, and up to 85% during the last night (Tab. 3.2.2). In the most favourable cases, we reached a complete rotation coverage with combinations of two nights (18 and 22 or 22 and 23 Oct) or more.

3.3 Stellar parameters

V530 Per is a member of the α Persei open cluster (Prosser, 1992), a relatively young open cluster with an age of 63^{+8}_{-27} Myr, as derived from GAIA DR1 data (Yen et al., 2018). This recent estimate is significantly smaller than the 90 ± 10 Myr reported by Stauffer et al. (1999). The global metallicity of the cluster is close to solar, with [Fe/H]$=-0.10 \pm 0.08$ reported by Balachandran et al. (2011), who further noticed that stars with $T_{\rm eff} >$ 5500 K have [Fe/H] ≈ -0.04, while stars with $T_{\rm eff} <$ 5500 K feature a lower metallicity [Fe/H] ≈ -0.13.

Table 3.2.1: Observation log of V530 Per for 29 Nov & 05 Dec 2006. From left to right, we list the date, the Julian date, the rotational phases calculated with Eq. 3.2.1, and the peak S/N.

Date (2006)	HJD (2454000+)	Phase ϕ	peak S/N
29Nov	69.71271	0.1366	94
29Nov	69.74455	0.0373	103
29Nov	69.77677	0.9368	103
29Nov	69.80806	0.8391	113
29Nov	69.84102	0.7363	116
29Nov	69.87316	0.6360	109
29Nov	69.91170	0.5158	130
05Dec	75.70177	0.5500	105
05Dec	75.73473	0.6528	117
05Dec	75.76595	0.7502	119
05Dec	75.79718	0.8477	111
05Dec	75.83026	0.9509	107
05Dec	75.86149	0.0483	106
05Dec	75.89713	0.1595	113

Since there is no available distance measurement for V530 Per itself, we used the average distance of the cluster in our work. Using the GAIA DR1 catalog, Yen et al. (2018) derived an average distance $d = 167.7 \pm 0.3$ pc. This value is smaller than the one derived from Hipparcos parallax (172.4 ± 2.7 pc, van Leeuwen 2009). Considering individual stellar parallaxes reported by Yen et al. (2018), we derived a standard deviation of 0.46 mas for α Per members, that we considered to be the cluster extent. We adopted this value as our uncertainty on the parallax of V530 Per, translating into a conservative distance uncertainty of about 15 pc.

We used our high-resolution spectral data to measure surface fundamental parameters of V530 Per (such as its surface temperature, gravity or metallicity) which are not documented in the literature. We mostly repeated here the procedure detailed by Folsom et al. (2016) and already applied to a sample of young solar-type stars (Folsom et al., 2016, 2018a). This approach iteratively fits synthetic spectra to the observation by χ^2 minimization. We computed spectra with the ZEEMAN spectrum synthesis code (Landstreet, 1988; Wade et al., 2001), which performs polarized radiative transfer in LTE and works well for stars as cool as 5200 K (e.g. Folsom et al. 2018a). We used MARCS model atmospheres (Gustafsson et al., 2008) as input, together with atomic data extracted from the VALD database (Ryabchikova et al., 1997; Kupka et al., 1999; Ryabchikova et al., 2015). This approach using ZEEMAN has been verified against alternate spectroscopic parameter determinations (Folsom et al., 2016, 2018a), and an interferometric determination (Folsom et al., 2018b) for stars in this range of spectral types, with good agreement consistently found. One should note that we used single spectra for the parameter determination. The S/N is sufficiently high that it is not the limiting factor on our

Table 3.2.2: Observation log of V530 Per on 17, 18, 22, 23 Oct 2018). Every Stokes V spectra consisted of 4 individual unpolarized subexposures with fixed exposure time equal to 600s. From left to right, we list the date, the Julian date, the rotational phases calculated with Eq.3.2.1, and the peak S/N.

Date (Oct 2018)	HJD (2458400+)	Phase ϕ	Peak S/N
17	8.99494	0.9655	105
17	9.02392	0.0559	106
17	9.05458	0.1516	105
17	9.08355	0.2420	106
17	9.11393	0.3368	98
17	9.14289	0.4271	97
18	9.90980	0.8200	100
18	9.93932	0.9121	100
18	9.96921	0.0053	99
18	9.99874	0.0975	98
18	10.02863	0.1907	99
18	10.05815	0.2828	103
18	10.08808	0.3762	100
18	10.11764	0.4685	98
22	13.85090	0.1167	108
22	13.88046	0.2089	102
22	13.91070	0.3033	100
22	13.94026	0.3955	88
22	13.97037	0.4895	94
22	13.99993	0.5817	91
22	14.03189	0.6814	91
22	14.06144	0.7736	95
22	14.09169	0.8680	97
22	14.12124	0.9602	97
23	14.83713	0.1939	106
23	14.86665	0.2860	108
23	14.89699	0.3806	110
23	14.92654	0.4728	107
23	14.95677	0.5671	109
23	14.98633	0.6594	110
23	15.01713	0.7555	107
23	15.04668	0.8477	107
23	15.07681	0.9417	108
23	15.10637	0.0339	103

results, and given the heavily spotted nature of the star, any parameter determination assuming a uniform atmosphere will necessarily be approximate.

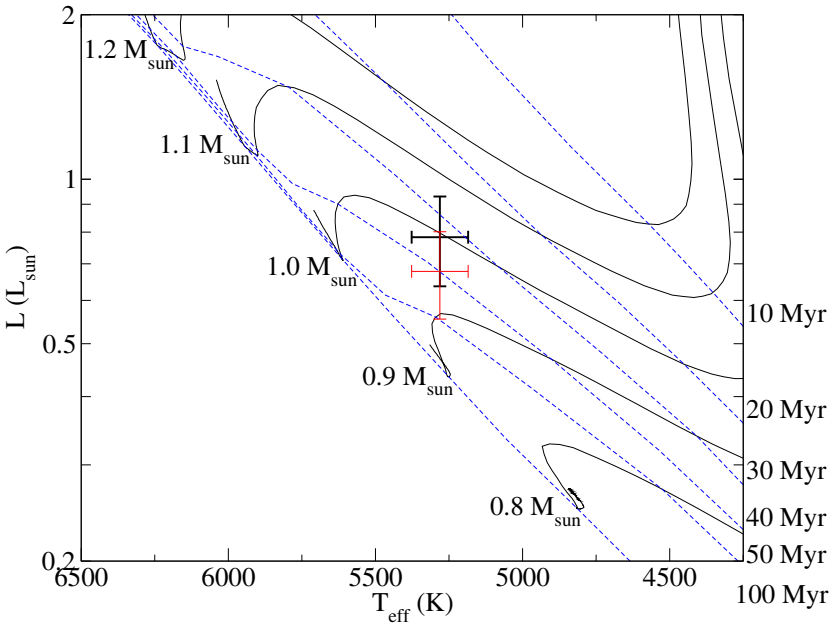

Figure 3.3.1: V530 Per in the Hertzsprung-Russell diagram, with evolutionary tracks generated by the STAREVOL code. Evolutionary tracks are given for 0.1 $M_{\odot}$ steps (full lines), and isochrones are overimposed for 10, 20, 30, 40, 50 and 100 Myr (dashed lines). The black and red crosses are obtained from the K and J magnitudes, respectively.

The observed spectrum of V530 Per was first renormalized, with the synthetic spectra providing guidelines for regions best approximating the continuum. The theoretical spectra were then compared to the renormalized spectrum, focusing on several spectral regions that are mostly uncontaminated by strong molecular lines, which are not taken into account by ZEEMAN, and telluric lines. A first fit was performed assuming a solar metallicity, which is a reasonable approximation since α Per members are known to have near solar metallicity (Balachandran et al., 2011). This fit was performed using 5 spectral regions ∼10 nm long, between 600 and 650 nm (specifically 600-610, 607.5-620.5, 619.6-627.55, 631.2-634.1 + 635.0-640.4, and 640.4-644.6 + 645.9-650.4 nm). The average of the best fits for individual windows was taken as the final value, and the standard deviation was taken as an uncertainty estimate. Assuming a solar metallicity, we obtained an effective temperature $T_{\rm eff}$= 5281 ± 96 K, a surface gravity $\log g = 4.10 \pm 0.19$, a projected rotational velocity $v \sin i = 116.70 \pm 2.38$ km s^{-1} (consistent with the estimate of Jackson & Jeffries 2010, but significantly larger than 102km s^{-1} estimated by Barnes et al. 2001) and a micro turbulence $v_{mic} = 1.3 \pm 0.4$ km s^{-1}. Although we checked on less noisy data sets that spectra of extremely active stars collected at different rotational phases do not produce significantly different results, except for $v \sin i$ estimates, our approach is still limited by the fact that we assumed the atmosphere to be homogeneous over the whole stellar surface. This is far from the actual situation of V530 Per, which is covered by a complex mixture of cool and hot spots (see Sec. 3.4). In particular, the giant, dark polar spot of this extremely active star impacts

Table 3.3.1: Fundamental parameters of V530 Per

Name	Value	References
Distance	167.7 ± 15 pc	1,2
Age	33^{+10}_{-7} Myr	1
$T_{\rm eff}$	5281 ± 96 K	1
$\log g$	4.4 ± 0.1 [cm s^{-2}]	1
$[Fe/H]$	-0.16 ± 0.08	1
m_V^{min}	11.657 ± 0.13	3
m_J	10.08 ± 0.019	4
m_K	9.422 ± 0.019	4
Luminosity	0.78 ± 0.15 $L_\odot$	1
Radius	1.06 ± 0.11 $R_\odot$	1
Mass	1.00 ± 0.05 $M_\odot$	1
$\log L_x$	31.2 [erg s^{-1}]	5
Rossby number	0.013 ± 0.002	1
Co-rotation radius	1.9 ± 0.2 R_*	1
Alfvén radius	5 R_*	1
v sin$i$	106 ± 1 km s^{-1}	1
Eq. rot. period	0.32055 ± 0.00005 d	1
$d\Omega_I$ (Epoch 2006)	0.042 ± 0.005 rad d^{-1}	1
$d\Omega_I$ (Epoch 2018)	0.053 ± 0.004rad d^{-1}	1
$d\Omega_V$ (Epoch 2018)	0.15 ± 0.01 rad d^{-1}	1
Inclination angle	$40 \pm 4°$	1
Radial velocity	-0.96 ± 0.1 km s^{-1}	1

References:

1. This work 2. Yen et al. (2018) 3. Zacharias et al. (2013) 4.Cutri et al. (2003a) 5. Pillitteri et al. (2013)

the line shape by generating a broad bump in the line bottom (Barnes et al., 2001), which has the effect of biasing our v sin$i$ estimate toward larger values. An independent estimate of v sin$i$, using Doppler mapping and incorporating the effect of surface spots in the model, leads to a significantly smaller value of about 105.6 km s^{-1} (Sec. 3.4.2). A second fit was performed with the metallicity left as a free parameter (as well as $T_{\rm eff}$, *log g* , and [Fe/H]), To better constrain the additional parameter, this round of fitting included an additional 5 spectral regions between 550 and 600 nm (specifically 550-560.7, 560.7-569.2, 569.2-580, 580-590.3, and 590.3-600 nm), to better constrain this parameter. These additional windows have more severe line blending and consequently an accurate continuum normalization is more difficult, but they improve the statistical validity and provide more data to better constrain parameters with similar effects on the spectrum. The outcome is a set of atmospheric parameters in good agreement with our previous estimate, and the metallicity is found to be [Fe/H] $= -0.16 \pm 0.08$. This is consistent with the average value of Balachandran et al. (2011), although our estimate

is sensitive to small departures from a perfect continuum normalization.

The V magnitude of V530 Per varies with time, with reported values between 11.657± 0.13 (Zacharias et al., 2013) and 11.981 ± 0.073 (Henden et al., 2015). Assuming that the brightness variations of V530 Per all come from rotating star spots, we considered the brightest available magnitude as the nonspotted magnitude. This magnitude was then used to estimate the luminosity $L = 0.78 \pm 0.18\ L_{\odot}$, using the distance discussed above (167.7 ± 15 pc), the V band bolometric correction $BC_{\rm v} = -0.23$ from Pecaut & Mamajek (2013) and the reddening correction $A_V = 0.312$ from Pinsonneault et al. (1998). Subsequently, we derive the stellar radius $R = 1.06 \pm 0.11\ R_{\odot}$ (See Sect. A.1 for more details). We then repeated the same procedure with the K magnitude, as it is much less affected by activity-induced fluctuations (e.g., Fang et al., 2010) and suffers less from the interstellar extinction. Using a K magnitude of 9.422 ± 0.019 from Cutri et al. (2003a), and the interpolated bolometric correction $BC_K = 1.706 \pm 0.056$ of Masana et al. (2006), we get $L = 0.78 \pm 0.15\ L_{\odot}$ and $R = 1.06 \pm 0.11\ R_{\odot}$. Alternately, using the J band magnitude and the bolometric correction $BC_J = 1.22 \pm 0.03$ from Pecaut & Mamajek (2013), we get $L = 0.68 \pm 0.12\ L_{\odot}$ and $R = 0.98 \pm 0.10\ R_{\odot}$, in good agreement with the K band estimate.

Using our values of the effective temperature and luminosity, we obtained the HR diagram of Fig. 3.3.1. According to evolutionary tracks computed with the STAREVOL code by Amard et al. (2016, 2019) for solar metallicity, we get $M = 1.00 \pm 0.05\ M_{\odot}$, $\log g = 4.4 \pm 0.1$ and an age of 33^{+10}_{-7} Myr using the K band, versus $M = 0.95 \pm 0.05\ M_{\odot}$, $\log g = 4.4 \pm 0.1$ and an age of 40^{+11}_{-8} Myr with the J band. Both ages are consistent, within uncertainties, with the 63^{+8}_{-27} Myr proposed by Yen et al. (2018). The *log g* values with this approach are larger than the one derived from spectrum fitting, possibly due to the impact on the ZEEMAN estimate of line distortions linked to dark spots, complicated by the heavily blended spectrum (the derivation of *log g* relies on the pressure broadened line wings, which are largely hidden by the high $v \sin i$). Using the K band values of the mass and radius, we derived a theoretical convective turnover time (from the STAREVOL models) at one pressure scale height above the base of the convective zone of $25.0^{+4.3}_{-3.1}$ days (following the method of Folsom et al. 2016). This implies a Rossby number $R_o = 0.013 \pm 0.002$ with the period obtained by ZDI (see Sec. 3.5). A summary of all parameters discussed above can be found in Table 3.3.1. The adopted values for the luminosity, radius, mass, *log g* , and age are taken from our K band calculation, since this band is the least impacted by stellar activity.

3.4 Brightness and Magnetic field distributions

3.4.1 ZDI for V530 Per

Following the fundamental parameters determined in Sec. 3.3, we selected a line list with an effective temperature $T_{\rm eff} = 5250K$ and a logarithmic gravity *log g* = 4.5, and included in our analysis all lines with a depth greater than 40% of the continuum level. This resulted in a total of 5726 lines, after removal of all lines plagued by telluric contam-

ination, as well as all lines blended with chromospheric lines. The LSD pseudo-profiles are computed for a velocity step of 1.8 $\mathrm{km\,s^{-1}}$(about ∼40% of the spectral resolution of ESPaDOnS, equal to 4.6 $\mathrm{km\,s^{-1}}$), a normalization Landé factor equal to 1.19, and a normalization wavelength of 650 nm (See Sec. 2.3.2 for a detailed description of the method).

Our study of V530 Per made use of a new version of the ZDI code described by Folsom et al. (2018a), which is a Python implementation of the ZDI algorithm presented by Donati et al. (2006b), based on the maximum entropy fitting routine of Skilling & Bryan (1984) (more details can be found in Chapter 2). The two codes are designed to invert a set of LSD pseudo-line profiles (see below). Using the same data set and identical input parameters, they were shown by Folsom et al. (2018a) to provide nearly identical outcomes. We repeated this test with our own set of observations and reached the same conclusion.

Our ZDI model considered a local line profile with a gaussian FWHM taken equal to the one adopted for low v sin$i$ stars of the same surface temperature as V530 Per (0.01 nm, Folsom et al. 2016), while the gaussian amplitude is equal to 0.533 to match the depth of LSD profiles (a fine-tuning of the line depth is performed with the adjustment of other input parameters, see Sec. 3.3). Variations in temperature, not modeled here, can cause small variations in the equivalent width of a line, due to the impact of temperature on local line formation. Generally the impact of small equivalent width variations have a minimal impact on the resulting map (mostly seen as an increase of the best achievable χ^2). This rough modeling can be traded for more realistic descriptions of the line shape (e.g., Voigt profiles, Folsom et al. 2018b), but given the large v sin$i$ of V530 Per its line shape is vastly dominated by rotational broadening, so that a local Gaussian line proves to produce a convincing fitting of the data. For Stokes V modeling, the model considers the brightness map as a prior assumption for the magnetic field reconstruction when Stokes V LSD profiles are inverted (e.g., Donati et al., 2014).

We chose a linear limb darkening coefficient $\eta = 0.73$, by interpolating between available values from the table of Magic et al. (2015), using the Kepler filter, as it is the closest in spectral coverage to our instrumental setup, and using stellar parameters of V530 Per given in Sec. 3.3. The gravity darkening coefficient $\beta = 4b = 0.46$ is interpolated from the table of Claret & Bloemen (2011) based on ATLAS atmospheres model (Kurucz, 1993), resulting that the brightness on equator is a factor of ~ 0.83 as it on the pole. Note that the the β coefficient has little impact on the resulting map.

3.4.2 ZDI adjustment of stellar parameters

Stellar parameters extracted from individual spectral lines (Sect. 3.3) can be biased when v sin$i$ is very large (increasing the number of blends), or when the line profile is distorted by photospheric inhomogeneities. In this case, the optimization of tomographic models can help improve the determination of some parameters, including v sin$i$, the radial velocity RV, the inclination of spin axis i, and give access to additional parameters like the rotation period of the equator P_{eq}, and the difference in rotational rate between the equator and pole $d\Omega$ (these two parameters will be investigated in Sect. 3.5).

Using a simple χ^2 minimization to determine v sin$i$ leads to significant residuals in phase averaged LSD profiles, showing up in the wings of the pseudo-line. Following Donati et al. (2003b), we therefore varied again v sin$i$ to minimize any systematic (Fig. 3.4.1), and finally adopted v sin$i$ = 106 km s^{-1}(versus 110 km s^{-1} using χ^2 minimization). This value is slightly larger than the 102 km s^{-1} obtained by Barnes et al. (2001). Although this empirical estimate is not associated to a formal error bar, 1 km s^{-1} is probably a reasonable order of magnitude for the uncertainty.

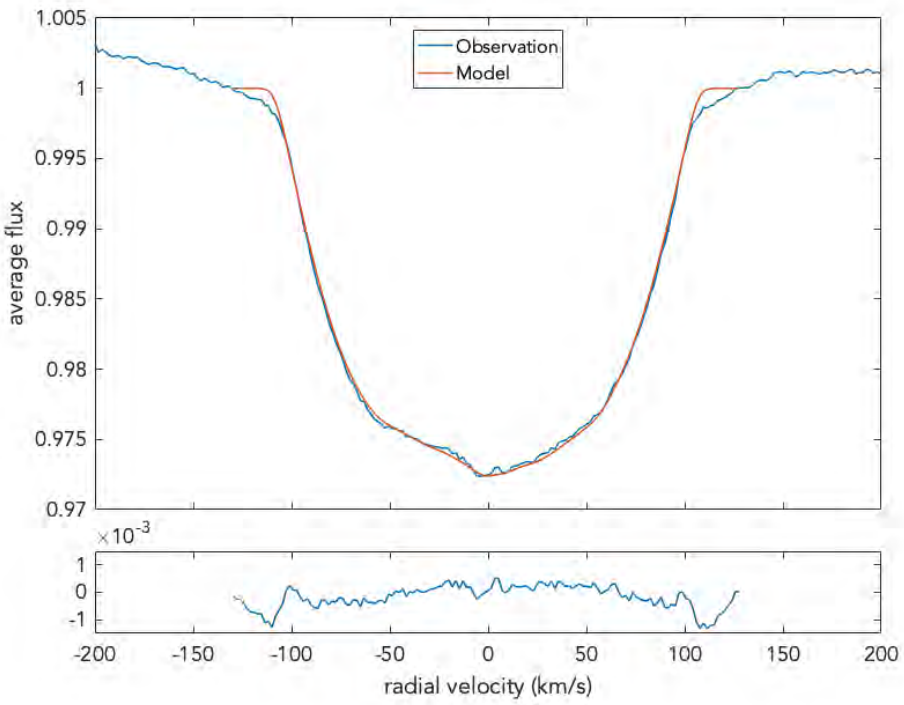

Figure 3.4.1: Phase-averaged LSD profile for the V530 Per observations (top panel, blue) and our DI model (top panel, red), as well as the residuals (bottom panel).

By combining our v sin$i$ estimate with the 0.3205 equatorial rotation period of Sect. 3.5 and the stellar radius derived in Sect. 3.3, we obtained an inclination angle equal to $40 \pm 4°$. Searching for a value of the inclination angle minimizing the χ^2 of the DI model provided us with inconsistent results, depending on whether we used a spherical or oblate model for the stellar shape. While a spherical surface is leading to $i = 35°$, the oblate model is optimized for values of i below 10°, in clear disagreement with other fundamental parameters of V530 Per (this latter value would, for instance, imply an absurdly large stellar radius). The value obtained by Barnes et al. (2001) was equal to 30°, in rough agreement with our spherical estimate (assuming a typical error bar, including systematics, on the order of 5 to 10°, Rice & Strassmeier 2000). Facing these discrepant estimates derived from tomographic inversion, we finally adopted $i = 40°$

hereafter.

The χ^2 of the brightness map was minimized for a radial velocity $RV = -0.96 \pm 0.04$ km s^{-1}, using a total of 7920 freedom degrees (the total number of data points) to estimate the statistical error bar (bearing in mind that instrumental systematics likely dominate this statistical uncertainty, with an absolute RV accuracy probably not better than 0.1 km s^{-1}). Although uncertainties were not provided by Barnes et al. (2001), our measurement seems to be significantly larger than their estimate ($RV = -3.1$ km s^{-1}), suggesting that V530 Per is possibly not a single object. We note that the local line depth was fine-tuned after each parameter adjustment (v sin$i$ and RV), leading to the final value listed in Sec. 3.3.

3.4.3 Brightness distribution

The dense phase coverage described in Sec. 3.2 enables us to trace the Doppler shifts of surface spot signatures over the stellar rotation period. Stellar parameters determined in Sec. 3.3, as well as the differential rotational rate $d\Omega$ and equatorial rotational period $P_{\rm eq}$ (Sec. 3.5) are taken as inputs for the brightness map reconstruction. For each epoch, the Stokes I dynamic spectrum (Fig. 3.4.2, 3.4.6) does not highlight any obvious variations of spot signatures from day to day. We then reconstructed brightness maps by using all Stokes I data together in each epoch, separately.

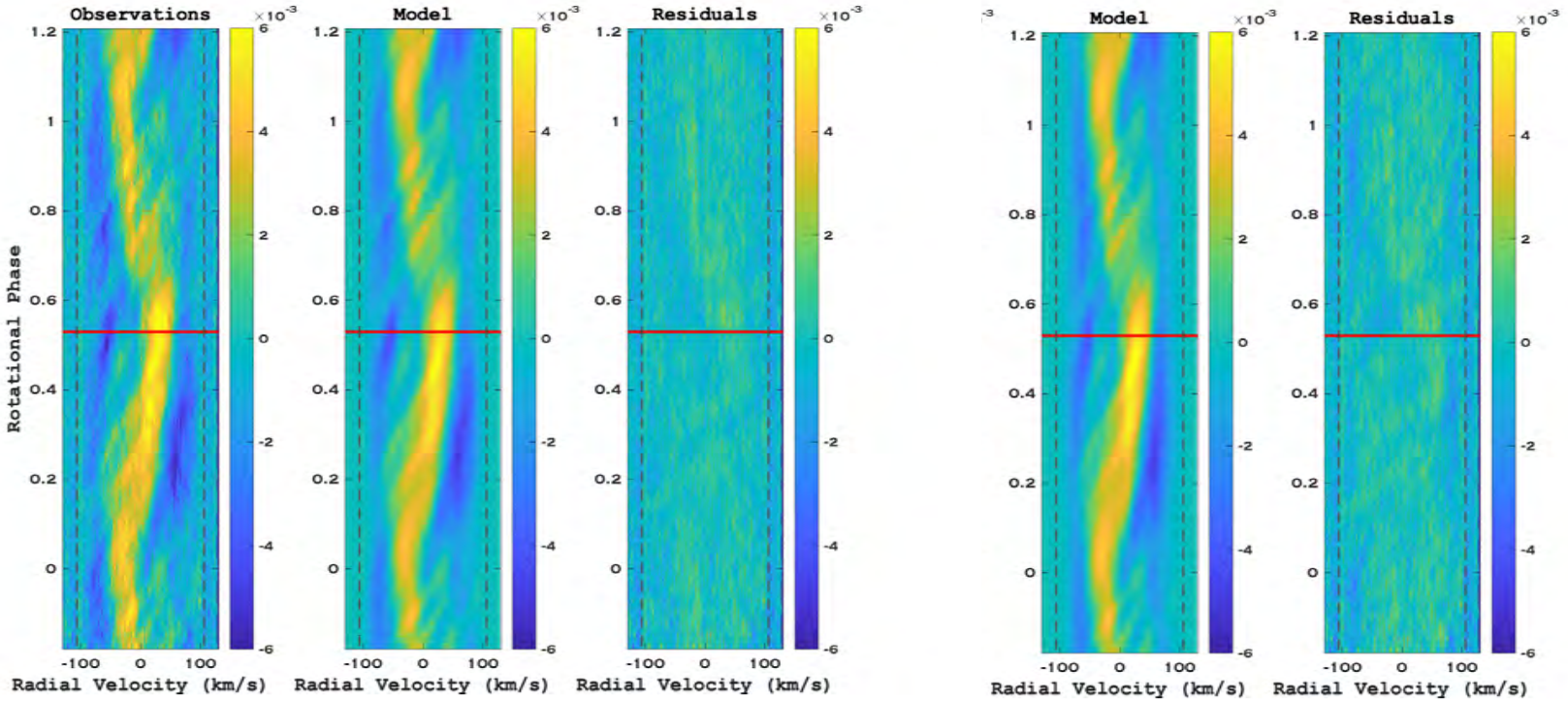

Figure 3.4.2: Stokes I dynamic spectrum of V530 Per, after subtraction of the averaged Stokes I profile. From left to right: observations, DI model with $\chi^2_r = 0.55$ including both bright dark spots, model residuals. The two additional panels on the right show our model with $\chi^2_r = 0.65$ and dark spots only, and the model residual. The vertical, black, dashed lines mark the $\pm$ v sin$i$ limit. The portion above the solid, horizontal red lines represents data from 05 Dec 2006, while the lower part represents data taken on 29 Nov 2006.

In order to test possible differences between a DI model restricted to dark spots, versus a more flexible model allowing for dark and bright features, a first map for E06 was reconstructed assuming dark spots only and an oblate surface (lower panel of Fig. 3.4.4), with a model reaching a reduced χ^2 of 0.65 (showing that error bars in Stokes I LSD pseudo-profiles are over-estimated, as documented by e.g., Petit et al. 2004). The main visible structure is a large spot located around a latitude of 75°, spreading between phases 0 and 0.5. A number of smaller spots are reconstructed as well. Most of the smaller structures are also seen at high latitude, but a few of them are found down to a latitude of 30°. The dynamic spectrum produced with synthetic line profiles of the DI model (see the two panels constituting the right part of Fig. 3.4.2) is able to reproduce most observed spectral features. There are, however, some small residuals that reveal the limits of this approach. These remaining signatures are mostly dips, suggesting that they are generated by bright patches (similarly to, e.g., Barnes et al. 2017). We therefore computed a second model where both dark and bright spots were allowed, which led us to a smaller reduced χ^2 of 0.55. In spite of the same limb darkening law assumed for dark and bright features, we obtained a nearly flat dynamic spectrum of residuals (third panel of Fig. 3.4.2). Although a limb darkening law optimized for the quiet photosphere may lead to minor biases in the reconstruction of bright spots, we noticed from the comparison of the two panels in Fig. 3.4.4 that dark spots, at least, do not seem to be noticeably modified by the inclusion of bright regions in the model. The corresponding brightness map shows almost the same distribution of dark spots as in the previous model. Bright spots appear to be concentrated at latitudes lower than the majority of dark spots, with a greater accumulation between 30 and 45° of latitude. Their size is generally smaller than that of dark spots, and their distribution extends down to equatorial latitudes. The brightest reconstructed spots are about 40% brighter than the quiet photosphere, which is a higher contrast than observed on the Sun (Hirayama & Moriyama, 1979). The total fraction $\mathcal{S}_{\rm tot}$ of the stellar surface covered by spots (including both dark and bright features) is equal to 10% in this model, as calculated by the following equation:

$$\mathcal{S}_{\rm tot} = \frac{\sum_{i=0}^{n} |I_i - I_0| A_i}{\sum_{i=0}^{n} A_i} \tag{3.4.1}$$

where $I_0 = 1$ is the brightness with no spot and I_i is the brightness on the cell of surface A_i.

We note that the brightness map obtained from a spherical model shown in Fig. 3.4.4 is characterized by a lower contrast of the spot pattern (both in the dark, high latitude spots and in the bright, low latitude features). In this case, the fractional spot coverage drops to about 6%, and the brightest faculae are about 30% brighter than the quiet photosphere, which remains larger than typical solar values. Another difference compared to the oblate model is a shift of all reconstructed features toward higher latitudes, although this effect is sufficiently subtle to be difficult to distinguish in the maps (the limit of the large polar spot, at latitude $\sim 60°$, is where the effect can be most easily seen).

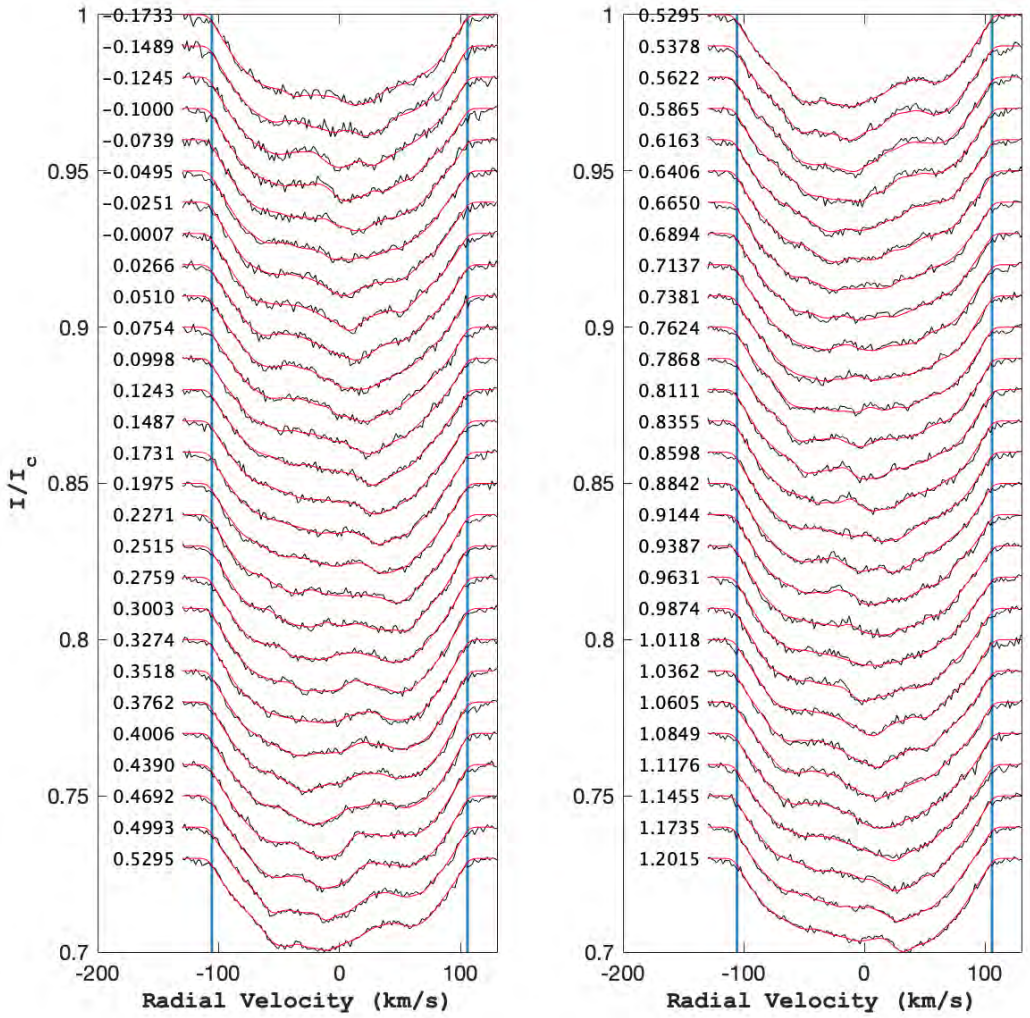

Figure 3.4.3: Observed (black) and modeled (red) Stokes I profiles, in a display similar to Fig. 3.4.9. Data from 29 Nov. 06 (resp. 05 Dec 06) is plotted on the left (resp. right). Successive profiles are vertically shifted for display clarity. Rotational phases are indicated on the left of the profiles. Blue vertical lines show the $\pm$ v sin$i$ limit.

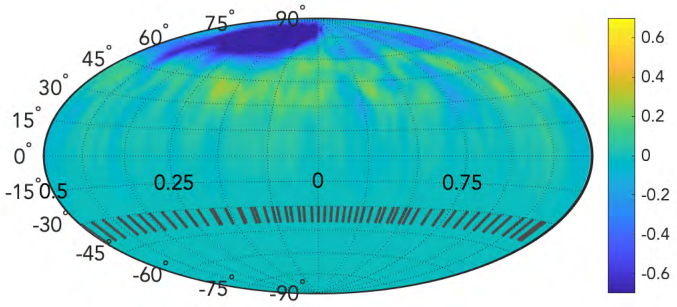

(a) Dark and brights spots and an spherical surface, 2006

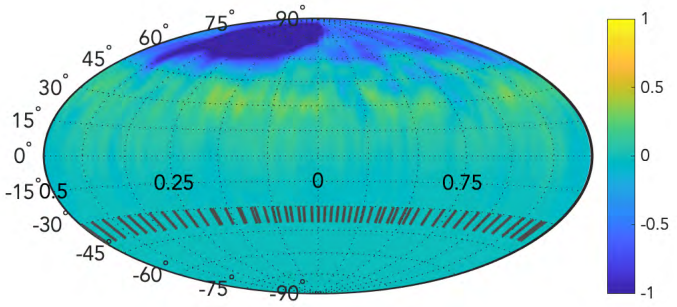

(b) Dark and bright spots and an oblate surface, 2006

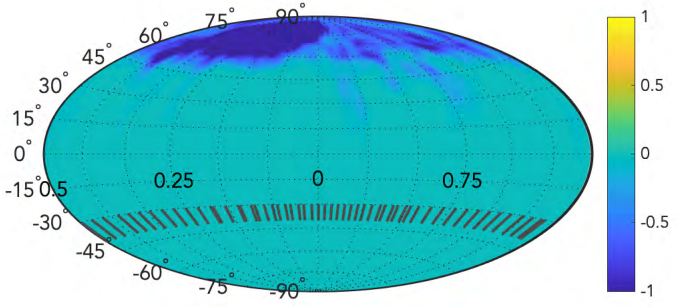

(c) Dark spots only and an oblate model, 2006

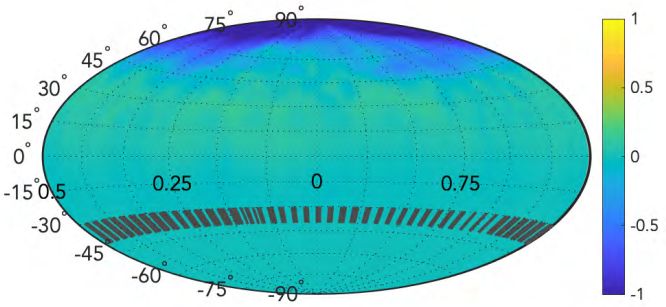

(d) Dark and bright spots and an oblate surface, 2018

Figure 3.4.4: Logarithmic normalized brightness maps of V530 Per reconstructed. We used here a Hammer projection of the stellar surface. Meridional ticks in the bottom of the maps mark the rotational phases of our observations. The portion of the maps below $-40°$ of latitude is set to 0, as it is invisible to the observer. We emphasize that the color scale is different for spherical and oblate models.

During E18, the overall stability, over several rotation periods, of activity signatures showing up in the Stokes I dynamic spectrum in individual nights, led us to group all Stokes I data together in the surface brightness reconstruction for a denser phase sampling. The inversion process also included the differential rotation parameters obtained in Sect. 3.5. The series of synthetic LSD profiles produced by the ZDI code is illustrated in Fig.3.4.6, showing that the DI model applied to E18 observations is able to fit the majority of activity features, resulting in a reduced χ^2 equal to 0.76. Although the level of residuals is negligible compared to the observed spectral signatures, there are some small features that the model cannot fully reproduce (e.g., the blue-shifted trail remaining at $\phi \sim 0.3 - 0.4$ on 23 Oct). Since the DI algorithm tries to reproduce co-rotating brightness structures that do not evolve with time, except under the predictable shifts owing to differential rotation, the model residuals may be linked to the intrinsic evolution of the brightness tracers (changes in area, shape or intensity of the active regions). Given that the residuals are not consistent from one night to the next, the short lifetime of some surface structures may be responsible for this modest mismatch.

We note that the χ^2_r we reached here is slightly larger than the one obtained with the E06 data (which was equal to 0.55). This slightly degraded fit may be caused by a greater intrinsic variability of the spot distribution (emergence or decay of surface spots occurring faster and/or over larger areas) in the surface structures observed in E18, bearing in mind that the S/N of both data sets is mostly the same, and that the time span of the new data is slightly shorter than in E06.

The most striking structure in the brightness map of Fig. 3.4.4 is a large, dark spot occupying the polar region. This prominent spot contrasts with the scarcity of smaller spots reconstructed at lower latitudes. The polar spot is centered close to a latitude of $\sim 80°$, and is slightly off-centered towards a phase between 0.3 and 0.5. Smaller and low contrast dark spots, separated from the polar spot, also show up at high to intermediate latitudes, down to $\sim 45°$. A predominance of bright features is observed from the equator to a latitude of about 40°, as illustrated in Fig. 3.4.5 The same accumulation was also reported in E06, although the bright features were structured in a series of more distinct individual spots in E06, while they here take the shape of a nearly continuous belt, possibly due to a denser distribution of spatially unresolved spots. The total fraction of the surface covered by bright or dark spots $\mathcal{S}_{\rm tot}$ is equal to $\sim 14\%$, as estimated by Eq. 3.4.1, which is slightly larger than the value calculated in E06.

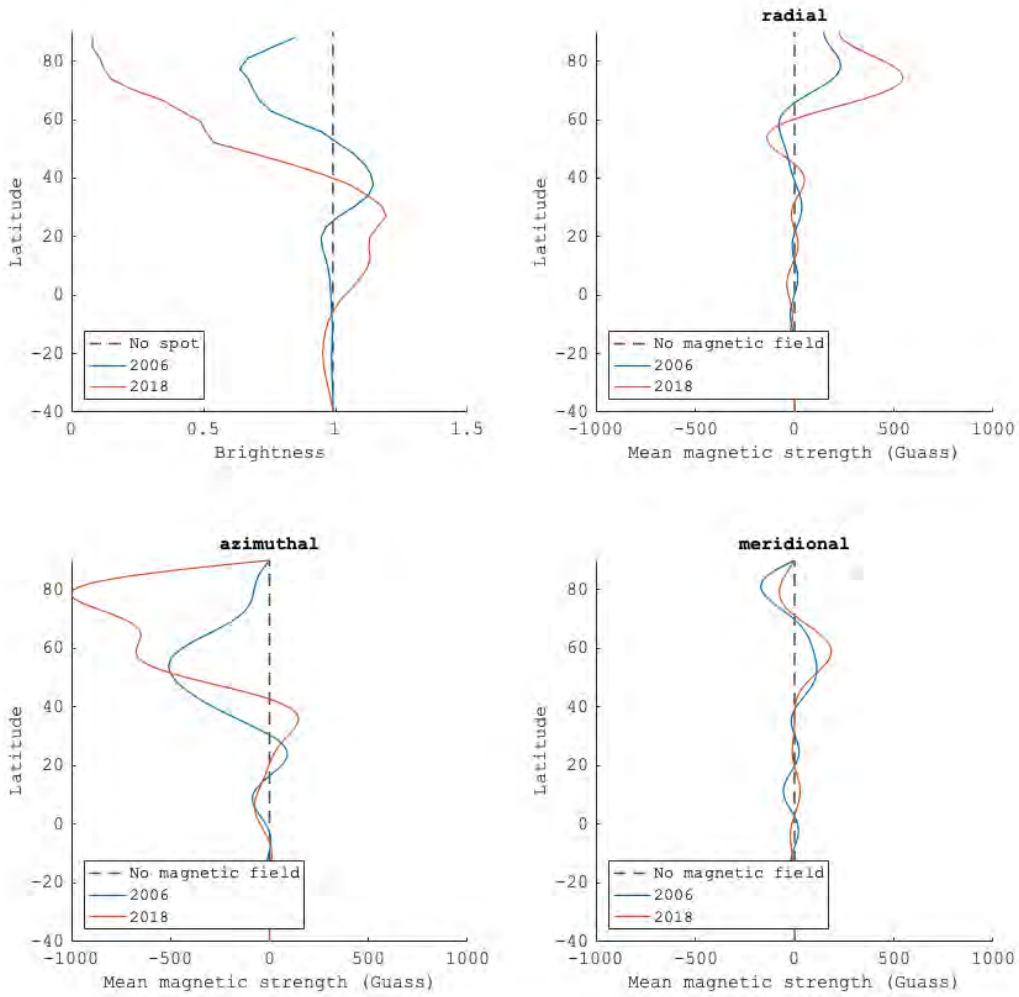

Figure 3.4.5: Brightness (left-top) and magnetic field as function of latitude. The blue lines show the data from 2006, and red lines show the data from 2018.

A large number of Doppler maps of young stars include dark spots only in their surface model, although some stars have benefited from temperature mapping based on the modeling of individual spectral lines (e.g., V1038 Tau by Rice & Strassmeier 2001, HD 171488 by Strassmeier et al. 2003, V410 Tau by Carroll et al. 2012, V1358 Ori by Kriskovics et al. 2019, LQ Hya by Cole-Kodikara et al. 2019). Our brightness modeling allows for bright surface patches as well, and the resulting map features a number of bright spots of relatively small area, with a specific concentration between latitudes 30°and 45°. The same set of techniques was also recently applied to the weak line T Tauri stars LkCa 4 (Donati et al., 2014), V830 Tau (Donati et al., 2016), TAP 26 (Yu et al., 2017) and V410 Tau (Yu et al., 2019). These four stars have masses relatively close to the one of V530 Per, although they all are significantly younger, and all rotate

slower than V530 Per. We observe a similar mid-latitude accumulation of bright spots on TAP 26 (which has a rotation period about twice that of V530 Per), while other stars from this series do not display this recognizable distribution of bright spots.

Brightness maps derived from E18 data show some clear similarities with the maps from E06. At both epochs, the brightness distribution was dominated by a dark spot anchored at high latitude. The second feature recognizable in both maps is an accumulation of bright spots at intermediate latitudes. Both maps display a spot coverage slightly larger than 10%. This consistent latitudinal dependence of the brightness is illustrated in the upper-left panel of Fig. 3.4.5. Beside the global consistency of the two maps, a clear evolution is seen regarding the high latitude spot, which is much darker in E18, with a minimum normalized brightness decreasing from ~ 0.7 in E06 to ~ 0.25 in E18. The shape and location of this giant spot varied as well, from a location that did not cover the pole in the Doppler map of Barnes et al. (2001) and in the E06 data, to a nearly centered spot in E18. We also note that the latitude of maximum brightness was shifted by approximately 10° towards lower latitudes in E18.

Large polar spots are commonly observed among the most active stars, most of the time through Doppler mapping as in the present study, but also with interferometry (Roettenbacher et al., 2016). A number of young solar-type stars at the end of the pre-main sequence phase or in their early main sequence have been found to host such extended polar caps, similar to the brightness map of V530 Per in E18. Typical examples include LQ Lup (named RX J1508.6-4423 in the paper, $P_{\rm rot} \sim 0.31d$, Mass $\sim 1.16 M_{\odot}$, Donati et al. 2000) and AB Dor ($P_{\rm rot} \sim 0.51$ d, Mass $\sim 1 M_{\odot}$, Donati & Collier Cameron 1997; Donati et al. 2003a). Both of them have a mass and rotation rate similar to those of V530 Per, but both of them display only a centered polar spot, which is similar to the high-latitude spot observed on V530 Per in E18, while in E06 it does not cover the pole. A few other young G dwarfs have been reported to show large off-centered, high-latitude spots (not covering the pole), like EK Dra ($P_{\rm rot} \sim 2.8$ d, Mass $\sim 0.95 M_{\odot}$, Strassmeier & Rice, 1998; Waite et al., 2017; Järvinen et al., 2018) or other rapidly rotating members of the α Per cluster (AP 193, He 520, He 699, Barnes et al. 2001).

In V530 Per as in other rapidly rotating stars, the preferential emergence of spots at high latitude can be interpreted as an indication that the Coriolis force can impose magnetic flux tubes to raise toward the stellar surface in a path mostly parallel to the stellar spin axis (Schuessler et al., 1996). Smaller spots are also observed at lower latitudes, which suggests that they may be formed in an internal layer closer to the photosphere.

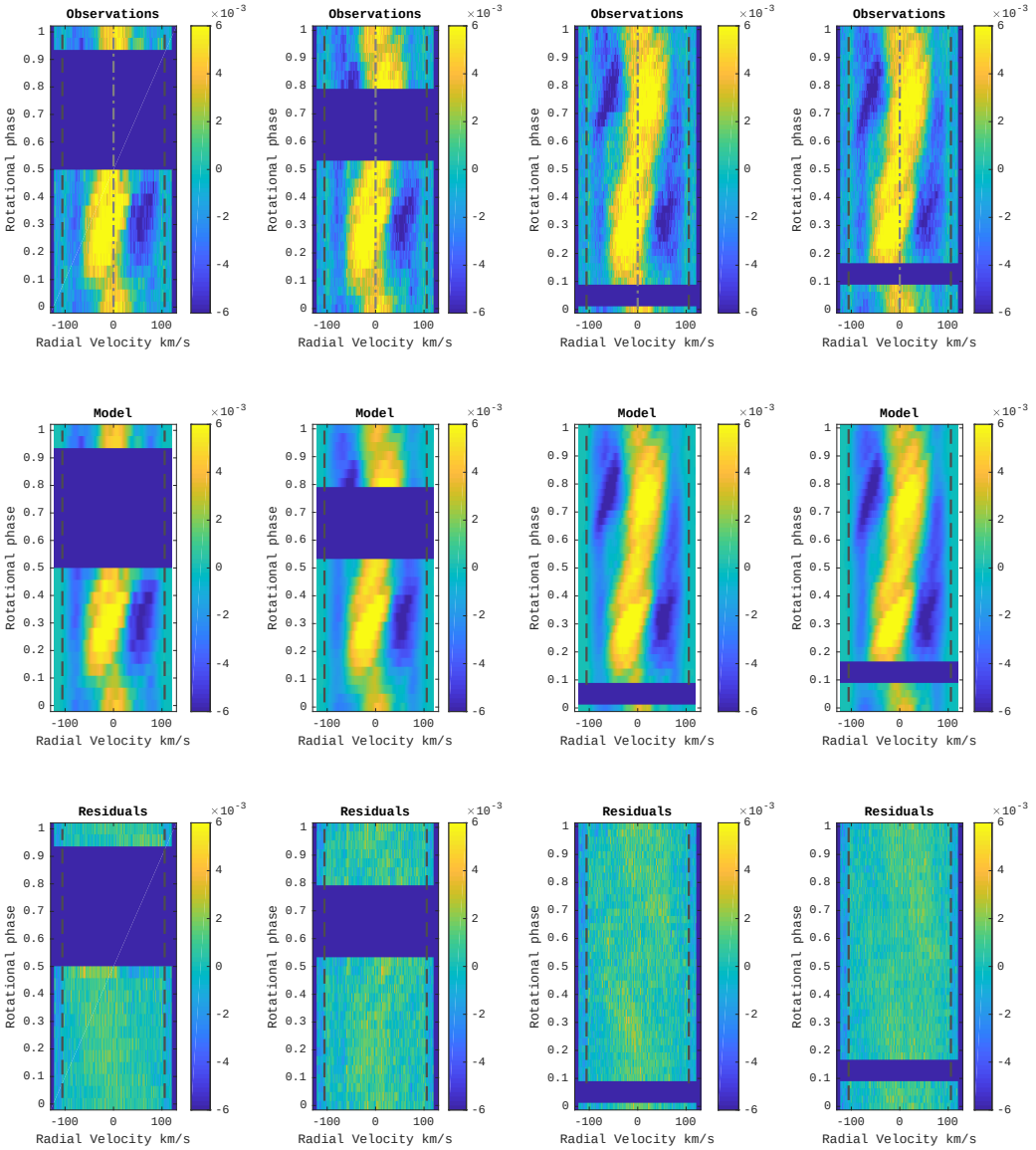

Figure 3.4.6: (Upper panels) The observational dynamic spectrum for each night in 2018 season, from left to right: 17, 18, 22, 23 Oct. (Lower panels) The dynamic spectrum for all data together with same data set, including the observation and model with fix χ^2=0.73, period 0.320391 d, $d\Omega = 0.0524$ rad/d. Similar color scale as brightness map in Fig. 3.4.4 is applied, with yellow traces cool spots (bump), yellow traces bright spots (sunken).

3.4.4 Magnetic geometry

The magnetic field reconstruction made use of the brightness map as a prior input. Similarly to the brightness inversion, the magnetic field reconstruction benefited from

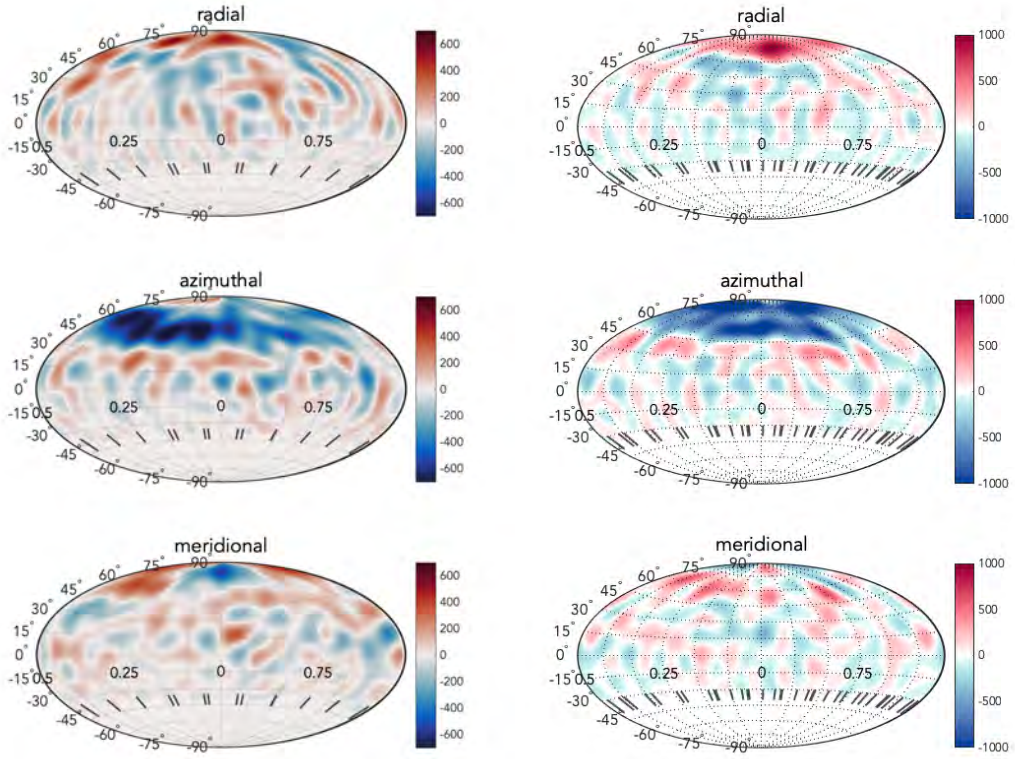

Figure 3.4.7: Magnetic maps of V530 Per for 2006 epoch (left) and 2018 epoch (right) data. The three panels show the different field components in spherical projection. The color scale illustrates the field strength in Gauss. A Hammer projection of the stellar surface is adopted, and vertical ticks in the bottom of the panels show the rotational phases of individual Stokes V sequences.The portion of the maps below $-40°$ of latitude is set to 0, as it is invisible to the observer.

the dense phase coverage of the set of Stokes V LSD profiles (Fig. 3.4.9, 3.4.10), which is especially critical here since the Zeeman signatures are barely detected in individual Stokes V LSD profiles. Owing to the large relative noise, it is also impossible to readily notice, to the naked eye, any changes in the profiles that could be attributed to a surface shear. The data can be fitted down to $\chi^2 = 0.9$ for E06 and 0.92 for E18, by including spherical harmonics modes up to $\ell = 15$. Increasing further the number of spherical harmonics coefficients to be fitted does not improve the model. In both of the two epoch, the resulting maps displays a complex pattern of magnetic regions, with field strength locally exceeding 1 kG (Fig. 3.4.7). Other models reconstructed with a slightly larger χ^2 of 1 still display small magnetic features with a slightly reduced strength, suggesting that overfitting is not responsible for the observed patchy field distribution.

In the maps of E06, the largest and strongest radial field region is reconstructed at the approximate location of the largest dark spot, around a latitude of 75°. Other radial field spots are more difficult to link to specific brightness patches. The azimuthal field component is dominated by a large belt of negative field encircling the visible pole

between latitudes 45 and 60°. In this prominent structure, the field reaches a maximum strength between phases 0 and 0.5, which roughly corresponds to the azimuthal location of the largest brightness spot. Its average latitude is comprised between the lower boundary of the polar spot, and the upper boundary of the group of smaller, bright features.

In E18, the reconstructed field is globally similar to the one obtained at the previous epoch, in the sense that it is complex, and features a strong azimuthal component. In these more recent data, however, the magnetic field is stronger in the polar region for both the radial and azimuthal components. Latitudinal distribution for all three components shown similar shapes as well in Fig. 3.4.5. The value of primary peaks of radial and azimuthal field also reach $\sim$ 2 times in 2018 than 2006 as brightness. We can, in a generally sense, conclude a latitudinal relationship between the brightness and magnetic field for V530 Per.

Table 3.4.1: Magnetic field characteristics of V530 Per in 2018 and 2006. The values include (a) the average magnetic field strength $\langle B \rangle$, (b) the unsigned peak magnetic field strength $|B_{peak}|$, (c) the ratio of toroidal field energy with respect to the total magnetic energy, (d) the ratio of magnetic energy in axisymmetric modes ($m = 0$) over the total energy, the same quantity but limited to the poloidal (e) and toroidal (f) magnetic component, the ratio of the dipole, quadrupole, and octopole (g, h, i) as a fraction of the poloidal component, and ($\ell = 1, 2, 3$) subcomponents of the toroidal field energy, as a fraction of the toroidal field energy (j, k, and l).

	Parameter	Value (2018)	Value (2006)
a	$\langle B \rangle$	222.552 G	177 G
b	$\|B_{peak}\|$	1616.341 G	1088 G
c	toroidal	68 % (tot)	64 % (tot)
d	axisymmetric	65 %(tot)	53 % (tot)
e	pol axisymmetric	36 % (pol)	16 % (pol)
f	tor axisymmetric	79 %(tor)	74 % (tor)
g	dipole	6.3 % (pol)	1.2 % (pol)
h	quadrupole	6.6 % (pol)	3.3 % (pol)
i	octopole	7.3 % (pol)	5.4 % (pol)
j	tor $\ell = 1$	2.6 % (tor)	8 % (tor)
k	tor $\ell = 2$	8.6 %(tor)	21 % (tor)
l	tor $\ell = 3$	13.7 % (tor)	20 % (tor)

`Note of shortcut:`
tot=totol, pol=poloidal, tor=toroidal

A list of magnetic parameters was calculated from the $\alpha_{\ell m}$, $\beta_{\ell m}$, and $\gamma_{\ell m}$ spherical harmonic coefficients of the ZDI model to further characterize the magnetic field structure of V530 Per. A detailed description of spherical harmonics coefficients we used can be found in Sec. 2.3.3. The resulting list of parameters is shown in Table 3.4.1. The large ratio between the average magnetic field strength $\langle B \rangle$ and the unsigned peak

magnetic strength $|B_{peak}|$ highlights the complexity of the field structure. We also note that a majority (about two thirds) of the photospheric magnetic energy (as estimated from B^2) is stored in the toroidal field component. Focusing on spherical harmonics modes with $m = 0$ (*i.e.*, axisymmetric modes), we note that they contain slightly more than half of the magnetic energy ($\sim 53\%$). But a closer look reveals that the poloidal field component is poorly axisymmetric, while the toroidal field energy is mostly reconstructed in axisymmetric structures ($\sim 74\%$). As a consequence of the field complexity, a very small fraction of the poloidal magnetic field energy is seen in the dipole ($\ell = 1$), quadrupole ($\ell = 2$) and octopole ($\ell = 3$). Here again, the situation is noticeably different if we consider the toroidal field component where nearly half the magnetic energy ends up in $\ell \leq 3$, revealing a higher level of geometrical simplicity in the toroidal field component. As a rough estimate of the uncertainty on these values, we varied the input stellar parameters (v sin$i$, the inclination angle, the equatorial rotation period, the surface shear) over their confidence interval, as well as the target χ^2. We conclude that the stellar parameters have little effect on the estimated magnetic energy ($\sim 2\%$), except v sin$i$ that is able to modify the magnetic values by up to 10%. Changing the χ^2 within a reasonable range can also modify the derived magnetic characteristics by $\sim 10\%$.

The similarities between the spatial structures displayed in the maps yield to clear similarities in the energy distribution (Table 3.4.1). More than half of the energy was contained in the high order components (ℓ>3), for both the poloidal and toroidal fields. The average magnetic field strength $\langle B \rangle \sim 222$ G and the unsigned peak magnetic field strength $|B_{peak}| \sim 1616$ G in E18 are both larger than E06 (177 G and 1088 G, respectively). We note that the reconstructed magnetic fields are more axisymmetric in E18 (∼65%) than in E06 (∼53%), and the majority of the variation came from the poloidal axisymmetric (∼16% to ∼36%). The difference in field strength suggests a fluctuating activity level, but the sparse monitoring does not allow us to confirm whether it is a cyclic variation, or chaotic changes, as reported for other rapidly-rotating stars like AB Dor or LQ Hya (Donati et al., 2003b).

The surface field distribution of V530 Per is characterized by a prominent toroidal component, where the majority of the magnetic energy is reconstructed (Table 3.4.1). This is consistent with the trends reported by Petit et al. (2008) or See et al. (2015), showing that the toroidal field component of cool stars increases faster than the poloidal field when the Rossby number decreases, to the point where the magnetic topology can become dominated by the toroidal component.

We also observe a very different level of complexity in the toroidal and poloidal field components. The toroidal component has a relatively high fraction of its magnetic energy in low degree modes ($\sim 40\%$ in modes with $\ell < 4$). It is mostly axisymmetric (73% in modes with $\ell = 0$), which is consistent with other stars where the toroidal component dominates (See et al., 2015). The outcome in the magnetic map is a well defined ring of negative azimuthal field. The latitude of this ring ($\sim 50 - 60°$) is higher than the one of bright spots showing up in the brightness map ($\sim 35°$) and lower than the latitude of the off-centered polar spot. We note that the phase of its maximal field strength is close to the phase of the main high-latitude spot ($\phi \sim 0.75$). Similar ring-like

structures have been identified in other rapid-rotating young dwarfs like AB Dor and LQ Hya (Donati et al., 2003b), EK Dra (Waite et al., 2017), or LO Peg (Folsom et al., 2016).

In contrast, the geometry of the poloidal field component is much more complex. The dipole, quadrupole and octopole contribute a small fraction of the poloidal magnetic energy ($\leq 10\%$ altogether), which is unusual in cool active stars (Folsom et al., 2016). The poloidal field is also highly nonaxisymmetric (15% in modes with $m = 0$). The main radial field region is an extended positive spot covering most of the dark polar spot. The strong radial field reconstructed at high latitude may contribute to generate the dark polar spot, although in other examples of young stars with a giant polar spot, such spatial correlation between the brightness and magnetic geometries is generally not reported (e.g., Donati et al. 2003b).

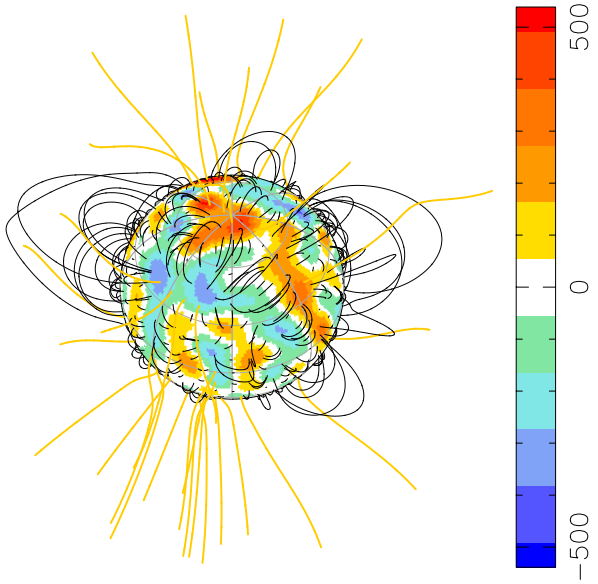

Figure 3.4.8: Large-scale potential field extrapolation of V530 Per, using the E06 magnetic geometry as boundary conditions. The star is seen at phase 0.0, with a 40° inclination angle. The blue and white lines represent open and closed field, respectively. The color scale on the surface show the strength of the radial field component (in Gauss), following Fig.3.4.7. The source surface is located at 2.5 R_*, which is a bit further away from the star than the corotation radius (at 1.9 R_*).

Finally, we used a potential field source surface model (Jardine et al., 2013) to extrapolate the coronal magnetic field, using the potential component of the E06 ZDI map as boundary conditions (Fig. 3.4.8). The surface toroidal field component is ignored in the extrapolation, as recent models suggest that purely potential field extrapolations provide a better match to prominence distribution (Jardine et al., 2020). We assumed that the field becomes purely radial above a source surface located at 2.5 R_*, which is slightly larger than the corotational radius (Jardine, 2004). Although the exact location

of the source surface is difficult to establish precisely, due to uncertainties in the wind properties, especially in an environment where the centrifugal force plays an important role, we chose this value considering that field lines will likely break open quickly above the corotational radius under the effect of centrifugal forces.

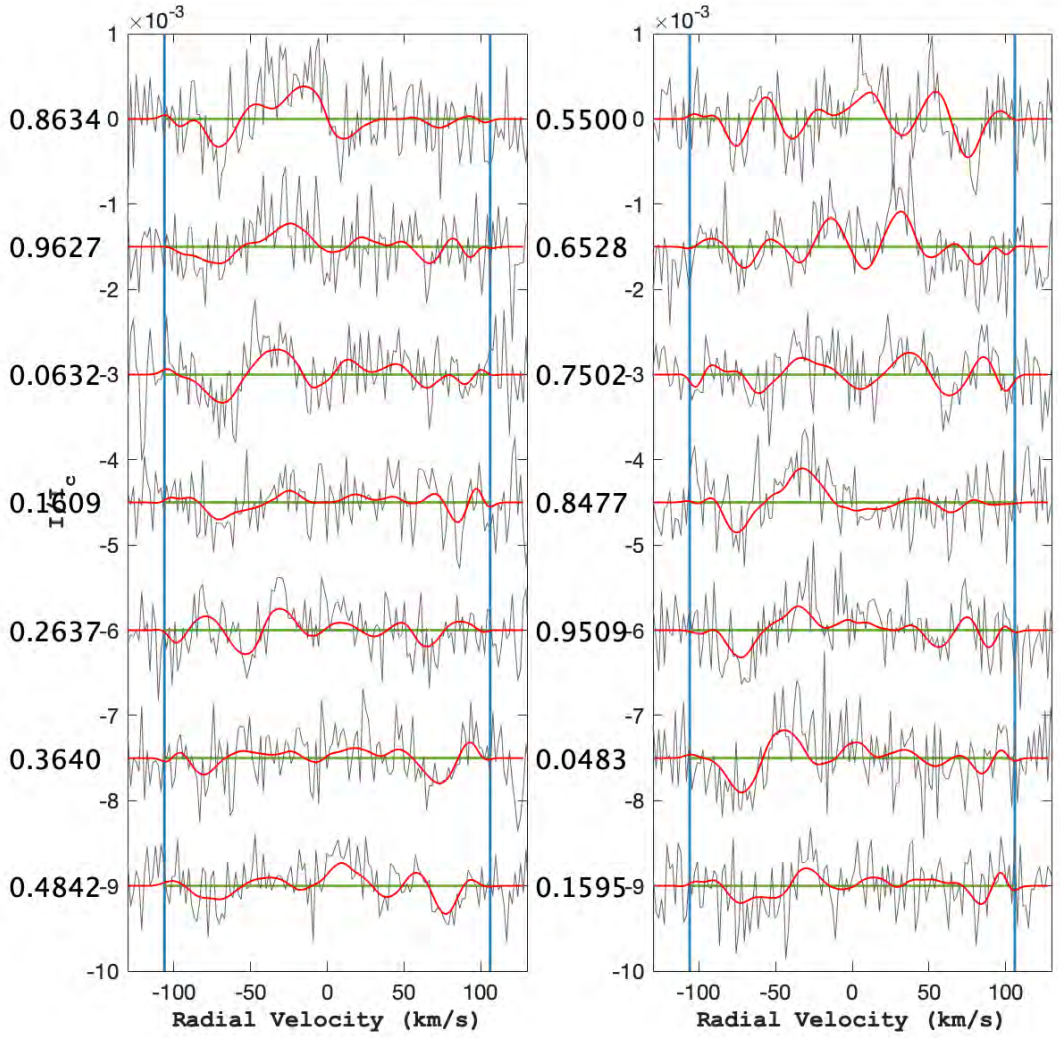

Figure 3.4.9: Stokes V LSD profiles of V530 Per. Gray lines represent the observations, while red lines show our ZDI model. Blue vertical lines mark the $\pm$ v sin$i$ limit. The left panel shows the data from 29 Nov, and the right panel represents 05 Dec. Rotational phases are indicated on the left of each panel.

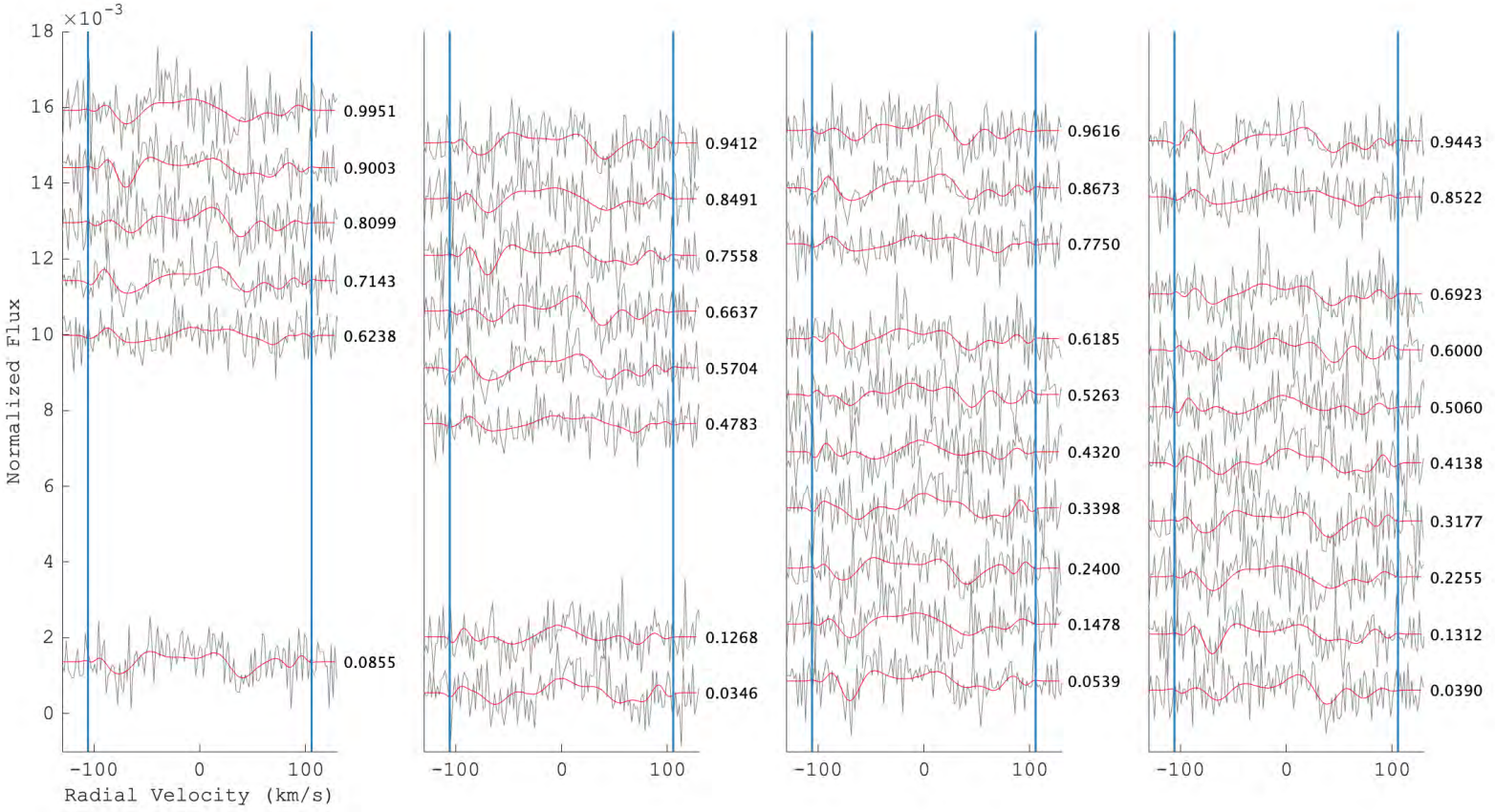

Figure 3.4.10: Observation and ZDI model for Stokes V data in 2018. The subpanels from left to right show results in 17, 18 ,22 , 23 Oct, respectively. Blue vertical lines mark the $\pm\, v \sin i$ limit. Rotational phases between 0-1 are indicated on the right side of each panel.

3.4.5 Activity-rotation relationship

The very rapid rotation of V530 Per results in a very small Rossby number, $R_o \approx 1.3 \times 10^{-2}$, indicative of a very efficient amplification of its internal magnetic field through a global dynamo. Main sequence stars with similarly small Rossby numbers for which ZDI maps are available generally belong to the M dwarf category, and V530 Per is one of the rare G/K dwarfs populating the low Rossby number branch (Vidotto et al., 2014; See et al., 2019). Fig. 3.4.11 is adapted from the Fig. 1 of See et al. (2019) (who present a compilation of ZDI measurements, extending on previous works by Vidotto et al. 2014; Folsom et al. 2016, 2018a). From the original plot, we have removed M dwarfs because of their much deeper convective envelope. We also discarded Hot Jupiter host stars, since at least τ Boo was clearly off the main trend, possibly due to significant tidal interaction between the star and its close planetary companion. We therefore end up with a list of F-G-K effectively single dwarfs. V530 Per stands at the very left of the diagram, making it an important object in the study of saturated dynamo action in ZAMS stars. The average strength of its large-scale magnetic field ($\sim$ 177 G) is roughly similar to other targets with $\log_{10}(R_o) \lesssim -1.5$, with an average field strength of 186 G for this group of five stars. This is in contrast with stars having $\log_{10}(R_o) \gtrsim -1.7$, for which the average field strength decreases according to a power law, with $\langle B \rangle \propto R_o^{-1.19}$. If we plot $\langle B \rangle$ as a function of the rotation period instead of the Rossby number (not shown here), the power law for non saturated stars is such that $\langle B \rangle \propto P^{-0.9}$.

We note that the four saturated stars display a marginally decreasing field strength for decreasing Rossby numbers, which could possibly be a hint of supersaturation. This finding would be consistent with X-ray observations of other stars in the α Per cluster, where a decrease of the X-ray flux was reported for stars with the fastest rotation (Prosser et al., 1996). A tentative power law fit using the four saturated stars is consistent with $\langle B \rangle \propto \sqrt{R_o}$. We stress, however, that this trend is based on a small number of objects, and mostly disappears if we include M dwarfs in the same plot or if we assume that the scatter observed a $\log_{10}(R_o) \gtrsim -1.7$ (which seems to be mostly due to stellar cycles, e.g., Boro Saikia et al. 2016, 2018 for 61 Cygni A) is also valid in the saturated regime.

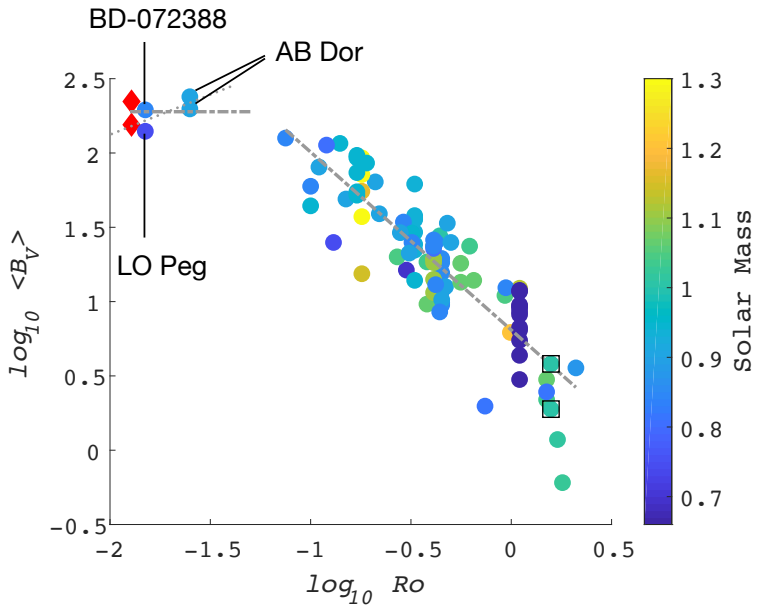

Figure 3.4.11: Average large-scale surface magnetic field as a function of the Rossby number for solar-like stars taken from See et al. (2019). Stars are marked by filled circles, color coded according to their mass. Two measurements representative of large-scale field at solar minimum and maximum are marked with squares (and come from Vidotto et al. 2014). V530 Per is the red diamond in the upper left corner. Dashed lines show power laws for the saturated and unsaturated regime, with a slope of -1.19 for unsaturated stars and an average $\langle B \rangle$ of 186 G for saturated stars. The dotted line is a tentative power law with an exponent of ≈ 0.5 for saturated stars.

3.5 Differential rotation

The very dense phase coverage of our time-series, including repeated observations of specific rotational phases separated by a few-day gap, constitutes a very good basis to study the short term evolution of photospheric brightness, especially under the action of differential rotation (DR hereafter). In this context, the large $v \sin i$ of V530 Per is also an asset as it gives the capability to spatially resolve small surface features.

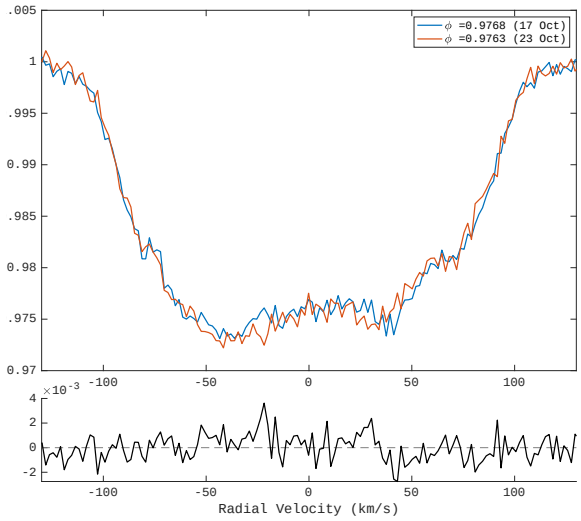

Figure 3.5.1: Top panel: example of LSD profiles for 17 Oct. (blue), and 23 Oct. (red) at close rotational phases ($\phi = 0.9768$ and 0.9763). The small differences between the two profiles (e.g. at RV$= -30$ km s^{-1}) are consistently observed in other couples and are mainly caused by latitudinal differential rotation. Bottom panel: difference between the two profiles.

The subtle changes seen in the intensity line profiles, at nearby phases repeatedly observed over the course of our observing run (Fig. 3.5.1), suggest that the brightness distribution is changing with time. We investigate whether a fraction of its variability can be modeled under the assumption of a differentially rotating surface. As an initial test of this idea, we compare two brightness maps (not shown here) reconstructed from data obtained on the two nights in E06 and on October 18 and 23 in E18, respectively. The specific choice of dates in E18 is a compromise between a sufficiently large temporal lever arm, and a good phase coverage. The comparison is performed as a cross-correlation of the two maps (Fig. 3.5.2), following Donati & Collier Cameron (1997). We observe that the surface structures are systematically shifted in phase between the two dates, and that the shift increases with the latitude. Most of the usable cross-correlation signal is seen at latitudes greater than about 40°, because of a lack of surface brightness tracers closer to the equator. The blue lines display a simple solar-like surface shear law (see below), showing that this simple description of the shear is consistent with our observations.

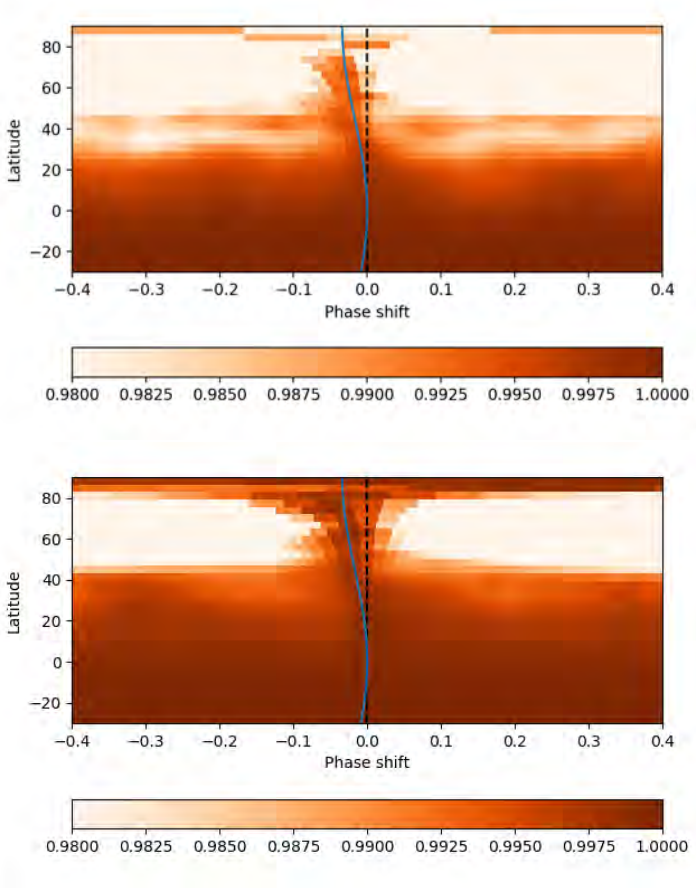

Figure 3.5.2: Cross-correlation map for the brightness maps between 29 Nov & 05 Dec (2006, Top), and 18 Oct & 23 Oct (2018, Bottom). Blue line shows the sun-like differential rotational law derived in Sect. 3.5. Black dash line marked $\phi = 0$

A simple solar-like shear was also reported for other rapid-rotating stars using the cross-correlation approach, for example K dwarf AB Dor Donati & Collier Cameron 1997, LO Peg (Barnes et al., 2005), HD 141943 (Marsden et al., 2011) and post T Tauri star LQ Lup Donati et al. 2000. More complex differential rotation patterns, like Jupiter-like zonal flows are suggested by numerical simulations (e.g., Brun et al. 2017). The more simple latitudinal dependence reported here may be a result of the noise level, or of the limited spatial resolution of DI maps.

As a second step, we used the built-in sheared image ZDI method (Donati et al., 2000; Petit et al., 2002), where a solar-like differential rotation is implemented as part of the ZDI model, following a simple solar-like prescription:

$$\Omega(\theta) = \Omega_{\rm eq} - d\Omega \sin^2 \theta \tag{3.5.1}$$

where $\Omega_{\rm eq}$ is the rotation rate of the equator, $d\Omega$ the pole to equator gradient in rotation rate, and θ the latitude. In practice, we estimate the two parameters of this simple law by computing a large number of DI/ZDI models over a grid of values of DR rate $d\Omega$ and

equatorial period P_{eq}. We then select the doublet that minimizes the model χ^2 (at fixed entropy), as described in Sec. 3.4.2. We show in Fig. 3.5.3 the χ^2 obtained in the $d\Omega - P_{eq}$ plane using Stokes I & Stokes V data. Clear minima are detected for Stokes I at both epochs, detected at $P_{\rm I} = 0.32055 \pm 0.00005$ d and $d\Omega = 0.042 \pm 0.005$ rad d^{-1}(E06), and $d\Omega_{\rm I} = 0.053 \pm 0.004$ rad/day (E18). Using the E06 data, we note that the differential parameters obtained assuming a spherical surface are very close to these values, with $P_{\rm I} = 0.3205 \pm 0.0001$ d and $d\Omega = 0.045 \pm 0.01$ rad d^{-1}, $P_{\rm I} = 0.032042 \pm 0.00005$ d. The shear in Stokes V was performed using the brightness map as a prior, implying that the brightness was sheared by the same differential rotation parameters as Stokes V. We repeated the differential rotation search for Stokes V but assumed a constant surface brightness (as done in most previous ZDI measurements), and found a shear value within error bars of our first Stokes V estimate. A similar attempt to measure the shear from Stokes V data was inconclusive for E06, most likely because the high relative noise of our polarized line profiles is enough to hide changes in the Zeeman signatures as subtle as those generated by a Sun-like surface shear. The estimation was suceessful in E18, with $P_{\rm V} = 0.32045 \pm 0.0001d$, $d\Omega_{\rm V} = 0.15 \pm 0.01$ rad/day.

We identified a higher shear level using Stokes V profiles (~ 0.15 rad/d, ~ 3 times larger than the Stokes I estimate). Similar results were repeatedly obtained for the young dwarfs AB Dor and LQ Hya (Donati et al., 2003b), and the T-Tauri stars Par 2244 (Hill et al., 2017) and V410 Tau (Yu et al., 2019). Assuming that this observation is not an artifact of the inversion procedure, it has been suggested by Donati et al. (2003b) that such differences may be linked to Stokes I and V tracing different depths within the star (depending on how deep the surface brightness and magnetic regions are actually generated), which is an interpretation also proposed for the Sun (Beck, 2000). We also note that the Stokes I shear measurement obtained in E18 is consistent within 3σ with the one obtained in E06, while temporal changes in this value were previously reported for AB Dor (Collier Cameron & Donati, 2002).

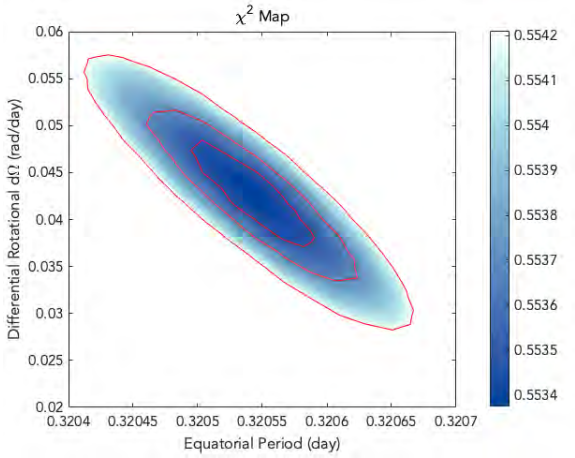

(a) Stokes I, 2006

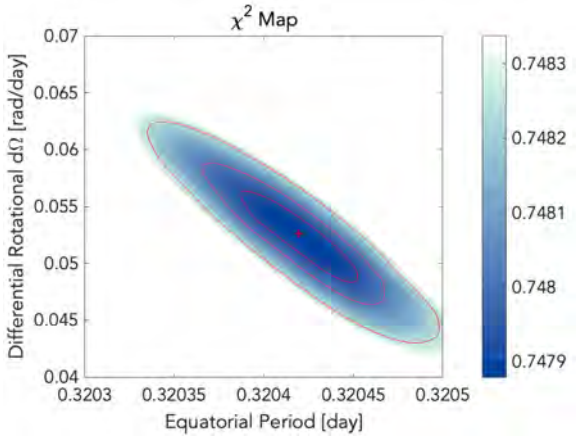

(b) Stokes I, 2018

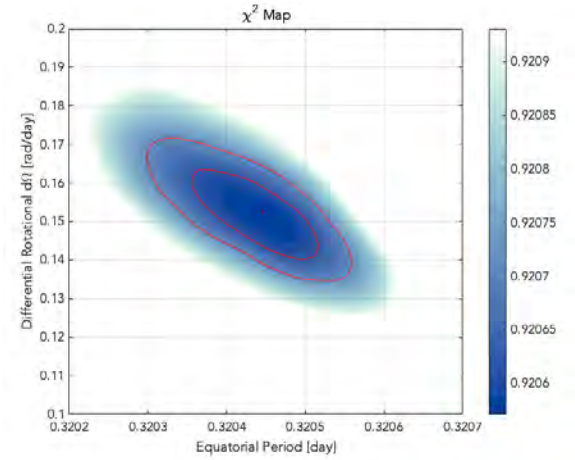

(c) Stokes V, 2018

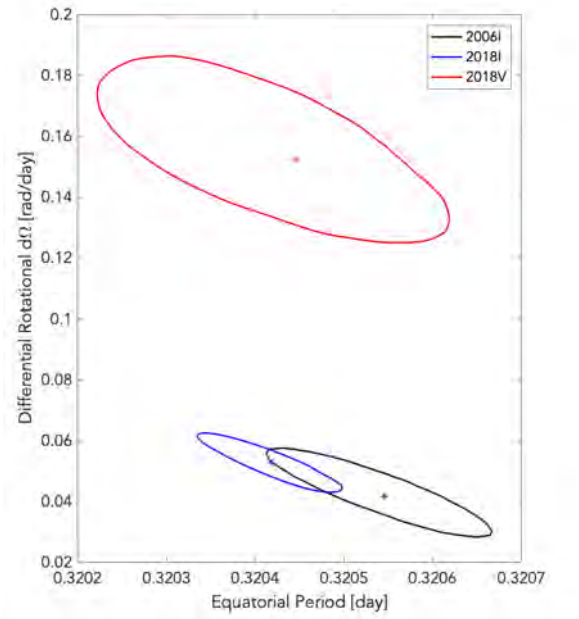

(d) All

Figure 3.5.3: (a-c) Reduced χ^2 map for the shear parameter equatorial rotational period $\Omega_{\rm eq}$ and differential rotation $d\Omega$ for Stokes I & Stokes V data. The three red solid lines illustrate the 1σ, 2σ, and 3σ confidence intervals. (d) A comparison of 3σ region for all 3 maps. Crosses marked the location of peak values.

3.6 Evolution of prominences

The Hα line profiles are always seen in emission throughout the observing run. For both epochs, as shown in the mean Hα line profile in Fig. 3.6.1, two peaks are observed at roughly $\pm$200 km s^{-1} from the line center (outer peaks hereafter). This velocity is much

larger than the projected equatorial velocity of the stellar surface (≈ 105 km s^{-1}). In E18, there was an extra peak close to the line center (central peak hereafter), forming a triple-peaked line profile.

The dynamic spectra (DS) obtained for the two nights in E06 (Fig. 3.6.3) show clear, similar trails with evidence of periodic modulation, at a period close to the stellar rotation period. Two tracks in the DS correspond to the outer peaks in the mean line profile. The largest emission shows up at similar rotational phases in the two nights (e.g. $\phi \sim 0.15, 0.55$). In general, the DS obtained in E18 (Fig. 3.6.4) shows significant day-to-day variations. For consecutive nights (i.e., 17 & 18 Oct or 22 & 23 Oct 2018) in E18, similar structures can be spotted in the DS at close rotational phases, which suggests that a fraction of the observed variability is dominated by rotational modulation.

The relatively stable Hα configuration observed during the first two nights in E18 is considerably different from the one observed on 22 Oct. After three nights without observations between 18 and 22 Oct in E18, several additional emission components are observed in the DS, resulting in an overall increase of the emission for this specific night. We first note a broad emission peak around phase 0.5 and at negative velocities (between roughly -200 km s^{-1} and 0 km s^{-1}). This line bump was not so prominent during the two previous nights (if it was present at all), and it becomes much weaker again during the last observing night. Another emission component takes the shape of a trail close to the line center and extending from phase $\phi \sim 0.4$ to phase $\phi \sim 0.9$. It is not easy to decide whether this trail was already there in the previous observing nights, owing to the incomplete phase sampling. It is, however, present in the fourth night, although with a much reduced brightness. This trail (which is responsible for the central peak seen in Fig. 3.6.1) is confined within a range of velocities going from ~ -50 km s^{-1} to $\sim +30$ km s^{-1}. The repeated observation over consecutive nights, at similar phases, definitely shows that this spectral feature is rotationally modulated. It is visible during only a fraction of the rotation period, suggesting that it is eclipsed behind the star during part of the rotation cycle. This is consistent with a hot chromospheric spot located at intermediate latitudes (since a prominence would more likely be seen as an absorption feature when transiting in front of the stellar disk). Finally, a burst-like event takes place at phase $\phi \sim 0.18$ on 22 Oct and with a blue shift of $\sim +230$ km s^{-1}, with a lifetime shorter that our temporal resolution (i.e. < 600 sec).

The Alfvén radius was calculated with a Weber-Davies model (Weber & Davis, 1967) using the numerical code of Johnston et al. (2017). For this, we have estimated the mass loss from the star using the relation of See et al. (2017) and the value of the Rossby number in Tab. 3.3.1. We obtain that V530 Per has a mass loss rate of $10^{-10} M_{\odot}.yr^{-1}$. A coronal temperature of 16×10^6 K was calculated applying the relation of Johnstone & Güdel (2015), and $F_x = L_x/(4\pi R_*)$ with the L_x value quoted in Tab. 3.3.1. We obtain an Alfvén radius of about $5R_*$ according to Fig. 3.6.2. This value is likely over-estimated, as centrifugal forces are neglected here. It is therefore possible that the actual Alfvén radius may be closer to the source surface proposed in Sec. 3.4, although it can be expected to be larger than the source surface radius (e.g., Schrijver et al. 2003). Even considering this point, the star is most likely in the centrifugal magnetosphere regime that allows it

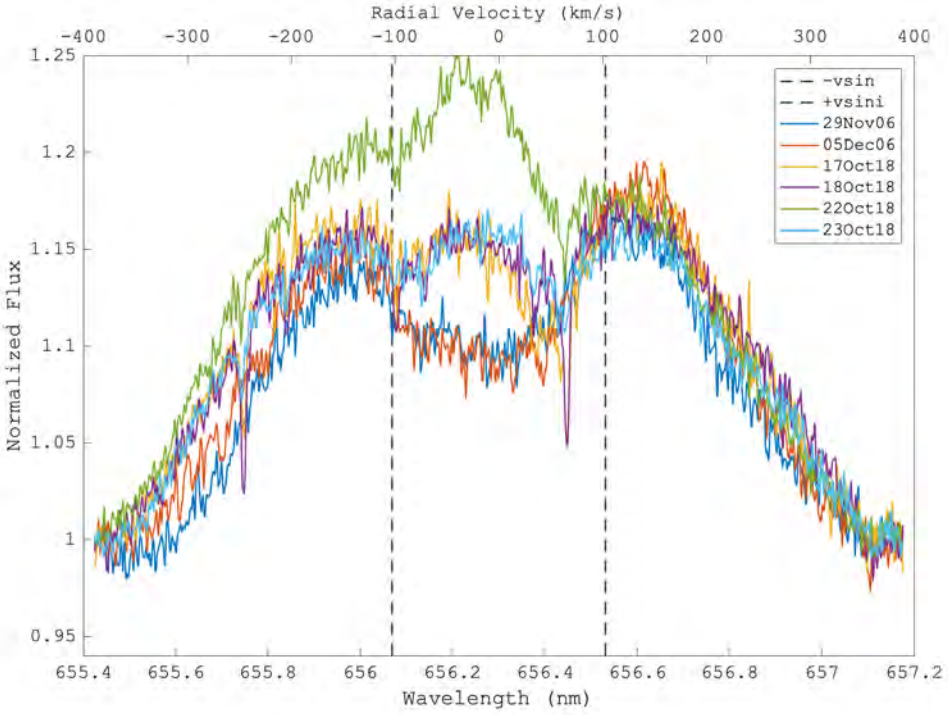

Figure 3.6.1: Mean Hα profile for each observational night in 2006 & 2018.

to support prominences (Ud-Doula et al., 2008). In this case, and as long as sufficiently short time-scales are considered, most of the observed variability can be attributed to the orbital motion of hydrogen clouds. We therefore adopt the assumption that the emission is due to large prominences trapped in the coronal large-scale magnetic field and forced to corotate with the stellar surface (Collier Cameron & Robinson, 1989a,b; Steeghs et al., 1996; Donati et al., 2000).

In order to visualize the spatial distribution of prominences, we made use of the simple maximum entropy tomographic code of Donati et al. (2000), which is inspired from an algorithm initially developed for cataclysmic variables by Marsh & Horne (1988). Through this inversion method (more details in Sec. 2.4), we attribute 2D Doppler velocities (V_x, V_y) to Hα emitting clouds, assuming a local Hα profile of gaussian shape with a 0.04 nm ($\sim$18 km s^{-1}) gaussian FWHM, under the assumption that the Hα emitting material is optically thin (Donati et al., 2000). We note that the outcome of the model is mostly unsensitive to the exact value of the local width. In the case of corotating material, the velocity distribution is a straightforward illustration of the spatial distribution. Here, the emission is modeled above the continuum (without subtraction of any reference profile). The reconstructed equivalent widths should therefore not be considered physically meaningful, the main objective of this simple model being to locate the emitting material in the velocity space and highlight its possible short term evolution.

The middle panel of Fig.3.6.4 illustrates the synthetic set of Hα profiles produced by

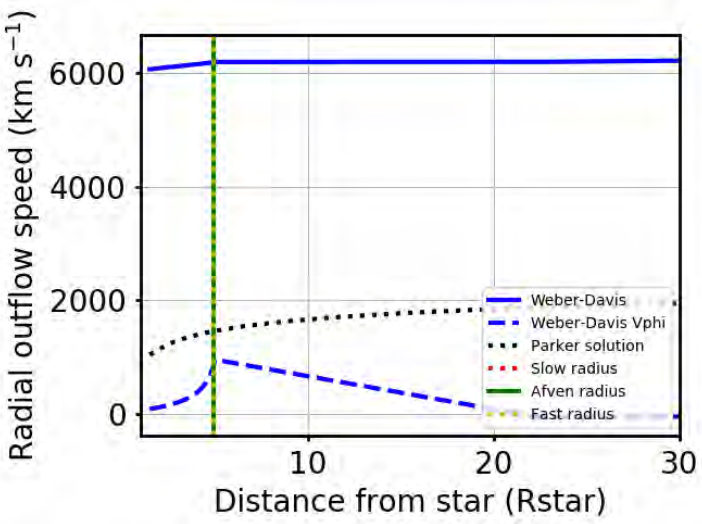

Figure 3.6.2: Determination of the Alfvén radius (here at $4.9R_*$), using a Weber-Davies model.

the code, showing that the main spectral features are correctly reproduced by the model. Residuals, however, remain above the noise level, which shows that the simple model used here is not able to fit the whole Hα signal (right panel of the same figure). This mismatch likely highlights that rotational modulation is not the only source of variability in our chromospheric data, even on timescales as short as one night. This observation justifies a posteriori our choice to model the two nights of observation separately. It is also likely that a more elaborated model, e.g., with the intensity of each pixel map allowed to vary sinusoidally with rotation phase (as in, e.g., Steeghs 2003), would likely allow one to achieve a better fit to the data. In particular, this additional flexibility may help mimicking, e.g., that some of the prominences may be partly hidden by the star as they rotate.

The resulting prominence patterns show similarities for the two nights in E06. Large clouds are reconstructed at most phases, at a velocity roughly equal to the one of the corotation radius ($\sim 1.9R_*$, Fig.3.6.5). We also note that significant variations are seen between the two nights in E06. In the first map, we reconstructed a higher concentration of material between the stellar surface and the corotational radius, between phases 0.75 and 0.95. During the second night however, the coronal material features a larger radial spread around the corotation radius, as well as azimuthally with a denser material between phases 0.7 and 1. In both cases, most of the Hα emission is observed within twice the corotation radius. The modeled DS in E18 are shown in the middle panels of Fig. 3.6.4, illustrating that the tomographic inversion is able to fit a majority of the observed features. We reached, however, a larger χ^2 ($\sim$ 9.5, with values ranging from 9 on 17 Oct to 10 on 22 Oct) than the one obtained from E06 ($\chi^2\sim$ 8). This slightly degraded fit suggests that our simple model is challenged by these observations, either because some level of non-rotational variability affects our data over individual nights, or because some basic assumptions of the model are not consistent with the data

(e.g., the fact that the emitting clouds are not supposed to be eclipsed by the star). The model residuals shown in the lower panels of Fig. 3.6.4 are generally an order of magnitude lower than the observed emission, which suggests that most of the periodic patterns were successfully reconstructed by the tomographic code. Some of the phases and velocities displaying a significant mismatch with the model correspond to burst-like events described above (structures that are too short-lived to follow a rotationally-modulated pattern). For instance, at $\phi \sim 0.18$ on 22 Oct in E18, the peak on the right of the line profile cannot be reproduced due to its very brief appearance in our data. Another example of mismatch is the trail seen close to the line core on 22 and 23 Oct. In this second case, where rotational modulation seems at play, the poor fit is likely owing to the intermittent visibility of the cloud, that spends part of the rotation cycle hidden behind the stellar disk.

Apart from the fast changing component of Hα emission that escapes our modeling attempts, most of the prominence pattern is correctly fit for all four nights of E18. In the resulting maps, the emitting material accumulates around the corotation radius ($\sim 1.9\ R_*$), and forms an extended ring-like structure. The reconstructed pattern inside the $v\ \sin i$ limit is confined within a relatively small phase interval, centered around phase $\phi \sim 0.4$ during the first two nights, then showing up around phase $\phi \sim 0.7$ during the last two nights, with a prominent emission peak on Oct 22 in relation to the emission trail observed close to the line center.

We stress, however, that fine details in the observed changes need to be considered with caution, given the very simple model used in our tomographic inversion. We note that the period optimizing our model is larger than the period actually used to reconstruct the prominence maps (taken equal to the rotation period of the stellar equator derived in Sec. 3.5), with about 0.39 d on 29 Nov and 0.36 d on 05 Dec in E06, and a value of 0.37 d on 17 Oct in E18. However, such period estimate is likely to be impacted by non-rotational short term variability occurring within each night, as well as by the incomplete phase coverage of individual nights.

The double-peaked emission of the Hα line, consistently observed throughout our time-series, agrees well with older observations of Barnes et al. (2001). As discussed by these authors, it is likely that the rotationally modulated Hα signal is seen in emission due to the small inclination angle of V530 Per, while stars with a higher inclination feature absorption signatures from their slingshot prominences. Another example of a young star with Hα emitting prominences is LQ Lup (Donati et al., 2000). Hα transients have been recorded in, e.g., AB Dor (Collier Cameron & Robinson, 1989a; Donati & Collier Cameron, 1997) and Speedy Mic (Dunstone et al., 2006a,b).

The tomogram displays multiple clouds corotating with the star and distributed in a ring-like structure at a velocity roughly equal to the one expected at the corotation radius. This is in striking agreement with similar inversions obtained by Barnes et al. (2001) for V530 Per, Donati et al. (2000) for RX J1508.6-4423 and Budding et al. (2006) for CC Eri. Our data suggest that the period of Hα emission could be on the order of $0.36 - 0.39$ d, which is longer than the rotation period of the stellar surface, even if we take into account the surface differential rotation. Although the evidence presented here

is too slim to reach a definite conclusion about the reality of this longer period (given that our observations in a given night span less than one complete rotation period), it may suggest that the corotating hypothesis is only partially valid, and that prominences sufficiently far away from the surface may experience a less efficient magnetic locking, possibly due to the radial decrease of the field strength. The densest accumulation of prominences shown in the tomograms of E06 is located between phases 0.75 and 1. This observation can be linked to the extended, close field lines of Fig. 3.4.8 (right-bottom part). We note that the preferred phases for prominences are located away from the phases covered by the large polar spot. Their location is also away from the maximum strength of the radial and azimuthal magnetic field components.

The dominant part of the Hα emission can be modeled by our simple tomographic model, showing that most of the observed system is stable over about 6 hr. Within each night, however, the residuals of the best model highlight non-rotational, short-term changes in the distribution of the coronal material, although we do not witness very fast blue-shifted events similar to those previously reported for AB Dor (Collier Cameron & Robinson, 1989b; Donati et al., 1999). The two tomograms of E06 display noticeable differences, especially in the azimuthal distribution of the prominence clouds, although the time gap between the two observing nights makes it difficult to say much about the turnover time of the cool coronal material. We note that models of prominence lifetimes in young active stars predict a short life expectancy for stars with a mass and rotation rate similar to V530 Per (Villarreal D'Angelo et al., 2018). A denser temporal monitoring is therefore carried out in E18 to monitor the short term evolution of slingshot prominences around V530 Per.

The central emission peak was not observed in 2006. In 2018, it is linked to a trail in the DS that shows evidence of rotational modulation, and remains confined at relative radial velocities smaller than about 50 km s^{-1}. This peak is responsible for the features inside the v sin$i$ limit in Fig. 3.6.5. The small Doppler shift, combined with the eclipse of this signal during about 30% of the rotation, suggests that it is produced by a hot chromospheric point anchored at intermediate latitudes. In the DS of 22 and 23 Oct, this central trail in Hα evolves in phase with the main, positive trail in the Stokes I DS. This phase correlation suggests that this bright, short lived chromospheric feature is lined up with the phase of the off-centered polar spot. A similar observation was reported for the K dwarf RE 1816+541 (Eibe, 1998), and the weak line T Tauri star TWA 6 (Skelly et al., 2008).

The observed differences in the shape and intensity of the Hα line between successive nights suggest a day-to-day variation of the prominence arrangement. The emission recorded at the corotating radial velocity is less dramatically affected by these fast changes than the central emission peak. Surface activity tracers do not obviously reflect this rapid evolution, as illustrated by the Stokes I data of Fig. 3.4.6, or by the Stokes V profiles of Fig. 3.4.10. The reconstruction of a series of brightness maps using data of individual nights (not shown here) does not unveil any noticeable changes in the spot pattern, or at least not at a level that can be safely trusted as a genuine evolution (versus spurious differences owing to the different phase coverage, for instance). The

reconstruction of magnetic maps for individual nights increases the noise contribution, which has the effect of hiding even more efficiently any possible variability. The only measured source of surface evolution is the latitudinal differential rotation, which effect remains fairly limited over the time span of our observations, and which is at a level similar to the one measured in 2006. We note, however, a systematically larger χ^2_r in 2018 compared to 2006 (for all mapping inversions presented here, and in spite of a slightly shorter time span in the 2018 time series), which may suggest a globally higher intrinsic surface variability in 2018. The absence of a clearly correlated evolution between the photosphere and the corona suggests that major reconnexion events can be triggered in the corona without any substantial reorganization of the magnetic field at the surface. It is also possible that very localized surface changes (occuring at spatial scales unresolved through ZDI) are enough to globally alter the stability of the prominence system. This disconnected evolution of the surface and the corona is reminiscent of recent observations of ϵ Eridani, where a sudden drop in CaII H and K emission was observed within a few days, with no simultaneous changes in the large-scale magnetic field (Petit et al., 2021).

We estimated the mass of the prominence system by using a method very similar to the one presented by Steeghs et al. (1996), and later used by Donati et al. (2000) or Zaire et al. (2021) (See A.2 for details). We first calculated the equivalent width (EW) of the emission component of Hα by subtracting from the measured EW a reference EW estimated from a PolarBase spectrum of HD 225261, a quiet star chosen for its low S-index (0.174) and effective temperature (5264K) close to the one of V530 Per (Marsden et al., 2014). By repeating this procedure with $H\beta$ (which DS, showing marginally detected emission signatures consistent with Hα, is displayed in Fig. 3.6.6), we estimated the Balmer decrement to be equal to ≈ 2.49, consistent with optically thin material.

We make the rough assumption that the hydrogen clouds are contained within a sphere of radius l, taken equal to the radius of the source surface $l = 2.5R_*$. The number density of hydrogen atoms is estimated to be $\approx 1.1 \times 10^{16}$ m^{-3} and the total mass stored as prominences is $\approx 4.6 \times 10^{17}$ kg ($\approx 2.3 \times 10^{-13} M_\odot$). The prominence system mass of V530 Per is, therefore, mostly consisten with the range of masses obtained for other rapidly rotating stars ($10^{-14} - 10^{-17} M_\odot$, Collier Cameron & Robinson 1989a; Donati et al. 2000; Dunstone et al. 2006b; Zaire et al. 2021), and close to the largest reported value ($\approx 5 \times 10^{-14} M_\odot$, Donati et al. 2000). For a comparison, the solar prominence mass established through H and He measurements is in the range $10^{11} - 2 \times 10^{12}$ kg (Labrosse et al., 2010).

While the prominence mass is mostly the same on 17 and 18 Oct in E18, we observe a $\approx 7\%$ increase in the mass measured on 22 Oct in E18. During the last observing night (23 Oct), the prominence mass is back to a value close to the one obtained at the start of the run. This suggests that as much as 3.5×10^{16} kg of material has been removed from the system within one day, although it is not possible to determine whether a fraction of this material was sent back to the star, or if it was entirely ejected towards the interstellar medium. Mass estimates from E06 are consistently below the values reported in E18, by about 5%, which may be linked to the globally weaker surface magnetic field measured at this earlier epoch.

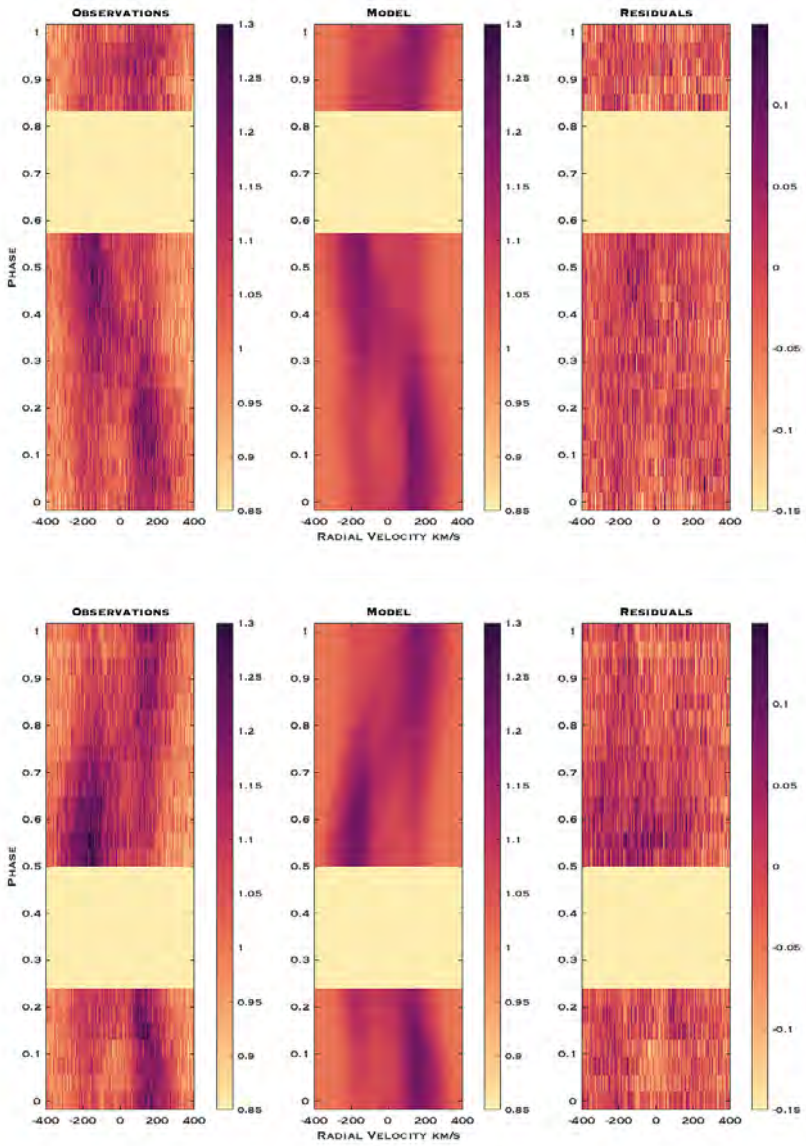

Figure 3.6.3: Dynamic Spectra showing the Hα line of V530 Per in 2006, color coded according to the normalized flux. Rotational phases are computed according to Eq. 3.2.1. The upper and lower panels are for 29 Nov and 05 Dec, respectively. From left to right, we display the observations, the outcome of the tomographic model, and the residuals. Hα mapping from the first night leads to a reduced χ^2 of 7.2, while the second night provides us with a reduced χ^2 of 7.6.

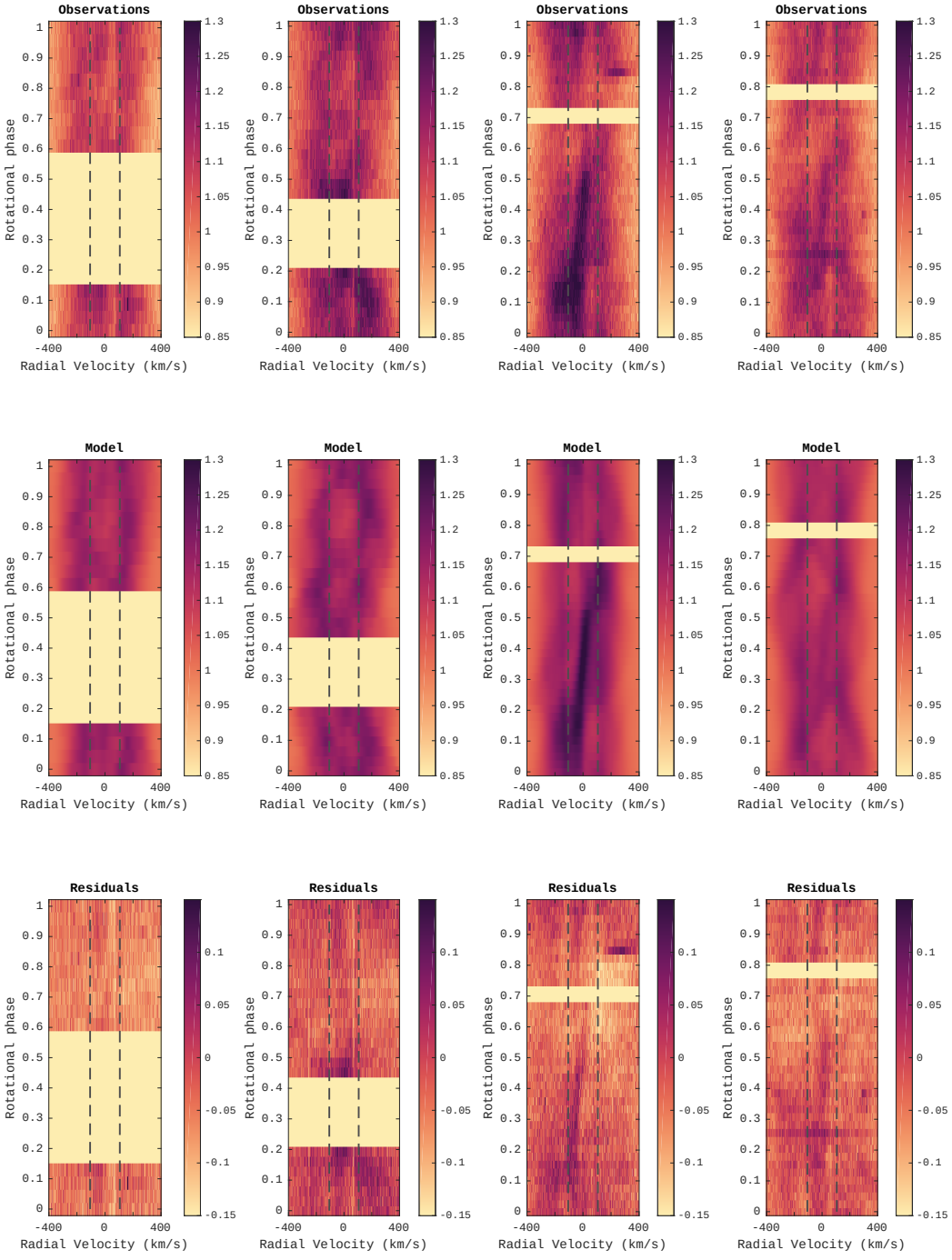

Figure 3.6.4: Dynamic spectrum for Hα, including the observations (Top), the tomography models (Middle), the residuals between observation and model (Bottom). From left to right, the figure show the data of 17, 18, 22, 23 Oct 2018, with color scale by the normalized flux. Rotational phases are computed according to Eq. 3.2.1. Vertical dash lines show the position of $v \sin i$.

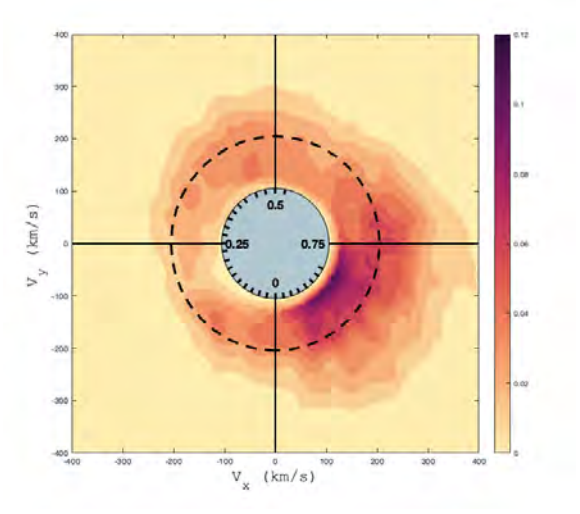

(a) 29Nov, 2006

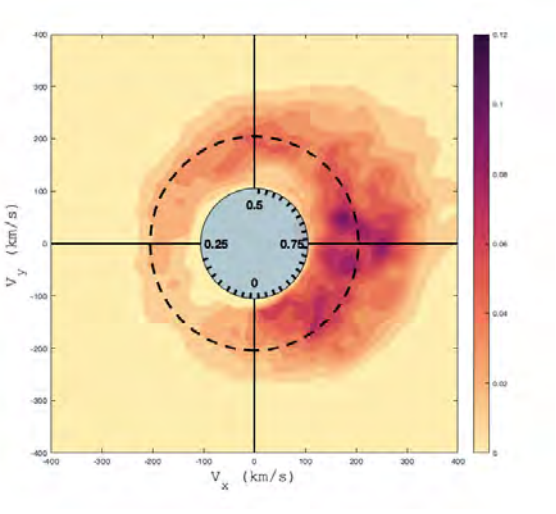

(b) 05Dec, 2006

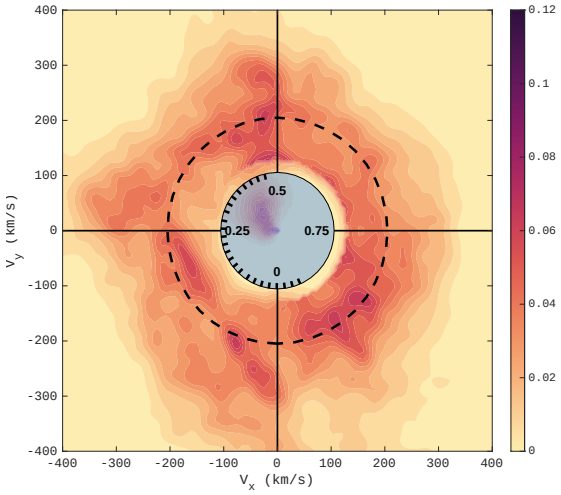

(c) 17Oct, 2018

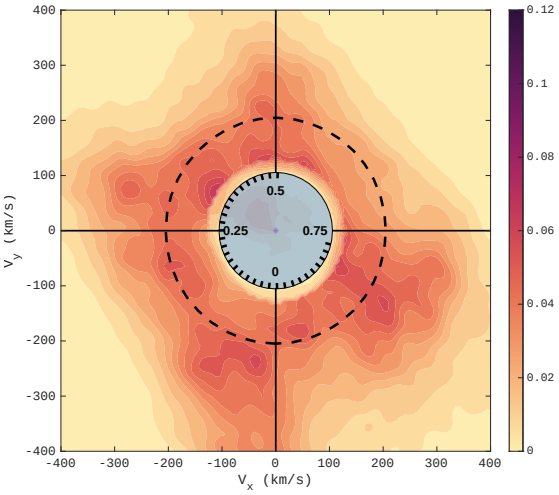

(d) 18Oct, 2018

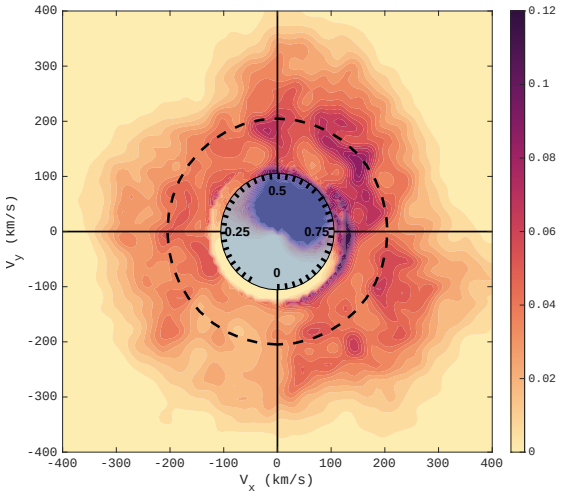

(e) 22Oct, 2018

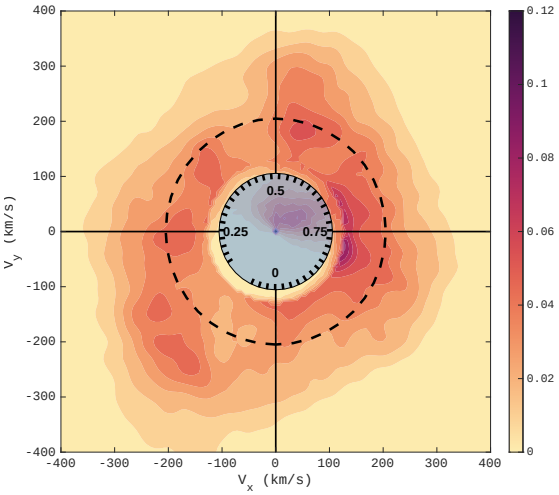

(f) 23Oct, 2018

Figure 3.6.5: Prominence maps of V530 Per reconstructed from the data of each observational night. The inner, filled blue circle represents the stellar surface. Radial ticks inside this circle give the rotational phases of Hα observations. The outer dashed circle is the corotation radius. The color scale depicts the local Hα equivalent width, in units of picometers per 8 km s^{-1} square pixel.

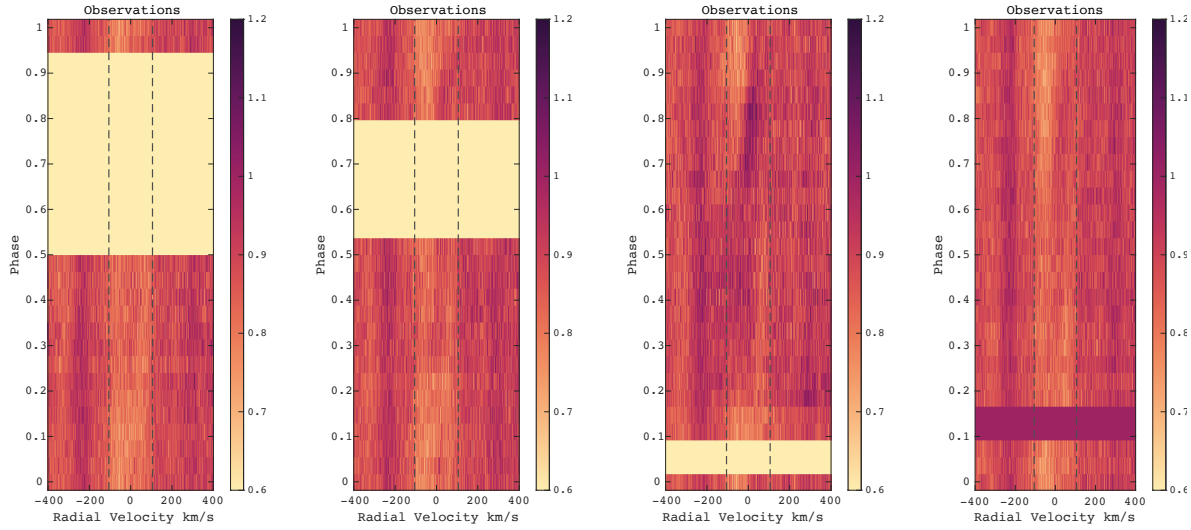

Figure 3.6.6: Dynamic spectra of Hβ, with the same conventions as in Fig. 3.6.4.

Chapter 4

MARSU CubeSat

4.1 Hunting new worlds around active stars

4.1.1 Transit detection of exoplanets around active stars

After the heliocentric revolution brought by Copernicus, people started realizing that there are possibly other worlds similar to Earth around distant stars. However, it was only in 1992 that the first evidence of planets outside of the solar system was obtained (Wolszczan & Frail, 1992). Three years later, the first planet detected around a Sun-like star was announced (Mayor & Queloz, 1995). As of today, thousands of exoplanets have been discovered ($\sim$ 4500 in September 2021). As shown in Fig. 4.1.1[1], the detection of exoplanets was mainly obtained by the indirect methods of transit photometry and Doppler velocimetry. Among the various classes of planets, studying Earth-mass rocky planets can be exceptionally attractive, especially those located within the habitable zones (HZs, where liquid water can be stable on the planetary surface) of their host stars. In planetary systems with a star as luminous as the Sun, these Earth-like habitable planets are far from the host star, resulting in extremely weak signatures (due to the distance in the case of Doppler spectroscopy, or to the large radius ratio between the star and the planet in transit photometry). Therefore, if the planet is orbiting closer to the star, the detection is facilitated. For low-mass M-dwarfs with a smaller luminosity (typically $\sim 5^{-5}\ L_{\odot}$), HZs are closer to the host star and Earth-like planets are easier to detect. Moreover, M-dwarfs account for most of the stellar population around our solar system, and they are more likely to have planets than more massive stars (Bonfils et al., 2013).

Another important and challenging population to explore is the class of hot giant planets orbiting young solar-type stars. These close-in planetary companions are expected to be formed further away from the star, past the ice limit. Their orbit is, therefore, the consequence of a migration process. Enlarging the available sample of young hot jupiters will help distinguish between the various possible channels leading to their presence close to the star, i.e. decide whether their migration is primarily due to

[1] https://exoplanetarchive.ipac.caltech.edu/exoplanetplots/

disc-planet or planet-planet interactions (Charbonneau et al., 2007; Donati et al., 2016).

After the first detection of a planet through the transit method by Charbonneau et al. (2000) (HD 209458b), this technique alone has led to well over half of the exoplanets confirmed up to now.

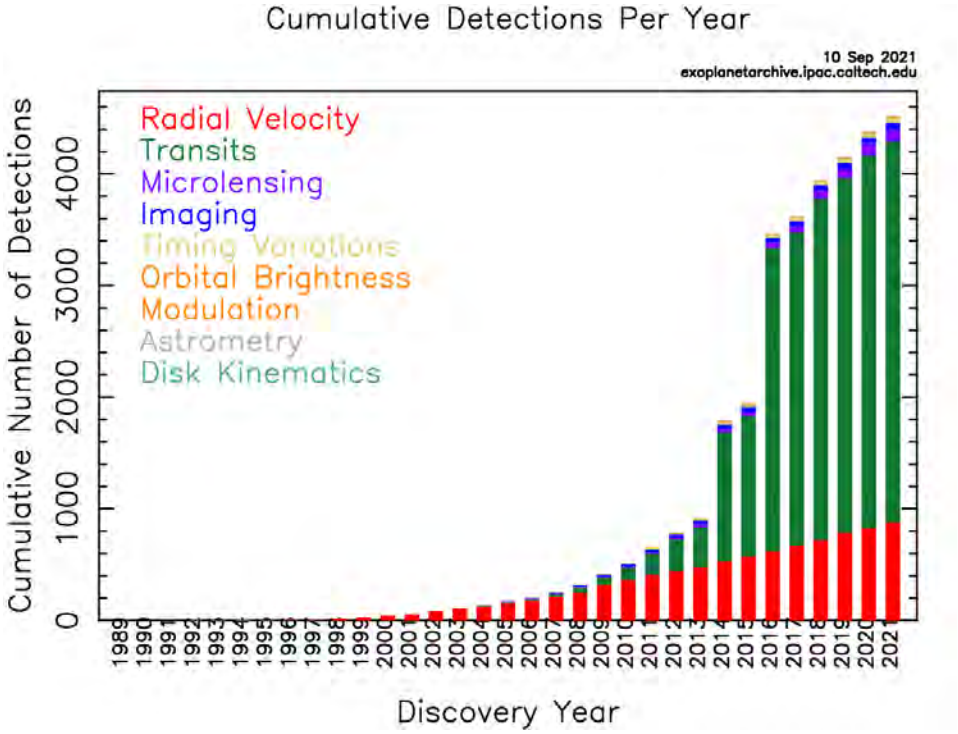

Figure 4.1.1: Cumulative numbers of detected planets, as a function of the discovery year. Different colors show the method of detection. Taken from the NASA exoplanet archive.

The transit method can detect a planet basically by observing the temporary flux decrease of the host star, when a planet is passing in front the stellar disk. As shown in Fig. 4.1.2, this geometric motion results in a periodicity in the light curve of the host star. The characterization of planetary transits is mainly based on three observed parameters: the transit depth δ, the transit duration T, and the transit shape. During a transit, the planet blocks a fraction of the starlight. The reduced flux (or depth) δ can be estimated by:

$$\delta = (R_p/R_*)^2 \tag{4.1.1}$$

where R_p and R_* are the radius of the planet and of the host star. The shape and the duration depend on the orbital parameters (mainly the orbital semi-major axis and the orbital inclination with respect to the line of sight).

Photometric monitoring is efficient to simultaneously characterize transiting exoplanets and other sources of brightness variations of the host stars (magnetic activity, pulsations). Space telescopes are ideal tools to carry out continuous observations of variable stars since they can avoid some critical drawbacks of ground-based observations,

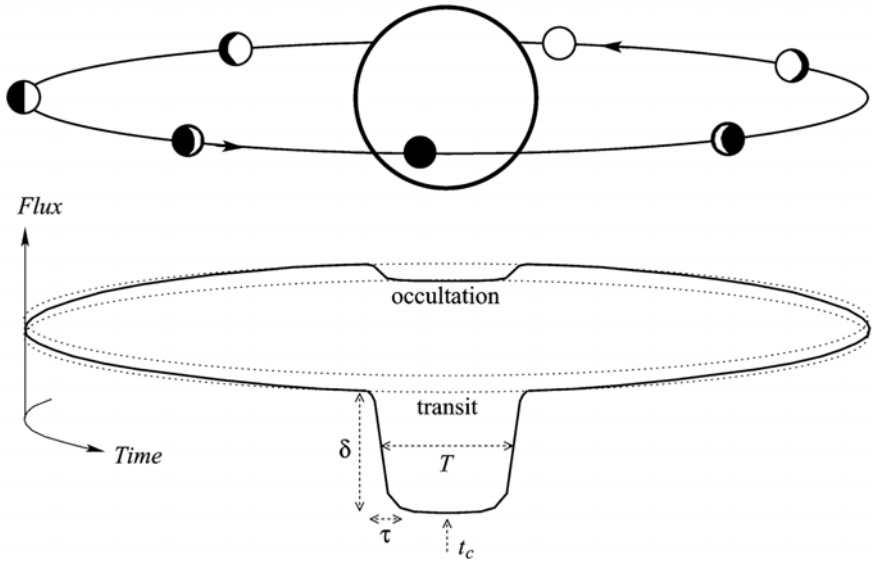

Figure 4.1.2: Sketch for planet transits, where the planet blocks a fraction of the starlight. Take from Winn (2009), Fig. 1.

like day/night alternation and atmospheric variations (e.g., variable cloud cover, turbulence). Table 4.1.1 lists some typical photometric space observatories dedicated to the detection of exoplanetary transits and to stellar physics, e.g., CoRoT Auvergne et al. (2009), CHEOPS (Benz et al., 2020), Kepler (Borucki et al., 2010), TESS (Ricker et al., 2014) and PLATO (Rauer et al., 2014).

Name	CoRoT	CHEOPS	Kepler	TESS	PLATO
Diameter	27 cm	33.5 cm	95 cm	10 cm	12 cm
Cadence	32 s / 512 s	30 s - 60 s	1 min / 30 min	2 min / 30 min	2.5 s / 25 s
Monitoring duration	20-150 days	13 or 50 days	4 years	27-351 days	20 days - 3 years
Mission duration	2006.12 - 2014.6	2019.12 - now	2009.3 - 2013.5	2018.4 - now	2026 - 2030
Bandpass	Visible light	330 - 1100 nm	430 - 890 nm	600 - 1000 nm	500 - 1000 nm
Sensitivity	-	150 ppm $M_v = 9$	20 ppm $M_v = 12$	10ppm $M_v = 11$	-

Table 4.1.1: Photometric space missions. The monitoring time describe the continuous observing time spent on one field.

However, large missions have very limited flexibility (if any) in their observing program, while a number of science cases would benefit from customised observations of specific targets. Tiny space telescopes based on the CubeSat concept, consist of stacking standard cubic units (1U) with 10 cm of width, and offer flexible and low cost opportunities for the monitoring of bright targets, as demonstrated by the ASTERIA (Knapp et al., 2020) proof of concept in the optical domain.

MARSU is a proposal for a near-infrared (nIR) CubeSat-type space photometer, working in parallel with SPIRou (Donati et al., 2020) and SPIP, two twin ground-based nIR spectropolarimeters and velocimeters for the Canada-France-Hawaii Telescope (CFHT, Maunakea observatory, Hawaii) and Télescope Bernard Lyot (TBL, Observa-

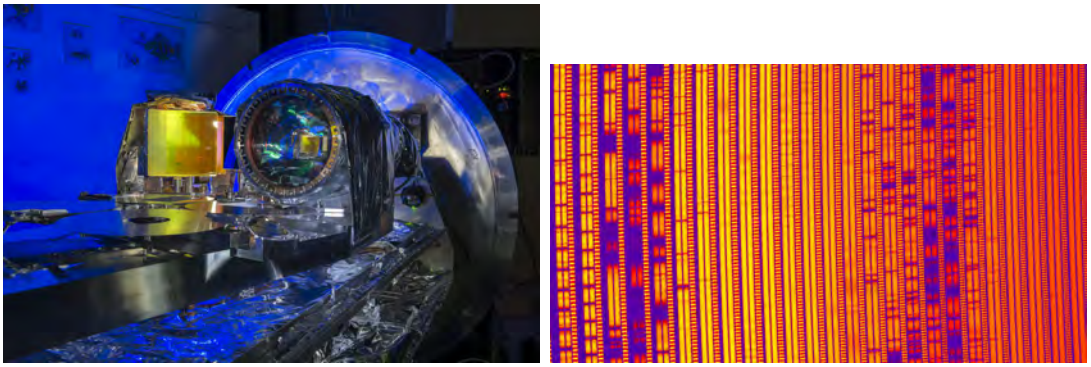

Figure 4.1.3: SPIRou spectrograph (left) during its integration at CFHT, and portion of a SPIRou frame recorded for AU Mic (right). Images taken from http://spirou.irap.omp.eu

Table 4.1.2: Scientific goals of MARSU

Requirement	Value
Stellar magnitude	Up to $\sim$ 11 H magnitude
Spectral domain	1-1.7 μm
Photometric precision	1 mmag rms
Exposure time	Up to 10 minutes
Monitoring period	Up to 3 months
Duty cycle	$\geq 90\%$

toire du Pic du Midi, France), respectively. SPIRou (Fig. 4.1.3) is in operation at CFHT since 2018, whereas the construction of SPIP is under way, for commissioning on the telescope in 2022. MARSU will mainly provide support to the SPIRou Legacy Survey (SLS), a large program aimed at (i) searching for Earth-like planets in the habitable zone of low-mass stars, and (ii) studying the formation of low-mass stars and planets in the presence of magnetic fields. MARSU aims at performing nIR photometry of SLS targets simultaneously with SPIRou observations, in order to (i) provide a continuous monitoring of the magnetic activity of target stars in the same wavelength rtange as SPIRou, with the objective to improve the filtering of the activity noise in radial velocity time series and (ii) search for possible transits of newly discovered SLS planets, or detect new occurrences of single transits reported by other photometric facilities.

4.1.2 Characterizing stellar activity and transiting exoplanets with a nIR CubeSat

As SPIRou and SPIP, the MARSU CubeSat will observe at near-infrared (nIR) wavelengths, where the target stars (nearby M dwarfs and young forming stars) emit most of their light. Photometric time-series of observations of MARSU targets will record temporal changes caused by stellar surface activity and flares, by transiting events, or

by accretion events over time scales of a few minutes to a few weeks (see Fig. 4.1.4 for an illustration based on TESS observations of the young, active, low mass star AU Mic Plavchan et al. 2020). Doppler shifts measured by SPIRou and SPIP can be polluted by stellar magnetic activity, the contribution of which can dominate the velocimetric signatures of exoplanets. Light curves from the MARSU CubeSat will improve the reliability of exoplanet detection and characterization by recording the photometric imprint of stellar activity, leading to a more efficient filtering of this polluting effect. Moreover, the MARSU CubeSat will search for potential transits of exoplanets detected from the ground, since combining spectroscopy and photometry enables one to measure both the mass and radius of exoplanets, thus constraining their bulk densities and thereby providing information on their internal structure for distinguishing between, e.g., telluric planets and gaseous ones.

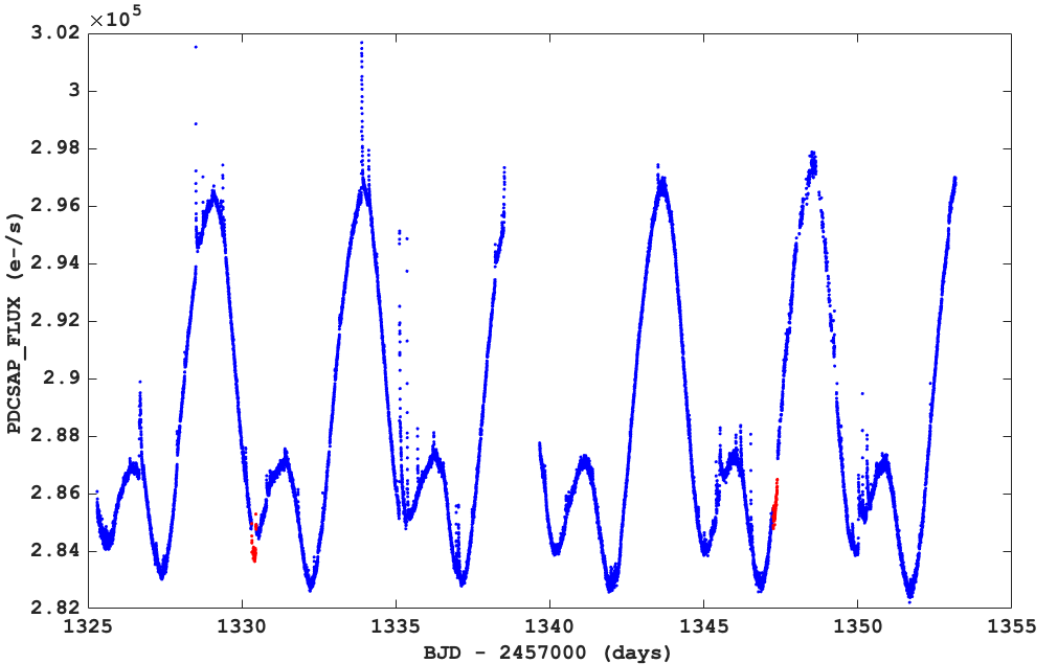

Figure 4.1.4: TESS light curve of the young, low-mass star AU Mic (light flux as a function of the barycentric Julian date). Transits of the exoplanet AU Mic b are indicated in red. Their signatures are vastly dominated by activity phenomena linked to stellar spots (the wave-like pattern) and flares (positive spikes).

In order to address these science questions, the goal of the MARSU CubeSat is to achieve continuous (duty cycle in excess of 90%) photometric monitoring in the YJH bands (1 –1.7 μm) for stars up to an H magnitude of ~ 11, at a precision better than 1 mmag for up to 10 minutes exposure times, over continuous periods of up to 3 months and simultaneously with SPIRou and SPIP observations, as summarized in Table. 4.1.2. Continuous observations in the anti-solar direction impose to use a heliosynchronous orbit. Another possible strategy is to alternate between up to three fields of view on a

timescale of $\sim$ 1 hr, in order to maximize the probability of detecting planetary transits.

In this work, we briefly introduce the preliminary design of MARSU, with details about the payload and the platform (Sec. 4.2). We then describe the numerical simulations of MARSU observations (Sec. 4.3), and the corresponding results (Sec. 4.4). Finally, we introduce the optical bench test bench of MARSU, as an extension of the numerical simulations performed during the thesis (Sec. 4.5).

4.2 Payload and Platform

4.2.1 Payload

In order to fit into a CubeSat, the optical system of the telescope is restricted to a diameter of less than 1U (10 cm). The main component of the payload is a dioptric telescope involving five lenses, with a diameter of 85 mm for the entrance pupil (Fig.4.2.1). This design leads to a focal length of 150 mm (F/1.7645) and a total length of 200 mm from the entrance lens to the detector plane. Three lenses are stacked together in the same barrel at the entrance of the refractor, followed by two more lenses (also stacked together) in front of the detector. Aluminum 6061 spacers are inserted between the lenses to create an athermal system, so that temperature variations up to 10 K do not produce any significant focus change. For any point source, the full width at half maximum (FWHM) of the point spread function (PSF) is equal to 25 μm, translating into slightly less than 2 pixels on the detector. The field of view is about 5°, translating into a 13.17 $\times$ 13.17 mm area on the focal plane (43.9 μm per arcmin). With optimized anti-reflection coatings (average reflectivity of 1% per surface), the overall throughput of the camera is in excess of 80% over the whole spectral range.

A shortwave infrared (SWIR) detector made with indium-gallium-arsenide (InGaAs, e.g., Raptor VIS-SWIR OWL 640 II, detailed in Ch. B) will be mounted in the payload. This 640 $\times$ 512 detector features a quantum efficiency larger than 70% over the selected spectral domain. The pixel size is 15 μm $\times$ 15 μm, with an overall area of 9.6 mm $\times$ 7.68 mm. SWIR detectors reach very short exposure times ($\geq 0.02s$), with very short readout time. The readout noise is expected to stay below 47 e^-, with a gain of 1 e^-/ADU.

4.2.2 Platform

A single payload shown in Fig.4.2.4 has a layout of 1 $\times$ 3 U with an estimated mass of $\sim$ 2.6 kg. The maximum diameter at the entrance of the optical system will be less than 96 mm ($\leq$ 1U). The total length of the payload is about 305 mm ($\sim$ 3U), consisting of the barrel (190 mm), camera (50 mm), and external baffle ($\geq$ 65 mm). The major part of the external baffle is included in the braced structures of the CubeSat (Fig. 4.2.3). The purpose of this first baffle is to block any light reaching the telescope with an angle $\geq$ 70° (note that a deployable baffle may also be considered for a more efficient rejection of contaminating light from the Earth, Moon or Sun). The internal baffles include four

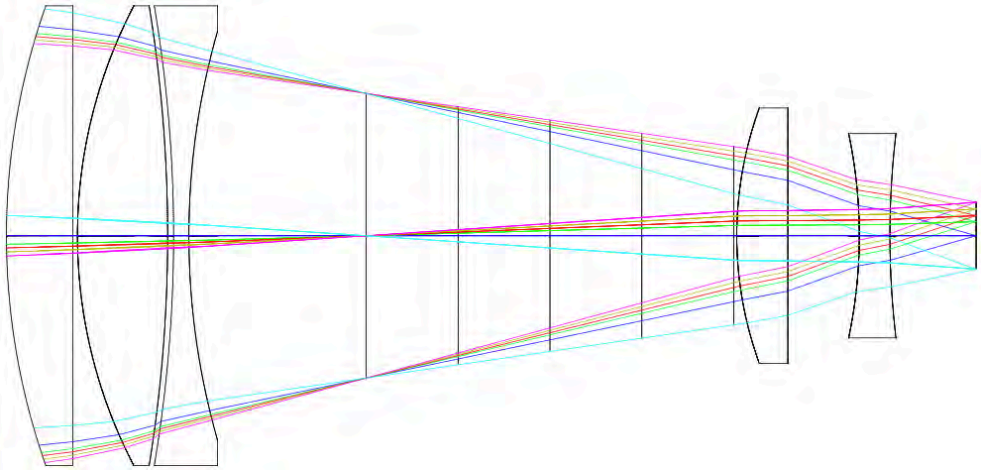

Figure 4.2.1: Optical design of the telescope.

knife rings to get rid of most internal reflections, and are coated to absorb any rogue reflection. The structure of the baffles is illustrated in Fig. 4.2.2.

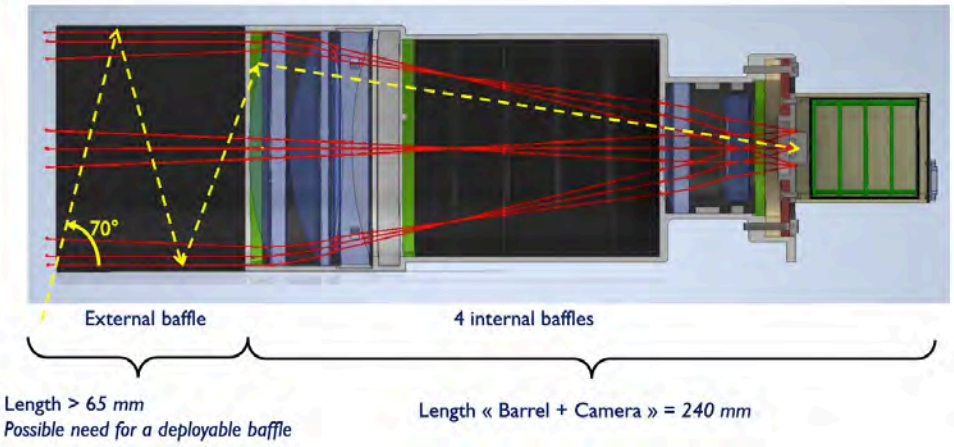

Figure 4.2.2: External and internal baffles.

A 3U payload can be mounted in a $2 \times 3 = 6$U platform as shown in Fig. 4.2.3. The remaining 3U volume will be occupied by the star tracker and control system.

4.3 Numerical simulations of MARSU observations

4.3.1 Basic principle of the simulator

We developed a numerical simulator of MARSU to model data acquired by the CubeSat. This tool include the simulation of a realistic light flux of typical targets (including stellar activity or planetary transits), the attitude jitter of the satellite, basic detector properties, and the extraction of a light curve. The main objective of this simulator is to

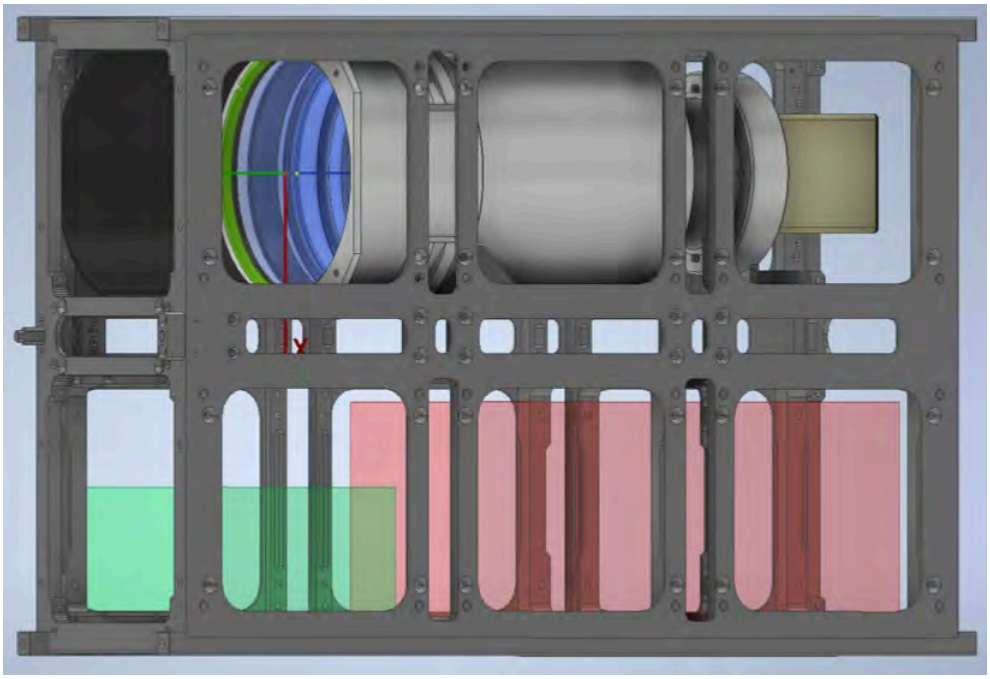

Figure 4.2.3: Single payload (= 3U) inserted in a 6U platform. The green and red volumes on the bottom are proposed to be the location of the star tracker (green) and the control system (red), respectively.

ensure that the technical limits of MARSU remain consistent with the science objective of the mission. We especially focus on various sources of noise arising at different steps of the acquisition chain. Other possible undesirable phenomena like dark currents or remanence, which are minor, are neglected.

4.3.2 Stellar flux

The lightcurve of a stellar target is first estimated from its black body emission, calculated using the effective temperature, the radius, and the distance of the simulated star. The spectral radiant emittance M received from the star follows a Plank function, scaled according to Lambert's cosine law:

$$\begin{aligned} M(\lambda, T) &= \int_0^{2\pi} d\phi \int_0^{\pi/2} B(\lambda, T) cos(\theta) sin(\theta) d\theta \\ &= \pi B(\lambda, T) \\ &= \frac{2\pi hc^2}{\lambda^5} \frac{1}{e^{\frac{hc}{\lambda k_B T}} - 1} \end{aligned} \tag{4.3.1}$$

,where B is the spectral emission power for the wavelength λ and the effective temperature T. If we know the distance d between the star and the detector, we are able to scale the spectral radiant emittance to the observed one (M_{obs}):

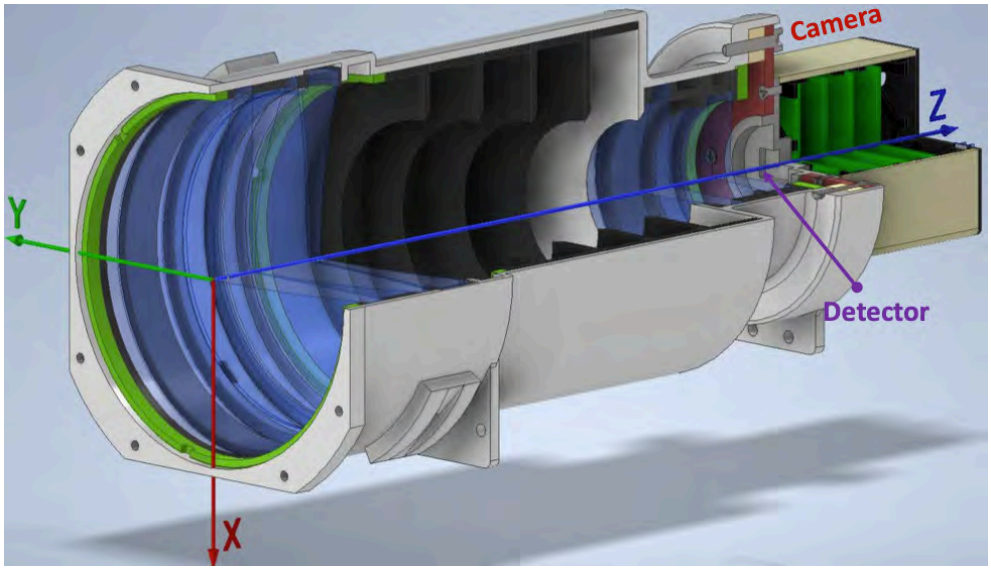

Figure 4.2.4: Mechanical design of the payload.

$$M_{obs} = A\frac{R_*^2}{d^2}M(\lambda, T) \tag{4.3.2}$$

, where A is the area receiving the radiation. We know that the energy of a photon is hc/λ, so the photon flux within a given filter is:

$$F_{phot} = \int_a^b \frac{\lambda}{hc} M_{obs} p(\lambda) d\lambda \tag{4.3.3}$$

, where a and b stand for the wavelength limits of filter, and $p(\lambda)$ is the transmission rate of the optical system as a function of the wavelength λ. In practice, numerical integration is applied for calculating F_{phot}. In our simulation, the flux is integrated over the wavelength range of MARSU ($1 - 1.7$ μm).

Stellar activity and exoplanet transits are optionally added to the model. Realistic stellar activity in the nIR is generated using a model developed for Trappist-1 (Klein & Donati, 2019). Planetary transits are generated by the `batman` transit modeling code (Kreidberg, 2015). The orbit of the simulated exoplanet is described by a typical two-body problem, and expressed by Kepler's Third Law:

$$\frac{a^3}{P^2} = G\frac{M_* + M_p}{4\pi^2}, \tag{4.3.4}$$

where a is the semi major axis of the elliptic orbit, P is the orbital period, M_* and M_p are the masses of the host star and the planet. A basic transit lightcurve is defined by a series of parameters: the transit phase ($t0$), the orbital period (P), the planet radius (R_p, in unit of the stellar radius), the semi-major axis (a, in unit of the stellar radius), the orbital inclination (i), the eccentricity (e), the longitude of periastron (ω), and the stellar limb-darkening coefficients.

Table 4.3.1: Fundamental parameters of stars and planets chosen for our simulations.

Host star	Trappist-1	V1298 Tau	Planet	Trappist-1e	V1298 Tau c
Radius ($R_\odot$)	0.121	1.345	Semi-major axis (AU)	0.029	0.0825
$T_{\rm eff}$ (K)	2516	4970	Orbital period (d)	6.099043	8.24958
Distance (pc)	12.14	108.5	Inclination (deg)	89.86	88.49
H mag	10.718	8.191	Radius ($R_\oplus$)	0.91	5.5932

Two typical targets were selected for the simulations: Trappist-1 and V1298 Tau. Both are surrounded by a multiple exoplanetary system, from which we choose to simulate one planet only. Trappist-1 is a relatively faint, very low-mass star observed with SPIRou, while V1298 Tau is a brighter target (Cutri et al., 2003b), typical of young stars also observed by SPIRou. Detailed information about the two stars is listed in Table 4.3.1.

4.3.3 Attitude of the satellite

The attitude control of the CubeSat is not perfect, which leads to an apparent motion of targets in the field of view. We assume here that the star tracker checks the pointing direction of the satellite every $\tau_{\rm tracker} = 30$ seconds, and adjusts the rotation of the reaction wheels to redirect the line of sight towards the default center. The reaction wheels are assumed to drive the satellite with a fixed angular velocity of $\nu = \sqrt{\nu_\alpha^2 + \nu_\delta^2} =$ 0.3 arcsec/s, where α (right ascension) and δ (declination) are the axis of astronomical coordinates. We also include a small random error in the angle adopted for each redirection, leading to a new correction at the next measurement of the star tracker. We finally assume that we can neglect any rotation of the field of view. An illustration of the simulated angular shifts over 10000 seconds is shown in Fig. 4.3.1. As a consequence of the changes in the attitude, we assume that our target appears at a new position on the detector for each successive image. We also assume that the target does not move during the integration time, which was checked to be a reasonable assumption given the typical adopted integration times and PSF width.

4.3.4 Image generation

The conversion from the starlight to the image received by the detector is simplified. The global transmission of MARSU (including the optical system and detector) is taken equal to $\eta = 0.65$ throughout the whole wavelength domain.

4.3.4.1 Point Spread Function

We assume here that the Point Spread Function (PSF) can be approximated by a 2D Gaussian model with the following expression:

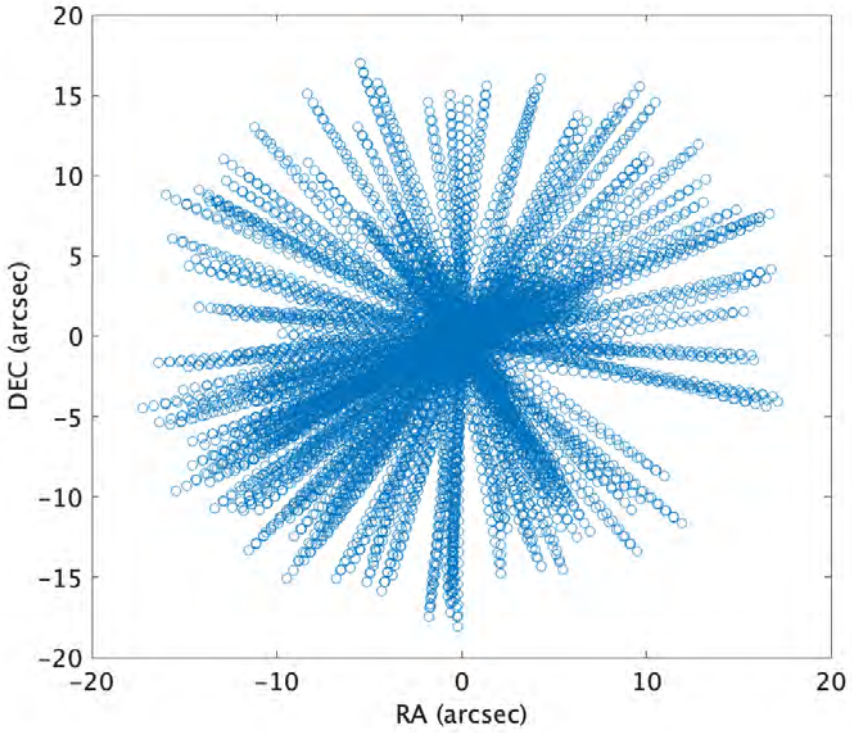

Figure 4.3.1: Apparent angular shifts of the target over 10000 seconds.

$$
\begin{aligned}
f(x,y) &= Ae^{-a(x-x0)^2-b(x-x0)(y-y0)-c(y-y0)^2} \\
a &= \frac{cos^2(\theta)}{2\sigma_x^2} + \frac{sin^2(\theta)}{2\sigma_y^2} \\
b &= \frac{sin(2\theta)}{2\sigma_x^2} - \frac{cos(2\theta)}{2\sigma_y^2} \\
c &= \frac{sin^2(\theta)}{2\sigma_x^2} + \frac{cos^2(\theta)}{2\sigma_y^2}
\end{aligned}
\tag{4.3.5}
$$

Here, θ is the (clockwise) angle of rotation of the 2D Gaussian. The amplitude A is taken at the position (x0, y0), while σ_x and σ_y are the two widths characterizing the Gaussian. For a Gaussian distribution, we have the full width at half maximum FWHM $= 2\sqrt{ln2}\sigma \approx 2.35482\sigma$, or $\sigma \approx 0.4247$ FWHM. In agreement with Sect. 4.2.1, we took a FWHM equal to 2 pixels, translating into a sky resolution of 0.005°/pixel.

4.3.4.2 Photon noise

Photons are converted into photo-electrons on the detector, according to the Quantum efficiency factor (QE). For each pixel, the photon noise follows a Poisson distribution:

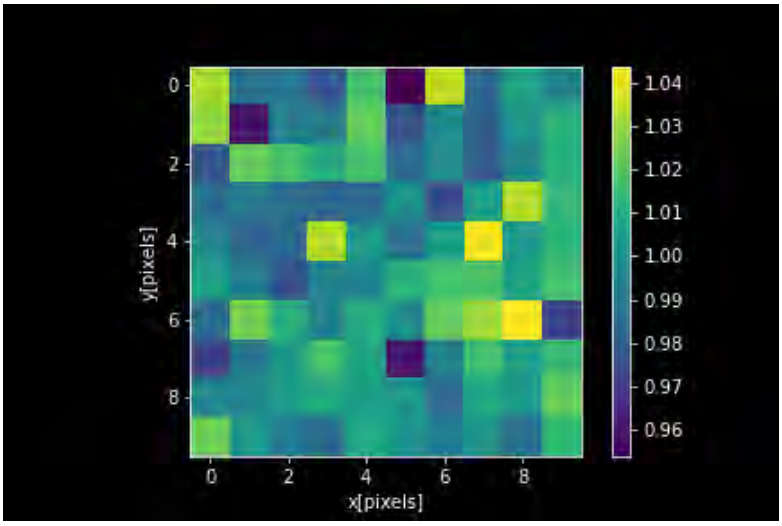

Figure 4.3.2: Example of Pixel-to-pixel Gain Fluctuation (PGF). The color scale shows the gain of each pixel.

$$P_n = \frac{\lambda^n e^{-\lambda}}{n!} \tag{4.3.6}$$

where n is the number of received electrons, λ is the average number of electrons, e is the base of the natural logarithms, and P_n is the possibility of n electrons. In our simulations, the photon noise has a distribution very close to a Gaussian distribution with a width $\sigma_{\text{phot}} = \sqrt{N_{\text{photon}}}$.

4.3.4.3 Read-out noise

Similarly to the photon noise, the read-out noise added on each pixel follows a Poisson distribution which can be approximated by a Gaussian distribution. The spread of the Gaussian distribution is σ_{ro}. In practice, we used a zero-mean Gaussian distribution to describe the read-out noise:

$$P(x) = \frac{1}{\sigma_{\text{ro}}\sqrt{2\pi}} e^{\frac{-x^2}{2\sigma_{\text{ro}}^2}} \tag{4.3.7}$$

4.3.4.4 Pixel-to-pixel Gain Fluctuations (PGF)

The gain is the conversion between the number of electrons recorded by the CCD and the number of digital units contained in the CCD image. We assume here that the gain is constant for each pixel, but displays small variations (PGF) from pixel to pixel, resulting in a fixed PGF frame for all images. The histogram of the PGF is assumed to follow a Gaussian distribution. The gain distribution used in the simulations is shown in Fig. 4.3.2.

4.3.4.5 Dead pixels

Some pixels on the detector stop working for various reasons, and become dead pixels. We assume that a fraction of the pixels are dysfunctional, and are set with a null signal in the simulations (ADU = 0). The positions of these pixels are arbitrary. As shown in Fig. 4.3.3, two dead pixels are set on the frame for the tests.

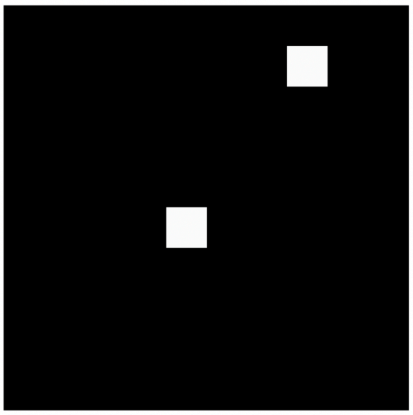

Figure 4.3.3: Example of dead pixels (here in white).

4.3.4.6 Subpixel Quantum efficiency

For each pixel on the detector, the quantum efficiency (QE) inside the pixel is not uniform (e.g., Hu et al. 2019). Since the satellite cannot focus on the same field perfectly, the effective QE applied on the source light can be affected by the apparent movement of the source on the detector. We model an inhomogeneous sub-pixel sensibility (sQE), to qualify the potential extra source of noise that can be generated by this effect.

In a simplified approach, each pixel is divided in a grid of 10 by 10 sub-pixels. The most basic model simply sets the sub-pixels on the edge to a null sQE, while all other subpixels have a constant sQE, so that the total QE of the pixel is expressed as:

$$\mathrm{QE} = \frac{1}{n}\sum_{i=1}^{n} \mathrm{sQE}_i \tag{4.3.8}$$

The value of sQE is chosen to ensure that the QE of the pixel is equal to the expected one. The scaled $\mathrm{sQE} = 100/(100-36).\mathrm{QE} = 1.5625.\mathrm{QE}$.

4.3.5 Lightcurve extraction

A set of images is generated using the input paramters detailed above, using the standard Flexible Image Transport System (FITS). The light curves of are extracted through PSF photometry, which is better adapted than aperture photometry to handle dead pixels (Fig. 4.3.5). A rough estimate of the PSF centroid is first determined. Given initial values of the FWHM on the x and y axis as 2 pixels, a 2D Gaussian fit is then performed

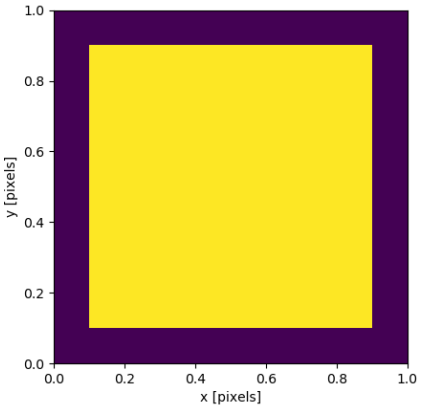

Figure 4.3.4: Subpixel Quantum efficiency (sQE), with edges of the pixel set to a null quantum efficiency.

with a Levenberg-Marquardt algorithm, as implemented in the AstroPy package (Astropy Collaboration et al., 2013, 2018). The flux F is extracted from the PSF fitting is simply using the integral of the 2D Gaussian function described in Eq. 4.3.5:

$$F = 2\pi A \sigma_x \sigma_y. \tag{4.3.9}$$

4.4 Results of simulations

We ran a series of simulations to test the impact of the various sources of noise on the final light curves. We first simulated each noise independently, then tested some typical combinations of them. In some simulations, we include a second, active star with the same fundamental parameters as Trappist-1 and an activity-induced photometric amplitude of 1% (see Fig. 4.4.1). We used Trappist-1 as the simulated target for most tests because it has an H magnitude close to the limit specified for the mission. An exposure time of 120s is applied for the tests, ensuring that the photon noise dominates over the readout noise. The results are summarized in Table. 4.4.2, where the blue cells mark the features included in the simulation. In the same table, we indicate the resulting noise (1σ level) in the extracted light curve, and the corresponding S/N.

The tests above show that photon noise dominates the S/N of observations in most situations, except when a dead pixel or a nearby variable star are significantly polluting the signal. If nearby stars can be a problem in the specific case of a crowded field (e.g. taken in an open cluster), the contamination by a dead pixel can in principle be avoided by adjusting the attitude of the satellite. We, therefore, decided to run full simulations including transit simulations of Trappis-1 e or V1298 Tau c, without any dead-pixel. The light curve was simulated over a 30 days observing run. After folding the lightcurve with the orbital phase, we obtained the transit lightcurves of these two systems in Fig. 4.4.2. The outcome of this numerical simulation, featuring clear detections of the transits,

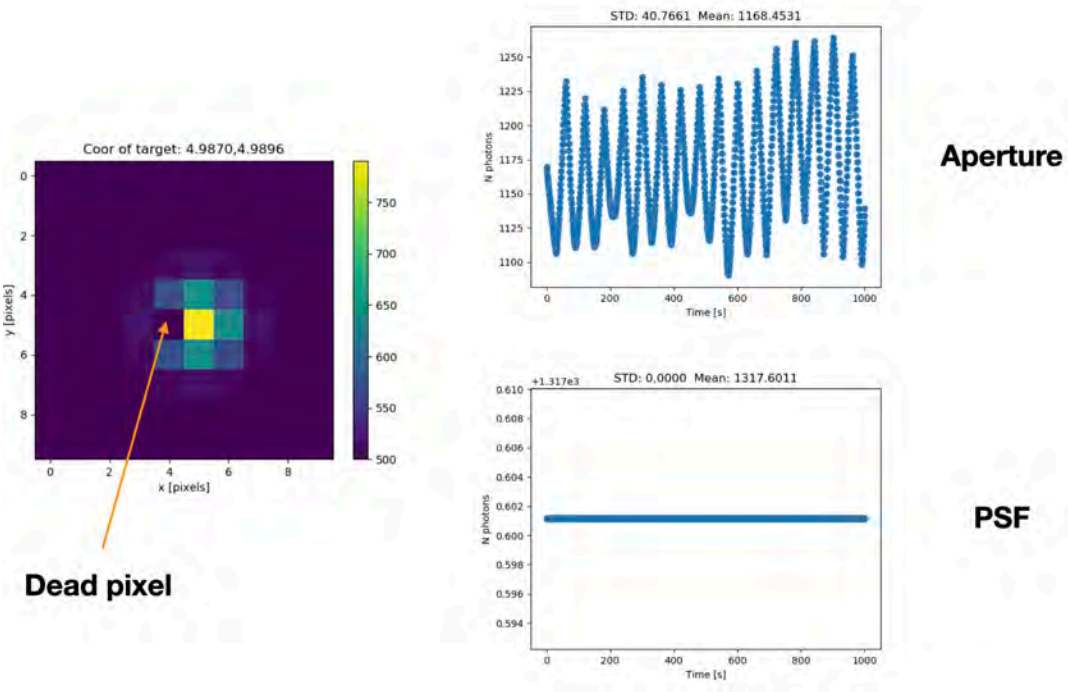

Figure 4.3.5: Extracted light curve for a constant flux source with dead pixel and attitude jitters by aperture and PSF fitting method.

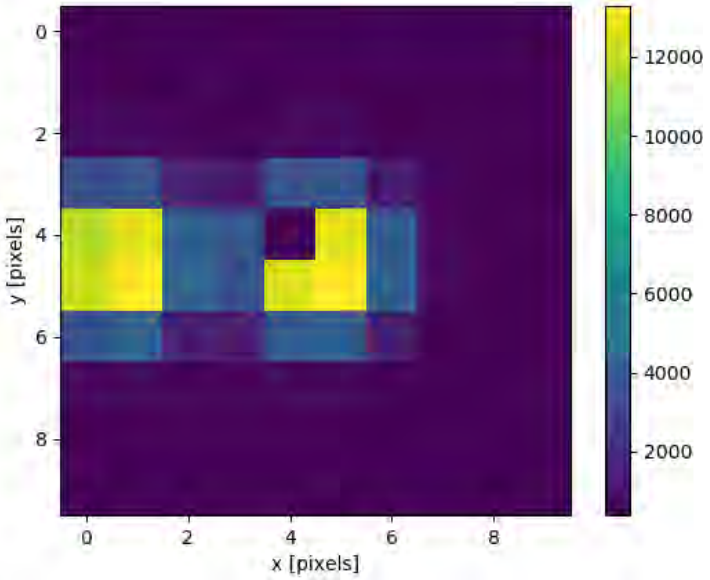

Figure 4.4.1: Exemple image of a fraction of the whole detector, with a dead pixel located at coordinates (4, 4) and overlaping with the PSF of the main target. A nearby star is also simulated, with a PSF overlap between the two stellar objects.

Table 4.4.1: Basic parameters of the simulator.

Parameter	Value
Transmission	0.65
Sky resolution	0.005 deg/pixel
Readout noise	47 e^-
Gain	1 ± 0.01 e^-/ADU
QE	0.8
FWHM of PSF	2 pixels
Exposure time	120 s
ν_{tracker}	0.3 arcsec/s
τ_{tracker}	30 s
phot. fluct. of nearby star	1%

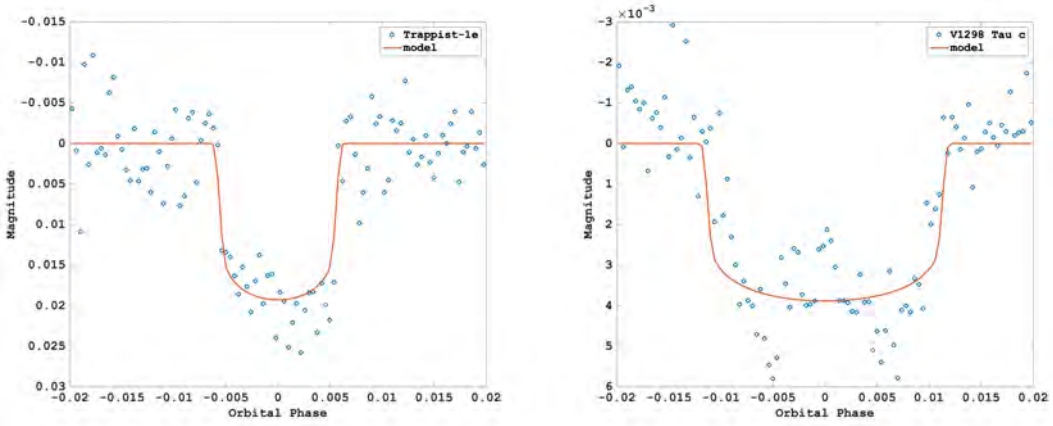

Figure 4.4.2: Simulated lightcurve of Trappist-1e (Top) and V1298 Tau c (Bottom) in 30 days with bins including ~ 10 individual measurements, and folded according to the orbital period, including 4 and 3 transits, respectively. In both cases, the exposure time is set to 120s.

demonstrates that the most challenging science objectives of the MARSU CubeSat are accessible in a CubeSat configuration with a single payload.

4.5 Optical bench

Numerical simulations give a first evidence that our science objectives are achievable with MARSU. In order to confirm the results and adopt more realistic input parameters, practical experiments are necessary. Thus, it was decided to build an infrared photometric test bench to simulate the performance of a simplied model of the payload.

The objective of this test bench is to characterize the MARSU SWIR detector (including the intra-pixel inhomogeneous quantum efficiency), the optical system, and the pointing accuracy. The bench includes an artificial, punctual light source with an XY

Table 4.4.2: Summary of the simulations. Blue cells indicate the source of noise activated in a given run. The numerical values without brackets show the 1σ uncertainty of the extracted light curve (counted in magnitude), and the values between brackets are the corresponding S/N.

Number	Photon noise	Readout noise	PGF	sQE	Dead pixel	Nearby star
1	0.0091 [274]					
2		0.0066 [381]				
3			0.003 [842]			
4				0.00015 [16345]		
5					0.22 [11]	
6						0.013 [195]
7	0.011 [225]					
8	0.012 [214]					
9	0.012 [214]					
10	0.22 [11]					
11	0.33 [7]					
12	0.04 [60]					

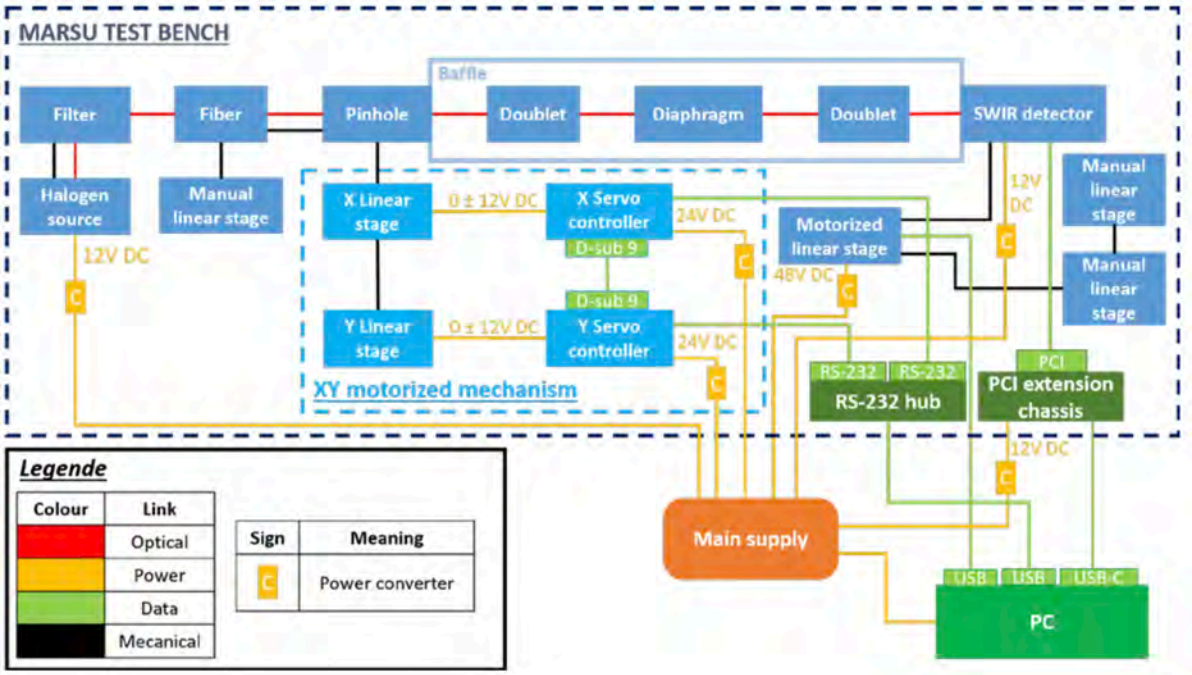

Figure 4.5.1: Principle of the MARSU bench

motorized mechanism to simulate the pointing jitter. A simplified optical system is set up, and the image is captured by a SWIR detector. Finally, a computer collects the data. Fig. 4.5.1 shows the different elements of the bench, as well as the different types of links between them (optics, power, data and mechanics). A picture of the bench can be found in Fig. 4.5.2.

To simulate the M dwarf star, which emits mostly in the infrared, a system composed of a halogen source, high-pass spectral filter for infrared wavelength, an optical fiber and a pinhole are used. By placing the fiber close to a pinhole with a diameter of about ten micrometres, it is then possible to reproduce the irradiation produced by an M dwarf star. A manual linear stage is added to move the pinhole along the optical axis during the installation. The optical system of the bench consists of two identical focal doublets (10cm) with an adjustable diaphragm. Concerning the detector, the same detector planned to be used in the cubesat is chosen (VIS-SWIR OWL 640 II from Raptor Photonics). This detector is mounted on a motorized linear stage in order to realize the focus of the camera. Finally, two more manual linear stages are added to facilitate the future alignment of the camera. To simulate the jitter of a CubeSat platform, an XY motorized mechanism composed of two motorized axes and two servo controllers is employed. A 2D Gaussian fit as described in Sec. 4.3.4.1 is used to calculate the flux.

Under the current bench tests, the intra-pixel flux displays a Gaussian like distribution (Fig. 4.5.3). The flux variations when a jitter is simulated is superior to 0.1%, which is larger than the outcome of the numerical simulations. This result is likely a consequence of the adopted PSF (with an FWHM of about one pixel), while the numerical simulations have shown that a PSF larger than 2 pixel is required to limit the impact

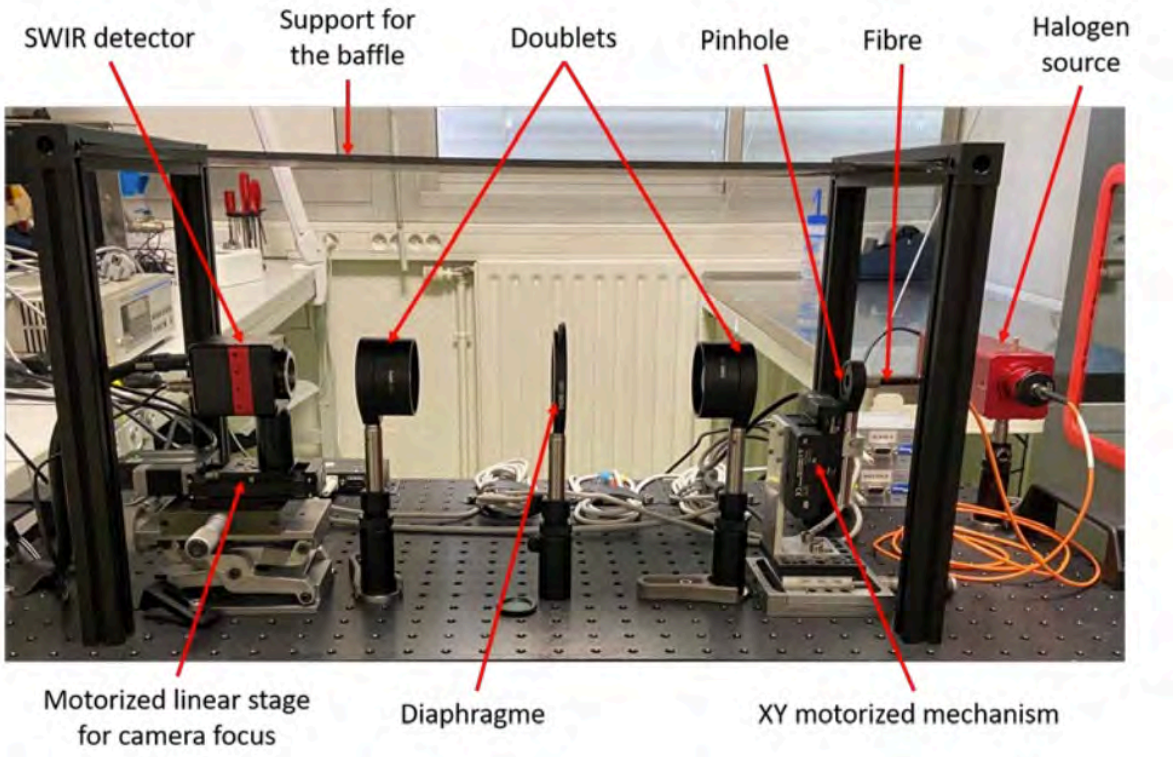

Figure 4.5.2: Picture of MARSU test bench

of the intra-pixel inhomogeneities in the light curve.

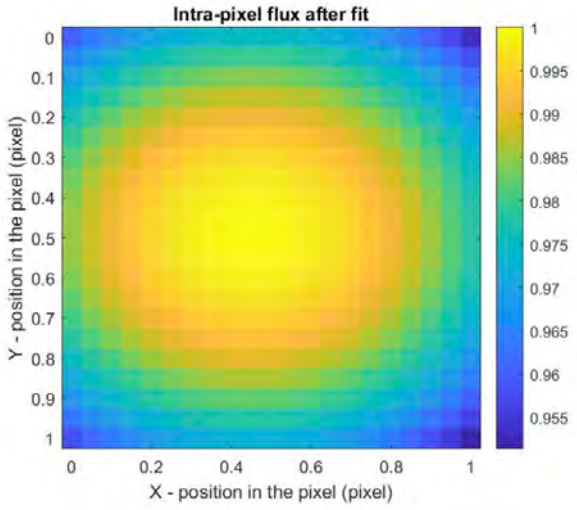

Figure 4.5.3: Flux according to the intra-pixel position

Conclusions and perspectives

This thesis firstly focused on the spectropolarimetric information we can get on the magnetic activity of young solar-like stars, and more specifically for stars with ultra-rapid rotational rates. By applying tomographic techniques on time-resolved spectroscopic and spectropolarimetric data, we were able to constrain the surface distribution of brightness, magnetic fields, and reconstruct the prominence structures of V530 Per. In the second part of the thesis, we assessed the feasibility of nIR transit detection using a CubeSat type space photometer. I developed an end-to-end simulator to generate simulated light curves. The outcome of the tests help to better constrain the payload and observing strategy of the satellite and confirmed that a low-cost space mission was capable of detecting Earth-like planets orbiting red dwarfs.

Magnetic activity on young, solar-like stars

Brightness mapping and magnetic field geometry

The surface brightness and large-scale magnetic field features reconstructed for V530 Per at two distinct epochs share clear similarities. The most obvious structure on the brightness map is a very large, dark spot close to the rotation pole for both observing epochs. The same recognizable feature was already reported by Barnes et al. (2001), using observations collected in 1998. It is therefore plausible that this giant spot is a long-lived structure, or at least an ordinary feature at the surface of V530 Per.

Large polar spots are commonly observed among the most active stars. A number of young solar-type stars at the end of the pre-MS phase or in their early main sequence have been found to host such extended polar caps. Typical examples include LQ Lup (Donati et al., 2000) and AB Dor (Donati & Collier Cameron, 1997; Donati et al., 2003a). In our first observing epoch, this high-latitude spot is clearly off-centered, to the point that the pole is not covered. A few other young G dwarfs have been reported with a similar pattern, for example, EK Dra (Strassmeier & Rice, 1998; Waite et al., 2017; Järvinen et al., 2018) or other rapidly rotating members of the α Per cluster (AP 193, He 520, He 699, Barnes et al. 2001). All these stars with large polar spots have a mass and rotation rate similar to those of V530 Per. In all these rapidly rotating stars, the preferential emergence of spots at high latitude can be interpreted as an indication that the Coriolis force can impose magnetic flux tubes to raise toward the stellar surface in a path mostly parallel to the stellar spin axis (Schuessler et al., 1996).

The magnetic geometry is characterized by a field strength in excess of 1 kG (locally), with a dominant toroidal component, where the majority of the magnetic energy is reconstructed (Table 3.4.1). This is consistent with the trends reported by Petit et al. (2008) or See et al. (2015), showing that the toroidal field component of cool stars increases faster than the poloidal field when the Rossby number decreases, to the point where the surface magnetic topology can become dominated by the toroidal component.

A very different level of complexity was determined in the toroidal and poloidal field components. The toroidal component has a relatively high fraction of its magnetic energy in low degree modes. It is mostly axisymmetric, which is consistent with other stars where the toroidal component dominates (See et al., 2015). The outcome in the magnetic map is a well-defined ring of negative azimuthal field. The latitude of this ring is higher than the one of bright spots showing up in the brightness map and lower than the latitude of the polar spot. Similar ring-like structures have been identified in other rapid-rotating young dwarfs like AB Dor and LQ Hya (Donati et al., 2003b), EK Dra (Waite et al., 2017), or LO Peg (Folsom et al., 2016).

In contrast, the geometry of the poloidal field component is much more complex. The dipole, quadrupole, and octopole contribute a small fraction of the poloidal magnetic energy ($\leq 10\%$ altogether), which is unusual in cool active stars (Folsom et al., 2016). The poloidal field is also highly nonaxisymmetric (15% in modes with $m = 0$). The main radial field region is an extended positive spot covering most of the dark polar spot. The strong radial field reconstructed at high latitude may contribute to generating the dark polar spot, although in other examples of young stars with a giant polar spot, such spatial correlation between the brightness and magnetic geometries is generally not reported (e.g., Donati et al. 2003b).

Further investigations following this study can be directed (i) on exploring the potential relationship between the axisymmetry level and the strength of the magnetic field, and (ii) the long-term evolution of the brightness and magnetic field, in a search for a possible activity cycle.

Differential rotation

The surface shear $d\Omega$ measured for V530 Per is close to the solar value. This estimate is obtained through the assumption that the latitudinal differential rotation follows a smooth solar-like law for both Stokes I and Stokes V data. The solar-like law also works for other rapid-rotating stars, for example, the K dwarfs AB Dor Donati & Collier Cameron 1997, LO Peg (Barnes et al., 2005), HD 141943 (Marsden et al., 2011) and the post T Tauri star LQ Lup Donati et al. 2000. More complex surface differential rotation, like a Jupiter-like pattern suggested by numerical simulations of rapidly rotating stars (e.g., Brun et al. 2017), are not necessary to reproduce our observations, although this may be the result of the limited spatial resolution of our tomographic inversion.

We identified a higher differential rotation using Stokes V profiles (~ 0.15 rad/d), which is ~ 3 times larger than the value reported with Stokes I. A similar observation was reported for all available shear measurements of AB Dor (e.g., Donati et al. 2003b), and some epochs for LQ Hya (Donati et al., 2003b) and V410 Tau (Yu et al., 2019).

It has been suggested that such differences can be related to the different depths of formation of the observed structures.

We do not report any noticeable variation of differential rotation, as previously observed in other stars, e.g. AB dor (Collier Cameron & Donati, 2002).

Prominences

Two components compose the prominence system accompanying V530 Per. The first component is confined around the corotation radius and has been observed in 2006 and 2018. This distinctive distribution of prominences was reported in other fast-rotating stars (Collier Cameron & Robinson, 1989a,b; Steeghs et al., 1996; Donati et al., 2000). We also observed a second, rapidly evolving Hα component, which was much closer to the stellar surface. This second component was absent from our 2006 observations and was especially intense during the third night of the new run. It was possibly linked to a hot chromospheric point, as its emission source was close to the stellar surface, and not seen in absorption. It was anchored at intermediate to low latitudes and at the phase of the main extension of the polar spot. An isolated event was also recorded with an extremely short lifetime < 10 min. These short-term events at the coronal level do not have any noticeable photospheric counterparts in the spot or magnetic coverage. These observations suggest that prominence systems hovering above the most active stars have a complex structure, spanning a range of spatial scales and lifetimes, and with a possible separation between a near-surface, short-lived system coexisting with a dynamically stable ring of material in the vicinity of the corotation radius.

In future works, the evolution of prominences is worth to be explored in greater detail. It would be interesting to identify these kinds of variations in other stars with different spectral types or activity levels, e.g. M dwarfs that are known to host strong and simply structured magnetic fields.

Exoplanet search with a CubeSat

Our end-to-end numerical simulations of the MARSU CubeSat provide a basic test for the instrument performance, and confirm the feasibility of detecting an Earth-like exoplanet in the habitable zone of low-mass stars. The simulations show that the main source of noise is the photon noise and that a typical guiding accuracy now available on CubeSats should be enough, provided that the FWHM of the PSF is larger than about 2 pixels. The MARSU CubeSat is based on a simple and standard design, which could serve as a template for a fleet of CubeSats dedicated to astrophotometry, using identical payloads or optimized for different wavelength domains.

For a physical investigation on the satellite performance, the team has built an optical bench in order to (a) explore an alternate strategy to simulate the performance of MARSU and (b) help to refine our numerical simulations by adopting more realistic input parameters. The tests conducted with the bench are largely in line with our conclusions based on numerical simulations.

Following the feasibility study, a comprehensive mission study will be engaged, aiming at a tentative launch in 2024. After completion of the study phase we, therefore, plan to set up an international science consortium with the ultimate goal of deploying a small fleet of probes to further optimize the science feedback of the project.

Conclusions et perspectives

Cette thèse s'est dans un premier temps focalisée sur les informations spectropolarimétriques que l'on peut obtenir sur l'activité magnétique des jeunes étoiles de type solaire, et plus particulièrement des étoiles à rotation ultra-rapide. En appliquant des techniques tomographiques sur des données spectroscopiques et spectropolarimétriques résolues en temps, nous avons pu contraindre la distribution de surface de la brillance, des champs magnétiques, et reconstruire l'arrangement des protubérance de V530 Per. Dans la deuxième partie de la thèse, nous avons évalué la faisabilité de la détection de transits nIR à l'aide d'un photomètre spatial de type CubeSat. J'ai développé un simulateur complet pour générer des courbes de lumière. Les résultats des tests aident à mieux contraindre la charge utile et la stratégie d'observation du satellite et ont confirmé qu'une mission spatiale à faible coût était capable de détecter des planètes semblables à la Terre en orbite autour de naines rouges.

Activité magnétique des étoiles jeunes de type solaire

Cartographie de la brillance et géométrie du champ magnétique

La luminosité de surface et les caractéristiques du champ magnétique à grande échelle reconstruites pour V530 Per à deux époques distinctes partagent des similitudes évidentes. La structure la plus marquante sur la carte de brillance est une tache sombre très étendue, proche du pôle de rotation pour les deux époques d'observation. La même caractéristique a déjà été signalée par Barnes et al. (2001), à partir d'observations recueillies en 1998. Il est donc plausible que cette tache géante soit une structure à longue durée de vie, ou au moins une caractéristique ordinaire à la surface de V530 Per.

De grandes taches polaires sont couramment observées parmi les étoiles les plus actives. Un certain nombre de jeunes étoiles de type solaire à la fin de la phase pré-séquence principale ou au début de leur séquence principale se sont avérées héberger de telles calottes polaires. Des exemples typiques incluent LQ Lup (Donati et al., 2000) et AB Dor (Donati & Collier Cameron, 1997; Donati et al., 2003a). Dans notre première époque d'observation, cette tache à haute latitude est clairement décentrée, au point que le pôle n'est pas couvert. D'autres jeunes naines G partagent cette caractéristique, comme EK Dra (Strassmeier & Rice, 1998; Waite et al., 2017; Järvinen et al., 2018) ou d'autres naines à rotation rapide, membres du cluster α Per (AP 193, He 520, He 699, Barnes et al. 2001). Toutes ces étoiles avec de grandes taches polaires ont une masse et

une vitesse de rotation similaires à celles de V530 Per. Dans toutes ces étoiles en rotation rapide, l'émergence préférentielle de taches à haute latitude peut être interprétée comme une indication que la force de Coriolis peut imposer aux tubes de flux magnétique de s'élever vers la surface stellaire selon un trajet principalement parallèle à l'axe de rotation stellaire (Schuessler et al., 1996).

La géométrie magnétique est caractérisée par une intensité de champ supérieure à 1 kG (localement), avec une composante toroïdale qui contient la majorité de l'énergie magnétique (tableau 3.4.1). Ce résultat est cohérent avec les tendances rapportées par Petit et al. (2008) ou See et al. (2015), montrant que la composante du champ toroïdal des étoiles froides augmente plus rapidement que le champ poloïdal lorsque le nombre de Rossby diminue, au point que la topologie magnétique de surface peut devenir dominée par la composante toroïdale.

Un niveau de complexité très différent caractérise les composantes toroïdale et poloïdale. La composante toroïdale a une fraction relativement élevée de son énergie magnétique dans les modes de faible degré. Elle est principalement axisymétrique, ce qui est cohérent avec d'autres étoiles où la composante toroïdale domine (See et al., 2015). Le résultat sur la carte magnétique est un anneau bien défini de champ azimutal négatif. La latitude de cet anneau est supérieure à celle des taches brillantes et inférieure à la latitude de la tache polaire. Des structures semblables à des anneaux ont été identifiées sur d'autres jeunes naines à rotation rapide comme AB Dor et LQ Hya (Donati et al., 2003b), EK Dra (Waite et al., 2017) ou LO Peg (Folsom et al., 2016).

En revanche, la géométrie de la composante poloïdale est beaucoup plus complexe. Le dipôle, le quadripôle et l'octopôle contribuent à une petite fraction de l'énergie magnétique poloïdale ($\leq 10\%$ au total), ce qui est inhabituel dans les étoiles froides actives (Folsom et al., 2016). Le champ poloïdal est également fortement non axisymétrique (15% dans les modes avec $m = 0$). La région principale du champ radial est une vaste tache positive couvrant la majeure partie de la tache polaire en brillance. Le fort champ radial reconstruit à haute latitude peut contribuer à générer la tache polaire, bien que dans d'autres exemples de jeunes étoiles avec une tache polaire géante, une telle corrélation spatiale entre la brillance et la géométrie magnétique ne soit généralement pas signalée (par exemple, Donati et al. 2003b).

Les extensions possibles de cette étude peuvent être dirigées vers (i) l'exploration de la relation potentielle entre le niveau d'axisymétrie et la force du champ magnétique, et (ii) l'évolution à long terme de la brillance et du champ magnétique, dans la recherche d'un possible cycle d'activité.

Rotation différentielle

Le cisaillement de surface $d\Omega$ mesuré pour V530 Per est proche de la valeur solaire. Cette estimation est obtenue en supposant que la rotation différentielle latitudinale suit une simple loi de type solaire pour les données Stokes I et Stokes V . Une loi de type solaire fonctionne également pour d'autres étoiles à rotation rapide, par exemple les naines K AB Dor Donati & Collier Cameron 1997, LO Peg (Barnes et al., 2005), HD 141943 (Marsden et al., 2011) et l'étoile post T Tauri LQ Lup Donati et al. 2000. Une

rotation différentielle de surface plus complexe, similaire à celle de Jupiter et suggérée par des simulations numériques d'étoiles en rotation rapide (par exemple, Brun et al. 2017), n'est pas nécessaire pour reproduire nos observations, bien que cela puisse être le résultat de la résolution spatiale limitée de notre inversion tomographique.

Nous avons identifié une rotation différentielle plus élevée en utilisant les profils Stokes V (~ 0.15 rad/d), soit un cisaillement ~ 3 fois plus grand que la valeur rapportée avec Stokes I. Une observation similaire a été rapportée pour toutes les mesures disponibles sur AB Dor (par exemple, Donati et al. 2003b), et à certaines époques pour LQ Hya (Donati et al., 2003b) et V410 Tau (Yu et al., 2019). Il a été suggéré que de telles différences peuvent être liées aux différentes profondeurs de formation des structures observées. Nous ne rapportons aucune variation notable de la rotation différentielle, comme précédemment observé dans d'autres étoiles, par ex. AB dor (Collier Cameron & Donati, 2002).

protubérances

Deux composantes composent le système de protubérances accompagnant V530 Per. La première composante est confinée autour du rayon de corotation et a été observée en 2006 et 2018. Cette organisation distinctive des protubérances a été rapportée dans d'autres étoiles en rotation rapide (Collier Cameron & Robinson, 1989a,b; Steeghs et al., 1996; Donati et al., 2000). Nous avons également observé une seconde composante Hα à évolution rapide, beaucoup plus proche de la surface stellaire. Cette deuxième composante était absente de nos observations de 2006 et était particulièrement intense pendant la troisième nuit de la nouvelle campagne. Elle était peut-être liée à un point chromosphérique chaud, car sa source d'émission était proche de la surface stellaire et n'était pas visible en absorption. Cette structure était ancrée aux latitudes basses ou intermédiaires et à la phase d'extension principale de la tache polaire. Un événement isolé a également été enregistré avec une durée de vie extrêmement courte de < 10 min. Ces événements à court terme au niveau coronal n'ont pas d'analogie nette au niveau de la photosphère, visibles dans les taches ou la couverture magnétique. Ces observations suggèrent que les systèmes de protubérances accompagnant les étoiles les plus actives ont une structure complexe, couvrant une gamme importante d'échelles spatiales et de durées de vie, et avec une séparation possible entre un système proche de la surface et de courte durée, coexistant avec un anneau de matière dynamiquement stable dans le voisinage du rayon de corotation.

Dans les travaux futurs, l'évolution des protubérances mérite d'être explorée plus en détail. Il serait intéressant d'identifier ces types de variations dans d'autres étoiles avec différents types spectraux ou niveaux d'activité, par ex. Nains M connus pour héberger des champs magnétiques puissants et simplement structurés.

Recherche d'exoplanètes avec un CubeSat

Nos simulations numériques de bout en bout de MARSU fournissent un test de base pour les performances de l'instrument et confirment la faisabilité de la détection d'une exoplanète semblable à la Terre dans la zone habitable des étoiles de faible masse. Les simulations montrent que la principale source de bruit est le bruit des photons et qu'une précision de guidage typique maintenant disponible sur CubeSat devrait être suffisante, à condition que la FWHM de la PSF soit supérieure à environ 2 pixels. MARSU repose sur une conception simple et standard, qui pourrait servir de modèle à une flotte de CubeSats dédiés à l'astrophotométrie, utilisant des charges utiles identiques ou optimisées pour différents domaines de longueurs d'onde.

Pour une évaluation plus réaliste des performances du satellite, l'équipe a construit un banc optique afin de (a) explorer une stratégie alternative pour simuler les performances de MARSU et (b) aider à affiner nos simulations numériques en adoptant des paramètres plus réalistes. Les tests menés sur banc sont largement en accord avec nos conclusions basées sur des simulations numériques.

À la suite de l'étude de faisabilité, une étude de mission complète sera engagée, visant un lancement en 2024. Après l'achèvement de la phase d'étude, nous prévoyons donc de mettre en place un consortium scientifique international dans le but ultime de déployer une petite flotte de satellites dans le but d'optimiser davantage le retour scientifique du projet.

Appendix A

Complements

A.1 Magnitude and radius estimation of a star

The absolute bolometric magnitude of star $M_{\mathrm{bol},*}$ can be expressed as:

$$M_{\mathrm{bol}} = m_\nu + BC_\nu - A_\nu - 5\log_{10}(D) + 5, \tag{A.1.1}$$

where m_ν, BC_ν and A_ν are the apparent magnitude, the bolometric correction and the interstellar reddening correction in the specific band ν, and where D is the distance of the star in parsecs. The luminosity of the star in solar unit can be expressed by:

$$\frac{L_*}{L_\odot} = 10^{0.4(M_{\mathrm{bol},*} - M_{\mathrm{bol},\odot})}, \tag{A.1.2}$$

where $M_{\mathrm{bol},\odot} = 4.74$ is the bolometric magnitude of the Sun. The radius of the star is simply estimated through the Stefan–Boltzmann law:

$$L = 4\pi R^2 \sigma T^4. \tag{A.1.3}$$

Leading to:

$$\frac{L_*}{L_\odot} = (\frac{R_*}{R_\odot})^2 (\frac{T_{\mathrm{eff},*}}{T_{\mathrm{eff},\odot}})^4 \tag{A.1.4}$$

A.2 Mass estimation of prominences for fully emitting Hα

We assume that the line profiles generated by prominences are under the situation of optically thin material and local thermodynamic equilibrium (LTE). The emission comes from the transitions from the upper energy level E_m to the lower level E_n: $h\nu_{mn} = E_m - E_n$. The linear absorption coefficient k_ν is defined by (using ν instead of ν_{mn} hereafter):

$$k_\nu = \frac{dI_\nu}{I_\nu ds} \tag{A.2.1}$$

where I_ν is the intensity at frequency ν. Note that k_ν can also be the emission coefficient for an emitting line under the LTE assumption. If we define N_m, N_n as the number density of the upper and lower energy levels, the absorption of a gas cylinder with unit bottom area and length ds is the difference between the actual absorption and emission:

$$-dI_\nu = (N_n B_{nm} I_\nu - N_m B_{mn} I_\nu)\frac{1}{4\pi} h\nu_{mn} ds \tag{A.2.2}$$

where B_{nm} and B_{mn} are average Einstein B coefficients for absorption and emission respectively, following the relationship:

$$B_{nm} = \frac{g_m}{g_n} B_{mn}, \qquad A_{mn}/B_{mn} = 2h\nu_{mn}^3/c^2 \tag{A.2.3}$$

where g_m, g_n are the statistical weights of the energy levels, and A_{mn} is the Einstein coefficient for spontaneous emission. We therefore have:

$$k_\nu = \frac{c^2}{8\pi\nu_{mn}^2}(N_n\frac{g_m}{g_n} - N_m)A_{mn} \tag{A.2.4}$$

For a spectral line, we can introduce a normalized line profile, so that:

$$\int_0^\infty \varphi_{mn}(\nu)d\nu = 1 \tag{A.2.5}$$

Leading to an extra term to the expression of k_ν:

$$k_\nu = \frac{c^2}{8\pi\nu_{mn}^2}(N_n\frac{g_m}{g_n} - N_m)A_{mn}\varphi_{mn} \tag{A.2.6}$$

In this case, the absorption of a line profile also has a distribution around ν_{mn}, and satisfies:

$$\int_0^\infty k_\nu d\nu = \frac{c^2}{8\pi\nu_{mn}^2}(N_n\frac{g_m}{g_n} - N_m)A_{mn} \tag{A.2.7}$$

The full width at half maximum (FWHM) of a line profile is $\Delta\nu_D$, so that we can approximete:

$$\int_0^\infty \varphi_{mn}(\nu)d\nu \approx \varphi_{mn}(\nu_{mn})\Delta\nu_D \tag{A.2.8}$$

with:

$$\varphi_{mn}(\nu_{mn}) \approx \frac{1}{\Delta\nu_D} \tag{A.2.9}$$

By substituting this equation into Eq. A.2.7, we obtain the absorption coefficient at line center k_L:

$$k_L = k_{\nu_{mn}} = \frac{c^2}{8\pi\nu_{mn}^2\Delta\nu_D}(N_n\frac{g_m}{g_n} - N_m)A_{mn} \tag{A.2.10}$$

To simplify the expression, we can use the relationship between the absorption oscillator strength f_{nm} and the spontaneous emission A_{mn}:

$$f_{nm} = \frac{g_m}{g_n}\frac{m_e c^3}{8\pi^2 e^2 \nu_{mn}^2}A_{mn} \tag{A.2.11}$$

where e, m_e are the charge and mass of the electron. In the LTE approximation, we can apply the Boltzmann equation:

$$\frac{N_m}{N_n} = \frac{g_m}{g_n}\exp(-\frac{h\nu_{mn}}{k_B T}) \tag{A.2.12}$$

where T is the electron temperature of the gas. Thus Eq. A.2.10 becomes:

$$k_L = k_{\nu_{mn}}(LTE) = \frac{\pi e^2}{m_e c} f_{nm} \frac{N_n}{\Delta\nu_D}[1 - \exp(-\frac{h\nu_{mn}}{k_B T})] \tag{A.2.13}$$

If the gas is optically thin ($\tau_c \ll 1$), homogeneous, and with a thickness of L, we can calculate the optical depth at the line center τ_ν:

$$\begin{aligned} \tau_{\nu_{mn}} &= \tau_L + \tau_c \approx \tau_L = L \cdot k_L \\ &= \frac{\pi e^2}{m_e c} f_{nm} \frac{N_n}{\Delta\nu_D}[1 - \exp(-\frac{h\nu_{mn}}{k_B T})]L \end{aligned} \tag{A.2.14}$$

If $\tau_c \ll 1$, then the intensity at line center ν_{mn} is:

$$\begin{aligned} I_L &= I_{\nu_{mn}} \approx k_\nu L B_\nu(T) \\ &= B_\nu(T) L N_n \frac{\pi e^2}{m_e c} f_{nm} \frac{1}{\Delta\nu_D}[1 - \exp(-\frac{h\nu_{mn}}{k_B T})] \end{aligned} \tag{A.2.15}$$

where $B_\nu(T)$ is the blackbody radiation:

$$B_\nu(T) = \frac{2h\nu_{mn}^3}{c^2} \frac{1}{\exp(-\frac{h\nu_{mn}}{k_B T}) - 1} \tag{A.2.16}$$

For an emission line, we need to use A_{mn}, so that:

$$I_\nu = \frac{1}{4\pi} \frac{1}{\Delta\nu_D} N_m A_{mn} h\nu_{mn} L \tag{A.2.17}$$

which can also expressed as a radiant flux:

$$F = 4\pi \int_0^\infty I_\nu d\nu = \mathcal{N}_m A_{mn} h\nu_{mn} \tag{A.2.18}$$

where column density $\mathcal{N}_m = N_m L$, and I_ν is the intensity of the spectral line at frequency ν. We also have the line emission coefficient (integrated over a 4π solid angle):

$$j_L = N_m A_{mn} h\nu_{mn} \quad (\mathrm{W \cdot m^{-3}}) \tag{A.2.19}$$

The mass estimation then basically follows the method of Steeghs et al. (1996), which was applied in Donati et al. (2000); Zaire et al. (2021). The emission of prominences is generated by electron collisional excitation. In this case, we can simply use $N_e N_n q_{nm}$ to express the number of atom reaching the higher energy level per unit time and volume

by collision with free electrons, where q_{nm} is collisional excitation rate coefficient. From this, $N_e N_m q_{mn}$ and $N_m A_{mn}$ are the number of atoms transiting to the lower level n, where q_{mn} is the collisional de-excitation rate coefficient. The equilibrium condition can be written as:

$$N_e N_n q_{nm} = N_e N_m q_{mn} + N_m A_{mn}. \tag{A.2.20}$$

from which we deduce the statistical distribution of N_m/N_n:

$$\frac{N_m}{N_n} = \frac{N_e q_{nm}}{N_e q_{mn} + A_{mn}}. \tag{A.2.21}$$

Note that Eq. A.2.20 is based on the assumption that the energy density of the radiation field is very low, so that the forced transition can be ignored. Furthermore, ion collisions are ignored in Eq. A.2.20, since the thermal motion of electrons (with much smaller mass) is much stronger than that of ions. Substituting Eq. A.2.20 into Eq. A.2.19, we can get the line emission coefficient for electron collisional excitation. In the limit case of $N_e \to 0$ and $N_e \to \infty$:

$$j_L = N_e N_n q_{nm} h\nu_{mn} \quad (N_e \to 0) \tag{A.2.22a}$$

$$j_L = N_n q_{nm} q_{mn} A_{mn} h\nu_{mn} \quad (N_e \to \infty). \tag{A.2.22b}$$

For the emission of prominences, we use the $N_e \to 0$ assumption (optically thin, collisionless), and the emission coefficient $K_{mn} = q_{nm} h\nu_{mn}$ can be found in Osterbrock (1989) (in their Section 4.2, Case B).

The definition of EW, units of wavelength (W_λ) is:

$$W_\lambda = \int_0^\infty |1 - \frac{I_\lambda}{I_c}| d\lambda \tag{A.2.23}$$

where I_c stands for the intensity of continuum. Note that the notation I_ν adopted above is $I_\nu = I_\lambda - I_c$ at the same wavelength/frequency. If I_c comes from a star with effective temperature $T_{\rm eff}$, we can write (applying the Lambert's cosine law):

$$I_c = \pi B(\lambda, T_{\rm eff}) = \frac{2hc\pi}{\lambda^5} \frac{1}{\exp(\frac{hc}{\lambda k_B T_{\rm eff}}) - 1} \tag{A.2.24}$$

The emission of prominences is generated from a sphere with radius of source surface $l = 2.5R_*$ in the case of V350 Per, with an average atom and electron density N_H and N_e, so that the emission flux can be approached by:

$$\pi B(\lambda_{H_\alpha}, T_{\rm eff}) W_\alpha \cdot 4\pi R_*^2 = N_e N_H K_{H_\alpha} \cdot \frac{4}{3}\pi l^3 \tag{A.2.25}$$

where $W_\alpha = 0.32$ nm is the equivalent width of the corresponding line (positive for emission). In the case of V350 Per, $W_\alpha/W_\beta \approx 2.7$, which suggests that the optically thin assumption can be applied here. We then take the value $K_{H_\alpha} = 2.87$, and $K_{H_\beta} = 3.56 \times 10^{-38}$ (J m^3 s^{-1}) at an electron temperature of $\sim 10000K$. Following Steeghs et al. (1996), we have $N_e \approx N_H$, and the total number of hydrogen atoms $\mathfrak{N}_H$ is:

$$\mathfrak{N}_H = (W_\alpha \frac{3\pi B(\lambda_{H_\alpha}, T_{\text{eff}}) R_*^2}{K_{H_\alpha} l^3})^{\frac{1}{2}}. \tag{A.2.26}$$

So we have $\mathfrak{N}_H \approx 1.05 \times 10^{16}$ m^{-3} and a mass of prominences $M_p = \mathfrak{N}_H m_H \cdot 4/3\pi R_*^3 \approx 4.6 \times 10^{17}$ kg.

A.3 Magnetic energy parameters

According to Vidotto (2016), the toroidal magnetic field component, according to Eq. 2.3.10, 2.3.11 and 2.3.12, can be expressed as:

$$B_{\text{tor},r}(\theta, \varphi) = 0, \tag{A.3.1}$$

$$B_{\text{tor},\theta}(\theta, \varphi) = \sum_{\ell=1}^{L} \sum_{m=0}^{\ell} \text{Re}[\gamma_{\ell m} \frac{imP_{\ell m} e^{im\varphi}}{(\ell+1)\sin\theta}], \tag{A.3.2}$$

$$B_{\text{tor},\varphi}(\theta, \varphi) = \sum_{\ell=1}^{L} \sum_{m=0}^{\ell} \text{Re}[\gamma_{\ell m} \frac{1}{\ell+1} \frac{\text{d}P_{\ell m}}{\text{d}\theta} e^{im\varphi}]. \tag{A.3.3}$$

Likewise, the radial, meridional and azimuthal components of the poloidal part of the field are:

$$B_{\text{pol},r}(\theta, \varphi) \equiv B_r(\theta, \varphi) = \sum_{\ell=1}^{L} \sum_{m=0}^{\ell} \text{Re}[\alpha_{\ell m} P_{\ell m}(\cos\theta) e^{im\varphi}], \tag{A.3.4}$$

$$B_{\text{pol},\theta}(\theta, \varphi) = \sum_{\ell=1}^{L} \sum_{m=0}^{\ell} \text{Re}[\beta_{\ell m} \frac{1}{\ell+1} \frac{\text{d}P_{\ell m}}{\text{d}\theta} e^{im\varphi}], \tag{A.3.5}$$

$$B_{\text{pol},\varphi}(\theta, \varphi) = -\sum_{\ell=1}^{L} \sum_{m=0}^{\ell} \text{Re}[\beta_{\ell m} \frac{imP_{\ell m} e^{im\varphi}}{(\ell+1)\sin\theta}], \tag{A.3.6}$$

The average squared poloidal component of the magnetic field is:

$$\langle B_{\text{pol}}^2 \rangle = \frac{1}{4\pi} \int \sum_k B_{\text{pol},k}^2(\theta, \varphi) \text{d}\Omega \tag{A.3.7}$$

where $k = r, \theta, \varphi$. The toroidal equivalent is:

$$\langle B_{\text{tor}}^2 \rangle = \langle B^2 \rangle - \langle B_{\text{pol}}^2 \rangle. \tag{A.3.8}$$

where:

$$\langle B^2 \rangle = \frac{1}{4\pi} \int \sum_k B_k^2(\theta, \varphi) \text{d}\Omega. \tag{A.3.9}$$

The fraction of poloidal fields is then $f_{\text{pol}} = \langle B_{\text{pol}}^2 \rangle / \langle B^2 \rangle$. In practice, the spherical components $\alpha_{\ell m}$, $\beta_{\ell m}$ and $\gamma_{\ell m}$ are known. We define the energy terms E_α, E_β, and E_γ,

such as:

$$
\begin{aligned}
E_\alpha &= \mathrm{Re}[\frac{\alpha_{\ell m}\bar{\alpha}_{\ell m}}{2} + \frac{\alpha_{\ell,0}^2 + \bar{\alpha}_{\ell,0}^2}{4}], \\
E_\beta &= \frac{\ell}{\ell+1}\mathrm{Re}[\frac{\beta_{\ell m}\bar{\beta}_{\ell m}}{2} + \frac{\beta_{\ell,0}^2 + \bar{\beta}_{\ell,0}^2}{4}], \\
E_\gamma &= \frac{\ell}{\ell+1}\mathrm{Re}[\frac{\gamma_{\ell m}\bar{\gamma}_{\ell m}}{2} + \frac{\gamma_{\ell,0}^2 + \bar{\gamma}_{\ell,0}^2}{4}],
\end{aligned}
\tag{A.3.10}
$$

where $\bar{\alpha}$, $\bar{\beta}$, and $\bar{\gamma}$ are complex conjugate. Note that $\alpha_{\ell,0}^2$, $\beta_{\ell,0}^2$ and $\gamma_{\ell,0}^2$ are taken equal to 0 when $m \neq 0$. So the poloidal field energy of each degree and order is $E_\alpha + E_\beta$ and the toroidal field energy is E_γ. The total magnetic energy $\langle B^2 \rangle$ is the sum of the poloidal and toroidal field energies:

$$
\begin{aligned}
\langle B^2 \rangle &= \langle B_{\mathrm{pol}}^2 \rangle + \langle B_{\mathrm{tot}}^2 \rangle \\
&= \sum_{\ell=1}^{L}\sum_{m=0}^{\ell}(E_\alpha + E_\beta) + \sum_{\ell=1}^{L}\sum_{m=0}^{\ell} E_\gamma.
\end{aligned}
\tag{A.3.11}
$$

The contribution of the axisymmetric field component can be calculated by setting $m = 0$.

Appendix B

Support Documents

B.1 Datasheet of SWIR detector Owl 640 N

Specification for Owl 640 N

Sensor Type	InGaAs PIN-Photodiode
Active Pixel	640 x 512
Pixel Pitch	15µm x 15µm
Active Area	9.6mm x 7.2mm
Spectral response[1]	0.6µm to 1.7µm
Noise (RMS) LG = Low Gain HG=High Gain	LG: <175e- (150e- typically) HG: <22e- (18e- typically)
Peak Quantum Efficiency	>90% @1.3µm
Pixel Well Depth	Low Gain: >250ke-, High Gain: >10ke-
Pixel Operability	>99.5%
Digital Output Format	14 bit CameraLink (Base Configuration) /SDR
Exposure Time	1µs to 1 / frame rate
Shutter Mode	Global shutter
Frame Rate	Up to 120Hz programmable, 25ns resolution
Dynamic Range (Typical) LG = Low Gain HG=High Gain	LG: 62dB HG: 55dB
Optical Interface	C mount
Trigger interface	Trigger IN and OUT - TTL compatible
Power supply	12V DC +/- 0.5V
TE Cooling	Active
Image Correction	3 point NUC (offset, Gain & Dark Current) + pixel correction
Functions controlled by serial communication	Exposure, intelligent AGC, Non Uniformity Correction, Gamma, Pk/Av, TEC, ROI
Camera Power Consumption[2]	<4W (TEC ON, NUC ON)
Operating Case Temperature[3]	-20˚C to +55˚C
Storage Temperature	-30˚C to +60˚C
Dimensions (L*W*H)[4]	69.4mm x 50mm x 50mm
Weight	282g

Ordering Information

Camera

Owl 640 N Digital Camera	NO1.7-VS-CL-640
OWL Power Supply Cable	RPL-HR4-K

Optional Accessories

EPIX(R) base CL card	RPL-EPIX-EB1
EPIX(R) XCAP STD software	RPL-XCAP-STD
MDR-SDR CameraLink Cable (2m)[5]	RPL-MCL-CBL-2M
Optical SWIR lenses[6]	RPL-xx-xxxx

Note 1: Optional filters available: Low, High or bandpass
Note 2: Measured in an ambient of 25°C with adequate heat sinking. For more detailed power consumption values, please refer to the user manual.
Note 3: Extended Operating Temperature range on request
Note 4: Dimensions include all connector parts on camera interface
Note 5: Longer CL cable available
Note 6: Please consult us to check our range of lenses

Demo is available on request.
Pricing AOR subject to volumes.

Detailed technical drawings can be downloaded at www.raptorphotonics.com

Quantum Efficiency

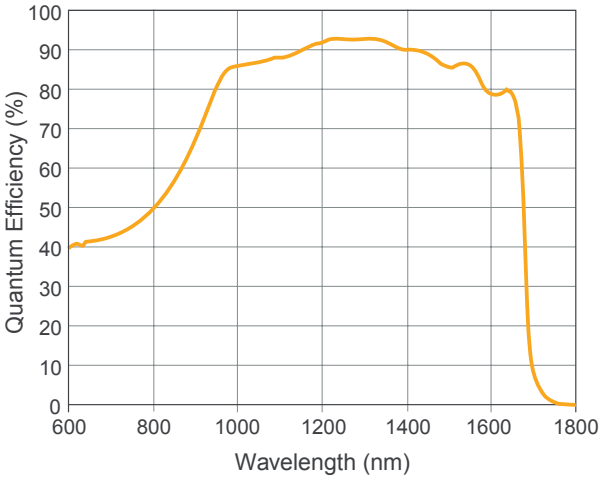

*Data supplied by sensor manufacturer

Applications

Surveillance

- 860, 1064 & 1550nm laser line detection
- Active Imaging
- Airborne Payload
- Hand Held Systems
- Imaging through Fog
- Range Finding
- Vision enhancement

Scientific

- Astronomy
- Beam Profiling
- Hyperspectral Imaging
- Semiconductor Inspection
- Solar Cell Inspection
- Thermography

Document #: INNO1.7-VS-CL-640 0521

Raptor photonics

Willowbank Business Park
Larne, Co Antrim
BT40 2SF,
Northern Ireland

Raptor Photonics Ltd. (UK)
T: +44(0)2828 270 141
E: sales@raptorphotonics.com
www.raptorphotonics.com

Raptor Photonics Inc. (USA)
T: +1 (877) 230-4836
E: sales@raptorphotonics.com
www.raptorphotonics.com

Appendix C

First author publications

C.1 A&A paper: Cang et.al 2020a

A&A 643, A39 (2020)
https://doi.org/10.1051/0004-6361/202037693

Astronomy & Astrophysics

Magnetic field and prominences of the young, solar-like, ultra-rapid rotator V530 Persei

T.-Q. Cang[1], P. Petit[1], J.-F. Donati[1], C. P. Folsom[1], M. Jardine[2], C. Villarreal D'Angelo[3], A. A. Vidotto[3], S. C. Marsden[4], F. Gallet[5], and B. Zaire[1]

[1] Institut de Recherche en Astrophysique et Planétologie, Université de Toulouse, CNRS, CNES, 14 avenue Edouard Belin, 31400 Toulouse, France
e-mail: tcang@irap.omp.eu
[2] SUPA, School of Physics and Astronomy, University of St Andrews, North Haugh, KY16 9SS, UK
[3] School of Physics, Trinity College Dublin, the University of Dublin, Dublin-2, Ireland
[4] University of Southern Queensland, Centre for Astrophysics, Toowoomba 4350, Australia
[5] Univ. Grenoble Alpes, CNRS, IPAG, 38000 Grenoble, France

Received 10 February 2020 / Accepted 27 August 2020

ABSTRACT

Context. Young solar analogs reaching the main sequence experience very strong magnetic activity, generating angular momentum losses through wind and mass ejections.
Aims. We investigate signatures of magnetic fields and activity at the surface and in the prominence system of the ultra-rapid rotator V530 Per, a G-type solar-like member of the young open cluster α Persei. This object has a rotation period that is shorter than all stars with available magnetic maps.
Methods. With a time-series of spectropolarimetric observations gathered with ESPaDOnS over two nights on the Canada-France-Hawaii Telescope, we reconstructed the surface brightness and large-scale magnetic field of V530 Per using the Zeeman-Doppler imaging method, assuming an oblate stellar surface. We also estimated the short term evolution of the brightness distribution through latitudinal differential rotation. Using the same data set, we finally mapped the spatial distribution of prominences through tomography of the Hα emission.
Results. The brightness map is dominated by a large, dark spot near the pole, accompanied by a complex distribution of bright and dark features at lower latitudes. Taking the brightness map into account, the magnetic field map is reconstructed as well. Most of the large-scale magnetic field energy is stored in the toroidal field component. The main radial field structure is a positive region of about 500 G, at the location of the dark polar spot. The brightness map of V530 Per is sheared by solar-like differential rotation, with roughly a solar value for the difference in rotation rate between the pole and equator. It is important to note that Hα is observed in emission and it is mostly modulated by the stellar rotation period over one night. The prominence system is organized in a ring at the approximate location of the corotation radius, and displays significant evolution between the two observing nights.
Conclusions. V530 Per is the first example of a solar-type star to have its surface magnetic field and prominences mapped together, which will bring important observational constraints to better understand the role of slingshot prominences in the angular momentum evolution of the most active stars.

Key words. stars: individual: V530 Per – stars: magnetic field – stars: solar-type – stars: rotation – starspots

1. Introduction

A large fraction of young Suns close to the early main sequence experience very large rotation rates, as they still possess most of the angular momentum acquired during the stellar formation process (see the review of Bouvier 2013). This type of rapid rotation is responsible for the efficient amplification of internal magnetic fields through the action of a global dynamo, as observed in most indirect activity tracers. This is the case, for example, in Ca II H&K emission (Noyes et al. 1984), X-ray flux (Wright et al. 2011), or photometric variability due to spots (Walkowicz & Basri 2013) and flares (Davenport 2016). However, for stars with sufficiently large rotation rates, magnetic activity seems to reach an upper limit although the exact rotation threshold for saturation depends on the magnetic tracer taken into account. X-ray observations clearly highlight this so-called saturation phenomenon (Pallavicini et al. 1981; Prosser et al. 1996; Wright et al. 2011), as well as Zeeman broadening measurements (Reiners 2012) or large-scale magnetic field measurements (Vidotto et al. 2014; See et al. 2019). Attempts to model this saturated state in global numerical simulations of G-K stars remain scarce (e.g., Augustson 2017; Guerrero et al. 2019).

Tomographic mapping is a powerful approach to characterize the large-scale surface magnetic fields of rapid rotators. Since its first application to an active solar-type star with HR 1099 (Donati et al. 1992), Zeeman-Doppler imaging (ZDI hereafter) has been applied to several dozens of cool active stars on the main sequence (e.g., Petit et al. 2008 for solar analogs, Morin et al. 2008 for M dwarfs, or See et al. 2019 for a global study). Several recent ZDI studies have specifically investigated how magnetic geometries of Sun-like stars evolve during the early main sequence (Vidotto et al. 2014; Folsom et al. 2016, 2018a; Rosén et al. 2016). Although the first cool ZDI targets were saturated stars as their Zeeman signatures are easier to detect, the most recent observing projects dealing with G-K stars have concentrated on objects in the unsaturated regime. As a consequence, while the unsaturated dynamo regime is now well

sampled by the ZDI models available so far, we are still left with few G-K dwarfs in the saturated regime, which is mostly populated by M dwarfs in ZDI surveys. Our observations of v530 Per are aimed at enlarging the sample of fast rotators studied with ZDI.

Fast rotators are also ideal laboratories for studying stellar prominences and their impact on angular momentum evolution in young stars. Prominences are dense clouds of gas at chromospheric temperature, trapped in closed stellar magnetic loops and extending into the hot and tenuous corona. Prominences, along with stellar winds, remove angular momentum from stars and therefore contribute to the early evolution of active stars (Aarnio et al. 2012; Jardine et al. 2020). For rapidly rotating stars, prominence systems become much more massive and extended than on the Sun (see the review by Collier Cameron 1999). Observational signatures of stellar prominences are usually extracted from Balmer lines. They show up as absorption features in the line profile when the prominence transits in front of the stellar disk, and generate line emission otherwise. Following a first detection by Collier Cameron & Robinson (1989a), prominence systems have been reported in a small number of active G and K stars (Donati et al. 2000; Dunstone et al. 2006a), M-dwarfs (Byrne et al. 1996; Eibe 1998), and PMS stars (Skelly et al. 2008, 2009). When spectral signatures are seen in emission (i.e., mainly if the line-of-sight inclination of the stellar rotation axis is small), the spatial distribution of prominences can be reconstructed through tomographic models inspired from the observation of cataclysmic variables (Donati et al. 2000; Barnes et al. 2001).

Here we investigated the large-scale photospheric magnetic field and prominence system of V530 Per (also named AP 149), which is a cool, rapidly rotating member of the young open cluster α Persei (Prosser 1992). Combining its X-ray flux and projected rotational velocity, V530 Per was proposed to be a saturated (O'dell et al. 1994) or even super-saturated (Prosser et al. 1996) star, making it an interesting object for ZDI studies lacking G-K stars in this extreme magnetic regime. Its sustained magnetic activity is also responsible for regular photometric variations attributed to a ~8 h rotation period (O'dell & Collier Cameron 1993). Doppler mapping performed by Barnes et al. (2001) revealed the presence of a large, dark spot near the visible rotation pole. They also recovered a first prominence map from their Hα time series, unveiling large prominences extending up to several stellar radii.

In this paper, we presented a time-series of spectropolarimetric observations of V530 Per (Sect. 2). We first refine and discuss its fundamental parameters (Sect. 3) and then reconstruct its brightness and magnetic field map (Sect. 4). We also modeled the latitudinal differential rotation of V530 Per (Sect. 5) and present two prominence maps reconstructed from two distinct nights (Sect. 6). Finally, we discuss our results in the light of previous works (Sect. 7).

2. Observational material

We obtained a time-series of spectropolarimetric observations of V530 Per in late 2006, over two nights separated by a 6-day gap (November 29 and December 05). The data were collected at Mauna Kea observatory by the ESPaDOnS spectropolarimeter (Donati et al. 2006a), mounted at the Cassegrain focus of the Canada-France-Hawaii Telescope (CFHT). We used the polarimetric mode of this instrument, delivering a spectral resolution of about 65,000 and simultaneous coverage of the wavelength domain between 0.37 and 1.05 μm. Circular polarization sequences (Stokes V parameter) were collected as part of our program, as Zeeman signatures are much larger in this polarization state (a factor of ~10 stronger than Q and U, e.g., Landi Degl'Innocenti 1992; Wade et al. 2000; Kochukhov et al. 2011). Every polarization sequence consists of four subexposures with a fixed integration time of 600 s, and different angles of the two half-wave rotatable Fresnel rhombs in the polarimetric module, following a procedure designed to remove spurious polarization signatures at first order (Semel et al. 1993). Normalized, reduced Stokes I and V spectra are extracted from the raw ESPaDOnS images using the `Libre-ESpRIT` automatic pipeline tool (Donati et al. 1997, 2006a). The typical peak signal-to-noise ratio (S/N) of our Stokes V spectra is slightly above 100, while Stokes I spectra corresponding to single subexposures have a peak S/N of about 50. In the rest of this study, all tasks involving Stokes I spectra alone make use of the subexposures, as they offer a denser temporal sampling. All reduced spectra analyzed here are available through the PolarBase archive (Petit et al. 2014).

Table 1. Observation log of V530 Per for 29 Nov. and 05 Dec. 2006.

Date (2006)	HJD (2454000+)	E	Peak S/N
29 Nov.	69.71271	−7.1366	94
29 Nov.	69.74455	−7.0373	103
29 Nov.	69.77677	−6.9368	103
29 Nov.	69.80806	−6.8391	113
29 Nov.	69.84102	−6.7363	116
29 Nov.	69.87316	−6.6360	109
29 Nov.	69.91170	−6.5158	130
05 Dec.	75.70177	11.5500	105
05 Dec.	75.73473	11.6528	117
05 Dec.	75.76595	11.7502	119
05 Dec.	75.79718	11.8477	111
05 Dec.	75.83026	11.9509	107
05 Dec.	75.86149	12.0483	106
05 Dec.	75.89713	12.1595	113

Notes. From left to right, we list the date, the Julian date, the rotational phases calculated with Eq. (1), and the peak S/N.

We obtained an equal number of observations during both telescope nights, leading to a total of 14 Stokes V spectra and 56 Stokes I spectra. To assign a rotational phase (E) to every observation, we used the ephemeris:

$$\mathrm{HJD_{obs}} = \mathrm{HJD_0} + P_{\mathrm{rot}} \times E \quad (1)$$

where $P_{\mathrm{rot}} = 0.3205$ d is the rotational period of the equator, taken from our differential rotation measurement (see Sect. 5), and the initial Heliocentric Julian date $\mathrm{HJD_0} = 2454072.0$ is arbitrarily selected between the two observing nights. The resulting phases, reported in Table 1, show that successive Stokes V spectra are separated by about 10% of a rotation cycle. The phase smearing during the collection of a Stokes V sequence, which is of the same order, may be responsible for a reduced amplitude of polarized signatures generated by low latitude features (experiencing the largest Doppler shifts). Our observations in each individual night were able to cover about 60% of one rotation cycle. The rotational phase reached at the end of the first night was within 10% of the phase observed at the beginning of the second night. We therefore end up with a complete phase coverage of the target, and with redundant observations between phases 0.85 and 0.15.

3. Fundamental parameters of V530 Per

V530 Per is a member of the α Persei open cluster (Prosser 1992), a relatively young open cluster with an age of 63^{+8}_{-27} Myr, as derived from *Gaia* DR1 data (Yen et al. 2018). This recent estimate is significantly smaller than the 90 ± 10 Myr reported by Stauffer et al. (1999). The global metallicity of the cluster is close to solar, with [Fe/H] $= -0.10 \pm 0.08$ reported by Balachandran et al. (2011), who further noticed that stars with $T_{\rm eff} > 5500$ K have [Fe/H] ≈ -0.04, while stars with $T_{\rm eff} < 5500$ K feature a lower metallicity with [Fe/H] ≈ -0.13.

Since there is no available distance measurement for V530 Per itself, we used the average distance of the cluster in our work. Using the *Gaia* DR1 catalog, Yen et al. (2018) derived an average distance $d = 167.7 \pm 0.3$ pc. This value is smaller than the one derived from HIPPARCOS parallax (172.4 ± 2.7 pc, van Leeuwen 2009). Considering individual stellar parallaxes reported by Yen et al. (2018), we derived a standard deviation of 0.46 mas for α Per members, that we considered to be the cluster extent. We adopted this value as our uncertainty on the parallax of V530 Per, translating into a conservative distance uncertainty of about 15 pc.

We used our high-resolution spectral data to measure surface fundamental parameters of V530 Per (such as its surface temperature, gravity or metallicity) which are not documented in the literature. We mostly repeated here the procedure detailed by Folsom et al. (2016) and already applied to a sample of young solar-type stars (Folsom et al. 2016, 2018a). This approach iteratively fits synthetic spectra to the observation by χ^2 minimization. We computed spectra with the ZEEMAN spectrum synthesis code (Landstreet 1988; Wade et al. 2001), which performs polarized radiative transfer in LTE and works well for stars as cool as 5200 K (e.g. Folsom et al. 2018a). We used MARCS model atmospheres (Gustafsson et al. 2008) as input, together with atomic data extracted from the VALD database (Ryabchikova et al. 1997, 2015; Kupka et al. 1999). This approach using ZEEMAN has been verified against alternate spectroscopic parameter determinations (Folsom et al. 2016, 2018a), and an interferometric determination (Folsom et al. 2018b) for stars in this range of spectral types, with good agreement consistently found. One should note that we used single spectra for the parameter determination. The S/N is sufficiently high that it is not the limiting factor on our results, and given the heavily spotted nature of the star, any parameter determination assuming a uniform atmosphere will necessarily be approximate.

The observed spectrum of V530 Per was first renormalized, with the synthetic spectra providing guidelines for regions best approximating the continuum. The theoretical spectra were then compared to the renormalized spectrum, focusing on several spectral regions that are mostly uncontaminated by strong molecular lines, which are not taken into account by ZEEMAN, and telluric lines. A first fit was performed assuming a solar metallicity, which is a reasonable approximation since α Per members are known to have near solar metallicity (Balachandran et al. 2011). This fit was performed using 5 spectral regions $\sim$10 nm long, between 600 and 650 nm (specifically 600–610, 607.5-620.5, 619.6-627.55, 631.2–634.1 + 635.0–640.4, and 640.4–644.6 + 645.9–650.4 nm). The average of the best fits for individual windows was taken as the final value, and the standard deviation was taken as an uncertainty estimate. Assuming a solar metallicity, we obtained an effective temperature $T_{\rm eff} = 5281 \pm 96$ K, a surface gravity $\log g = 4.10 \pm 0.19$, a projected rotational velocity $v \sin i = 116.70 \pm 2.38$ km s^{-1} (consistent with the estimate of Jackson & Jeffries 2010, but significantly larger than the value of Barnes et al. 2001) and a micro turbulence $v_{\rm mic} = 1.3 \pm 0.4$ km s^{-1}. Although we checked on less noisy data sets that spectra of extremely active stars collected at different rotational phases do not produce significantly different results, except for $v \sin i$ estimates, our approach is still limited by the fact that we assumed the atmosphere to be homogeneous over the whole stellar surface. This is far from the actual situation of V530 Per, which is covered by a complex mixture of cool and hot spots (see Sect. 4.4). In particular, the giant, dark polar spot of this extremely active star impacts the line shape by generating a broad bump in the line bottom (Barnes et al. 2001), which has the effect of biasing our $v \sin i$ estimate toward larger values. An independent estimate of $v \sin i$, using Doppler mapping and incorporating the effect of surface spots in the model, leads to a significantly smaller value of about 105.6 km s^{-1} (Sect. 4.3). A second fit was performed with the metallicity left as a free parameter (as well as $T_{\rm eff}$, $\log g$, and [Fe/H]), To better constrain the additional parameter, this round of fitting included an additional 5 spectral regions between 550 and 600 nm (specifically 550–560.7, 560.7–569.2, 569.2–580, 580–590.3, and 590.3–600 nm), to better constrain this parameter. These additional windows have more severe line blending and consequently an accurate continuum normalization is more difficult, but they improve the statistical validity and provide more data to better constrain parameters with similar effects on the spectrum. The outcome is a set of atmospheric parameters in good agreement with our previous estimate, and the metallicity is found to be [Fe/H] $= -0.16 \pm 0.08$. This is consistent with the average value of Balachandran et al. (2011), although our estimate is sensitive to small departures from a perfect continuum normalization.

The V magnitude of V530 Per varies with time, with reported values between 11.657 ± 0.13 (Zacharias et al. 2013) and 11.981 ± 0.073 (Henden et al. 2015). Assuming that the brightness variations of V530 Per all come from rotating star spots, we considered the brightest available magnitude as the nonspotted magnitude. This magnitude was then used to estimate the luminosity $L = 0.78 \pm 0.18$ $L_\odot$, using the distance discussed above (167.7 ± 15 pc), the V band bolometric correction BC$_{\rm v} = -0.23$ from Pecaut & Mamajek (2013) and the reddening correction $A_V = 0.312$ from Pinsonneault et al. (1998). Subsequently, we derive the stellar radius $R = 1.06 \pm 0.11$ $R_\odot$. We then repeated the same procedure with the K magnitude, as it is much less affected by activity-induced fluctuations (e.g., Fang et al. 2010) and suffers less from the interstellar extinction. Using a K magnitude of 9.422 ± 0.019 from Cutri et al. (2003), and the interpolated bolometric correction BC$_K = 1.706 \pm 0.056$ of Masana et al. (2006), we get $L = 0.78 \pm 0.15$ $L_\odot$ and $R = 1.06 \pm 0.11$ $R_\odot$. Alternately, using the J band magnitude and the bolometric correction BC$_J = 1.22 \pm 0.03$ from Pecaut & Mamajek (2013), we get $L = 0.68 \pm 0.12$ $L_\odot$ and $R = 0.98 \pm 0.10$ $R_\odot$, in good agreement with the K band estimate.

Using our values of the effective temperature and luminosity, we obtained the HR diagram of Fig. 1. According to evolutionary tracks computed with the STAREVOL code by Amard et al. (2016, 2019) for solar metallicity, we get $M = 1.00 \pm 0.05$ $M_\odot$, $\log g = 4.4 \pm 0.1$ and an age of 33^{+10}_{-7} Myr using the K band, versus $M = 0.95 \pm 0.05$ $M_\odot$, $\log g = 4.4 \pm 0.1$ and an age of 40^{+11}_{-8} Myr with the J band. Both ages are consistent, within uncertainties, with the 63^{+8}_{-27} Myr proposed by Yen et al. (2018). The $\log g$ values with this approach are larger than the one derived from spectrum fitting, possibly due to the impact on the ZEEMAN estimate of line distortions linked to dark spots,

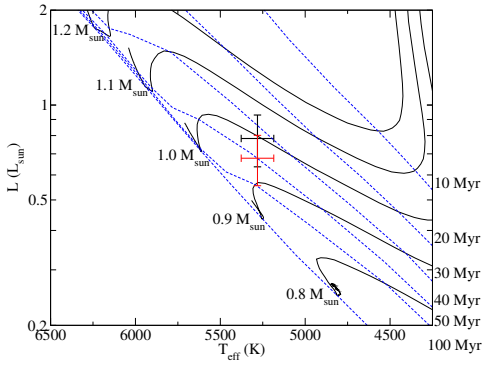

Fig. 1. V530 Per in the Hertzsprung-Russell diagram, with evolutionary tracks generated by the STAREVOL code. Evolutionary tracks are given for 0.1 $M_{\odot}$ steps (full lines), and isochrones are overimposed for 10, 20, 30, 40, 50 and 100 Myr (dashed lines). The black and red crosses are obtained from the K and J magnitudes, respectively.

Table 2. Fundamental parameters of V530 Per.

Name	Value	References
Distance	167.7 ± 15 pc	1,2
Age	33^{+10}_{-7} Myr	1
$T_{\rm eff}$	5281 ± 96 K	1
$\log g$	4.4 ± 0.1 [cm s^{-2}]	1
[Fe/H]	-0.16 ± 0.08	1
$m_V^{\rm min}$	11.657 ± 0.13	3
m_J	10.08 ± 0.019	4
m_K	9.422 ± 0.019	4
Luminosity	$0.78 \pm 0.15\ L_{\odot}$	1
Radius	$1.06 \pm 0.11\ R_{\odot}$	1
Mass	$1.00 \pm 0.05\ M_{\odot}$	1
$\log L_x$	31.2 [erg s^{-1}]	5
Rossby number	0.013 ± 0.002	1
Co-rotation radius	$1.9 \pm 0.2\ R_*$	1
Alfvén radius	$5\ R_*$	1
$v \sin i$	106 ± 1 km s^{-1}	1
Eq. rot. period	0.32055 ± 0.00005 d	1
$d\Omega$	0.042 ± 0.005 rad d^{-1}	1
Inclination angle	$40 \pm 4°$	1
Radial velocity	-0.96 ± 0.1 km s^{-1}	1

References. 1. This work 2. Yen et al. (2018) 3. Zacharias et al. (2013) 4. Cutri et al. (2003) 5. Pillitteri et al. (2013).

complicated by the heavily blended spectrum (the derivation of $\log g$ relies on the pressure broadened line wings, which are largely hidden by the high $v \sin i$).

Using the K band values of the mass and radius, we derived a theoretical convective turnover time (from the STAREVOL models) at one pressure scale height above the base of the convective zone of $25.0^{+4.3}_{-3.1}$ days (following the method of Folsom et al. 2016). This implies a Rossby number $R_o = 0.013 \pm 0.002$ with the period obtained by ZDI (see Sect. 5).

A summary of all parameters discussed above can be found in Table 2. The adopted values for the luminosity, radius, mass, $\log g$, and age are taken from our K band calculation, since this band is the least impacted by stellar activity.

4. Brightness and magnetic field imaging

4.1. Multi-line analysis

The S/N obtained for single spectral lines of V530 Per is too low to extract information about the line profile distortions produced by spots (in Stokes I) or magnetic fields (in Stokes V). This situation is especially problematic for V530 Per, due to the rotational broadening resulting in increased blending of lines. We take advantage here of the fact that all photospheric lines mostly display the same shape, with differences from line to line originating from the line depth (in Stokes I), or from a combination of the line depth, Landé factor and wavelength (in Stokes V). A multi-line approach is therefore a great help to increase the S/N and get rid of the blending issue.

All polarized spectra were treated using the Least-Squares Deconvolution method (LSD, see Donati et al. 1997). This widely employed method computes an average pseudo-line profile from a theoretical list of photospheric spectral lines extracted from the VALD database (getting rid of spectral ranges plagued by telluric or chromospheric lines), using the nearest line list in a grid computed by Marsden et al. (2014). Following the fundamental parameters determined in Sect. 3, we selected a line list with an effective temperature $T_{\rm eff} = 5250$ K and a logarithmic gravity $\log g = 4.5$, and included in our analysis all lines with a depth greater than 40% of the continuum level. This resulted in a total of 5726 lines, after removal of all lines plagued by telluric contamination, as well as all lines blended with chromospheric lines. The LSD pseudo-profiles are computed for a velocity step of 1.8 km s^{-1} (about ~40% of the spectral resolution of ESPaDOnS, equal to 4.6 km s^{-1}), a normalization Landé factor equal to 1.19, and a normalization wavelength of 650 nm. The resulting set of LSD profiles is plotted in Fig. B.1 for Stokes I, and in Fig. 2 for Stokes V.

It was noticed by Folsom et al. (2016) that LSD profiles obtained from spectra with S/N below about 70 are sometimes affected by spurious polarized signatures that show up in the polarized line profile and in the Null profile (which is a control parameter that is expected to display only noise). This effect is much less prominent (but sometimes spotted as well) with S/N values between 100 and 150. Given that our observations fall within this second S/N range, we checked that our set of Null LSD profiles were free from any detectable spurious signal, and that the same outcome was reached after averaging all available data together.

The dynamic spectrum for Stokes I shows obvious line distortions which clearly vary with time and self-repeat after one rotation period. This behavior is typical of surface dark spots (producing intensity bumps) or bright regions (translating as intensity dips). The most prominent feature is a systematic bump staying close to the line center, which is indicative of a surface structure anchored at high latitude. The large radial velocity span of this spectral structure tells us that it affects a significant fraction of the visible hemisphere, and its large positive deviation from the average profile reveals a very dark region. Apart from this large spot, a number of smaller trails of both signs in the dynamic spectrum reveal a complex distribution of smaller dark and bright spots. Contrary to the largest spot signature, most of these spectral features can be seen transiting from the blue wing to the red wing of the line profile, but not during their red-to-blue

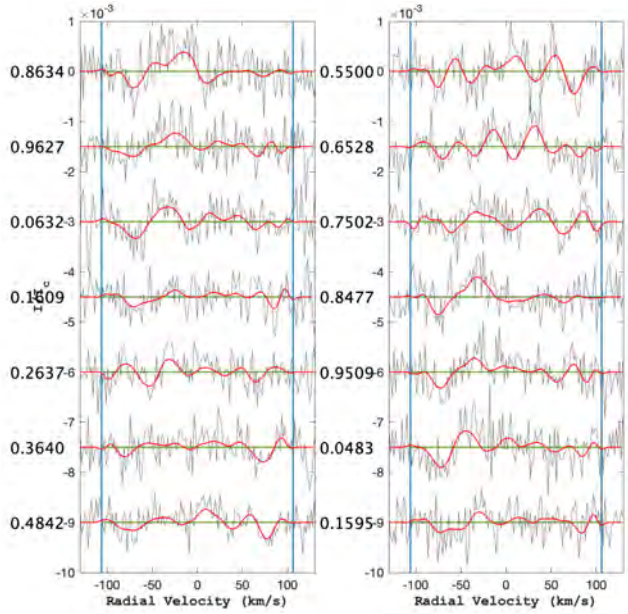

Fig. 2. Stokes V LSD profiles of V530 Per. Gray lines represent the observations, while red lines show our ZDI model. Blue vertical lines mark the $\pm v \sin i$ limit. *Left panel*: data from 29 Nov., and *right panel*: 05 Dec. Rotational phases are indicated on the left of each panel.

transit (i.e., when they are located behind the visible pole). We can therefore conclude that they are eclipsed during part of the rotation cycle, so that they are likely caused by surface features located at lower latitude than the largest spot which stays visible all the time.

The time-series of Stokes V profiles shows a complex pattern of polarized signatures. We interpret this line polarization as a manifestation of the Zeeman effect. According to the detection criteria proposed by Donati et al. (1997), only three LSD profiles from 29 Nov. 06 reach the "marginal detection" threshold. All other observations fall in the "no detection" category.The relatively large number of observed rotational phases (and the repeated observation of specific phases) compensates for this poor statistics. Because of the relatively large noise, it is not totally obvious to track progressive changes in the radial velocity and amplitude of the polarized signal. We can however stress that the large polarized feature observed on Nov. 29 at phase 0.8634 for negative radial velocities is also observed on Dec. 5, at the close-by phase 0.8477. Similar analogies can be observed for other rotational phases that are covered during the two observing nights (e.g., phase 0.0632 versus phase 0.0483, or phase 0.1609 versus phase 0.1595).

4.2. Zeeman-Doppler imaging

Our study of V530 Per made use of a new version of the ZDI code described by Folsom et al. (2018a), which is a Python implementation of the ZDI algorithm presented by Donati et al. (2006b), based on the maximum entropy fitting routine of Skilling & Bryan (1984). The two codes are designed to invert a set of LSD pseudo-line profiles. Using the same data set and identical input parameters, they were shown by Folsom et al. (2018a) to provide nearly identical outcomes. We repeated this test with our own set of observations and reached the same conclusion.

Using Stokes I data, the code can compute a DI map of the stellar photosphere assuming that the brightness inhomogeneities are purely generated by dark spots (e.g., Donati & Collier Cameron 1997), or by a combination of dark and bright patches (e.g., Donati et al. 2016). The code can also invert Stokes V time series to produce a magnetic map, with the additional possibility to use the DI map as a prior assumption. This implementation also includes a basic model of surface differential rotation, that will be detailed in Sect. 5.

The surface in the model is divided into a grid of pixels whose edges lie along lines of latitude and longitude with the area of each pixel being roughly the same, as described by, e.g., Vogt et al. (1987). For Stokes I modeling, every pixel is associated with a local line profile, using a simple Gaussian function with a central wavelength taken equal to the normalization wavelength of the LSD profile, a Gaussian FWHM taken equal to the one adopted for low $v \sin i$ stars of the same surface temperature as V530 Per (0.01 nm, Folsom et al. 2016), while the Gaussian amplitude is equal to 0.533 to match the depth of LSD profiles (a fine-tuning of the line depth is performed with the adjustment of other input parameters, see Sect. 4.3). Variations in temperature, not modeled here, can cause small variations in the equivalent width of a line, due to the impact of temperature on local line formation. Generally the impact of small equivalent width variations have a minimal impact on the resulting map (mostly seen as an increase of the best achievable χ^2). This rough modeling can be traded for more realistic descriptions of the line shape (e.g., Voigt profiles, Folsom et al. 2018b), but given the large $v \sin i$ of V530 Per its line shape is vastly dominated by rotational broadening, so that a local Gaussian line proves to produce a convincing fitting of the data. For Stokes V modeling, the model considers the brightness map as a prior assumption for the magnetic field reconstruction when Stokes V LSD profiles are inverted (e.g., Donati et al. 2014). The magnetic model

is computed under the weak field approximation (Stokes V is assumed to be proportional to the derivative of Stokes I), which is a valid approach over the range of field values encountered hereafter (i.e., a few hundred Gauss, e.g., Kochukhov et al. 2010). The final calculated line profile is a sum of all visible surface elements. In addition to a projection factor depending on the limb angle, and scaling by the brightness map, the continuum is rescaled to follow a linear limb darkening law of the following form (e.g., Gray 2005):

$$I_c/I_c^0 = 1 - \eta + \eta\cos(\Phi) \tag{2}$$

where η is the limb darkening coefficient, Φ is the angle from disk center, and I_c/I_c^0 is the ratio of local brightness at the limb angle Φ. We chose a linear limb darkening coefficient $\eta = 0.73$, by interpolating between available values from the table of Magic et al. (2015), using the Kepler filter, as it is the closest in spectral coverage to our instrumental setup, and using stellar parameters of V530 Per given in Sect. 3. Variations in local line depth relative to the local continuum as a function of limb angle are neglected.

In most available ZDI studies, the stellar surface is assumed to be spherical, implying that the rotational oblateness is neglected. Considering for simplicity the hydrostatic equilibrium in an incompressible, uniform-density star, we obtain to first order (see Tatebe et al. 2007):

$$\frac{R_\mathrm{p}}{R_\mathrm{e}} \approx 1 - \frac{3\Omega^2}{8G\pi\rho} \tag{3}$$

where R_p and R_e stand for the polar and equatorial radii, Ω for the rotational rate, G for the gravitational constant and ρ for the density. This rough approach can provide us with an order of magnitude of the oblateness, with $R_\mathrm{p}/R_\mathrm{e} \approx 0.92$. We therefore modified the local velocities assuming that the stellar surface shape can be described by a Roche model (Tassoul 1978), in which the equipotentials $A(R_*, \theta)$ include a centrifugal term:

$$A(R_*, \theta) = -\frac{GM_*}{R_*} - \frac{1}{2}\Omega^2 R_*^2 \sin^2\theta \tag{4}$$

where R_* is the stellar radius at colatitude θ. Whenever Ω is smaller than the break-up angular velocity Ω_c, the surface shape is expressed as follows (Collins 1965; Collins & Harrington 1966; Cranmer 1996):

$$x(\omega, \theta) = \frac{3}{\omega\sin\theta}\cos\left[\frac{\pi + \cos^{-1}(\omega\sin\theta)}{3}\right] \tag{5}$$

where $x(\omega, \theta) = R_*(\theta)/R_p$ and $\omega = \Omega/\Omega_c$. Taking $\theta = \pi/2$, we can calculate again the oblateness, and obtain $R_\mathrm{p}/R_\mathrm{e} \approx 0.91$, in agreement with our first approach. Finally, we assume that the surface brightness is affected by gravity darkening. Following the prescription of Lucy (1967), the brightness is therefore assumed to vary as g^{4b}, where g is the effective gravity and $b = 0.08$, leading to a brightness ratio of 0.88 between the equator and the pole. The exact value that should be used for b is still a matter of debate today (see van Belle 2012 for a review), but we checked that our model is poorly dependent on the adopted exponent. Changes in the line shape with and without gravity darkening remain modest, as illustrated in Fig. C.1.

To express the magnetic field geometry, the model uses a spherical harmonics decomposition of the field based on Donati et al. (2006b; see also Vidotto 2016 for more discussion) by following the set of equations below:

$$B_r(\theta, \phi) = \sum_{\ell=1}^{L}\sum_{m=0}^{\ell}\mathrm{Re}[\alpha_{\ell m}Y_{\ell m}(\theta, \phi)] \tag{6}$$

$$B_\theta(\theta, \phi) = -\sum_{\ell=1}^{L}\sum_{m=0}^{\ell}\mathrm{Re}[\beta_{\ell m}Z_{\ell m}(\theta, \phi) + \gamma_{\ell m}X_{\ell m}(\theta, \phi)] \tag{7}$$

$$B_\phi(\theta, \phi) = -\sum_{\ell=1}^{L}\sum_{m=0}^{\ell}\mathrm{Re}[\beta_{\ell m}X_{\ell m}(\theta, \phi) - \gamma_{\ell m}Z_{\ell m}(\theta, \phi)] \tag{8}$$

where:

$$Y_{\ell m} = c_{\ell m}P_{\ell m}(\cos\theta)e^{im\phi} \tag{9}$$

$$X_{\ell m}(\theta, \phi) = \frac{c_{\ell m}}{\ell + 1}\frac{im}{\sin\theta}P_{\ell m}(\cos\theta)e^{im\phi} \tag{10}$$

$$Z_{\ell m}(\theta, \phi) = \frac{c_{\ell m}}{\ell + 1}\frac{\partial P_{\ell m}(\cos\theta)}{\partial\theta}e^{im\phi} \tag{11}$$

and

$$c_{\ell m} = \sqrt{\frac{2\ell + 1}{4\pi}\frac{(\ell - m)!}{(\ell + m)!}}. \tag{12}$$

Here (θ, ϕ) are the colatitude and longitude on the stellar surface, P_{lm} is the associated Legendre polynomial with ℓ and m giving the degree and order of the spherical harmonics mode. In practice, the model is described by a series of three complex coefficients: $\alpha_{\ell m}$ corresponding to the radial poloidal field, $\beta_{\ell m}$ the tangential poloidal field and $\gamma_{\ell m}$ the toroidal field component. We note that the spherical harmonics decomposition is used for both the spherical and oblate stellar geometries described above.

4.3. ZDI adjustment of stellar parameters

Stellar parameters extracted from individual spectral lines (Sect. 3) can be biased when $v \sin i$ is very large (increasing the number of blends), or when the line profile is distorted by photospheric inhomogeneities. In this case, the optimization of tomographic models can help improve the determination of some parameters, including $v \sin i$, the radial velocity RV, the inclination of spin axis i, and give access to additional parameters like the rotation period of the equator P_eq, and the difference in rotational rate between the equator and pole $d\Omega$ (these two parameters will be investigated in Sect. 5).

Using a simple χ^2 minimization to determine $v \sin i$ leads to significant residuals in phase averaged LSD profiles, showing up in the wings of the pseudo-line. Following Donati et al. (2003a), we therefore varied again $v \sin i$ to minimize any systematics (Fig. D.1), and finally adopted $v \sin i = 106$ km s^{-1} (versus 110 km s^{-1} using χ^2 minimization). This value is slightly larger than the 102 km s^{-1} obtained by Barnes et al. (2001). Although this empirical estimate is not associated to a formal error bar, 1 km s^{-1} is probably a reasonable order of magnitude for the uncertainty.

By combining our $v \sin i$ estimate with the 0.3205 equatorial rotation period of Sect. 5 and the stellar radius derived in Sect. 3, we obtained an inclination angle equal to $40 \pm 4°$. Searching for a value of the inclination angle minimizing the χ^2 of the DI model provided us with inconsistent results, depending

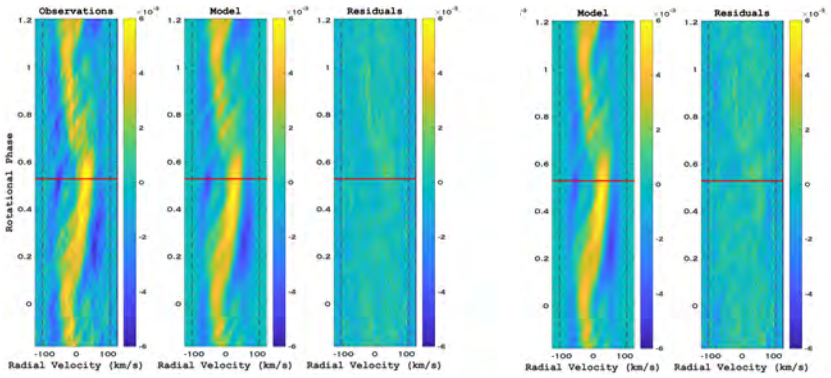

Fig. 3. Stokes *I* dynamic spectrum of V530 Per, after subtraction of the averaged Stokes *I* profile. *From left to right*: observations, DI model with $\chi^2 = 0.55$ including both bright dark spots, model residuals. The two additional panels on the right show our model with $\chi^2 = 0.65$ and dark spots only, and the model residual. The vertical, black, dashed lines mark the $\pm v \sin i$ limit. The portion above the solid, horizontal red lines represents data from 05 Dec. 2006, while the lower part represents data taken on 29 Nov. 2006.

on whether we used a spherical or oblate model for the stellar shape. While a spherical surface is leading to $i = 35°$, the oblate model is optimized for values of i below 10°, in clear disagreement with other fundamental parameters of V530 Per (this latter value would, for instance, imply an absurdly large stellar radius). The value obtained by Barnes et al. (2001) was equal to 30°, in rough agreement with our spherical estimate (assuming a typical error bar, including systematics, on the order of 5 to 10°, Rice & Strassmeier 2000). Facing these discrepant estimates derived from tomographic inversion, we finally adopted $i = 40°$ hereafter.

The χ^2 of the brightness map was minimized for a radial velocity RV $= -0.96 \pm 0.04$ km s^{-1}, using a total of 7920 freedom degrees (the total number of data points) to estimate the statistical error bar (bearing in mind that instrumental systematics likely dominate this statistical uncertainty, with an absolute RV accuracy probably not better than 0.1 km s^{-1}). Although uncertainties were not provided by Barnes et al. (2001), our measurement seems to be significantly larger than their estimate RV $= -3.1$ km s^{-1}), suggesting that V530 Per is possibly not a single object. We note that the local line depth was fine-tuned after each parameter adjustment ($v \sin i$ and RV), leading to the final value listed in Sect. 4.2.

4.4. Resulting surface maps

4.4.1. Brightness map

Thanks to the dense phase coverage described in Sect. 2, we are able to trace the Doppler shifts of surface spot signatures over the stellar rotation period. Stellar parameters determined in Sect. 3, as well as $d\Omega$ and $P_{\rm eq}$ (Sect. 5) are taken as input for the brightness map reconstruction. To the naked eye, the Stokes *I* dynamic spectrum of Fig. 3 does not highlight any obvious variations of spot signatures between the two nights of observation, so that we chose to reconstruct the surface brightness distribution using all Stokes *I* data together.

A first map was reconstructed assuming dark spots only and an oblate surface (lower panel of Fig. 4), with a model reaching a reduced χ^2 of 0.65 (showing that error bars in Stokes *I* LSD pseudo-profiles are over-estimated, as documented by e.g., Petit et al. 2004). The main visible structure is a large spot located around a latitude of 75°, spreading between phases 0 and 0.5. A number of smaller spots are reconstructed as well. Most of the smaller structures are also seen at high latitude, but a few of them are found down to a latitude of 30°. The dynamic spectrum produced with synthetic line profiles of the DI model (see the two panels constituting the right part of Fig. 3) is able to reproduce most observed spectral features. There are, however, some small residuals that reveal the limits of this approach. These remaining signatures are mostly dips, suggesting that they are generated by bright patches (similarly to, e.g., Barnes et al. 2017). We therefore computed a second model where both dark and bright spots were allowed, which led us to a smaller reduced χ^2 of 0.55. In spite of the same limb darkening law assumed for dark and bright features, we obtained a nearly flat dynamic spectrum of residuals (third panel of Fig. 3). Although a limb darkening law optimized for dark spots may lead to minor biases in the reconstruction of bright spots, we noticed from the comparison of the two panels in Fig. 4 that dark spots, at least, do not seem to be noticeably modified by the inclusion of bright regions in the model. The corresponding brightness map shows almost the same distribution of dark spots as in the previous model. Bright spots appear to be concentrated at latitudes lower than the majority of dark spots, with a greater accumulation between 30 and 45° of latitude. Their size is generally smaller than that of dark spots, and their distribution extends down to equatorial latitudes. The brightest reconstructed spots are about 40% brighter than the quiet photosphere, which is a higher contrast than observed on the Sun (Hirayama & Moriyama 1979). The total fraction $S\,p_{\rm tot}$ of the stellar surface covered by spots (including both dark and bright features) is equal to 10% in this model, calculated by the following equation:

$$S\,p_{\rm tot} = \frac{\sum_{i=0}^{n} |I_i - I_0| A_i}{\sum_{i=0}^{n} A_i} \tag{13}$$

where $I_0 = 1$ is the brightness with no spot and I_i is the brightness on the cell of surface A_i.

We note that the brightness map obtained from a spherical model (top panel of Fig. 4) is characterized by a lower contrast of the spot pattern (both in the dark, high latitude spots and in the bright, low latitude features). In this case, the fractional spot coverage drops to about 6%, and the brightest faculae are about 30% brighter than the quiet photosphere, which remains larger

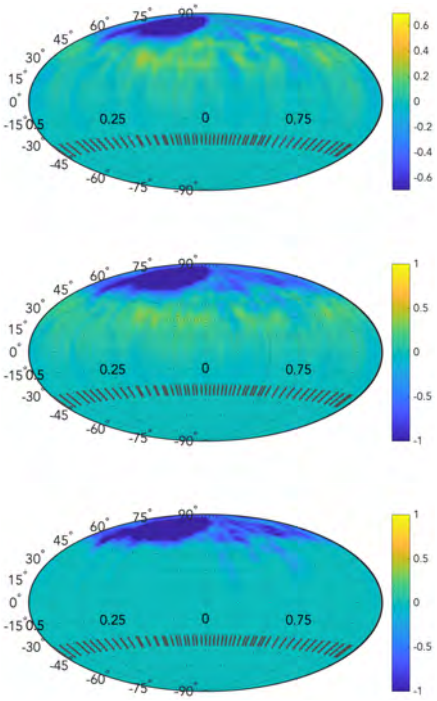

Fig. 4. Logarithmic normalized brightness maps of V530 Per reconstructed assuming a combination of dark and brights spots and an spherical surface (*upper panel*), dark and bright spots and an oblate surface (*middle*), or dark spots only and an oblate model (*lower panel*). For display clarity, the gravity darkening was subtracted from the brightess distribution of oblate models. The dark spot model provides us with a reduced $\chi^2 = 0.65$, while introducing bright spots reduces this value to 0.55. We used here a Hammer projection of the stellar surface. Meridional ticks in the bottom of the maps mark the rotational phases of our observations. The portion of the maps below −40° of latitude is set to 0, as it is invisible to the observer. We emphasize that the color scale is different for spherical and oblate models.

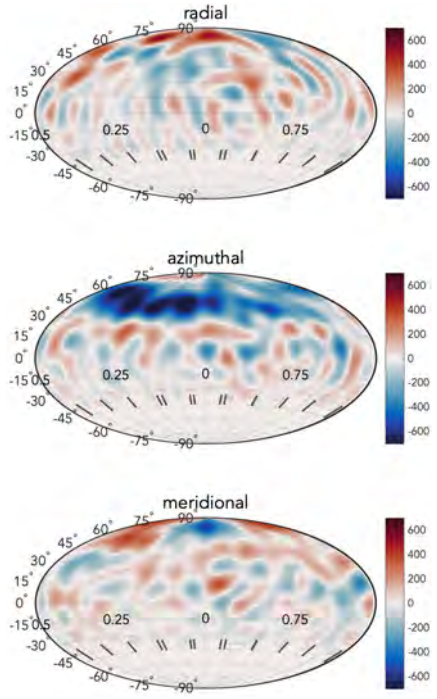

Fig. 5. Magnetic map of V530 Per. The three panels show the different field components in spherical projection. The color scale illustrates the field strength in Gauss. A Hammer projection of the stellar surface is adopted, and vertical ticks in the bottom of the panels show the rotational phases of individual Stokes *V* sequences.The portion of the maps below −40° of latitude is set to 0, as it is invisible to the observer.

than typical solar values. Another difference compared to the oblate model is a shift of all reconstructed features toward higher latitudes, although this effect is sufficiently subtle to be difficult to distinguish in the maps (the limit of the large polar spot, at latitude ∼60°, is where the effect can be most easily seen).

4.4.2. Magnetic map

The magnetic field reconstruction made use of the brightness map as a prior input. The data can be fitted down to $\chi^2 = 0.9$ by including spherical harmonics modes up to $\ell = 15$ (Fig. 2). Increasing further the number of spherical harmonics coefficients to be fitted does not improve the model. The resulting map displays a complex pattern of magnetic regions, with field strength locally exceeding 1 kG (Fig. 5). Other models reconstructed with larger χ^2 values (up to $\chi^2 = 1$) still display small magnetic features at roughly the same field strength, suggesting that overfitting is not responsible for the observed patchy field distribution.

The largest and strongest radial field region is reconstructed at the approximate location of the largest dark spot, around a latitude of 75°. Other radial field spots are more difficult to link to specific brightness patches. The azimuthal field component is dominated by a large belt of negative field encircling the visible pole between latitudes 45 and 60°. In this prominent structure, the field reaches a maximum strength between phases 0 and 0.5, which roughly corresponds to the azimuthal location of the largest brightness spot. Its average latitude is comprised between the lower boundary of the polar spot, and the upper boundary of the group of smaller, bright features.

A list of magnetic parameters was calculated from the $\alpha_{\ell m}$, $\beta_{\ell m}$, and $\gamma_{\ell m}$ spherical harmonics coefficients of the ZDI model to further characterize the magnetic field structure of V530 Per. The resulting list of parameters is shown in Table 3. The large ratio between the average magnetic field strength $\langle B_V \rangle$ and the unsigned peak magnetic strength $|B_{\rm peak}|$ highlights the complexity of the field structure. We also note that a majority (about two thirds) of the photospheric magnetic energy (as estimated from B^2) is stored in the toroidal field component. Focusing on spherical harmonics modes with $m = 0$ (i.e., axisymmetric modes), we note that they contain slightly more than half of the magnetic energy (∼53%). But a closer look reveals that the poloidal field component is poorly axisymmetric, while the

Table 3. Magnetic field characteristics of AP 149.

	Parameter	Value
(a)	$\langle B \rangle$	177 G
(b)	$\lvert B_{\rm peak} \rvert$	1088 G
(c)	toroidal	64% (total)
(d)	axisymmetric	53% (total)
(e)	poloidal axisymmetric	16% (poloidal)
(f)	toroidal axisymmetric	74% (toroidal)
(g)	dipole ($\ell = 1$)	1.2% (poloidal)
(h)	quadrupole ($\ell = 2$)	3.3% (poloidal)
(i)	octopole ($\ell = 3$)	5.4% (poloidal)
(j)	toroidal $\ell = 1$	8% (toroidal)
(k)	toroidal $\ell = 2$	21% (toroidal)
(l)	toroidal $\ell = 3$	20% (toroidal)

Notes. The values include (a) the average magnetic field strength $\langle B \rangle$, (b) the unsigned peak magnetic field strength $\lvert B_{\rm peak} \rvert$, (c) the ratio of toroidal field energy to the total magnetic energy, (d) the ratio of magnetic energy in axisymmetric modes ($m = 0$) over the total energy, the same quantity but limited to the poloidal (e) and toroidal (f) magnetic component, the ratio of the dipole, quadrupole, and octopole (g, h, i) to the total poloidal component, and ($\ell = 1, 2, 3$) subcomponents of the toroidal field energy, as percentages to the toroidal field energy (j, k, and l).

toroidal field energy is mostly reconstructed in axisymmetric structures (∼74%). As a consequence of the field complexity, a very small fraction of the poloidal magnetic field energy is seen in the dipole ($\ell = 1$), quadrupole ($\ell = 2$) and octopole ($\ell = 3$). Here again, the situation is noticeably different if we consider the toroidal field component where nearly half the magnetic energy ends up in $\ell \leq 3$, revealing a higher level of geometrical simplicity in the toroidal field component.

Finally, we used a potential field source surface model (Jardine et al. 2013) to extrapolate the coronal magnetic field, using the potential component of the ZDI map as boundary conditions (Fig. 6). The surface toroidal field component is ignored in the extrapolation, as recent models suggest that purely potential field extrapolations provide a better match to prominence distribution (Jardine et al. 2020). We assumed that the field becomes purely radial above a source surface located at 2.5 R_*, which is slightly larger than the corotational radius (Jardine 2004). Although the exact location of the source surface is difficult to establish precisely, due to uncertainties in the wind properties, especially in an environment where the centrifugal force plays an important role, we chose this value considering that field lines will likely break open quickly above the corotational radius under the effect of centrifugal forces.

5. Differential rotation

The very dense phase coverage of our time-series, including repeated observations of specific rotational phases separated by a six day gap, constitutes a very good basis to study the short term evolution of photospheric brightness, especially under the action of differential rotation. In this context, the large $v \sin i$ of V530 Per is also an asset as it gives the capability to spatially resolve small surface features.

We applied the sheared image method presented by Donati et al. (2000) and Petit et al. (2002). This technique incorporates a built-in latitudinal shear of the stellar surface into the DI or ZDI model, and provides robust results even for sparse data sets

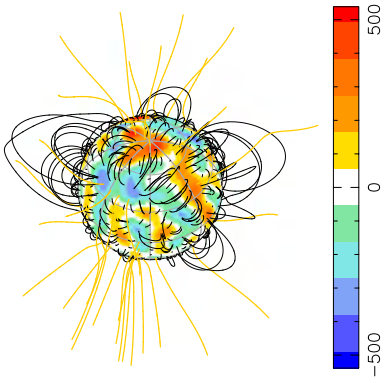

Fig. 6. Large-scale potential field extrapolation of V530 Per. The star is seen at phase 0.0, with a 40° inclination angle. The blue and white lines represent open and close field, respectively. The color scale on the surface show the strength of the radial field component (in Gauss), following Fig. 5. The source surface is located at 2.5 R_*, which is a bit further away from the star than the corotation radius (at 1.9 R_*).

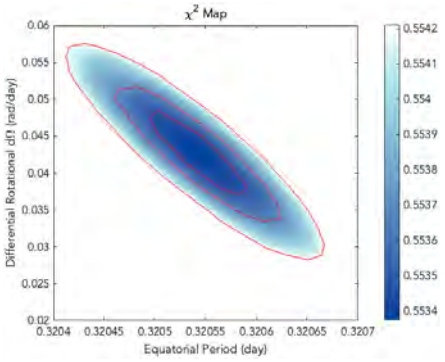

Fig. 7. Reduced χ^2 map for the shear parameter $d\Omega$ and the equatorial rotation period $P_{\rm eq}$. The three red solid lines illustrate the 1σ, 2σ, and 3σ confidence intervals.

(Petit et al. 2002; Donati et al. 2003b). In our model, the rotation rate Ω is assumed to vary with the latitude θ, following a simple solar-like dependence:

$$\Omega(\theta) = \Omega_{\rm eq} - d\Omega \sin^2 \theta \qquad (14)$$

where $\Omega_{\rm eq}$ is the rotation rate of the equator and $d\Omega$ the pole to equator gradient in rotation rate.

In practice, we estimate the two parameters of this simple law by computing a large number of DI/ZDI models over a grid of values of $d\Omega$ and $\Omega_{\rm eq}$. We then select the doublet that minimizes the model χ^2 (at fixed entropy), as described in Sect. 4.3. We show in Fig. 7 the χ^2 obtained in the $d\Omega - \Omega_{\rm eq}$ plane using Stokes I data, and notice a clear minimum, detected at $P_{\rm eq} = 0.32055 \pm 0.00005$ d and $d\Omega = 0.042 \pm 0.005$ rad d^{-1}. We note that the differential parameters obtained assuming a spherical surface are very close to these values, with $P_{\rm eq} = 0.3205 \pm 0.0001$ d and $d\Omega = 0.045 \pm 0.01$ rad d^{-1}. We also

inferred the surface shear from a cross-correlation approach similar to the one detailed by Donati & Collier Cameron (1997) and used in a number of more recent papers (e.g., Barnes et al. 2017; Kriskovics et al. 2019; Kővári et al. 2019), and obtain a result (not shown here) in agreement with the sheared image method.

The same procedure was applied to the Stokes V data, in order to look for a similar shear of the magnetic geometry. This attempt was not conclusive, most likely because the high relative noise of our polarized line profiles is enough to hide changes in the Zeeman signatures as subtle as those generated by a Sun-like surface shear.

6. Prominence maps

The Hα line profiles are always seen in emission throughout the observing run. As shown in the dynamic spectra of Hα in Fig. 8, two peaks are generally observed at roughly ± 200 km s^{-1} from the line center, and their variations show clear signs of periodic modulation, at a period close to the stellar rotation period. The radial velocities of Hα emitting material is much larger than the projected equatorial velocity of the stellar surface ($\approx$105 km s^{-1}).

The Alfvén radius was calculated with a Weber-Davies model (Weber & Davis 1967) using the numerical code of Johnston et al. (2017). For this, we have estimated the mass loss from the star using the relation of See et al. (2015) and the value of the Rossby number in Table 2. We obtain that V530 Per has a mass loss rate of $10^{-10}\,M_\odot$ yr^{-1}. A coronal temperature of 16×10^6 K was calculated applying the relation of Johnstone & Güdel (2015), and $F_x = L_x/(4\pi R_*)$ with the L_x value quoted in Table 2. We obtain an Alfvén radius of about $5R_*$. This value is likely over-estimated, as centrifugal forces are neglected here. It is therefore possible that the actual Alfvén radius may be closer to the source surface proposed in Sect. 4.4, although it can be expected to be larger than the source surface radius (e.g., Schrijver et al. 2003). Even considering this point, the star is most likely in the centrifugal magnetosphere regime that allows it to support prominences (Ud-Doula et al. 2008). In this case, and as long as sufficiently short time-scales are considered, most of the observed variability can be attributed to the orbital motion of hydrogen clouds. We therefore adopt the assumption that the emission is due to large prominences trapped in the coronal large-scale magnetic field and forced to corotate with the stellar surface (Collier Cameron & Robinson 1989a; Collier Cameron & Robinson 1989b; Steeghs et al. 1996; Donati et al. 2000).

In order to visualize the spatial distribution of prominences, we made use of the simple maximum entropy tomographic code of Donati et al. (2000), which is inspired from an algorithm initially developed for cataclysmic variables by Marsh & Horne (1988). Through this inversion method, we attribute 2D Doppler velocities (V_x, V_y) to Hα emitting clouds, assuming a local Hα profile of Gaussian shape with a 0.04 nm (~18 km s^{-1}) Gaussian FWHM, under the assumption that the Hα emitting material is optically thin (Donati et al. 2000). We note that the outcome of the model is mostly unsensitive to the exact value of the local width. In the case of corotating material, the velocity distribution is a straightforward illustration of the spatial distribution. Here, the emission is modeled above the continuum (without subtraction of any reference profile). The reconstructed equivalent widths should therefore not be considered physically meaningful, the main objective of this simple model being to locate the emitting material in the velocity space and highlight its possible short term evolution.

The middle panel of Fig. 8 illustrates the synthetic set of Hα profiles produced by the code, showing that the main spectral features are correctly reproduced by the model. Residuals, however, remain above the noise level, which shows that the simple model used here is not able to fit the whole Hα signal (right panel of the same figure). This mismatch likely highlights that rotational modulation is not the only source of variability in our chromospheric data, even on timescales as short as one night. This observation justifies a posteriori our choice to model the two nights of observation separately. It is also likely that a more elaborated model, e.g., with the intensity of each pixel map allowed to vary sinusoidally with rotation phase (as in, e.g., Steeghs 2003), would likely allow one to achieve a better fit to the data. In particular, this additional flexibility may help mimicking, e.g., that some of the prominences may be partly hidden by the star as they rotate.

The resulting prominence patterns show similarities for the two nights. Large clouds are reconstructed at most phases, at a velocity roughly equal to the one of the corotation radius (~$1.9R_*$, Fig. 9). We also note that significant variations are seen between the two nights. In the first map, we reconstructed a higher concentration of material between the stellar surface and the corotational radius, between phases 0.75 and 0.95. During the second night however, the coronal material features a larger radial spread around the corotation radius, as well as azimuthally with a denser material between phases 0.7 and 1. In both cases, most of the Hα emission is observed within twice the corotation radius. We stress, however, that fine details in the observed changes need to be considered with caution, given the very simple model used in our tomographic inversion.

For the two nights, we note that the period optimizing our model is larger than the rotation period used to reconstruct the prominence maps (taken equal to the rotation period of the stellar equator derived in Sect. 5), with about 0.39 d on 0189 Nov. and 0.36 d on 05 Dec. However, such period estimate is likely to be impacted by nonrotational short term variability occurring within each night, as well as by the fact that our data set for each night does not cover a full rotation period.

7. Discussion

7.1. Brightness map

The most obvious structure on the brightness map of V530 Per is a very large, dark spot close to the rotation pole (Fig. 4). This prominent feature is however not axisymmetric, with a latitude of about 75°. The same recognizable feature was already reported by Barnes et al. (2001), using observations collected in 1998. It is therefore plausible that this giant spot is a long-lived structure, or at least an ordinary feature at the surface of V530 Per.

Large polar spots are commonly observed among the most active stars, most of the time through Doppler mapping as in the present study, but also with interferometry (Roettenbacher et al. 2016). A number of young solar-type stars at the end of the pre-main sequence phase or in their early main sequence have been found to host such extended polar caps. Typical examples include LQ Lup (named RX J1508.6-4423 in the paper, $P_{\rm rot} \sim 0.31$d, Mass $\sim 1.16\,M_\odot$, Donati et al. 2000) and AB Dor ($P_{\rm rot} \sim 0.51$ d, Mass $\sim 1\,M_\odot$, Donati & Collier Cameron 1997; Donati et al. 2003b). Both of them have a mass and rotation rate similar to those of V530 Per, but both of them display a centered polar spot, while the high-latitude spot observed on V530 Per does not cover the pole. A few other young G dwarfs have been reported to show large off-centered, high-latitude spots (not covering the pole), like EK Dra ($P_{\rm rot} \sim 2.8$ d, Mass $\sim 0.95\,M_\odot$, Strassmeier & Rice 1998; Waite et al. 2017; Järvinen et al. 2018) or other

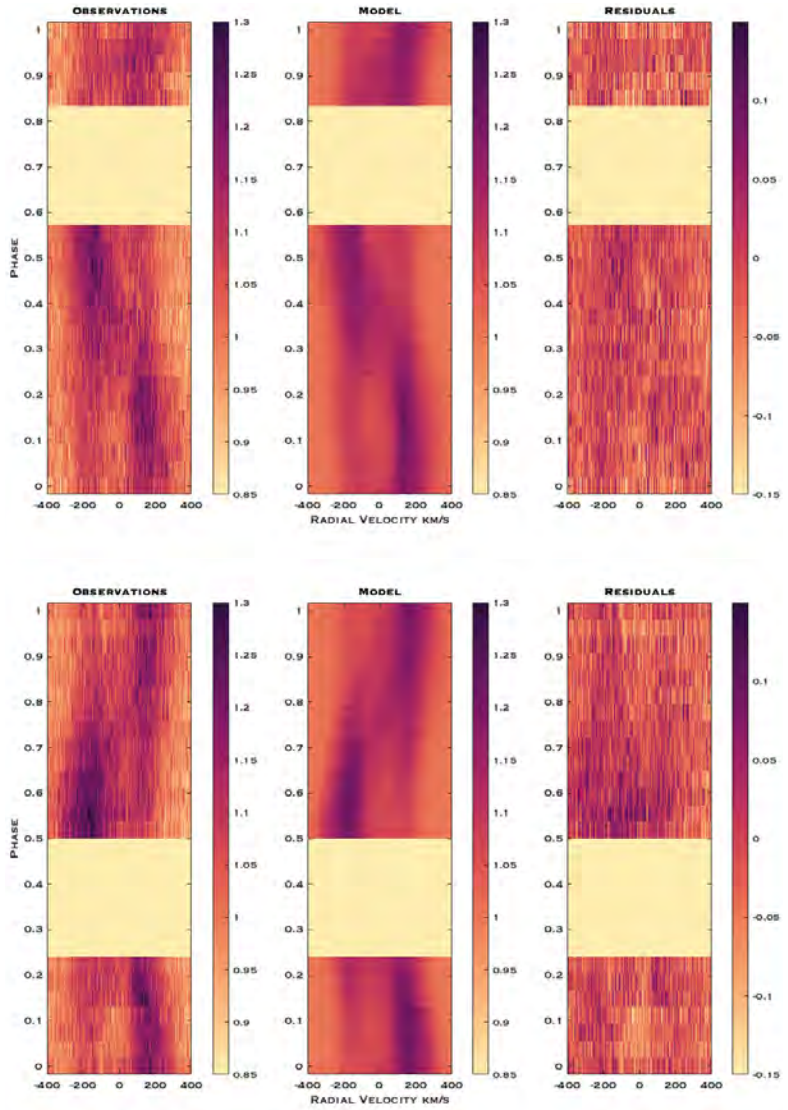

Fig. 8. Dynamic spectra showing the Hα line of V530 Per, color coded according to the normalized flux. Rotational phases are computed according to Eq. (1). *Upper and lower panels*: 29 Nov. and 05 Dec., respectively. *From left to right*: we display the observations, the outcome of the tomographic model, and the residuals. Hα mapping from the first night leads to a reduced χ^2 of 7.2, while the second night provides us with a reduced χ^2 of 7.6.

rapidly rotating members of the α Per cluster (AP 193, He 520, He 699, Barnes et al. 2001). In V530 Per as in other rapidly rotating stars, the preferential emergence of spots at high latitude can be interpreted as an indication that the Coriolis force can impose magnetic flux tubes to raise toward the stellar surface in a path mostly parallel to the stellar spin axis (Schuessler et al. 1996). Smaller spots are also observed at lower latitudes, which suggests that they may be formed in an internal layer closer to the photosphere.

A large number of Doppler maps of young stars include dark spots only in their surface model, although some stars have benefited from temperature mapping based on the modeling of individual spectral lines (e.g., V1038 Tau by Rice & Strassmeier 2001, HD 171488 by Strassmeier et al. 2003, V410 Tau by

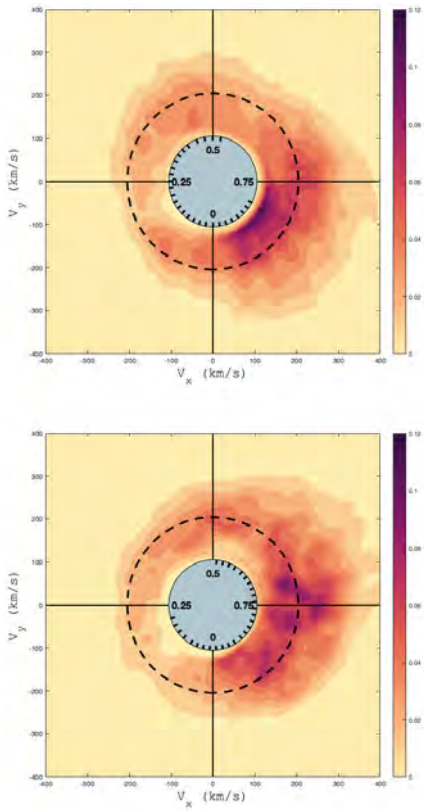

Fig. 9. Prominence maps of V530 Per reconstructed from the data of 29 Nov., 2006 (*top*) and 05 Dec., 2006 (*bottom*). The inner, filled blue circle represents the stellar surface. Radial ticks inside this circle give the rotational phases of our observations. The outer dashed circle is the corotation radius. The color scale depicts the local Hα equivalent width, in units of picometers per 8 km s^{-1} square pixel.

Carroll et al. 2012, V1358 Ori by Kriskovics et al. 2019, LQ Hya by Cole-Kodikara et al. 2019). Our brightness modeling allows for bright surface patches as well, and the resulting map features a number of bright spots of relatively small area, with a specific concentration between latitudes 30° and 45°. The same set of techniques was also recently applied to the weak line T Tauri stars LkCa 4 (Donati et al. 2014), V830 Tau (Donati et al. 2016), TAP 26 (Yu et al. 2017) and V410 Tau (Yu et al. 2019). These four stars have masses relatively close to the one of V530 Per, although they all are significantly younger, and all rotate slower than V530 Per. We observe a similar mid-latitude accumulation of bright spots on TAP 26 (which has a rotation period about twice that of V530 Per), while other stars from this series do not display this recognizable distribution of bright spots.

7.2. Differential rotation

The surface shear $d\Omega$ measured for V530 Per is close to the solar value. This estimate is obtained through the assumption that the latitudinal differential rotation follows a smooth solar-like law. This starting point can be questioned in the light of recent numerical simulations, where the most rapidly rotating stars experience a more complex surface rotation pattern in the form of Jupiter-like zonal flows (Brun et al. 2017). The relatively high noise level in our data prevents us from investigating a more complex latitudinal flow pattern in any reliable way. Our simple model tells us at least that solid-body rotation cannot provide us with an optimal model of our time series, and that low latitudes of the visible hemisphere seem to rotate on average faster than the higher latitudes.

A number of rapid rotators benefit from differential rotation measurements obtained with an approach similar to ours. A compilation of these results can be found in Barnes et al. (2005, 2017), highlighting empirical relationships between the surface shear and the rotation rate or surface temperature. Our analysis of V530 Per suggests that the observed shear is roughly in line with previous observations of very rapidly rotating stars of similar Ω_{eq} values (Barnes et al. 2005). The observed shear is also in good agreement with the temperature trend reported by the same authors.

7.3. Magnetic field

The very rapid rotation of V530 Per results in a very small Rossby number, $R_o \approx 1.3 \times 10^{-2}$, indicative of a very efficient amplification of its internal magnetic field through a global dynamo. Main sequence stars with similarly small Rossby numbers for which ZDI maps are available generally belong to the M dwarf category, and V530 Per is one of the rare G/K dwarfs populating the low Rossby number branch (Vidotto et al. 2014; See et al. 2019). Figure 10 is adapted from the Fig. 1 of See et al. (2019; who present a compilation of ZDI measurements, extending on previous works by Vidotto et al. 2014; Folsom et al. 2016, 2018a). From the original plot, we have removed M dwarfs because of their much deeper convective envelope. We also discarded Hot Jupiter host stars, since at least τ Boo was clearly off the main trend, possibly due to significant tidal interaction between the star and its close planetary companion. We therefore end up with a list of F-G-K effectively single dwarfs. V530 Per stands at the very left of the diagram, making it an important object in the study of saturated dynamo action in ZAMS stars. The average strength of its large-scale magnetic field (~177 G) is roughly similar to other targets with $\log_{10}(R_o) \lesssim -1.5$, with an average field strength of 186 G for this group of five stars. This is in contrast with stars having $\log_{10}(R_o) \gtrsim -1.7$, for which the average field strength decreases according to a power law, with $\langle B_V \rangle \propto R_o^{-1.19}$. If we plot $\langle B_V \rangle$ as a function of the rotation period instead of the Rossby number (not shown here), the power law for non saturated stars is such that $\langle B_V \rangle \propto P^{-0.9}$.

We note that the four saturated stars display a marginally decreasing field strength for decreasing Rossby numbers, which could possibly be a hint of supersaturation. This finding would be consistent with X-ray observations of other stars in the α Per cluster, where a decrease of the X-ray flux was reported for stars with the fastest rotation (Prosser et al. 1996). A tentative power law fit using the four saturated stars is consistent with $\langle B_V \rangle \propto \sqrt{R_o}$. We stress, however, that this trend is based on a small number of objects, and mostly disappears if we include M dwarfs in the same plot or if we assume that the scatter observed a $\log_{10}(R_o) \gtrsim -1.7$ (which seems to be mostly due to stellar cycles, e.g., Boro Saikia et al. 2016, 2018 for 61 Cygni A) is also valid in the saturated regime.

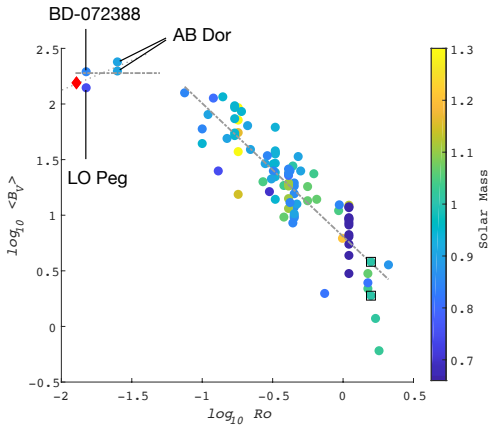

Fig. 10. Average large-scale surface magnetic field as a function of the Rossby number for solar-like stars taken from See et al. (2019). Stars are marked by filled circles, color coded according to their mass. Two measurements representative of large-scale field at solar minimum and maximum are marked with squares (and come from Vidotto et al. 2014). V530 Per is the red diamond in the upper left corner. Dashed lines show power laws for the saturated and unsaturated regime, with a slope of −1.19 for unsaturated stars and an average $\langle B_V \rangle$ of 186 G for saturated stars. The dotted line is a tentative power law with an exponent of ≈0.5 for saturated stars.

The surface field distribution of V530 Per is characterized by a prominent toroidal component, where the majority of the magnetic energy is reconstructed (Table 3). This is consistent with the trends reported by Petit et al. (2008) or See et al. (2015), showing that the toroidal field component of cool stars increases faster than the poloidal field when the Rossby number decreases, to the point where the magnetic topology can become dominated by the toroidal component.

We also observe a very different level of complexity in the toroidal and poloidal field components. The toroidal component has a relatively high fraction of its magnetic energy in low degree modes (∼40% in modes with $\ell < 4$). It is mostly axisymmetric (73% in modes with $\ell = 0$), which is consistent with other stars where the toroidal component dominates (See et al. 2015). The outcome in the magnetic map is a well defined ring of negative azimuthal field. The latitude of this ring (∼50–60°) is higher than the one of bright spots showing up in the brightness map (∼35°) and lower than the latitude of the off-centered polar spot (a polar view grouping the brightness map and the magnetic geometry can be found in Appendix A). We note that the phase of its maximal field strength is close to the phase of the main high-latitude spot (∼0.75). Similar ring-like structures have been identified in other rapid-rotating young dwarfs like AB Dor and LQ Hya (Donati et al. 2003a), EK Dra (Waite et al. 2017), or LO Peg (Folsom et al. 2016).

In contrast, the geometry of the poloidal field component is much more complex. The dipole, quadrupole and octopole contribute a small fraction of the poloidal magnetic energy (≤10% altogether), which is unusual in cool active stars (Folsom et al. 2016). The poloidal field is also highly nonaxisymmetric (15% in modes with $m = 0$). The main radial field region is an extended positive spot covering most of the dark polar spot. The strong radial field reconstructed at high latitude may contribute to generate the dark polar spot, although in other examples of young stars with a giant polar spot, such spatial correlation between the brightness and magnetic geometries is generally not reported (e.g., Donati et al. 2003a).

7.4. Prominence system

The double-peaked emission of the Hα line, consistently observed throughout our time-series, agrees well with older observations of Barnes et al. (2001). As discussed by these authors, it is likely that the rotationally modulated Hα signal is seen in emission due to the small inclination angle of V530 Per, while stars with a higher inclination feature absorption signatures from their slingshot prominences. Another example of a young star with Hα emitting prominences is LQ Lup (Donati et al. 2000). Hα transients have been recorded in, e.g., AB Dor (Collier Cameron & Robinson 1989a; Donati & Collier Cameron 1997) and Speedy Mic (Dunstone et al. 2006a,b).

The tomogram displays multiple clouds corotating with the star and distributed in a ring-like structure at a velocity roughly equal to the one expected at the corotation radius. This is in striking agreement with similar inversions obtained by Barnes et al. (2001) for V530 Per, Donati et al. (2000) for LQ Lup and Budding et al. (2006) for CC Eri. Our data suggest that the period of Hα emission could be on the order of 0.36−0.39 d, which is longer than the period of the stellar surface, even if we take into account the surface differential rotation. Although the evidence presented here is too slim to reach a definite conclusion about the reality of this longer period (given that our observations in a given night span less than one complete rotation period), it may suggest that the corotating hypothesis is only partially valid, and that prominences sufficiently far away from the surface may experience a less efficient magnetic locking, possibly due to the radial decrease of the field strength. The densest accumulation of prominences shown in the tomogram is located between phases 0.75 and 1. This observation can be linked to the extended, close field lines of Fig. 6 (right-bottom part). We note that the preferred phases for prominences are located away from the phases covered by the large polar spot. Their location is also away from the maximum strength of the radial and azimuthal magnetic field components.

The dominant part of the Hα emission can be modeled by our simple tomographic model, showing that most of the observed system is stable over about 6 h. Within each night, however, the residuals of the best model highlight nonrotational, short-term changes in the distribution of the coronal material, although we do not witness very fast blue-shifted events similar to those previously reported for AB Dor (Collier Cameron & Robinson 1989b; Donati et al. 1999). The two tomograms display noticeable differences, especially in the azimuthal distribution of the prominence clouds, although the time gap between the two observing nights makes it difficult to say much about the turnover time of the cool coronal material. We note that models of prominence lifetimes in young active stars predict a short life expectancy for stars with a mass and rotation rate similar to V530 Per (Villarreal D'Angelo et al. 2018). A denser temporal monitoring is therefore likely necessary to monitor the short term evolution of slingshot prominences around V530 Per.

Acknowledgements. This work benefited from the support of Programme National de Physique Stellaire (PNPS). T.C. would like to acknowledge financial support from the China Scholarship Council (CSC). J.F.D. and A.A.V. acknowledges funding from from the European Research Council (ERC) under the H2020 research & innovation programme (grant agreement # 740651 NewWorlds and # 817540 ASTROFLOW). This research made use of the SIMBAD database

operated at CDS, Strasbourg, France, and the NASA's Astrophysics Data System Abstract Service. Finally, we thank the referee for insightful suggestions that helped improve this study.

References

Aarnio, A. N., Matt, S. P., & Stassun, K. G. 2012, ApJ, 760, 9
Amard, L., Palacios, A., Charbonnel, C., Gallet, F., & Bouvier, J. 2016, A&A, 587, A105
Amard, L., Palacios, A., Charbonnel, C., et al. 2019, A&A, 631, A77
Augustson, K. 2017, EPJ Web Conf., 160, 02010
Balachandran, S. C., Mallik, S. V., & Lambert, D. L. 2011, MNRAS, 410, 2526
Barnes, J. R., Collier Cameron, A., James, D. J., & Steeghs, D. 2001, MNRAS, 326, 1057
Barnes, J. R., Collier Cameron, A., Donati, J. F., et al. 2005, MNRAS, 357, L1
Barnes, J. R., Jeffers, S. V., Haswell, C. A., et al. 2017, MNRAS, 471, 811
Boro Saikia, S., Jeffers, S. V., Morin, J., et al. 2016, A&A, 594, A29
Boro Saikia, S., Lueftinger, T., Jeffers, S. V., et al. 2018, A&A, 620, L11
Bouvier, J. 2013, EAS Pub. Ser., 62, 143
Brun, A. S., Strugarek, A., Varela, J., et al. 2017, ApJ, 836, 192
Budding, E., Bembrick, C., Carter, B. D., et al. 2006, Ap&SS, 304, 13
Byrne, P. B., Eibe, M. T., & Rolleston, W. R. J. 1996, A&A, 311, 651
Carroll, T. A., Strassmeier, K. G., Rice, J. B., & Künstler, A. 2012, A&A, 548, A95
Cole-Kodikara, E. M., Käpylä, M. J., Lehtinen, J. J., et al. 2019, A&A, 629, A120
Collier Cameron, A. 1999, ASP Conf. Ser., 158, 146
Collier Cameron, A., & Robinson, R. D. 1989a, MNRAS, 236, 57
Collier Cameron, A., & Robinson, R. D. 1989b, MNRAS, 238, 657
Collins George, W. I. 1965, ApJ, 142, 265
Collins George, W. I., & Harrington, J. P. 1966, ApJ, 146, 152
Cranmer, S. R. 1996, PhD thesis, Bartol Research Institute, University of Delaware, USA
Cutri, R. M., Skrutskie, M. F., van Dyk, S., et al. 2003, 2MASS All Sky Catalog of point sources.
Davenport, J. R. A. 2016, ApJ, 829, 23
Donati, J. F., & Collier Cameron, A. 1997, MNRAS, 291, 1
Donati, J. F., Brown, S. F., Semel, M., et al. 1992, A&A, 265, 682
Donati, J. F., Semel, M., Carter, B. D., Rees, D. E., & Collier Cameron, A. 1997, MNRAS, 291, 658
Donati, J. F., Collier Cameron, A., Hussain, G. A. J., & Semel, M. 1999, MNRAS, 302, 437
Donati, J. F., Mengel, M., Carter, B. D., et al. 2000, MNRAS, 316, 699
Donati, J. F., Collier Cameron, A., Semel, M., et al. 2003a, MNRAS, 345, 1145
Donati, J. F., Collier Cameron, A., & Petit, P. 2003b, MNRAS, 345, 1187
Donati, J. F., Catala, C., Landstreet, J. D., & Petit, P. 2006a, ASP Conf. Ser., 358, 362
Donati, J. F., Howarth, I. D., Jardine, M. M., et al. 2006b, MNRAS, 370, 629
Donati, J. F., Hébrard, E., Hussain, G., et al. 2014, MNRAS, 444, 3220
Donati, J. F., Moutou, C., Malo, L., et al. 2016, Nature, 534, 662
Dunstone, N. J., Barnes, J. R., Collier Cameron, A., & Jardine, M. 2006a, MNRAS, 365, 530
Dunstone, N. J., Collier Cameron, A., Barnes, J. R., & Jardine, M. 2006b, MNRAS, 373, 1308
Eibe, M. T. 1998, A&A, 337, 757
Fang, X.-S., Gu, S.-H., Cheung, S.-L., et al. 2010, Res. A&A, 10, 253
Folsom, C. P., Petit, P., Bouvier, J., et al. 2016, MNRAS, 457, 580
Folsom, C. P., Bouvier, J., Petit, P., et al. 2018a, MNRAS, 474, 4956
Folsom, C. P., Fossati, L., Wood, B. E., et al. 2018b, MNRAS, 481, 5286
Gray, D. F. 2005, The Observation and Analysis of Stellar Photospheres (Cambridge: Cambridge University Press)
Guerrero, G., Zaire, B., Smolarkiewicz, P. K., et al. 2019, ApJ, 880, 6
Gustafsson, B., Edvardsson, B., Eriksson, K., et al. 2008, A&A, 486, 951
Henden, A. A., Levine, S., Terrell, D., & Welch, D. L. 2015, AAS Meeting Abstracts, 225, 336.16
Hirayama, T., & Moriyama, F. 1979, Sol. Phys., 63, 251
Jackson, R. J., & Jeffries, R. D. 2010, MNRAS, 402, 1380
Jardine, M. 2004, A&A, 414, L5
Jardine, M., Vidotto, A. A., van Ballegooijen, A., et al. 2013, MNRAS, 431, 528
Jardine, M., Collier Cameron, A., Donati, J. F., & Hussain, G. A. J. 2020, MNRAS, 491, 4076
Järvinen, S. P., Strassmeier, K. G., Carroll, T. A., Ilyin, I., & Weber, M. 2018, A&A, 620, A162
Johnstone, C. P., & Güdel, M. 2015, A&A, 578, A129
Johnston, C. D., Hood, A. W., Cargill, P. J., & De Moortel, I. 2017, A&A, 597, A81
Kochukhov, O., Makaganiuk, V., & Piskunov, N. 2010, A&A, 524, A5
Kochukhov, O., Makaganiuk, V., Piskunov, N., et al. 2011, ApJ, 732, L19
Kővári, Z., Strassmeier, K. G., Oláh, K., et al. 2019, A&A, 624, A83
Kriskovics, L., Kővári, Z., Vida, K., et al. 2019, A&A, 627, A52
Kupka, F., Piskunov, N., Ryabchikova, T. A., Stempels, H. C., & Weiss, W. W. 1999, A&AS, 138, 119
Landi Degl'Innocenti, E. 1992, Magnetic field measurements., eds. F. Sanchez, M. Collados, & M. Vazquez, 71 (Cambridge New York: Cambridge University Press)
Landstreet, J. D. 1988, ApJ, 326, 967
Lucy, L. B. 1967, ZAp, 65, 89
Magic, Z., Chiavassa, A., Collet, R., & Asplund, M. 2015, A&A, 573, A90
Marsden, S. C., Petit, P., Jeffers, S. V., et al. 2014, MNRAS, 444, 3517
Marsh, T. R., & Horne, K. 1988, MNRAS, 235, 269
Masana, E., Jordi, C., & Ribas, I. 2006, A&A, 450, 735
Morin, J., Donati, J. F., Petit, P., et al. 2008, MNRAS, 390, 567
Noyes, R. W., Hartmann, L. W., Baliunas, S. L., Duncan, D. K., & Vaughan, A. H. 1984, ApJ, 279, 763
O'dell, M. A., & Collier Cameron, A. 1993, MNRAS, 262, 521
O'dell, M. A., Hendry, M. A., & Collier Cameron, A. 1994, MNRAS, 268, 181
Pallavicini, R., Golub, L., Rosner, R., et al. 1981, ApJ, 248, 279
Pecaut, M. J., & Mamajek, E. E. 2013, ApJS, 208, 9
Petit, P., Donati, J. F., & Collier Cameron, A. 2002, MNRAS, 334, 374
Petit, P., Donati, J. F., Wade, G. A., et al. 2004, MNRAS, 348, 1175
Petit, P., Dintrans, B., Solanki, S. K., et al. 2008, MNRAS, 388, 80
Petit, P., Louge, T., Théado, S., et al. 2014, PASP, 126, 469
Pillitteri, I., Remage Evans, N., Wolk, S. J., & Bruck Syal, M. 2013, AJ, 145, 143
Pinsonneault, M. H., Stauffer, J., Soderblom, D. R., King, J. R., & Hanson, R. B. 1998, ApJ, 504, 170
Prosser, C. F. 1992, AJ, 103, 488
Prosser, C. F., Randich, S., Stauffer, J. R., Schmitt, J. H. M. M., & Simon, T. 1996, AJ, 112, 1570
Reiners, A. 2012, Liv. Rev. Sol. Phys., 9, 1
Rice, J. B., & Strassmeier, K. G. 2000, A&AS, 147, 151
Rice, J. B., & Strassmeier, K. G. 2001, A&A, 377, 264
Roettenbacher, R. M., Monnier, J. D., Korhonen, H., et al. 2016, Nature, 533, 217
Rosén, L., Kochukhov, O., Hackman, T., & Lehtinen, J. 2016, A&A, 593, A35
Ryabchikova, T. A., Piskunov, N. E., Kupka, F., & Weiss, W. W. 1997, Balt. Astron., 6, 244
Ryabchikova, T., Piskunov, N., Kurucz, R. L., et al. 2015, Phys. Scr., 90, 054005
Schrijver, C. J., De Rosa, M. L., & Title, A. M. 2003, ApJ, 590, 493
Schuessler, M., Caligari, P., Ferriz-Mas, A., Solanki, S. K., & Stix, M. 1996, A&A, 314, 503
See, V., Jardine, M., Vidotto, A. A., et al. 2015, MNRAS, 453, 4301
See, V., Matt, S. P., Folsom, C. P., et al. 2019, ApJ, 876, 118
Semel, M., Donati, J. F., & Rees, D. E. 1993, A&A, 278, 231
Skelly, M. B., Unruh, Y. C., Collier Cameron, A., et al. 2008, MNRAS, 385, 708
Skelly, M. B., Unruh, Y. C., Barnes, J. R., et al. 2009, MNRAS, 399, 1829
Skilling, J., & Bryan, R. K. 1984, MNRAS, 211, 111
Stauffer, J. R., Barrado y Navascués, D., Bouvier, J., et al. 1999, ApJ, 527, 219
Steeghs, D. 2003, MNRAS, 344, 448
Steeghs, D., Horne, K., Marsh, T. R., & Donati, J. F. 1996, MNRAS, 281, 626
Strassmeier, K. G., & Rice, J. B. 1998, A&A, 330, 685
Strassmeier, K. G., Pichler, T., Weber, M., & Granzer, T. 2003, A&A, 411, 595
Tassoul, J.-L. 1978, Theory of Rotating Stars (Princeton: Princeton University Press)
Tatebe, K., Chandler, A. A., Wishnow, E. H., Hale, D. D. S., & Townes, C. H. 2007, ApJ, 670, L21
Ud-Doula, A., Owocki, S. P., & Townsend, R. H. D. 2008, MNRAS, 385, 97
van Belle, G. T. 2012, A&ARv, 20, 51
van Leeuwen, F. 2009, A&A, 497, 209
Vidotto, A. A. 2016, MNRAS, 459, 1533
Vidotto, A. A., Gregory, S. G., Jardine, M., et al. 2014, MNRAS, 441, 2361
Villarreal D'Angelo, C., Jardine, M., & See, V. 2018, MNRAS, 475, L25
Vogt, S. S., Penrod, G. D., & Hatzes, A. P. 1987, ApJ, 321, 496
Wade, G. A., Donati, J. F., & Landstreet, J. D. 2000, New Astron., 5, 455
Wade, G. A., Bagnulo, S., Kochukhov, O., et al. 2001, A&A, 374, 265
Waite, I. A., Marsden, S. C., Carter, B. D., et al. 2017, MNRAS, 465, 2076
Walkowicz, L. M., & Basri, G. S. 2013, MNRAS, 436, 1883
Weber, E. J., & Davis, L. J. 1967, ApJ, 148, 217
Wright, N. J., Drake, J. J., Mamajek, E. E., & Henry, G. W. 2011, ApJ, 743, 48
Yen, S. X., Reffert, S., Schilbach, E., et al. 2018, A&A, 615, A12
Yu, L., Donati, J. F., Hébrard, E. M., et al. 2017, MNRAS, 467, 1342
Yu, L., Donati, J. F., Grankin, K., et al. 2019, MNRAS, 489, 5556
Zacharias, N., Finch, C. T., Girard, T. M., et al. 2013, AJ, 145, 44

Appendix A: Polar view of the brightness map and magnetic geometry

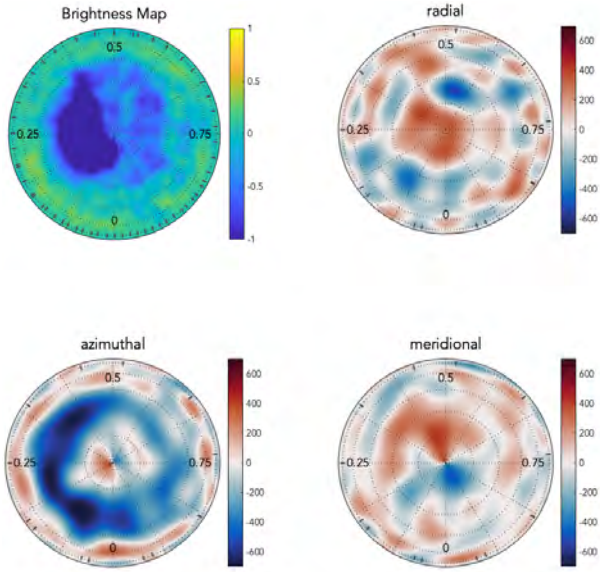

Fig. A.1. Orthographic polar projection of V530 Per, with the same components and color scale as Figs. 4 and 5. The latitudinal dash lines represent every 15° from 0° to 90°. Radial ticks close to the equator show the observed phases.

Appendix B: Stokes *I* LSD profiles

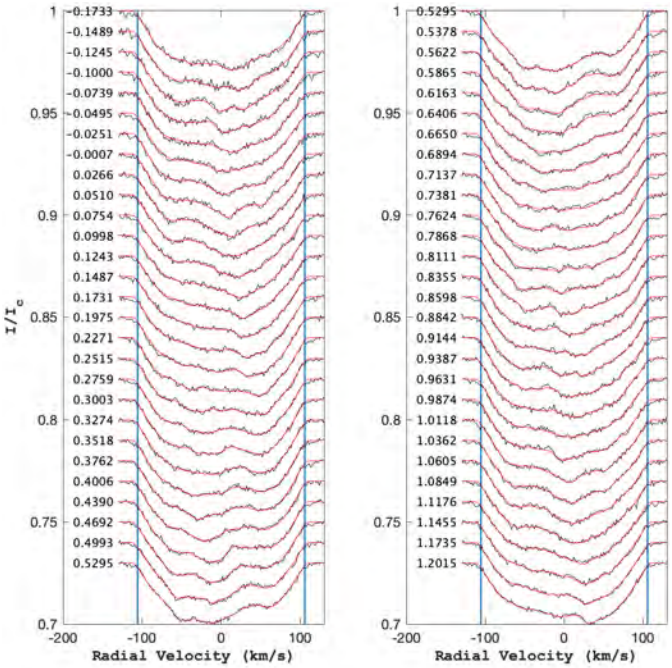

Fig. B.1. Observed (black) and modeled (red) Stokes *I* profiles, in a display similar to Fig. 2. Data from 29 Nov. 06 (resp. 05 Dec. 06) is plotted on the left (resp. right). Successive profiles are vertically shifted for display clarity. Rotational phases are indicated on the left of the profiles. Blue vertical lines show the $\pm v \sin i$ limit.

Appendix C: Spot free line profiles

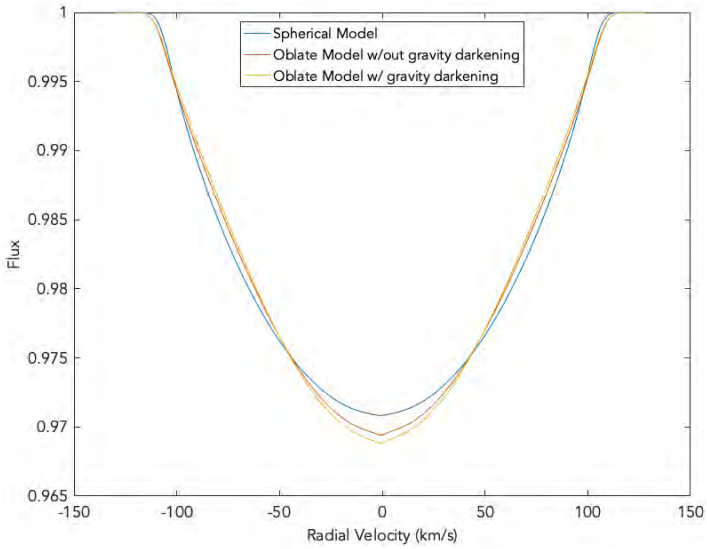

Fig. C.1. Synthetic, LSD pseudo-line profiles obtained for an unspotted stellar surface assuming a spherical stellar shape (blue), a Roche model (red) and a Roche model with gravity darkening (orange). All other input parameters of ZDI are taken equal in the three models.

Appendix D: DI optimization of the inclination angle

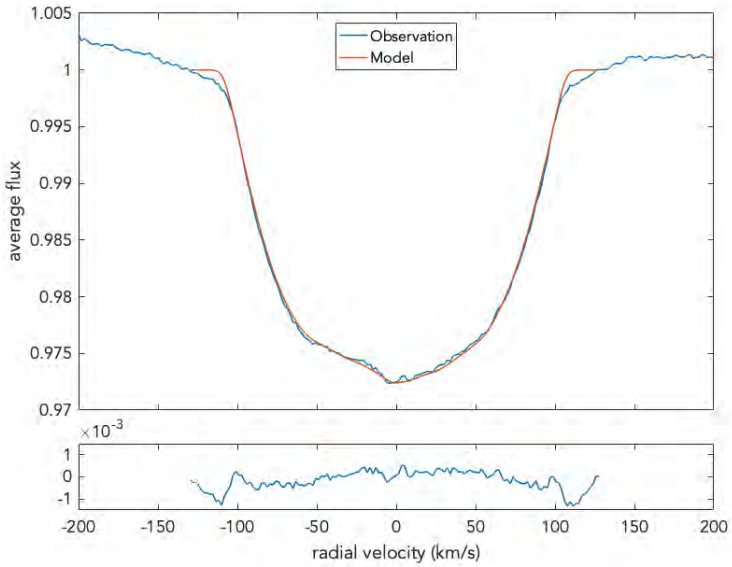

Fig. D.1. Phase-averaged LSD profile for the V530 Per observations (*top panel*, blue) and our DI model (*top panel*, red), as well as the residuals (*bottom panel*).

C.2 SPIE proceeding: Cang et.al 2020b

PROCEEDINGS OF SPIE

SPIEDigitalLibrary.org/conference-proceedings-of-spie

The MARSU CubeSat: monitoring the activity and planetary transits of low-mass stars and young solar analogues

Cang, Tianqi, Petit, Pascal, Donati, Jean-François, Kouach, Driss, Parès, Laurent

Tianqi Cang, Pascal Petit, Jean-François Donati, Driss Kouach, Laurent Parès, "The MARSU CubeSat: monitoring the activity and planetary transits of low-mass stars and young solar analogues," Proc. SPIE 11443, Space Telescopes and Instrumentation 2020: Optical, Infrared, and Millimeter Wave, 1144319 (13 December 2020); doi: 10.1117/12.2560343

SPIE.

Event: SPIE Astronomical Telescopes + Instrumentation, 2020, Online Only

The MARSU CubeSat: monitoring the activity and planetary transits of low-mass stars and young solar analogues

Tianqi Cang[a,*], Pascal Petit[a], Jean-François Donati[a], Driss Kouach[b], and Laurent Parès[a]

[a]Institut de Recherche en Astrophysique et Planétologie, OMP, Université de Toulouse, CNRS, CNES, 14 avenue Edouard Belin, 31400 Toulouse, France
[b]Observatoire Midi-Pyrénées, 14 avenue Edouard Belin, 31400 Toulouse, France

ABSTRACT

MARSU is a CubeSat mission designed to monitor transits of planetary systems around nearby M-dwarfs and young Sun-like stars, and characterize the magnetic activity of the host stars. As a dedicated infrared space photometer, MARSU is expected to be able to detect Earth-like planets in the habitable zone of M dwarfs. It will achieve continuous (duty cycle in excess of 90%) photometric monitoring in the YJH bands (1 – 1.7 μm) for stars up to an H magnitude of 11, at a precision better than one mmag over continuous periods of up to 3 months. A heliosynchronous orbit is selected to ensure nearly continuous monitoring of stellar targets in the anti-solar direction. MARSU will include a photometric telescope occupying 1x1x3U in a 6U platform. The payload features an 8.5cm dioptric telescope with an athermal optical system and a Short-Wave InfraRed (SWIR) type detector. End-to-end simulations have been carried out and confirm that the quality of photometric data will be consistent with the primary science goals and that the subsequent technical constraints (e.g., pointing stability) are consistent with the expected performance of a 6U CubeSat. MARSU will work in parallel with SPIRou and SPIP, which are twin ground-based infrared spectropolarimeters & velocimeters operated as new generation instruments for the Canada-France-Hawaii Telescope (CFHT, Maunakea Observatory, Hawaii) and Télescope Bernard Lyot (TBL, Pic du Midi, France) respectively. The multi-source data will be analyzed together to optimize the activity filtering and exoplanet characterization (mass from the ground, radius from space).

Keywords: CubeSat; infrared photometry; exoplanets; transits; stellar activity

1. INTRODUCTION

Photometric monitoring is a widely used method for characterizing stars with variable brightness, such as active stars, young accreting stars, and stars with transiting exoplanets. Space telescopes are ideal tools to carry out continuous observations of variable stars since they can avoid some critical drawbacks of ground-based observations, like day/night alternation and atmospheric variations (e.g., variable cloud cover, turbulence). Currently, several photometric space observatories are dedicated to the detection of exoplanetary transits and to stellar physics (e.g., TESS,[1] CHEOPS[2]). However, large missions have very limited flexibility (if any) in their observing program, while a number of science cases would benefit from costumed observations of specific targets. Tiny space telescopes based on the CubeSat concept, which consists in stacking standard cubic units (1U) with 10 cm

*Tianqi Cang, tcang@irap.omp.eu

Space Telescopes and Instrumentation 2020: Optical, Infrared, and Millimeter Wave, edited by Makenzie Lystrup, Marshall D. Perrin, Proc. of SPIE Vol. 11443, 1144319 · © 2020 SPIE
CCC code: 0277-786X/20/$21 · doi: 10.1117/12.2560343

Table 1. Scientific goal of MARSU

Requirement	Value
Stellar magnitude	Up to $\sim$ 11 H magnitude
Spectral domain	1-1.7 μm
Photometric precision	1 mmag rms
Exposure time	Up to 10 minutes
Monitoring period	Up to 3 months
Duty cycle	$\geq$ 90%

of width, offer a flexible and low cost opportunity for the monitoring of bright targets, as demonstrated by the ASTERIA[3] proof of concept in the optical domain.

We propose to build a near-infrared (nIR) CubeSat-type space photometer named MARSU (for Millimag Astrophotometry of Red SPIRou/SPIP stars as a University space probe), working in parallel with SPIRou[4] and SPIP, two twin ground-based nIR spectropolarimeters & velocimeters for the Canada-France-Hawaii Telescope (CFHT, Maunakea observatory, Hawaii) and Télescope Bernard Lyot (TBL, Observatoire du Pic du Midi, France), respectively. SPIRou is in operation at CFHT since 2018, whereas the construction of SPIP is under way, for a commissioning on the telescope in 2021. MARSU will mainly come in support to the SPIRou Legacy Survey (SLS), a large program aimed at (i) searching for Earth-like planets in the habitable zone of low-mass stars, and (ii) studying the formation of low-mass stars and planets in the presence of magnetic fields. MARSU aims at performing nIR photometry of SLS targets simultaneously with SPIRou observations, in order to (i) provide a continuous monitoring of the magnetic activity of target stars, with the objective to improve the filtering of the activity noise in radial velocity time series and (ii) search for possible transits of newly discovered SLS planets, or detect new occurrences of single transits reported by other photometric facilities.

This paper introduces MARSU, including its science objective (Sect. 2), the payload and platform (Sect. 3), numerical simulations of MARSU observations (Sect. 4), and the perspectives of the mission (Sect. 5)

2. SCIENCE GOALS

As SPIRou and SPIP, the MARSU CubeSat will observe at near-infrared (nIR) wavelengths, where the target stars (nearby M dwarfs and young forming stars) emit most of their light. Photometric time-series of observations of MARSU targets will record temporal changes caused by stellar surface activity and flares, by transiting events, or by accretion events over time scales of a few minutes to a few weeks (see Fig. 1 for an illustration based on

TESS observations of the young, active, low mass star AU Mic[5]). Doppler shifts measured by SPIRou and SPIP can be polluted by stellar magnetic activity, the contribution of which can dominate the velocimetric signatures of exoplanets. Light curves from the MARSU CubeSat will improve the reliability of exoplanet detection and characterization by recording the photometric imprint of stellar activity, leading to a more efficient filtering of this polluting effect. Moreover, the MARSU CubeSat will search for potential transits of exoplanets detected from the ground, since combining spectroscopy and photometry enables one to measure both the mass and radius of exoplanets, thus constraining their bulk densities and thereby providing information on their internal structure for distinguishing between, e.g., telluric planets and gaseous ones.

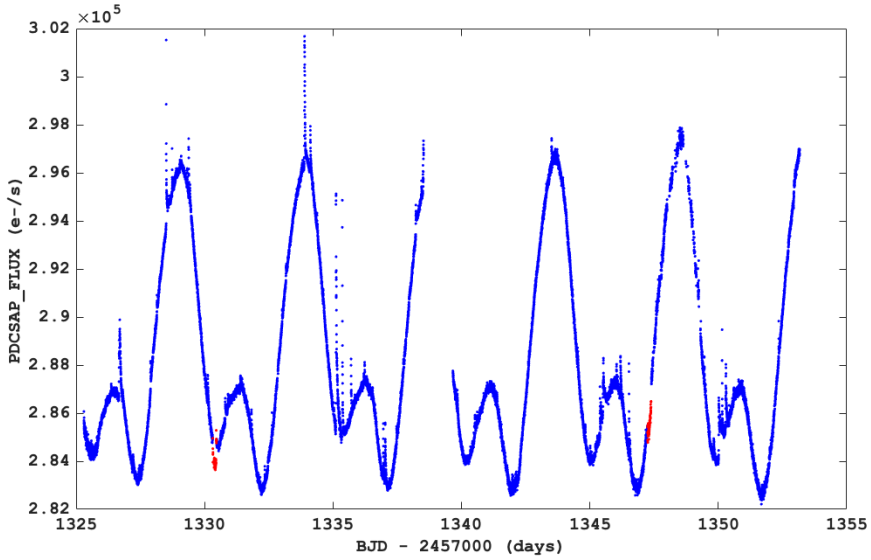

Figure 1. TESS light curve of the young, low-mass star AU Mic (light flux as a function of the barycentric Julian date). Transits of the exoplanet AU Mic b are indicated in red. Their signatures are vastly dominated by activity phenomena linked to stellar spots (wave-like pattern) and flares (positive spikes).

In order to address these science questions, the goal of the MARSU CubeSat is to achieve continuous (duty cycle in excess of 90%) photometric monitoring in the YJH bands ($1 - 1.7\ \mu m$) for stars up to an H magnitude of ~ 11, at a precision better than 1 mmag for up to 10 minutes exposure times, over continuous periods of up

to 3 months and simultaneously with SPIRou and SPIP observations, as summarized in Table. 1. Continuous observations in the anti-solar direction impose to use of a heliosynchronous orbit. An optional strategy is to alternate between up to three fields of view on a timescale of $\sim$ 1 hr in order to maximize the probability of detecting planetary transits.

3. PAYLOAD AND PLATFORM

3.1 Payload

The main structure of the payload is a refracting telescope involving five lenses, with a diameter of 85 mm for the entrance pupil (Fig.2). This design leads to a focal length of 150 mm (F/1.7645) and a total length of 200 mm from the entrance lens to the detector plane. Three lenses are stacked together in a same barrel at the entrance of the refractor, followed by two more lenses (also stacked together) in front of the detector. Aluminum 6061 spacers are inserted between the lenses to create an athermal system, so that temperature variations up to 10 K do not produce any significant focus change. For any point source, the full width at half maximum (FWHM) of the point spread function (PSF) is equal to 25 μm, translating into slightly less than 2 pixels on the detector. The field of view is about 5°, translating into a 13.17×13.17 mm area on the focal (43.9 μm per arcmin). With optimized anti-reflection coatings (average reflectivity of 1% per surface), the overall throughput of the camera is in excess of 80% over the whole spectral range.

A shortwave infrared (SWIR) detector (e.g., Raptor VIS-SWIR OWL 640 II) will be mounted in the payload. This 640 $\times$ 512 detector features a quantum efficiency larger than 70% over the selected spectral domain. The pixel size is 15 μm $\times$ 15 μm, with an overall area of 9.6 mm $\times$ 7.68 mm. SWIR detectors reach very short exposure times ($\geq 0.02s$), with very short readout time. The readout noise is expected to stay below 47 e^-, with a gain of 1 e^-/ADU.

3.2 Platform

A single payload shown in Fig.5 has a layout of 1 $\times$ 3 U with an estimated mass of $\sim$ 2.6 kg. The maximum diameter at the entrance of the optical system will be less than 96 mm ($\leq$ 1U). The total length of the payload is about 305 mm ($\sim$ 3U), consisting of the barrel (190 mm), camera (50 mm), and external baffle ($\geq$ 65 mm).

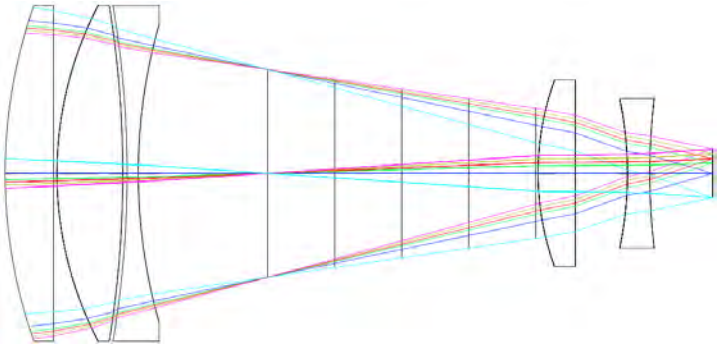

Figure 2. Optical design of the telescope.

The major part of the external baffle is included in the braced structures of the CubeSat (Fig. 4). The purpose of this first baffle is to block any light reaching the telescope with an angle $\geq 70°$ (note that a deployable baffle may also be considered for a more efficient rejection of contaminating light from the Earth, Moon or Sun). The internal baffles include four knife rings to get rid of most internal reflections, and are coated to absorb any rogue reflection. The structure of the baffles is illustrated in Fig. 3.

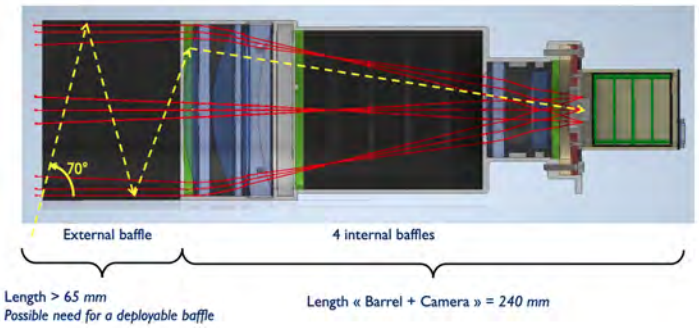

Figure 3. External and internal baffles.

A 3U payload can be mounted in a $2 \times 3 = 6$U platform as shown in Fig. 4. The remaining 3U volume will be occupied by the star tracker and control system.

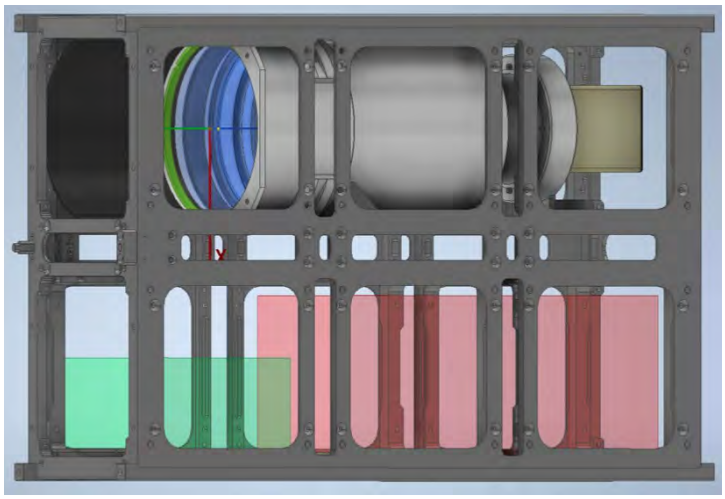

Figure 4. Single payload (= 3U) inserted in a 6U platform. The green and red volumes on the bottom are proposed to be the location of star tracker (green) and control system (red), respectively.

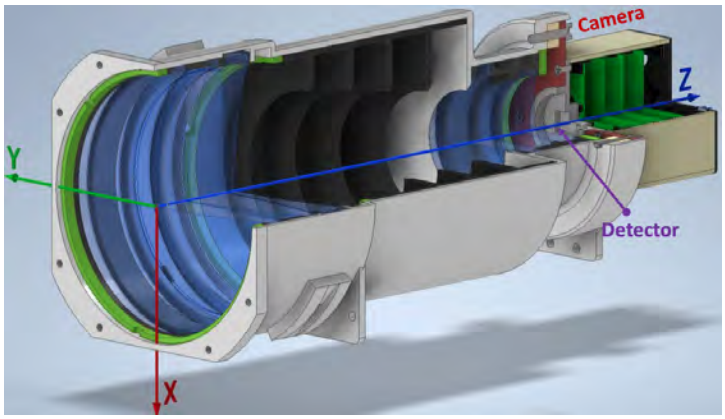

Figure 5. Mechanical design of the payload.

4. NUMERICAL SIMULATIONS OF MARSU OBSERVATIONS

4.1 Basic principle of the simulator

We developed a numerical simulator of MARSU to model data acquired by the CubeSat. This tool mainly includes the simulation of realistic light flux of typical targets (including stellar activity or planetary transits),

Table 2. Fundamental parameters of stars and planets chosen for our simulations.

Host star	Trappist-1	V1298 Tau	Planet	Trappist-1e[9]	V1298 Tau c[10]
Radius ($R_\odot$)	0.121[11]	1.345[10]	Semi-major axis (AU)	0.029	0.0825
$T_{\rm eff}$ (K)	2516[11]	4970[12]	Orbital period (d)	6.099043	8.24958
Distance (pc)	12.14[11]	108.5[13]	Inclination (deg)	89.86	88.49
H mag	10.718[8]	8.191[8]	Radius ($R_\oplus$)	0.91	5.5932

the attitude jitter of the satellite, and the extraction of a light curve. The main objective of this simulator is to ensure that the technical limits of MARSU remain consistent with the science objective of the mission. We especially focus on various sources of noise arising at different steps of the acquisition chain.

4.1.1 Stellar nIR flux

The lightcurve from stellar targets is first estimated by the black body emission calculated using the effective temperature, the radius, and the distance of the simulated stars. The flux is then integrated over the selected wavelength range ($1-1.7$ μm). Stellar activity and exoplanet transits are optionally added to the model. Realistic stellar activity in the nIR is generated using a model developed for Trappist-1.[6] Planetary transits are generated by the `batman` transit modeling code.[7]

Two typical targets were selected for the simulation: Trappist-1 and V1298 Tau. Both are surrounded by a multiple exoplanetary system, from which we choose to simulate one planet only. Trappist-1 is a relatively faint, very low-mass star observed with SPIRou, while V1298 Tau is a brighter target,[8] typical of young stars also observed in nIR velocimetry. Detailed information about the two stars is listed in Table 2.

4.1.2 Attitude of the satellite

The attitude control of the CubeSat is not perfect, which leads to an apparent motion of targets in the field of view. We assume here that the star tracker checks the pointing direction of the satellite every $\tau_{\rm tracker} = 30$ seconds, and adjusts the rotation of the reaction wheels to redirect the line of sight towards the default center. The reaction wheels are assumed to drive the satellite with a fixed angular velocity of $\nu = \sqrt{\nu_\alpha^2 + \nu_\delta^2} = 0.3$ arcsec/s, where α (right ascension) and δ (declination) are the axis of astronomical coordinates. We also include a small random error in the angle adopted for each re-direction, leading to a new correction at the next measurement of the star tracker. We finally assume that we can neglect any rotation of the field of view. An illustration of the simulated angular shifts over 10000 seconds is shown in Fig. 6. As a consequence of the changes in the attitude,

we assume that our target appears at a new position on the detector for each successive image. We also assume that the target does not move during the integration time, which was checked to be a reasonable assumption given the typical adopted integration times and PSF width.

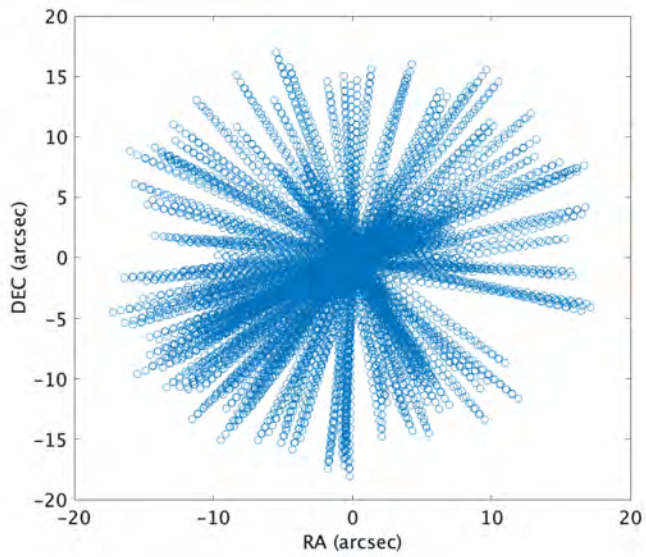

Figure 6. Apparent angular shifts of the target over 10000 seconds.

4.1.3 Image generation

The global transmission of MARSU (including the optical system and detector) is taken equal to $\eta = 0.65$. We model the PSF as a 2D Gaussian model where the FWHM is, by default, assumed to be the same along the two axis (although an elongated PSF is also left as an option). In agreement with Sect. 3.2, we took an FWHM equal to 2 pixels, translating into a sky resolution of 0.005°/pixel. In addition to the photon noise and readout noises, several additional sources of noise are implemented in our simulation tool and described below.

For every pixels, the quantum efficiency (QE) inside the pixel is assumed to be non-uniform, as typically observed in actual detectors. As a rough model of this affect, we assume that there is no response if a photon is captured in the area close to the edge of the pixel, leaving 10% of the pixel area unsensitive to incoming light.

Since the satellite cannot focus on the same field perfectly, the subpixel quantum efficiency (sQE hereafter) will introduce extra noise to the photometric measurement. In our simulation, each pixel is divided in a grid of 10 × 10 subpixels. The subpixels on the edge have a null sQE, while others have a constant, scaled sQE that follows:

$$\mathrm{QE} = \frac{1}{n} \sum_{i=1}^{n} \mathrm{sQE}_i \tag{1}$$

so that the global quantum efficiency of the pixel is kept equal to the value provided by the constructor.

We assumed that the gain is constant for each pixel, but that there is also a small gain fluctuation between different pixels. This pixel-to-pixel gain fluctuation (PGF hereafter) is modeled with a Gaussian distribution, using an FWHM of 1%. We also simulate dead pixels, which are assumed to have a null response. If a dead pixel is overlaping with the PSF, it can generate a bias in the extracted light flux. To mitigate this effect, we chose to extract the light curve through PSF fitting (assuming a 2D Gaussian for the PSF shape), instead of aperture photometry.

We finally neglected other possible undesirable phenomena like dark currents or remanence. The parameters adopted in most of our simulations are listed in Table. 3.

4.2 Results of simulations

We ran a series of simulations to test the impact of the various sources of noise on the final light curves. We first simulated each noise independently, then tested some typical combinations of them. In some simulations, we include a second, active star with the same fundamental parameters as Trappist-1 and an activity-induced photometric amplitude of 1% (see Fig. 7). We used Trappist-1 as the target for most tests because it has an H magnitude close to the limit specified for the mission. An exposure time of 120s is applied for the tests, ensuring that the photon noise dominates over the readout noise. The results are summarized in Table. 4, where the blue cells mark the features included in the simulation. In the same table, we indicate the resulting noise (1σ level) in the extracted light curve, and the corresponding S/N.

The tests above show that photon noise dominates the S/N of observations in most situations, except when a dead pixel or a nearby variable star are significantly polluting the signal. If nearby stars can be a problem in the

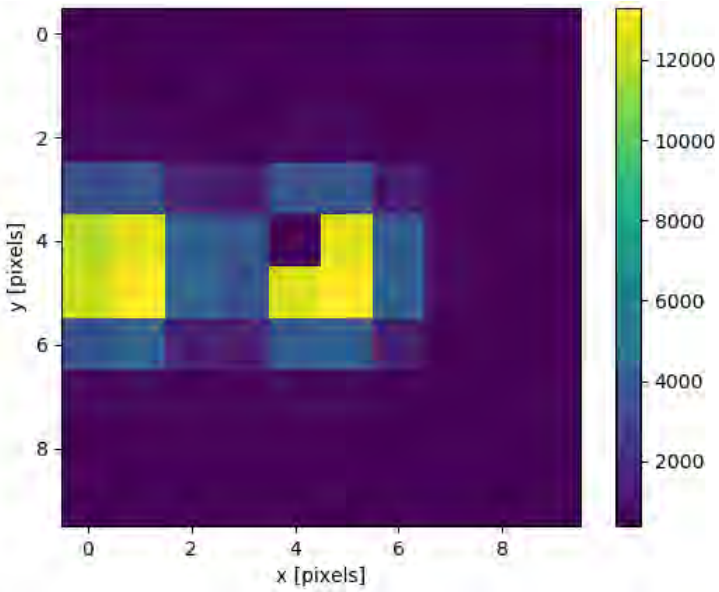

Figure 7. Exemple image of a fraction of the whole detector, with a dead pixel located at coordinates (4, 4) and overlaping with the PSF of the main target. A nearby star is also simulated, with a PSF overlap between the two stellar objects.

Table 3. Basic parameters of the simulator.

Parameter	Value
Transmission	0.65
Sky resolution	0.005 deg/pixel
Readout noise	47 e^-
Gain	1 ± 0.01 e^-/ADU
QE	0.8
FWHM of PSF	2 pixels
Exposure time	120 s
ν_{tracker}	0.3 arcsec/s
τ_{tracker}	30 s
phot. fluct. of nearby star	1%

Table 4. Summary of the simulations. Blue cells indicate the source of noise activated in a given run. The numerical values without brackets show the 1σ uncertainty of the extracted light curve (counted in magnitude), and the values between brackets are the corresponding S/N.

Number	Photon noise	Readout noise	PGF	sQE	Dead pixel	Nearby star
1	0.0091 [274]					
2		0.0066 [381]				
3			0.003 [842]			
4				0.00015 [16345]		
5					0.22 [11]	
6						0.013 [195]
7	0.011 [225]					
8	0.012 [214]					
9	0.012 [214]					
10	0.22 [11]					
11	0.33 [7]					
12	0.04 [60]					

specific case of a crowded field (e.g. taken in an open cluster), the contamination by a dead pixel can in principle be avoided by adjusting the attitude of the satellite. We, therefore, decided to run full simulations including transit simulations of Trappis-1 e or V1298 Tau c, without any dead-pixel. The light curve was simulated over a 30 days observing run. After folding the lightcurve with the orbital phase, we obtained the transit lightcurves of these two systems in Fig. 8. The outcome of this numerical simulation, featuring clear detections of the transits, demonstrates that the most challenging science objectives of the MARSU CubeSat are accessible in a CubeSat configuration with a single payload.

5. CONCLUSIONS AND PROSPECT

Our end-to-end numerical simulations of the MARSU CubeSat provide a basic test for the instrument performance and shows the feasibility of observing an Earth-like exoplanet in the habitable zone of low mass stars. To further investigate the satellite performance, we have started to build an optical bench in order to (a) explore an alternate strategy to simulate the performance of MARSU and (b) help refining our numerical simulations by adopting more realistic input parameters. Following the feasibility study, a comprehensive mission study will be engaged, aiming at a tentative launch in 2023.

The MARSU CubeSat is based on a simple and standard design, which could serve as a template for a fleet of CubeSats dedicated to astrophotometry, using identical payloads or optimized for different wavelength domains. After completion of the study phase, we therefore plan to set up an international science consortium with the

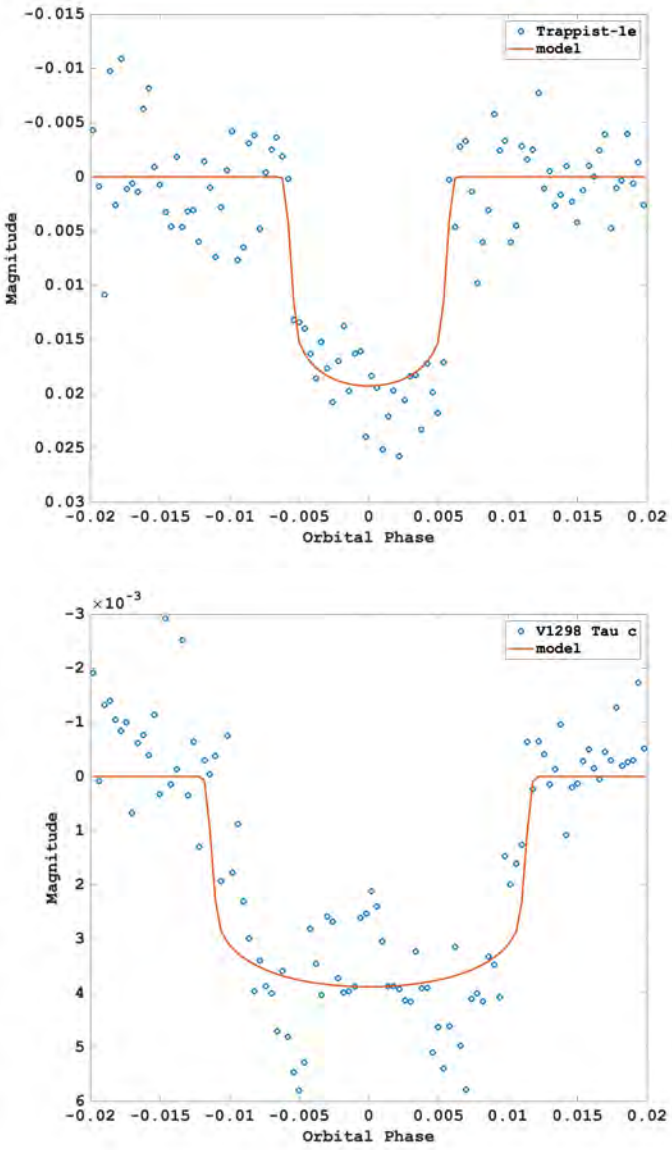

Figure 8. Simulated lightcurve of Trappist-1e (Top) and V1298 Tau c (Bottom) in 30 days with bins including $\sim$ 10 individual measurements, and folded according to the orbital period, including 4 and 3 transits, respectively. In both cases, the exposure time is set to 120s.

ultimate goal of deploying a small fleet of probes to further optimize the science feedback of the project.

ACKNOWLEDGMENTS

This work benefited from the financial support of CNES and IRAP/OMP. TC would like to acknowledge financial support from the China Scholarship Council (CSC). JFD acknowledges funding from from the European Research Council (ERC) under the H2020 research & innovation programme (grant agreement # 740651 NewWorlds). This research made use of the SIMBAD database operated at CDS, Strasbourg, France, and the NASA's Astrophysics Data System Abstract Service.

REFERENCES

[1] Ricker, G. R., Winn, J. N., Vanderspek, R., Latham, D. W., Bakos, G. Á., Bean, J. L., Berta-Thompson, Z. K., Brown, T. M., Buchhave, L., Butler, N. R., Butler, R. P., Chaplin, W. J., Charbonneau, D., Christensen-Dalsgaard, J., Clampin, M., Deming, D., Doty, J., De Lee, N., Dressing, C., Dunham, E. W., Endl, M., Fressin, F., Ge, J., Henning, T., Holman, M. J., Howard, A. W., Ida, S., Jenkins, J., Jernigan, G., Johnson, J. A., Kaltenegger, L., Kawai, N., Kjeldsen, H., Laughlin, G., Levine, A. M., Lin, D., Lissauer, J. J., MacQueen, P., Marcy, G., McCullough, P. R., Morton, T. D., Narita, N., Paegert, M., Palle, E., Pepe, F., Pepper, J., Quirrenbach, A., Rinehart, S. A., Sasselov, D., Sato, B., Seager, S., Sozzetti, A., Stassun, K. G., Sullivan, P., Szentgyorgyi, A., Torres, G., Udry, S., and Villasenor, J., "Transiting Exoplanet Survey Satellite (TESS)," in [*Space Telescopes and Instrumentation 2014: Optical, Infrared, and Millimeter Wave*], *Society of Photo-Optical Instrumentation Engineers (SPIE) Conference Series* **9143**, 914320 (Aug. 2014).

[2] Benz, W., Broeg, C., Fortier, A., Rand o, N., Beck, T., Beck, M., Queloz, D., Ehrenreich, D., Maxted, P., Isaak, K., Billot, N., Alibert, Y., Alonso, R., António, C., Asquier, J., Bandy, T., Bárczy, T., Barrado, D., Barros, S., Baumjohann, W., Bekkelien, A., Bergomi, M., Biondi, F., Bonfils, X., Borsato, L., Brand eker, A., Busch, M.-D., Cabrera, J., Cessa, V., Charnoz, S., Chazelas, B., Collier Cameron, A., Corral Van Damme, C., Cortes, D., Davies, M., Deleuil, M., Deline, A., Delrez, L., Demangeon, O., Demory, B.-O., Erikson, A., Farinato, J., Fossati, L., Fridlund, M., Futyan, D., Gand olfi, D., Garcia Munoz, A., Gillon, M., Guterman, P., Gutierrez, A., Hasiba, J., Heng, K., Hernandez, E., Hoyer, S., Kiss, L., Kovacs, Z., Kuntzer,

T., Laskar, J., Lecavelier des Etangs, A., Lendl, M., López, A., Lora, I., Lovis, C., Lüftinger, T., Magrin, D., Malvasio, L., Marafatto, L., Michaelis, H., de Miguel, D., Modrego, D., Munari, M., Nascimbeni, V., Olofsson, G., Ottacher, H., Ottensamer, R., Pagano, I., Palacios, R., Pallé, E., Peter, G., Piazza, D., Piotto, G., Pizarro, A., Pollaco, D., Ragazzoni, R., Ratti, F., Rauer, H., Ribas, I., Rieder, M., Rohlfs, R., Safa, F., Salatti, M., Santos, N., Scandariato, G., Ségransan, D., Simon, A., Smith, A., Sordet, M., Sousa, S., Steller, M., Szabó, G., Szoke, J., Thomas, N., Tschentscher, M., Udry, S., Van Grootel, V., Viotto, V., Walter, I., Walton, N., Wildi, F., and Wolter, D., "The CHEOPS mission," *arXiv e-prints* , arXiv:2009.11633 (Sept. 2020).

[3] Knapp, M., Seager, S., Demory, B.-O., Krishnamurthy, A., Smith, M. W., Pong, C. M., Bailey, V. P., Donner, A., Pasquale, P. D., Campuzano, B., Smith, C., Luu, J., Babuscia, A., Bocchino, Robert L., J., Loveland, J., Colley, C., Gedenk, T., Kulkarni, T., Hughes, K., White, M., Krajewski, J., and Fesq, L., "Demonstrating High-precision Photometry with a CubeSat: ASTERIA Observations of 55 Cancri e," *AJ* **160**, 23 (July 2020).

[4] Donati, J. F., Kouach, D., Moutou, C., Doyon, R., Delfosse, X., Artigau, E., Baratchart, S., Lacombe, M., Barrick, G., Hébrard, G., Bouchy, F., Saddlemyer, L., Parés, L., Rabou, P., Micheau, Y., Dolon, F., Reshetov, V., Challita, Z., Carmona, A., Striebig, N., Thibault, S., Martioli, E., Cook, N., Fouqué, P., Vermeulen, T., Wang, S. Y., Arnold, L., Pepe, F., Boisse, I., Figueira, P., Bouvier, J., Ray, T. P., Feugeade, C., Morin, J., Alencar, S., Hobson, M., Castilho, B., Udry, S., Santos, N. C., Hernandez, O., Benedict, T., Vallée, P., Gallou, G., Dupieux, M., Larrieu, M., Perruchot, S., Sottile, R., Moreau, F., Usher, C., Baril, M., Wildi, F., Chazelas, B., Malo, L., Bonfils, X., Loop, D., Kerley, D., Wevers, I., Dunn, J., Pazder, J., Macdonald, S., Dubois, B., Carrié, E., Valentin, H., Henault, F., Yan, C. H., and Steinmetz, T., "SPIRou: nIR velocimetry & spectropolarimetry at the CFHT," *MNRAS* (Aug. 2020).

[5] Plavchan, P., Barclay, T., Gagné, J., Gao, P., Cale, B., Matzko, W., Dragomir, D., Quinn, S., Feliz, D., Stassun, K., Crossfield, I. J. M., Berardo, D. A., Latham, D. W., Tieu, B., Anglada-Escudé, G., Ricker, G., Vanderspek, R., Seager, S., Winn, J. N., Jenkins, J. M., Rinehart, S., Krishnamurthy, A., Dynes, S., Doty, J., Adams, F., Afanasev, D. A., Beichman, C., Bottom, M., Bowler, B. P., Brinkworth, C., Brown,

C. J., Cancino, A., Ciardi, D. R., Clampin, M., Clark, J. T., Collins, K., Davison, C., Foreman-Mackey, D., Furlan, E., Gaidos, E. J., Geneser, C., Giddens, F., Gilbert, E., Hall, R., Hellier, C., Henry, T., Horner, J., Howard, A. W., Huang, C., Huber, J., Kane, S. R., Kenworthy, M., Kielkopf, J., Kipping, D., Klenke, C., Kruse, E., Latouf, N., Lowrance, P., Mennesson, B., Mengel, M., Mills, S. M., Morton, T., Narita, N., Newton, E., Nishimoto, A., Okumura, J., Palle, E., Pepper, J., Quintana, E. V., Roberge, A., Roccatagliata, V., Schlieder, J. E., Tanner, A., Teske, J., Tinney, C. G., Vanderburg, A., von Braun, K., Walp, B., Wang, J., Wang, S. X., Weigand , D., White, R., Wittenmyer, R. A., Wright, D. J., Youngblood, A., Zhang, H., and Zilberman, P., "A planet within the debris disk around the pre-main-sequence star AU Microscopii," *Nature* **582**, 497–500 (June 2020).

[6] Klein, B. and Donati, J. F., "Simulating radial velocity observations of trappist-1 with SPIRou," *MNRAS* **488**, 5114–5126 (Oct. 2019).

[7] Kreidberg, L., "batman: BAsic Transit Model cAlculatioN in Python," *PASP* **127**, 1161 (Nov. 2015).

[8] Cutri, R. M., Skrutskie, M. F., van Dyk, S., Beichman, C. A., Carpenter, J. M., Chester, T., Cambresy, L., Evans, T., Fowler, J., Gizis, J., Howard, E., Huchra, J., Jarrett, T., Kopan, E. L., Kirkpatrick, J. D., Light, R. M., Marsh, K. A., McCallon, H., Schneider, S., Stiening, R., Sykes, M., Weinberg, M., Wheaton, W. A., Wheelock, S., and Zacarias, N., "VizieR Online Data Catalog: 2MASS All-Sky Catalog of Point Sources (Cutri+ 2003)," *VizieR Online Data Catalog* , II/246 (June 2003).

[9] Grimm, S. L., Demory, B.-O., Gillon, M., Dorn, C., Agol, E., Burdanov, A., Delrez, L., Sestovic, M., Triaud, A. H. M. J., Turbet, M., Bolmont, É., Caldas, A., de Wit, J., Jehin, E., Leconte, J., Raymond, S. N., Van Grootel, V., Burgasser, A. J., Carey, S., Fabrycky, D., Heng, K., Hernandez, D. M., Ingalls, J. G., Lederer, S., Selsis, F., and Queloz, D., "The nature of the TRAPPIST-1 exoplanets," *A&A* **613**, A68 (May 2018).

[10] David, T. J., Petigura, E. A., Luger, R., Foreman-Mackey, D., Livingston, J. H., Mamajek, E. E., and Hillenbrand, L. A., "Four Newborn Planets Transiting the Young Solar Analog V1298 Tau," *ApJ* **885**, L12 (Nov. 2019).

[11] Van Grootel, V., Fernandes, C. S., Gillon, M., Jehin, E., Manfroid, J., Scuflaire, R., Burgasser, A. J., Barkaoui, K., Benkhaldoun, Z., Burdanov, A., Delrez, L., Demory, B.-O., de Wit, J., Queloz, D., and Triaud, A. H. M. J., "Stellar Parameters for Trappist-1," *ApJ* **853**, 30 (Jan. 2018).

[12] David, T. J., Cody, A. M., Hedges, C. L., Mamajek, E. E., Hillenbrand, L. A., Ciardi, D. R., Beichman, C. A., Petigura, E. A., Fulton, B. J., Isaacson, H. T., Howard, A. W., Gagné, J., Saunders, N. K., Rebull, L. M., Stauffer, J. R., Vasisht, G., and Hinkley, S., "A Warm Jupiter-sized Planet Transiting the Pre-main-sequence Star V1298 Tau," *AJ* **158**, 79 (Aug. 2019).

[13] Gaia Collaboration, Brown, A. G. A., Vallenari, A., Prusti, T., de Bruijne, J. H. J., Babusiaux, C., Bailer-Jones, C. A. L., Biermann, M., Evans, D. W., Eyer, L., Jansen, F., Jordi, C., Klioner, S. A., Lammers, U., Lindegren, L., Luri, X., Mignard, F., Panem, C., Pourbaix, D., Randich, S., Sartoretti, P., Siddiqui, H. I., Soubiran, C., van Leeuwen, F., Walton, N. A., Arenou, F., Bastian, U., Cropper, M., Drimmel, R., Katz, D., Lattanzi, M. G., Bakker, J., Cacciari, C., Castañeda, J., Chaoul, L., Cheek, N., De Angeli, F., Fabricius, C., Guerra, R., Holl, B., Masana, E., Messineo, R., Mowlavi, N., Nienartowicz, K., Panuzzo, P., Portell, J., Riello, M., Seabroke, G. M., Tanga, P., Thévenin, F., Gracia-Abril, G., Comoretto, G., Garcia-Reinaldos, M., Teyssier, D., Altmann, M., Andrae, R., Audard, M., Bellas-Velidis, I., Benson, K., Berthier, J., Blomme, R., Burgess, P., Busso, G., Carry, B., Cellino, A., Clementini, G., Clotet, M., Creevey, O., Davidson, M., De Ridder, J., Delchambre, L., Dell'Oro, A., Ducourant, C., Fernández-Hernández, J., Fouesneau, M., Frémat, Y., Galluccio, L., García-Torres, M., González-Núñez, J., González-Vidal, J. J., Gosset, E., Guy, L. P., Halbwachs, J. L., Hambly, N. C., Harrison, D. L., Hernández, J., Hestroffer, D., Hodgkin, S. T., Hutton, A., Jasniewicz, G., Jean-Antoine-Piccolo, A., Jordan, S., Korn, A. J., Krone-Martins, A., Lanzafame, A. C., Lebzelter, T., Löffler, W., Manteiga, M., Marrese, P. M., Martín-Fleitas, J. M., Moitinho, A., Mora, A., Muinonen, K., Osinde, J., Pancino, E., Pauwels, T., Petit, J. M., Recio-Blanco, A., Richards, P. J., Rimoldini, L., Robin, A. C., Sarro, L. M., Siopis, C., Smith, M., Sozzetti, A., Süveges, M., Torra, J., van Reeven, W., Abbas, U., Abreu Aramburu, A., Accart, S., Aerts, C., Altavilla, G., Álvarez, M. A., Alvarez, R., Alves, J., Anderson, R. I., Andrei, A. H., Anglada Varela, E., Antiche, E., Antoja, T., Arcay, B., Astraatmadja, T. L., Bach, N., Baker, S. G., Balaguer-Núñez, L., Balm, P., Barache, C., Barata, C.,

Barbato, D., Barblan, F., Barklem, P. S., Barrado, D., Barros, M., Barstow, M. A., Bartholomé Muñoz, S., Bassilana, J. L., Becciani, U., Bellazzini, M., Berihuete, A., Bertone, S., Bianchi, L., Bienaymé, O., Blanco-Cuaresma, S., Boch, T., Boeche, C., Bombrun, A., Borrachero, R., Bossini, D., Bouquillon, S., Bourda, G., Bragaglia, A., Bramante, L., Breddels, M. A., Bressan, A., Brouillet, N., Brüsemeister, T., Brugaletta, E., Bucciarelli, B., Burlacu, A., Busonero, D., Butkevich, A. G., Buzzi, R., Caffau, E., Cancelliere, R., Cannizzaro, G., Cantat-Gaudin, T., Carballo, R., Carlucci, T., Carrasco, J. M., Casamiquela, L., Castellani, M., Castro-Ginard, A., Charlot, P., Chemin, L., Chiavassa, A., Cocozza, G., Costigan, G., Cowell, S., Crifo, F., Crosta, M., Crowley, C., Cuypers, J., Dafonte, C., Damerdji, Y., Dapergolas, A., David, P., David, M., de Laverny, P., De Luise, F., De March, R., de Martino, D., de Souza, R., de Torres, A., Debosscher, J., del Pozo, E., Delbo, M., Delgado, A., Delgado, H. E., Di Matteo, P., Diakite, S., Diener, C., Distefano, E., Dolding, C., Drazinos, P., Durán, J., Edvardsson, B., Enke, H., Eriksson, K., Esquej, P., Eynard Bontemps, G., Fabre, C., Fabrizio, M., Faigler, S., Falcão, A. J., Farràs Casas, M., Federici, L., Fedorets, G., Fernique, P., Figueras, F., Filippi, F., Findeisen, K., Fonti, A., Fraile, E., Fraser, M., Frézouls, B., Gai, M., Galleti, S., Garabato, D., García-Sedano, F., Garofalo, A., Garralda, N., Gavel, A., Gavras, P., Gerssen, J., Geyer, R., Giacobbe, P., Gilmore, G., Girona, S., Giuffrida, G., Glass, F., Gomes, M., Granvik, M., Gueguen, A., Guerrier, A., Guiraud, J., Gutiérrez-Sánchez, R., Haigron, R., Hatzidimitriou, D., Hauser, M., Haywood, M., Heiter, U., Helmi, A., Heu, J., Hilger, T., Hobbs, D., Hofmann, W., Holland, G., Huckle, H. E., Hypki, A., Icardi, V., Janßen, K., Jevardat de Fombelle, G., Jonker, P. G., Juhász, Á. L., Julbe, F., Karampelas, A., Kewley, A., Klar, J., Kochoska, A., Kohley, R., Kolenberg, K., Kontizas, M., Kontizas, E., Koposov, S. E., Kordopatis, G., Kostrzewa-Rutkowska, Z., Koubsky, P., Lambert, S., Lanza, A. F., Lasne, Y., Lavigne, J. B., Le Fustec, Y., Le Poncin-Lafitte, C., Lebreton, Y., Leccia, S., Leclerc, N., Lecoeur-Taibi, I., Lenhardt, H., Leroux, F., Liao, S., Licata, E., Lindstrøm, H. E. P., Lister, T. A., Livanou, E., Lobel, A., López, M., Managau, S., Mann, R. G., Mantelet, G., Marchal, O., Marchant, J. M., Marconi, M., Marinoni, S., Marschalkó, G., Marshall, D. J., Martino, M., Marton, G., Mary, N., Massari, D., Matijevič, G., Mazeh, T., McMillan, P. J., Messina, S., Michalik, D., Millar, N. R., Molina, D., Molinaro, R., Molnár, L., Montegriffo, P., Mor, R., Morbidelli, R., Morel, T., Morris, D., Mulone, A. F., Muraveva, T., Musella, I., Nelemans,

G., Nicastro, L., Noval, L., O'Mullane, W., Ordénovic, C., Ordóñez-Blanco, D., Osborne, P., Pagani, C., Pagano, I., Pailler, F., Palacin, H., Palaversa, L., Panahi, A., Pawlak, M., Piersimoni, A. M., Pineau, F. X., Plachy, E., Plum, G., Poggio, E., Poujoulet, E., Prša, A., Pulone, L., Racero, E., Ragaini, S., Rambaux, N., Ramos-Lerate, M., Regibo, S., Reylé, C., Riclet, F., Ripepi, V., Riva, A., Rivard, A., Rixon, G., Roegiers, T., Roelens, M., Romero-Gómez, M., Rowell, N., Royer, F., Ruiz-Dern, L., Sadowski, G., Sagristà Sellés, T., Sahlmann, J., Salgado, J., Salguero, E., Sanna, N., Santana-Ros, T., Sarasso, M., Savietto, H., Schultheis, M., Sciacca, E., Segol, M., Segovia, J. C., Ségransan, D., Shih, I. C., Siltala, L., Silva, A. F., Smart, R. L., Smith, K. W., Solano, E., Solitro, F., Sordo, R., Soria Nieto, S., Souchay, J., Spagna, A., Spoto, F., Stampa, U., Steele, I. A., Steidelmüller, H., Stephenson, C. A., Stoev, H., Suess, F. F., Surdej, J., Szabados, L., Szegedi-Elek, E., Tapiador, D., Taris, F., Tauran, G., Taylor, M. B., Teixeira, R., Terrett, D., Teyssandier, P., Thuillot, W., Titarenko, A., Torra Clotet, F., Turon, C., Ulla, A., Utrilla, E., Uzzi, S., Vaillant, M., Valentini, G., Valette, V., van Elteren, A., Van Hemelryck, E., van Leeuwen, M., Vaschetto, M., Vecchiato, A., Veljanoski, J., Viala, Y., Vicente, D., Vogt, S., von Essen, C., Voss, H., Votruba, V., Voutsinas, S., Walmsley, G., Weiler, M., Wertz, O., Wevers, T., Wyrzykowski, Ł., Yoldas, A., Žerjal, M., Ziaeepour, H., Zorec, J., Zschocke, S., Zucker, S., Zurbach, C., and Zwitter, T., "Gaia Data Release 2. Summary of the contents and survey properties," *A&A* **616**, A1 (Aug. 2018).

C.3 A&A paper: Cang et.al 2021

Astronomy & Astrophysics manuscript no. output
September 28, 2021

Short-term variations of surface magnetism and prominences of the young Sun-like star V530 Per

T.-Q. Cang[1], P. Petit[1], J.-F. Donati[1], and C.P. Folsom[2]

[1] Institut de Recherche en Astrophysique et Planétologie, Université de Toulouse, CNRS, CNES, 14 avenue Edouard Belin, 31400 Toulouse, France
e-mail: Tianqi.Cang@irap.omp.eu
[2] Tartu Observatory, University of Tartu, Observatooriumi 1, Tõravere, 61602 Tartumaa, Estonia

September 28, 2021

ABSTRACT

Aims. We investigate magnetic tracers in the photosphere and the chromosphere of the ultra-rapid rotator ($P \sim 0.32d$) V530 Per, a cool member of the open cluster α Persei, to characterize the short-term variability of the magnetic activity and large-scale magnetic field of this prototypical young, rapidly rotating solar-like star.
Methods. With time-resolved spectropolarimetric observations spread over four close-by nights, we reconstructed the brightness distribution and large-scale magnetic field geometry of V530 Per through Zeeman-Doppler imaging. Simultaneously, we estimated the short-term variability of the surface through latitudinal differential rotation. Using the same data set, we also mapped the spatial distribution of prominences through tomography of Hα emission.
Results. As in our previous study, a large dark spot occupies the polar region of V530 Per with smaller, dark, and bright spots at lower latitudes. The large-scale magnetic field is dominated by a toroidal, mostly axisymmetric component. The maximal radial field strength is equal to $\sim$ 1 kG. The surface differential rotation is consistent with a smooth Sun-like shear $d\Omega = 0.053 \pm 0.004$ rad.d^{-1}, close to the solar shear level. The prominence pattern displays a stable component that is confined close to the corotation radius. We also observe rapidly evolving Hα emitting structures, over timescales ranging from minutes to days. The fast Hα evolution was not linked to any detected photospheric changes in the spot or magnetic coverage.

Key words. stars: individual: V530 Per, stars: magnetic field, stars: solar-type, stars: rotation, stars: spots

1. Introduction

Stellar activity is an important aspect of the early evolution of solar-type stars. A large fraction of young Suns rotate rapidly (Gallet & Bouvier 2015), and the sustained rotation is the root of strong activity, as empirically illustrated by the well-known relationship between X-ray emission and the rotation rate (e.g., Wright et al. 2011). For stars at the higher end of the rotation rate distribution, however, the activity stops increasing with the rotation rate (e.g., Wright et al. 2011; Vidotto et al. 2014; See et al. 2019). This phenomenon is believed to be linked to a so-called saturation of the stellar dynamo. There were several theoretical attempts to model this specific dynamo state (Kitchatinov & Olemskoy 2015; Augustson 2017; Guerrero et al. 2019), but currently we still lack a detailed knowledge of dynamo saturation and few Sun-like dwarfs with a saturated large-scale field strength have benefited from a detailed investigation of their magnetic activity (LO Peg, Folsom et al. 2016; AB Dor, Donati et al. 2003b; and BD-072388, Folsom et al. 2018).

One major physical ingredient responsible for the amplification of magnetic fields through global dynamos in cool stars is the differentially rotating stellar envelope. Zeeman-Doppler imaging (ZDI) of stellar surfaces (Semel 1989; Donati et al. 2006b; Folsom et al. 2018) offers an efficient way to study the spot patterns and the large-scale magnetic field geometries of active stars, as well as the progressive modification of the surface tracers under the influence of differential rotation. The solar surface differential rotation measured through different photospheric tracers displays relatively consistent and stable shear levels (Beck 2000). ZDI investigations of young, active stars reveal a more diverse situation, where temporal changes of differential rotation were observed, and shear values were reported to depend on the adopted surface tracer (brightness or magnetic field, e.g., Donati et al. 2003a; Yu et al. 2019).

Above the photosphere, magnetic fields create local accumulations of gas at chromospheric temperatures supported by magnetic loops and extending into the stellar corona. Stellar prominences can be used as a proxy to estimate the loss of mass and angular momentum through the stellar wind (e.g., Villarreal D'Angelo et al. 2019; Jardine & Collier Cameron 2019; Vidotto 2021), which is of prime importance in our understanding of the early evolution of cool stars. Although the knowledge we get from the Sun can provide rich information to understand the physics of prominences in a stellar context, available observations of prominence systems in other stars remain scarce as of today, so that the precise loss of mass and angular momentum through ejected prominence material is still uncertain. For rapidly rotating objects, the centrifugal force becomes involved in the equilibrium and dynamics of the so-called slingshot prominences (e.g., Collier Cameron & Robinson

1989a,b; Donati et al. 1999). Slingshot prominences were witnessed in corotation with a few, young solar-like objects (e.g., Donati et al. 2000; Dunstone et al. 2006; Cang et al. 2020; Zaire et al. 2021), and were shown to evolve over time scales as short as a few days.

V530 Per (also named AP 149) is a member of the young open cluster α Persei (Prosser 1992), with an age of around 60 Myr (Yen et al. 2018). It is a close analogue to the young Sun, with a mass of 1.00 ± 0.05 $M_{\odot}$, a radius of 1.06 ± 0.11 $R_{\odot}$, and an effective temperature of 5281 ± 96 K (Cang et al. 2020, C20 hereafter). As an ultra-rapid rotator with a rotational period P $\sim$ 0.32d (Rossby number of $\sim$ 0.013), it lies in the saturated regime of the dynamo action, and may even reach super-saturation. The spectropolarimetric study of C20, based on data obtained in 2006, highlighted the surface distribution of brightness structures, as well as a complex magnetic field geometry. The rotationally modulated Hα emission was consistent with an extended prominence system, characterized by an accumulation of hydrogen clouds near the corotation radius (in agreement with the previous work of Barnes et al. 2001), and variations of the prominence system within a few days. Since this first data set was not optimized to highlight fast changes, the purpose of the present study is to investigate in greater details the short-term variability of the prominence pattern, as well as the possible links of the coronal variability with the evolution of surface magnetic features, by investigating a denser time-series of observations.

We first present the new time-series of spectropolarimetric observations of V530 Per (Sect. 2), the reconstruction of brightness and magnetic field maps (Sect. 3), our estimates of surface differential rotation from both Stokes I and Stokes V data (Sect. 4), and the tomography of Hα line profiles (Sect. 5). We then discuss our results with respect to previous works (Sect. 6). In the final section, the main conclusions of this work are summarized (Sect. 7).

2. Observations

We carried out spectropolarimetric observations of V530 Per during four close nights (17, 18, 22, and 23 Oct 2018), using the 3.6-m Canada-France-Hawaii Telescope (Mauna Kea Observatory, Hawaii) equipped with the ESPaDOnS spectropolarimeter (Donati et al. 2006a). The observational set up is identical to the one adopted by C20. ESPaDOnS is used in polarimetric mode, in which a spectral resolution of $\sim 65,000$ is achieved over a spectral range covering the whole optical domain (370 - 1050 nm). Under this mode, each polarimetric sequence is obtained from four independent subexposures with fixed 600 s exposure time, using different angles of two half-wave, rotatable Fresnel rhombs (Semel et al. 1993; Donati & Collier Cameron 1997). Each sequence provides us with one circularly polarized (Stokes V) spectrum. We also use intensity (Stokes I) spectra reduced from the Stokes V subexposures to improve the temporal sampling in classical spectroscopy. We obtained in total 34 Stokes V spectra, and 136 Stokes I spectra (see Tab. A.1). The raw images were automatically reduced, and normalized 1D spectra were extracted by the `Libre-ESpRIT` pipeline (Donati et al. 1997). The number of exposures was not identical for every night, because of variable weather conditions. For most available observations, the peak signal-to-noise ration (S/N) of Stokes V spectra reaches around 100, which is close to the level obtained with previous observations in late 2006. The weather on 22 Oct was slightly worse than the other nights, with a lower S/N (mostly below 100), while the following night was the best, with S/N levels larger than 106. All reduced spectra can be accessed through the PolarBase archive (Petit et al. 2014).

The determination of the rotational cycle (E) for every observation is done according to the ephemeris of C20:

$$HJD_{\rm obs} = 2454072.0 + 0.3205 \times E. \quad (1)$$

Following the ephemeris, we can order the spectra according to their rotational phase and generate the dynamic spectra of Fig. C.1 and D.1, showing that the rotation coverage in each individual night was always over 50%, and up to 85% during the last night. Given the adopted integration time, the phase smearing during the acquisition of a Stokes V sequence is around $\sim$ 10% ($\sim$ 2% for Stokes I), which may reduce our sensitivity to the polarized signal generated by low latitude features, which have faster variations of their Doppler shift.

3. Brightness and magnetic field mapping

Because of the similarity of the observational material used here and by C20, and to allow for a better comparison between the two studies, all modeling tools used for this work were strictly identical to C20, unless specifically stated. A summary of the various steps involved in the tomographic analysis is provided below.

3.1. Least squares deconvolution

The spectral line profiles of V530 Per are heavily distorted, because of the very inhomogeneous surface brightness (recorded in Stokes I) and complex magnetic field geometry (in Stokes V). It is, however, especially difficult to study the profile shape in single lines of V530 Per, first because of the insufficient S/N, and also because of heavy blending generated by the rotational broadening. We take advantage, however, of the fact that all photospheric lines share a similar profile shape, with line-to-line differences mostly related to the line depth and wavelength (in Stokes I) or a combination of line depth, Landé factor, and wavelength (in Stokes V). To exploit this property and turn it into a statistical asset, we applied the so-called Least squares deconvolution (LSD) method to a list of photospheric lines (Donati et al. 1997). Using this procedure, we obtain an average line profile, with a significantly increased S/N.

The selected atomic line list was the nearest line list in the grid computed by Marsden et al. (2014), using the effective temperature $T_{\rm eff} = 5250K$, and an logarithmic gravity $log\ g = 4.5$, making use of the same set of atmospheric parameters as C20. We ignored wavelength windows polluted by telluric or chromospheric lines, and finally picked a total of 5,726 lines. The LSD pseudo-profiles were obtained with velocity steps of 1.8 km s^{-1} and are produced with an equivalent Landé factor of 1.19 and an equivalent wavelength of 650 nm. An example of Stokes I profile can be seen in Fig. B.1, and all Stokes V profiles are shown in Fig. D.1.

The dynamic spectrum (DS hereafter) of Stokes I profiles illustrated in Fig. C.1 highlights a complex pattern of

bumps and dips consistently repeated at different stellar rotation cycles. These signatures, interpreted as the spectral imprint of dark and bright spots, generate trails progressively drifting in RV according to their rotational Doppler shifts. The thickest, positive trail close to the line center suggests the presence of a large, dark spot close to the visible rotational pole, but not exactly centered on the pole (which would not produce any variable Doppler shifts at all). A few smaller trails are visible superimposed on the main trail and several of them are also observed at higher Doppler velocities, which suggests the presence of smaller spots, located at lower latitudes.

Although the patterns look almost the same for every night, a closer look reveals subtle differences between LSD profiles obtained during different nights, but at close-by phases (e.g., as shown in Fig.B.1). These differences are consistently observed at other phases and obey to progressive radial velocity drifts of spectral signatures. They are likely the combined product of the surface differential rotation and any other type of intrinsic variability. As for Stokes V profiles in Fig.D.1, we can also see structures repeatedly observed at close rotational phases. These features can be attributed to rotationally modulated Zeeman signatures produced by a complex magnetic field geometry.

3.2. Zeeman-Doppler imaging

From the time-series of LSD profiles, we reconstructed the surface brightness and large-scale magnetic field geometries of V530 Per with a ZDI code developed in Python and described in Folsom et al. (2018). The algorithm underlying this code is the one of Donati et al. (2006b), which used the maximum entropy fitting routine of Skilling & Bryan (1984) for this ill-posed inverse problem, and a spherical harmonics decomposition of the magnetic field distribution. Assuming that the variations in the Stokes I and Stokes V spectra are primarily caused by the stellar rotation, we can reconstruct a Doppler imaging (DI) map of the stellar photosphere by using Stokes I data, or a magnetic map with both Stokes I and Stokes V data (the surface brightness distribution being taken as a prior input of the Stokes V inversion). A simplified model of surface differential rotation, described in Sect. 4, is included in the inversion procedure. Owing to the very fast rotation of V530 Per that leads to a $\sim 10\%$ difference in radius between the pole and the equator, the code also includes a Roche model to take into account the oblate shape of the star, as initially implemented by C20.

The synthetic line profile produced by each surface element is modeled by a Gaussian function and is shifted according to its projected rotational velocity and scaled by the projection angle, a linear limb darkening function (e.g., Gray 2005) and a gravity darkening model (e.g., Lucy 1967). The limb darkening coefficient is interpolated from the table of Magic et al. (2015) (using the Kepler filter) and taken to be equal to $\eta = 0.73$. The gravity darkening coefficient $\beta = 4b = 0.32$ adopted by C20 was an average value obtained for cool stars (Lucy 1967). We applied here a different value $\beta = 0.46$, which is interpolated from the table of Claret & Bloemen (2011) according to the fundamental parameters of V530 Per, and results in an equatorial brightness equal to $\sim 83\%$ of the polar one. As already stressed in C20, the β coefficient has little impact on the resulting map.

All other input parameters of the tomographic inversion are equal to those discussed and adopted in C20. They include a projected rotational velocity equal to 106 $\mathrm{km\,s^{-1}}$, and a stellar inclination angle equal to 40°.

3.2.1. Brightness map

The overall stability, over several rotation periods, of activity signatures showing up in the Stokes I DS in individual nights, led us opt to group all Stokes I data together in the surface brightness reconstruction for a denser phase sampling. The inversion process also included the differential rotation parameters obtained in Sect. 4. The series of synthetic LSD profiles produced by the ZDI code is illustrated in Fig.C.1, showing that the DI model is able to fit the majority of activity features, resulting in a reduced χ^2 (χ^2_r hereafter) equal to 0.76. Although the level of residuals is negligible compared to the observed spectral signatures, there are some small features that the model cannot fully reproduce (e.g., the blue-shifted trail remaining at $\phi \sim 0.3 - 0.4$ on 23 Oct). Since the DI algorithm tries to reproduce corotating brightness structures that do not evolve with time, except under the predictable shifts owing to differential rotation, the model residuals may be linked to the intrinsic evolution of the brightness tracers (changes in area, shape or intensity of the active regions). Given that the residuals are not consistent from one night to the next, the short lifetime of some surface structures may be responsible for this modest mismatch.

We note that the χ^2_r we reached here is slightly larger than the one obtained with the 2006 data (which was equal to 0.55). This slightly degraded fit may be caused by a greater intrinsic variability of the spot distribution (emergence or decay of surface spots occurring faster and/or over larger areas) in the surface structures observed in 2018, bearing in mind that the S/N of both data sets is mostly the same, and that the time span of the new data is slightly shorter than in 2006.

The most striking structure in the brightness map of Fig. 1 is a large, dark spot occupying the polar region. This prominent spot contrasts with the scarcity of smaller spots reconstructed at lower latitudes. The polar spot is centered close to a latitude of $\sim 80°$, and is slightly off-centered toward a phase between 0.3 and 0.5. Smaller and low contrast dark spots, separated from the polar spot, also show up at high to intermediate latitudes, down to $\sim 45°$. A predominance of bright features is observed from the equator to a latitude of about 40°, as illustrated in Fig. 2 (see also the polar projection of the brightness map in Fig. G.1, where the color scale was modified to highlight better the bright features). The same accumulation was reported by C20, although the bright features were structured in a series of more distinct individual spots in 2006, while they here take the shape of a nearly continuous belt, possibly due to a denser distribution of spatially unresolved spots. The total fraction of the surface covered by bright or dark spots $\mathcal{S}_{\rm tot}$ is equal to $\sim 14\%$, as estimated by the following equation:

$$\mathcal{S}_{\rm tot} = \frac{\sum_{i=0}^{n} |I_i - I_0| A_i}{\sum_{i=0}^{n} A_i} \quad (2)$$

where $I_0 = 1$ is the unspotted brightness and I_i is the brightness of the $i^{\rm th}$ pixel, of surface area A_i.

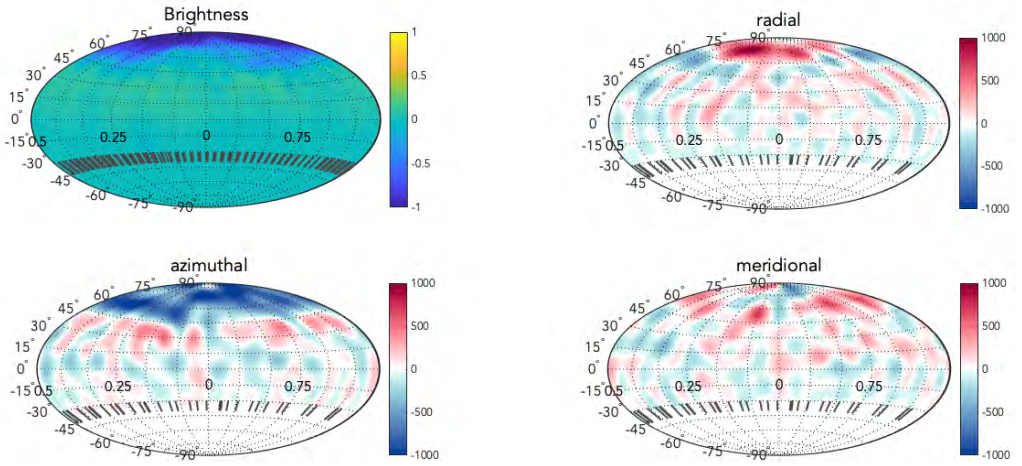

Fig. 1. Reconstructed brightness and magnetic field maps of V530 Per in 2018. Top-left: Logarithmic brightness (normalized to the nonspotted brightness). For the sake of clarity, the Hammer projection was adopted and the gravity darkening was subtracted. Top-right, bottom-left, and bottom-right: radial, azimuthal, and meridional components of the magnetic field. The color scale illustrates the field strength, in Gauss. Meridional ticks at the bottom of the maps mark the rotational phases of our observations. The portion of the map below -40° of latitude is set to 0, as it is invisible to the observer. A polar view of the same maps can be found in Fig. G.1.

3.2.2. Magnetic map

Similarly to the brightness inversion, the magnetic field reconstruction benefited from the dense phase coverage of the set of Stokes V LSD profiles (Fig. D.1), which is especially critical here since the Zeeman signatures are barely detected in individual Stokes V LSD profiles. Owing to the large relative noise, it is also impossible to readily notice, with the naked eye, any changes in the profiles that could be attributed to a surface shear. A search for signatures of differential rotation was however performed (Sect. 4), and the resulting parameters were used in the field reconstruction. The model fit the data with a reduced χ^2 of 0.92, again slightly larger than the one achieved with the 2006 data (χ^2 of 0.9). The magnetic field model includes spherical harmonics modes up to $\ell = 15$. The resulting map, shown in Fig. 1, unveils a complex surface distribution of magnetic fields. Similarly to C20, the small structures are also reconstructed, but with a slightly reduced strength, if we adopt a slightly larger χ^2 of 1. For the radial field component, the strongest and most visible structure is a positive magnetic spot close to the polar region. Its peak value is in excess of 1 kG, at a latitude of $\sim 75°$ and a rotation phase of $\phi \sim 0.2$. The main structures visible in the azimuthal field component is of negative polarity, and occupies the whole region at latitudes greater than $\sim 45°$. Apart from these two distinctive magnetic features, at lower latitudes a complex distribution of spots is reconstructed in the radial, azimuthal, and meridional field components, with no obvious counterpart in the brightness map.

We estimated a series of magnetic energy parameters from the modeled spherical harmonics coefficients, detailed in Tab. 1. There is a large difference between the unsigned average magnetic field strength $\langle B \rangle$, and the unsigned peak magnetic field strength $|B_{peak}|$, which is a consequence of the complex field structure, exhibiting strong magnetic fields in localized spots. Simply considering that the magnetic energy is proportional to B^2, the toroidal field component stores most of the energy ($\sim 68\%$) and has a mostly axisymmetric structure ($\sim 79\%$ of its energy shows up in modes with $m = 0$). The poloidal field component displays a lower axisymmetry ($\sim$ 36% of the energy with $m = 0$). For both the toroidal and poloidal field, most of the energy is stored in the high order spherical harmonics components ($\ell > 3$), which is another way to illustrate the complexity of the large-scale magnetic field. As a rough estimate of the uncertainty on these values, we varied the input stellar parameters ($v \sin i$, the inclination angle, the equatorial rotation period, and the surface shear) over their confidence interval, as well as the target χ^2. We conclude that the stellar parameters have little effect on the estimated magnetic energy ($\sim 2\%$), except $v \sin i$ that is able to modify the magnetic values by up to 10%. Changing the χ^2 within a reasonable range can also modify the derived magnetic characteristics by $\sim 10\%$.

4. Differential rotation

The subtle changes seen in the intensity line profiles, at nearby phases repeatedly observed over the course of our

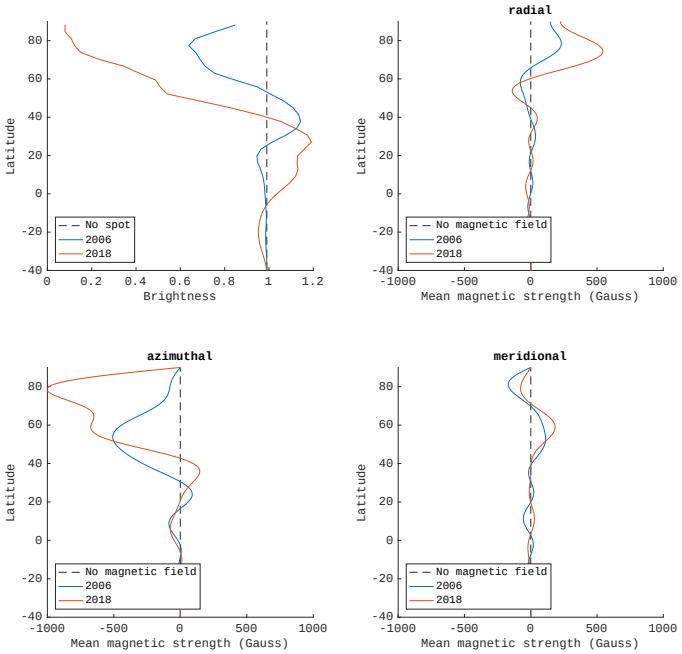

Fig. 2. Normalized brightness (top left panel) and magnetic field components in spherical coordinates, as a function of stellar latitude. The blue and red lines show the data from 2006 and 2018, respectively.

observing run (Fig. B.1), suggest that the brightness distribution is changing with time. In this section, we investigate whether a fraction of its variability can be modeled under the assumption of a differentially rotating surface. As an initial test of this idea, we compare two brightness maps (not shown here) reconstructed from data obtained on Oct 18 and 23, respectively. This specific choice of dates is a compromise between a sufficiently large temporal lever arm, and a good phase coverage. The comparison is performed as a cross-correlation of the two maps (Fig. 3), following Donati & Collier Cameron (1997). We observe that the surface structures are systematically shifted in phase between the two dates, and that the shift increases with the latitude. Most of the usable cross-correlation signal is seen at latitudes greater than about 40°, because of a lack of surface brightness tracers closer to the equator. In the same figure, we show the same approach applied to the data of C20, leading to very similar conclusions. The blue lines display a simple solar-like surface shear law (see below), showing that this simple description of the shear is consistent with our observations.

As a second step, we used the built-in sheared image ZDI method (Donati et al. 2000; Petit et al. 2002), where a solar-like differential rotation is implemented as part of the ZDI model, following a simple solar-like prescription:

$$\Omega(\theta) = \Omega_{\rm eq} - d\Omega \sin^2 \theta \qquad (3)$$

where $\Omega_{\rm eq}$ is the rotation rate of the equator, $d\Omega$ the pole to equator gradient in rotation rate, and θ the latitude.

We used the same ZDI model parameters as those discussed in Sect. 3, and carried out a grid search by varying $\Omega_{\rm eq}$ and $d\Omega$. We choose here to fix the entropy of the model, so that the output is a χ^2_r landscape, over a range of parameter values (Fig.4).

For Stokes I, the peak value is located at an equatorial period $P_{\rm I} = 0.32042 \pm 0.00005$ d, and a shear $\mathrm{d}\Omega_{\rm I} = 0.053 \pm 0.004$ rad.d^{-1}, in overall agreement with C20. While a previous search for differential rotation using Stokes V was inconclusive with the 2006 observations, the much denser phase coverage in 2018 led to a detection, with the best parameters equal to $P_{\rm V} = 0.32045 \pm 0.0001$ d, and $d\Omega_{\rm V} = 0.15 \pm 0.01$ rad.d^{-1}. The $d\Omega$ value derived from the large-scale magnetic field is, therefore, ~ 3 times larger than the value estimated from surface brightness. The shear search in Stokes V was performed using the brightness map as a prior, implying that the brightness was sheared by the same differential rotation parameters as Stokes V. We repeated the differential rotation search for Stokes V but assumed a constant surface brightness (as done in most previous ZDI measurements), and found a shear value within error bars of our first Stokes V estimate.

Table 1. Magnetic field characteristics of V530 Per in 2018 and 2006 (2006 values taken from C20).

	Parameter	Value (2018)	Value (2006)
a	$\langle B \rangle$	222 G	177 G
b	$\lvert B_{peak} \rvert$	1616 G	1088 G
c	toroidal	68 % (tot)	64 % (tot)
d	axisymmetric	65 %(tot)	53 % (tot)
e	pol axisymmetric	36 % (pol)	16 % (pol)
f	tor axisymmetric	79 %(tor)	74 % (tor)
g	dipole	6.3 % (pol)	1.2 % (pol)
h	quadrupole	6.6 % (pol)	3.3 % (pol)
i	octopole	7.3 % (pol)	5.4 % (pol)
j	pol $\ell > 3$	79.3 % (pol)	90.1 % (pol)
k	tor $\ell = 1$	2.6 % (tor)	8 % (tor)
l	tor $\ell = 2$	8.6 %(tor)	21 % (tor)
m	tor $\ell = 3$	13.7 % (tor)	20 % (tor)
n	tor $\ell > 3$	75.1 % (tor)	51 % (tor)

`Abbreviations:` tot=total, pol=poloidal, tor=toroidal
`Note:` The quantities listed include (a) the average magnetic field strength $\langle B \rangle$, (b) the unsigned peak magnetic field strength $|B_{peak}|$, (c) the ratio of toroidal field energy with respect to the total magnetic energy, (d) the ratio of magnetic energy in axisymmetric modes ($m = 0$) over the total energy, the same quantity but limited to the poloidal (e) and toroidal (f) magnetic component, the ratio of the dipole, quadrupole, octopole, and $\ell > 3$ (g, h, i, j) as a fraction of the poloidal component, and ($\ell = 1, 2, 3, > 3$) subcomponents of the toroidal field energy, as a fraction of the toroidal field energy (k, l, m, and n).

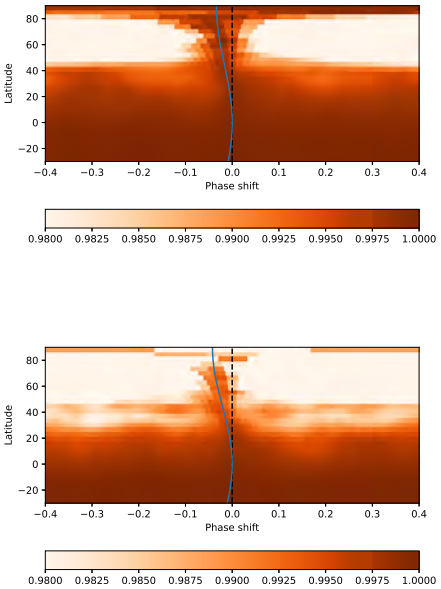

Fig. 3. Top: cross-correlation map obtained by comparing two brightness maps obtained using 2018 data from 18 Oct, versus 23 Oct (with a gap of 15.6 rotation periods between the two maps). Bottom: same, but for the two observing nights of our 2006 data (18.7 rotation periods apart). The blue lines show the differential rotational law derived using the sheared imaged method in Sect. 4 (top panel), and in C20 (bottom panel). The black, dashed line marks a null phase shift (which is equivalent to a solid-body rotation).

5. Prominences

The Hα line is observed in emission in all of our observations. In this section, we investigate the short-term evolution of this spectral feature within individual nights and over the full duration of our observing run.

When all observations of a single night are averaged together, a triple-peaked profile is observed (Fig. 5), as opposed to the 2006 data where a double peak was repeatedly reported. Both side peaks show up at around $\pm 150 \mathrm{km\,s^{-1}}$ from the line center (in 2006 and 2018), while the central peak is close to the line center. The Hα profile of Oct 22 stands out, with a distinctly larger amplitude of the central and blue-shifted peaks. The other nights display similar profiles, and the amplitude of their red and blue peaks tend also to agree with the 2006 observations.

The evolution of Hα within individual nights is illustrated as a set of dynamic spectra in Fig. 6. A fraction of the observed variability is consistent with the rotational modulation of hydrogen clouds trapped in corotation with the star, since part of the observed emission is stable over more than one day, when phased according to stellar rotation cycles given by Eq. 1. This is shown by, for example, similarities in the emission patterns observed on 17 and 18 Oct (three rotation cycles away from each other), especially at rotational phases smaller than 0.4. According to the estimate of C20, the coronal large-scale magnetic field of V530 Per is able to trap and support large prominences, which we assumed to be responsible for this rotationally modulated Hα emission.

The relatively stable Hα configuration observed during the first two nights is, however, considerably different from the one observed on 22 Oct. After three nights without observations, several additional emission components are observed, resulting in an overall increase of the emission for this specific night. We first note a broad emission peak around phase 0.5 and at negative velocities (between roughly -200 $\mathrm{km\,s^{-1}}$ and 0 $\mathrm{km\,s^{-1}}$). This line bump was not so prominent during the two previous nights (if it was present at all), and it becomes much weaker again during the last observing night. Another emission component takes the shape of a trail close to line center and extending from phase $\phi \sim 0.4$ to phase $\phi \sim 0.9$. It is not easy to decide whether this trail was already there in the previous observing nights, owing to the incomplete phase sampling. It is, however, present in the fourth night, although with a much reduced brightness. This trail (which is responsible for the central peak seen in Fig. 5) is confined within a range of velocities going from ~ -50 $\mathrm{km\,s^{-1}}$ to $\sim +30$ $\mathrm{km\,s^{-1}}$. The repeated observation over consecutive nights, at similar phases, definitely shows that this spectral feature is rotationally modulated. It is visible during only a fraction of the rotation period, suggesting that it is eclipsed behind the star during part of the rotation cycle. This is consistent with a hot chromospheric spot located at intermediate latitudes (since a prominence would more

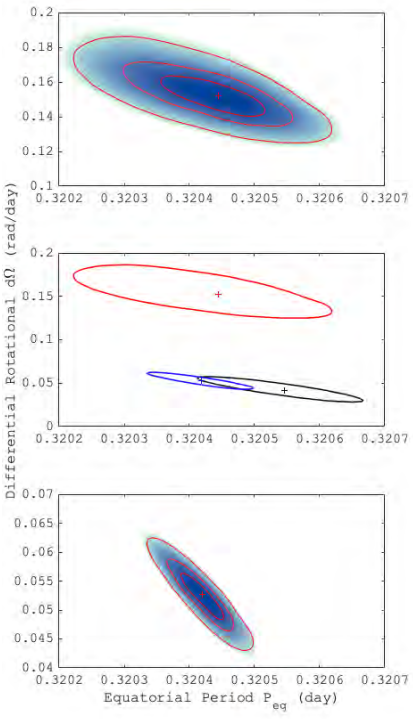

Fig. 4. Reduced χ^2 maps for the equatorial rotational period $\Omega_{\rm eq}$ and differential rotation $d\Omega$ for Stokes I (bottom panel) & Stokes V data (top panel). The three, red solid lines illustrate the 1σ, 2σ, and 3σ confidence intervals. Middle panel: a comparison of 3σ regions for Stokes I in 2018 (blue), Stokes I in 2006 (black), and Stokes V (red). Crosses mark the location of peak values.

likely be seen as an absorption feature when transiting in front of the stellar disk). Finally, a burst-like event takes place at phase $\phi \sim 0.18$ on 22 Oct and with a blue shift of $\sim +230$ km s^{-1}, with a lifetime shorter that our temporal resolution (i.e. < 600 sec).

Using this material, we followed the tomographic procedure described by C20 to reconstruct the velocity distribution of the prominences, using individual nights data. The Doppler tomography inversion uses the code of Donati et al. (2000), inspired from the tomographic approach developed by Marsh & Horne (1988) or Steeghs et al. (1996). In this simplified model, we assume that the Hα emitting material is optically thin, and corotates with the star. A description of this simple model can be found in Donati et al. (2000) and C20.

The modeled DS are shown in the middle panels of Fig. F.1, illustrating that the tomographic inversion is able to fit a majority of the observed features. We reached, however, a larger χ^2 (~ 9.5, with values ranging from 9 on 17 Oct to 10 on 22 Oct) than the one obtained from the 2006 data ($\chi^2 \sim 8$). This slightly degraded fit suggests that our simple model is challenged by these observations, either because some level of non-rotational variability affects our data over individual nights, or because some basic assumptions of the model are not consistent with the data (e.g., the fact that the emitting clouds are not supposed to be eclipsed by the star). The model residuals shown in the lower panels of Fig. F.1 are generally an order of magnitude lower than the observed emission, which suggests that most of the periodic patterns were successfully reconstructed by the tomographic code. Some of the phases and velocities displaying a significant mismatch with the model correspond to burst-like events described above (structures that are too short-lived to follow a rotationally-modulated pattern). For instance, at $\phi \sim 0.18$ on 22 Oct, the peak on the right of the line profile cannot be reproduced due to its very brief appearance in our data. Another example of mismatch is the trail seen close to the line core on 22 and 23 Oct. In this second case, where rotational modulation seems at play, the poor fit is likely owing to the intermittent visibility of the cloud, that spends part of the rotation cycle hidden behind the stellar disk.

Apart from the fast changing component of Hα emission that escapes our modeling attempts, most of the prominence pattern is correctly fit for all four nights. In the resulting maps, the emitting material accumulates around the corotation radius ($\sim 1.9\ R_*$), and forms an extended ring-like structure. The reconstructed pattern inside the $v \sin i$ limit is confined within a relatively small phase interval, centered around phase $\phi \sim 0.4$ during the first two nights, then showing up around phase $\phi \sim 0.7$ during the last two nights, with a prominent emission peak on Oct 22 in relation to the emission trail observed close to the line center.

We varied the rotation period in our tomographic model, and identified a preferred period of 0.37 d on 17 Oct. This estimate is consistent with previous findings of C20, who reported that their inversion was optimized with a 0.36-0.39 d period (depending on the night), possibly owing to a less effective corotational locking of prominences at large distances from the star. The period search was inconclusive for all other nights in 2018, possibly because of the fast variability hiding the rotational modulation.

6. Discussion

6.1. Surface brightness and magnetic field

Large-scale brightness and magnetic field geometries derived in this work show some clear similarities with the maps presented by C20. At both epochs, the brightness distribution was dominated by a dark spot anchored at high latitude. The second feature recognizable in both maps is an accumulation of bright spots at intermediate latitudes. Both maps display a spot coverage slightly larger than 10%. This consistent latitudinal dependence of the brightness is illustrated in the upper-left panel of Fig. 2. Beside the global consistency of the two maps, a clear evolution is seen regarding the high latitude spot, which is much darker at the new epoch, with a minimum normalized brightness decreasing from ~ 0.7 in 2006 to ~ 0.25 in 2018. The shape and location of this giant spot varied as well, from a location that did not cover the pole in the Doppler map of Barnes et al. (2001) and in our 2006 data, to a nearly centered spot in 2018. Such a clear evolution in the axisymmetry of the

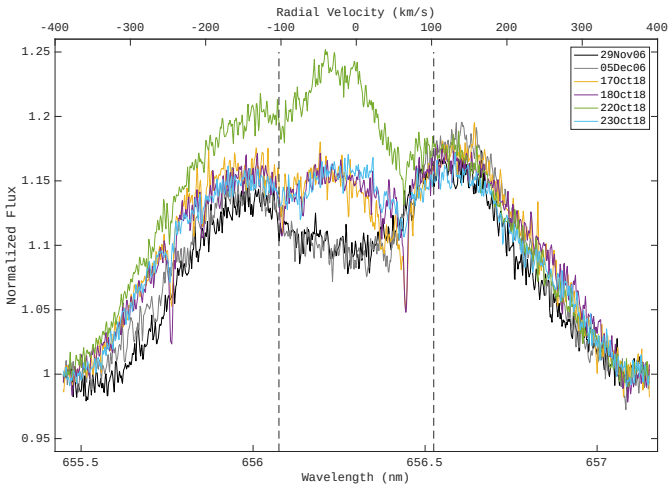

Fig. 5. Hα profiles averaged over individual nights in 2006 and 2018. Two vertical dashed lines show the $\pm v$ sin$i$ radial velocities.

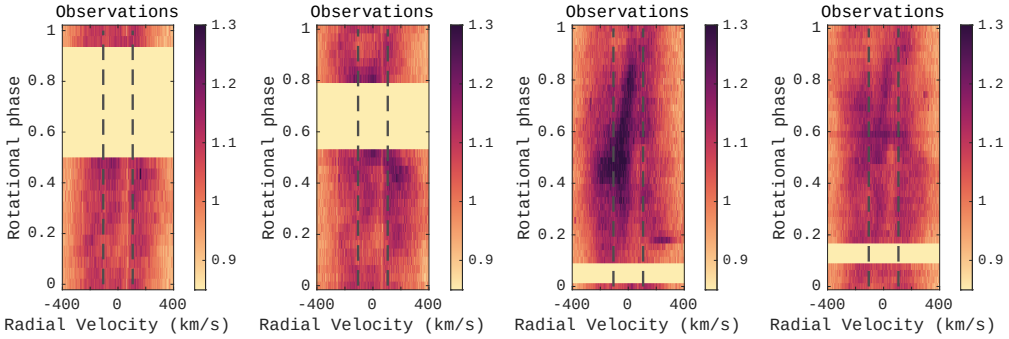

Fig. 6. Dynamic spectra of Hα line profiles, phased according to the stellar rotation period. From left to right, the panels show the data of 17, 18, 22, and 23 Oct 2018. Rotational phases are computed according to Eq. 1. Vertical dashed lines show $\pm$ v sin$i$.

main polar spot was not reported in other young solar-type stars with long-term monitoring (e.g., AB Dor, Donati & Collier Cameron 1997; Donati et al. 2003a). We also note that the latitude of maximum brightness was shifted by approximately 10° towards lower latitudes in 2018.

Similarly to the larger spot coverage observed close to the pole, we reconstructed stronger magnetic fields at high latitudes, for both the radial and azimuthal field components (Fig. 2). The latitude where the radial field strength is maximal is roughly the same in 2006 and 2018, while the latitude of maximal (unsigned) azimuthal field has been shifted by about 20°towards the pole. While the unsigned azimuthal field was maximal close to the limit of the polar spot in 2006, in 2018 the azimuthal component was strong well inside the dark polar structure (Fig. G.1). The field strengths of the latitudinal maxima of the radial and azimuthal field components roughly doubled from 2006 to 2018, with no observed polarity reversal.

The 2006 and 2018 magnetic geometries translate into relatively similar distributions of the magnetic energy (Table 1). More than half of the energy was contained in the high order components (ℓ>3) for both poloidal and toroidal field. We note that the reconstructed magnetic field is more axisymmetric in 2018 (∼65% of the energy in modes with $m = 0$) than in 2006 (∼53%), and the majority of this variation can be attributed to the poloidal axisymmetric component (with an increase from ∼16% to ∼36%). The average magnetic field strength obtained in 2018 ($\langle B \rangle \sim 222$ G) and the unsigned peak magnetic field strength ($|B_{peak}| \sim 1616$ G) are both larger than in 2006 (where 177 G and 1088 G were measured, respectively). The overall increased magnetism observed in 2018 suggests a variable activity level, but the very scarce available monitoring makes it impossible to conclude about the long-term nature of this variability, which may be mostly chaotic as

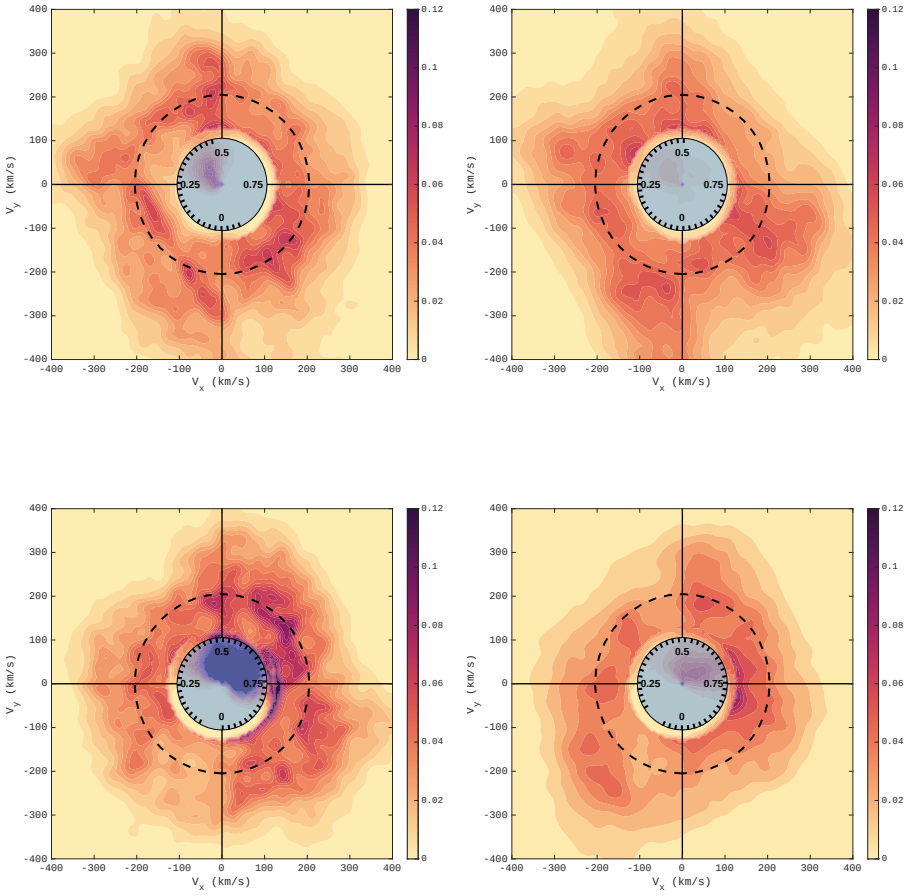

Fig. 7. Prominences Map of V530 Per in 17 (upper-left),18 (upper-right), 22 (lower-left),23(lower-right) Oct. The inner, filled blue circle represents the stellar surface. Radial ticks inside this circle give the rotational phases of Hα observations. The outer dashed circle is the corotation radius. The color scale depicts the local Hα equivalent width, in units of picometers per 8 km s^{-1} square pixel.

reported for other young, rapidly-rotating dwarfs like AB Dor or LQ Hya (Donati et al. 2003b).

6.2. Differential rotation

The progressive, latitude-dependent phase shift of brightness spots can be convincingly approximated by a solar-like differential rotation law, as illustrated in Fig. 3 where a simple cross-correlation of latitudinal strips is calculated, without any prior on the shear law. Using the same methodology, a solar-like shear pattern was also found consistent with successive Doppler maps of other young, rapidly rotating stars, e.g., the K dwarfs AB Dor (Donati & Collier Cameron 1997) and LO Peg (Barnes et al. 2005), the young G dwarf HD 141943 (Marsden et al. 2011), and the post T Tauri star LQ Lup (Donati et al. 2000). Recent reports on GJ791.2A and GJ 65 AB (Barnes et al. 2017), again based on the cross-correlation approach, suggest that very active M dwarfs can also follow a solar-like differential rotation law. A more complex latitudinal rotational dependence, similar to a Jupiter-like pattern, was suggested by numerical simulations at very fast rotation rates (Brun et al. 2017). The smoother dependence observed for V530 Per may suggest that zonal flows would require even shorter rotation

periods (which, in practice, would make this phenomenon fairly marginal among young Sun-like stars), or that any departures from a simple solar law are sufficiently subtle to remain hidden in the noise.

We identified a higher shear level using Stokes V profiles ($\sim$ 0.15 rad/d, $\sim$ 3 times larger than the Stokes I estimate). Similar results were repeatedly obtained for the young dwarfs AB Dor and LQ Hya (Donati et al. 2003b), and the T-Tauri stars Par 2244 (Hill et al. 2017) and V410 Tau (Yu et al. 2019). Assuming that this observation is not an artifact of the inversion procedure, it has been suggested by Donati et al. (2003b) that such differences may be linked to Stokes I and V tracing different depths within the star (depending on how deep the surface brightness and magnetic regions are actually generated), which is an interpretation also proposed for the Sun (Beck 2000). We also note that the Stokes I shear measurement obtained in 2018 is consistent within 3σ with the one obtained in 2006, while temporal changes in this value were previously reported for AB Dor (Collier Cameron & Donati 2002).

6.3. Short-term variability of the prominence distribution

Similarly to the previous observations of C20, the Hα emission of V530 Per in 2018 shows signatures of rotational modulation (Fig. 6), suggesting that most of the prominence system is forced to corotate with the star. Two emission peaks show up at a similar velocity of about $\pm 150 \mathrm{km\,s^{-1}}$ at both epochs (Fig. 5), with similar flux levels. We attributed them to the large hydrogen clouds accumulated around the corotational radius and trapped by coronal magnetic loops, as already proposed in other fast-rotating stars (Collier Cameron & Robinson 1989a,b; Steeghs et al. 1996; Donati et al. 2000).

The central emission peak was not observed in 2006. In 2018, it is linked to a trail in the DS that shows evidence of rotational modulation, and remains confined at relative radial velocities smaller than about 50 $\mathrm{km\,s^{-1}}$. This peak is responsible for the features inside the $v \sin i$ limit in Fig. 7. The small Doppler shift, combined with the eclipse of this signal during about 30% of the rotation, suggests that it is produced by a hot chromospheric point anchored at intermediate latitudes.

In the DS of 22 and 23 Oct, this central trail in Hα evolves in phase with the main, positive trail in the Stokes I DS. This phase correlation suggests that this bright, short lived chromospheric feature is lined up with the phase of the off-centered polar spot. A similar observation was reported for the K dwarf RE 1816+541 (Eibe 1998), and the weak line T Tauri star TWA 6 (Skelly et al. 2008).

The observed differences in the shape and intensity of the Hα line between successive nights suggest a day-to-day variation of the prominence arrangement. The emission recorded at the corotating radial velocity is less dramatically affected by these fast changes than the central emission peak. Surface activity tracers do not obviously reflect this rapid evolution, as illustrated by the Stokes I data of Fig. C.1, or by the Stokes V profiles of Fig. D.1. The reconstruction of a series of brightness maps using data of individual nights (not shown here) does not unveil any noticeable changes in the spot pattern, or at least not at a level that can be safely trusted as a genuine evolution (versus spurious differences owing to the different phase coverage, for instance). The reconstruction of magnetic maps for individual nights increases the noise contribution, which has the effect of hiding even more efficiently any possible variability. The only measured source of surface evolution is the latitudinal differential rotation, which effect remains fairly limited over the time span of our observations, and which is at a level similar to the one measured in 2006. We note, however, a systematically larger χ^2_r in 2018 compared to 2006 (for all mapping inversions presented here, and in spite of a slightly shorter time span in the 2018 time series), which may suggest a globally higher intrinsic surface variability in 2018. The absence of a clearly correlated evolution between the photosphere and the corona suggests that major reconnexion events can be triggered in the corona without any substantial reorganization of the magnetic field at the surface. It is also possible that very localized surface changes (occuring at spatial scales unresolved through ZDI) are enough to globally alter the stability of the prominence system. This disconnected evolution of the surface and the corona is reminiscent of recent observations of ϵ Eridani, where a sudden drop in CaII H and K emission was observed within a few days, with no simultaneous changes in the large-scale magnetic field (Petit et al. 2021).

We estimated the mass of the prominence system by using a method very similar to the one presented by Steeghs et al. (1996), and later used by Donati et al. (2000) or Zaire et al. (2021). We first calculated the equivalent width (EW) of the emission component of Hα by subtracting from the measured EW a reference EW estimated from a PolarBase spectrum of HD 225261, a quiet star chosen for its low S-index and effective temperature close to the one of V530 Per (Marsden et al. 2014). By repeating this procedure with $H\beta$ (which DS, showing marginally detected emission signatures consistent with Hα, is displayed in Fig. E.1), we estimated the Balmer decrement to be equal to $\approx$ 2.49, consistent with optically thin material. We make the rough assumption that the hydrogen clouds are contained within a sphere of radius l, taken equal to the radius of the source surface proposed by C20 ($l = 2.5R_*$). The number density of hydrogen atoms is estimated to be $\approx 1.1 \times 10^{16}$ $\mathrm{m^{-3}}$ and the total mass stored as prominences is $\approx 4.6 \times 10^{17}$ kg ($\approx 2.3 \times 10^{-13} M_\odot$). The prominence system mass of V530 Per is, therefore, mostly consisten with the range of masses obtained for other rapidly rotating stars ($10^{-14} - 10^{-17} M_\odot$, Collier Cameron & Robinson 1989a; Donati et al. 2000; Dunstone et al. 2006; Zaire et al. 2021), and close to the largest reported value ($\approx 5 \times 10^{-14} M_\odot$, Donati et al. 2000).

While the prominence mass is mostly the same on 17 and 18 Oct, we observe a $\approx 7\%$ increase in the mass measured on 22 Oct. During the last observing night (23 Oct), the prominence mass is back to a value close to the one obtained at the start of the run. This suggests that as much as 3.5×10^{16} kg of material has been removed from the system within one day, although it is not possible to determine whether a fraction of this material was sent back to the star, or if it was entirely ejected towards the interstellar medium. Mass estimates from 2006 are consistently below the values reported in 2018, by about 5%, which may be linked to the globally weaker surface magnetic field measured at this earlier epoch.

7. Conclusions

We confirmed the main conclusions of C20 regarding the surface distribution of brightness spots and magnetic re-

gions. A dark spot is again reported at high latitudes, and the magnetic geometry is characterized by a field strength in excess of 1 kG (locally), with a dominant toroidal component. The surface differential rotation is shown to follow a simple solar-like law. Using brightness tracers, its intensity is solar-like, while the measured shear is roughly three times larger using magnetic tracers.

Two components compose the prominence system accompanying V530 Per. The first component is confined around the corotation radius and has been observed in 2006 and 2018. We also observed a second, rapidly evolving Hα component, which was much closer to the stellar surface. This second component was absent from our 2006 observations, and was especially intense during the third night of the new run. It was possibly linked to a hot chromospheric point, as its emission source was close to the stellar surface, and not seen in absorption. It was anchored at intermediate to low latitudes, and at the phase of the main extension of the polar spot. An isolated event was also recorded with an extremely short lifetime < 10 min. These short term events at coronal level do not have any noticeable photospheric counterparts in the spot or magnetic coverage. These observations suggest that prominence systems hovering above the most active stars have a complex structure, spanning a range of spatial scales and lifetimes, and with a possible separation between a near-surface, short lived system coexisting with a dynamically stable ring of material in the vicinity of the corotation radius.

Acknowledgements. We are grateful to the anonymous referee for careful comments that helped to clarify the paper. TC would like to acknowledge financial support from the China Scholarship Council (CSC). JFD acknowledges funding from from the European Research Council (ERC) under the H2020 research & innovation programme (grant agreement # 740651 NewWorlds). This research made use of the SIMBAD database operated at CDS, Strasbourg, France, and the NASA's Astrophysics Data System Abstract Service.

References

Augustson, K. 2017, in European Physical Journal Web of Conferences, Vol. 160, European Physical Journal Web of Conferences, 02010
Barnes, J. R., Collier Cameron, A., James, D. J., & Steeghs, D. 2001, MNRAS, 326, 1057
Barnes, J. R., Collier Cameron, A., Lister, T. A., Pointer, G. R., & Still, M. D. 2005, MNRAS, 356, 1501
Barnes, J. R., Jeffers, S. V., Haswell, C. A., et al. 2017, MNRAS, 471, 811
Beck, J. G. 2000, Sol. Phys., 191, 47
Brun, A. S., Strugarek, A., Varela, J., et al. 2017, ApJ, 836, 192
Cang, T. Q., Petit, P., Donati, J. F., et al. 2020, A&A, 643, A39
Claret, A. & Bloemen, S. 2011, A&A, 529, A75
Collier Cameron, A. & Donati, J. F. 2002, MNRAS, 329, L23
Collier Cameron, A. & Robinson, R. D. 1989a, MNRAS, 236, 57
Collier Cameron, A. & Robinson, R. D. 1989b, MNRAS, 238, 657
Donati, J. F., Catala, C., Landstreet, J. D., & Petit, P. 2006a, Astronomical Society of the Pacific Conference Series, Vol. 358, ESPaDOnS: The New Generation Stellar Spectro-Polarimeter. Performances and First Results, ed. R. Casini & B. W. Lites, 362
Donati, J. F. & Collier Cameron, A. 1997, MNRAS, 291, 1
Donati, J. F., Collier Cameron, A., Hussain, G. A. J., & Semel, M. 1999, MNRAS, 302, 437
Donati, J. F., Collier Cameron, A., & Petit, P. 2003a, MNRAS, 345, 1187
Donati, J. F., Collier Cameron, A., Semel, M., et al. 2003b, MNRAS, 345, 1145
Donati, J. F., Howarth, I. D., Jardine, M. M., et al. 2006b, MNRAS, 370, 629
Donati, J. F., Mengel, M., Carter, B. D., et al. 2000, MNRAS, 316, 699
Donati, J. F., Semel, M., Carter, B. D., Rees, D. E., & Collier Cameron, A. 1997, MNRAS, 291, 658
Dunstone, N. J., Collier Cameron, A., Barnes, J. R., & Jardine, M. 2006, MNRAS, 373, 1308
Eibe, M. T. 1998, A&A, 337, 757
Folsom, C. P., Bouvier, J., Petit, P., et al. 2018, MNRAS, 474, 4956
Folsom, C. P., Petit, P., Bouvier, J., et al. 2016, MNRAS, 457, 580
Gallet, F. & Bouvier, J. 2015, A&A, 577, A98
Gray, D. F. 2005, The Observation and Analysis of Stellar Photospheres
Guerrero, G., Zaire, B., Smolarkiewicz, P. K., et al. 2019, ApJ, 880, 6
Hill, C. A., Carmona, A., Donati, J. F., et al. 2017, MNRAS, 472, 1716
Jardine, M. & Collier Cameron, A. 2019, MNRAS, 482, 2853
Kitchatinov, L. L. & Olemskoy, S. V. 2015, Research in Astronomy and Astrophysics, 15, 1801
Lucy, L. B. 1967, ZAp, 65, 89
Magic, Z., Chiavassa, A., Collet, R., & Asplund, M. 2015, A&A, 573, A90
Marsden, S. C., Jardine, M. M., Ramírez Vélez, J. C., et al. 2011, MNRAS, 413, 1939
Marsden, S. C., Petit, P., Jeffers, S. V., et al. 2014, MNRAS, 444, 3517
Marsh, T. R. & Horne, K. 1988, MNRAS, 235, 269
Petit, P., Donati, J. F., & Collier Cameron, A. 2002, MNRAS, 334, 374
Petit, P., Folsom, C. P., Donati, J. F., et al. 2021, A&A, 648, A55
Petit, P., Louge, T., Théado, S., et al. 2014, PASP, 126, 469
Prosser, C. F. 1992, AJ, 103, 488
See, V., Matt, S. P., Folsom, C. P., et al. 2019, ApJ, 876, 118
Semel, M. 1989, A&A, 225, 456
Semel, M., Donati, J. F., & Rees, D. E. 1993, A&A, 278, 231
Skelly, M. B., Unruh, Y. C., Collier Cameron, A., et al. 2008, MNRAS, 385, 708
Skilling, J. & Bryan, R. K. 1984, MNRAS, 211, 111
Steeghs, D., Horne, K., Marsh, T. R., & Donati, J. F. 1996, MNRAS, 281, 626
Vidotto, A. A. 2021, Living Reviews in Solar Physics, 18, 3
Vidotto, A. A., Gregory, S. G., Jardine, M., et al. 2014, MNRAS, 441, 2361
Villarreal D'Angelo, C., Jardine, M., Johnstone, C. P., & See, V. 2019, MNRAS, 485, 1448
Wright, N. J., Drake, J. J., Mamajek, E. E., & Henry, G. W. 2011, ApJ, 743, 48
Yen, S. X., Reffert, S., Schilbach, E., et al. 2018, A&A, 615, A12
Yu, L., Donati, J. F., Grankin, K., et al. 2019, MNRAS, 489, 5556
Zaire, B., Donati, J. F., & Klein, B. 2021, MNRAS, 504, 1969

Appendix A: Observation log

Table A.1. Observation log of V530 Per in 17, 18, 22, 23 Oct 2018).

Date (Oct 2018)	HJD (2458400+)	Phase	Peak S/N
17	8.99494	0.9655	105
17	9.02392	0.0559	106
17	9.05458	0.1516	105
17	9.08355	0.2420	106
17	9.11393	0.3368	98
17	9.14289	0.4271	97
18	9.90980	0.8200	100
18	9.93932	0.9121	100
18	9.96921	0.0053	99
18	9.99874	0.0975	98
18	10.02863	0.1907	99
18	10.05815	0.2828	103
18	10.08808	0.3762	100
18	10.11764	0.4685	98
22	13.85090	0.1167	108
22	13.88046	0.2089	102
22	13.91070	0.3033	100
22	13.94026	0.3955	88
22	13.97037	0.4895	94
22	13.99993	0.5817	91
22	14.03189	0.6814	91
22	14.06144	0.7736	95
22	14.09169	0.8680	97
22	14.12124	0.9602	97
23	14.83713	0.1939	106
23	14.86665	0.2860	108
23	14.89699	0.3806	110
23	14.92654	0.4728	107
23	14.95677	0.5671	109
23	14.98633	0.6594	110
23	15.01713	0.7555	107
23	15.04668	0.8477	107
23	15.07681	0.9417	108
23	15.10637	0.0339	103

`Note:` Every Stokes V spectra consisted of 4 individual unpolarized subexposures with fixed exposure time equal to 600s. From left to right, we list the date, the Julian date, the rotational phases calculated with Eq.1, and the peak S/N.

Appendix B: Example Stokes I LSD profiles

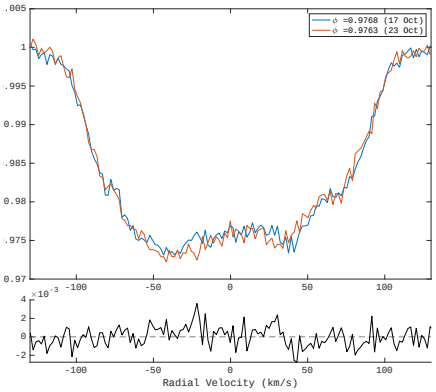

Fig. B.1. Top panel: example of LSD profiles for 17 Oct. (blue), and 23 Oct. (red) at close rotational phases (ϕ = 0.9768 and 0.9763). The small differences between the two profiles (e.g., at RV= $-30\,\mathrm{km\,s^{-1}}$) are consistently observed in other couples and are mainly caused by latitudinal differential rotation. Bottom panel: difference between the two profiles.

Appendix C: Dynamic spectrum of Stokes *I* for each night

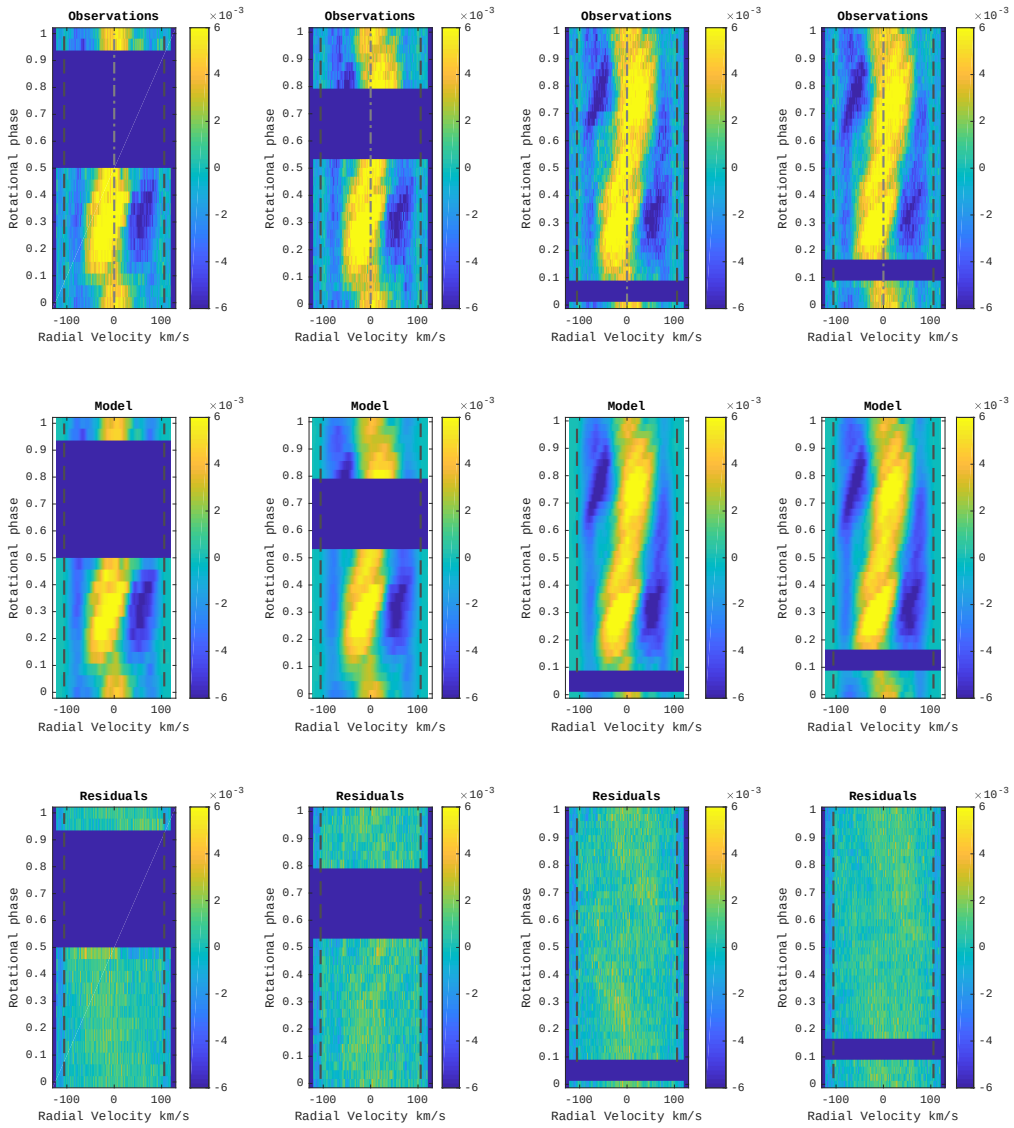

Fig. C.1. Dynamic spectra for V530 Per. From left to right: 17, 18, 22, 23 Oct. 2018. Upper panels: Stokes *I* profiles for each night Middle panels: ZDI brightness model. Bottom panels: model residuals.

Appendix D: Dynamic spectrum of Stokes *V*

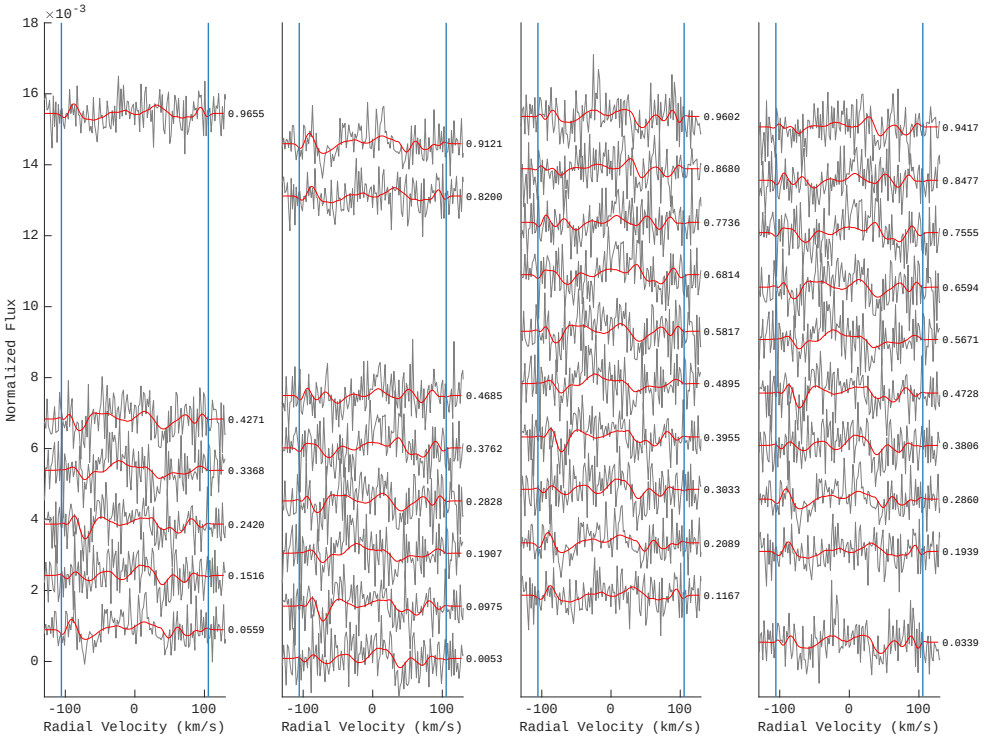

Fig. D.1. Observed (black) and synthetic (red) Stokes V profiles. The subpanels from left to right show data of the 17, 18, 22, and 23 Oct, respectively. Blue vertical lines mark the $\pm\ v\ \sin i$ limit. Rotational phases are indicated on the right side of each panel, next to the corresponding profile.

Appendix E: Dynamic spectrum of Hβ

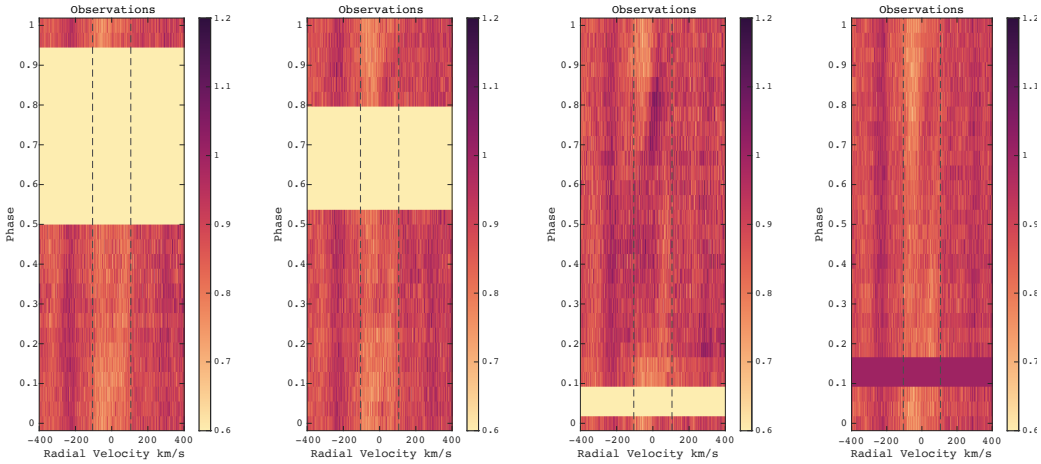

Fig. E.1. Dynamic spectra of Hβ, with the same conventions as in Fig. F.1.

Appendix F: Dynamic spectrum of Hα

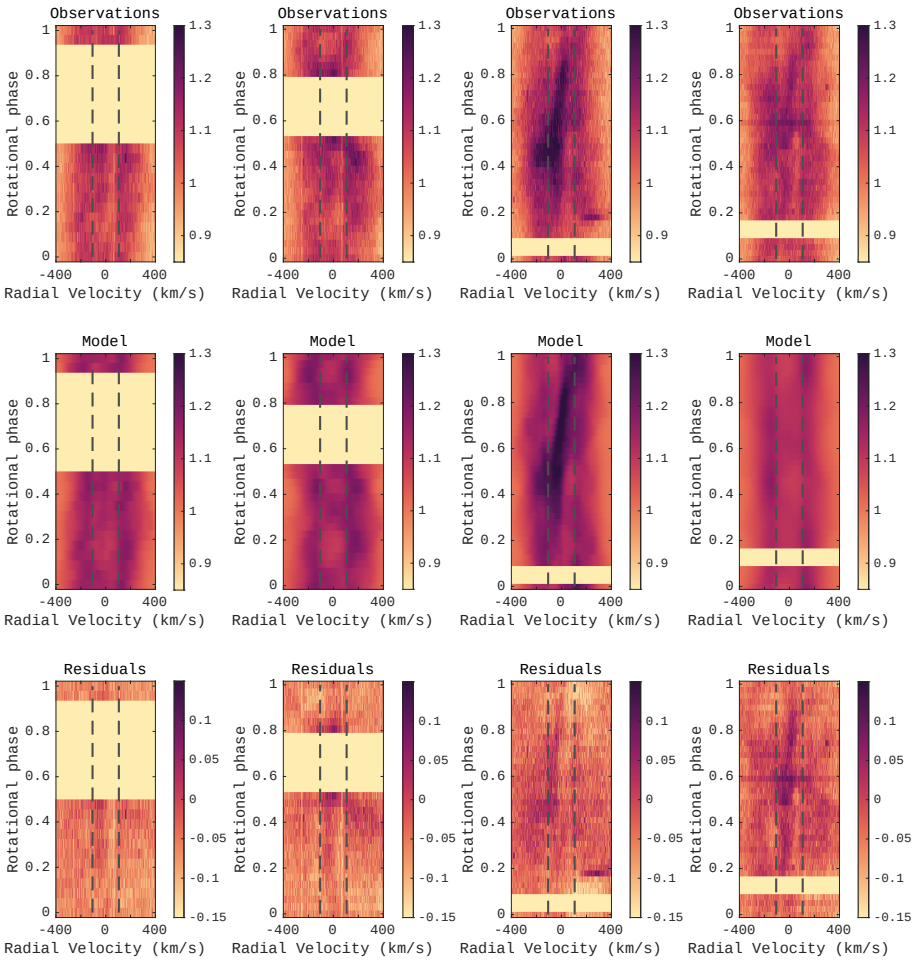

Fig. F.1. Dynamic spectra for Hα, including the observations (Top), the tomography models (Middle), the residuals between observation and model (Bottom). From left to right, the figure shows the data of 17, 18, 22, 23 Oct 2018, with color scale according to the normalized flux. Rotational phases are computed according to Eq. 1. Vertical dashed lines show the position of $\pm$ v sin$i$.

Appendix G: Polar view of reconstructed brightness and magnetic field maps

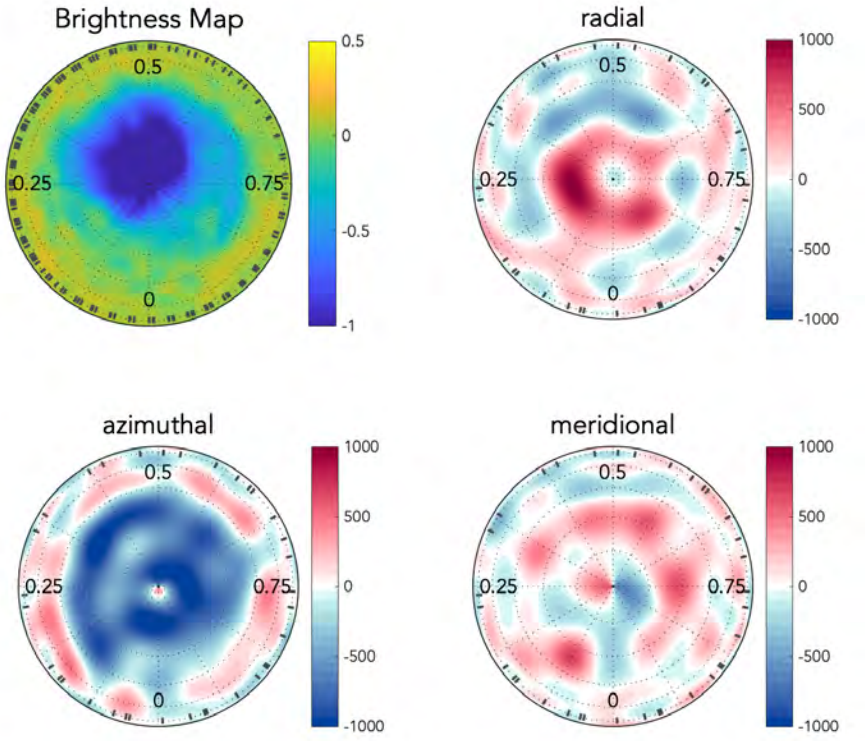

Fig. G.1. Same as Figure 1, but with a polar view. The color scale of the brightness map (upper left panel) is asymmetric to highlight the low-contrast bright spots.

Bibliography

Aarnio, A. N., Matt, S. P., & Stassun, K. G. 2012, ApJ, 760, 9, doi: 10.1088/0004-637X/760/1/9

Amard, L., Palacios, A., Charbonnel, C., Gallet, F., & Bouvier, J. 2016, A&A, 587, A105, doi: 10.1051/0004-6361/201527349

Amard, L., Palacios, A., Charbonnel, C., et al. 2019, A&A, 631, A77, doi: 10.1051/0004-6361/201935160

Andre, P., Aubreton, J., Barinov, Y., et al. 2002, Journal of Physics D Applied Physics, 35, 1846, doi: 10.1088/0022-3727/35/15/305

Astropy Collaboration, Robitaille, T. P., Tollerud, E. J., et al. 2013, A&A, 558, A33, doi: 10.1051/0004-6361/201322068

Astropy Collaboration, Price-Whelan, A. M., Sipőcz, B. M., et al. 2018, AJ, 156, 123, doi: 10.3847/1538-3881/aabc4f

Augustson, K. 2017, in European Physical Journal Web of Conferences, Vol. 160, European Physical Journal Web of Conferences, 02010, doi: 10.1051/epjconf/201716002010

Auvergne, M., Bodin, P., Boisnard, L., et al. 2009, A&A, 506, 411, doi: 10.1051/0004-6361/200810860

Babcock, H. W. 1961, ApJ, 133, 572, doi: 10.1086/147060

Balachandran, S. C., Mallik, S. V., & Lambert, D. L. 2011, MNRAS, 410, 2526, doi: 10.1111/j.1365-2966.2010.17630.x

Barnes, J. R., Collier Cameron, A., James, D. J., & Steeghs, D. 2001, MNRAS, 326, 1057, doi: 10.1046/j.1365-8711.2001.04648.x

Barnes, J. R., Collier Cameron, A., Lister, T. A., Pointer, G. R., & Still, M. D. 2005, MNRAS, 356, 1501, doi: 10.1111/j.1365-2966.2004.08588.x

Barnes, J. R., Jeffers, S. V., Haswell, C. A., et al. 2017, MNRAS, 471, 811, doi: 10.1093/mnras/stx1482

Beck, J. G. 2000, Sol. Phys., 191, 47, doi: 10.1023/A:1005226402796

Benz, W., Broeg, C., Fortier, A., et al. 2020, arXiv e-prints, arXiv:2009.11633. https://arxiv.org/abs/2009.11633

Berdyugina, S. V. 2005, Living Reviews in Solar Physics, 2, 8, doi: 10.12942/lrsp-2005-8

Bonfils, X., Delfosse, X., Udry, S., et al. 2013, A&A, 549, A109, doi: 10.1051/0004-6361/201014704

Boro Saikia, S., Jeffers, S. V., Morin, J., et al. 2016, A&A, 594, A29, doi: 10.1051/0004-6361/201628262

Boro Saikia, S., Lueftinger, T., Jeffers, S. V., et al. 2018, A&A, 620, L11, doi: 10.1051/0004-6361/201834347

Borucki, W. J., Koch, D., Basri, G., et al. 2010, Science, 327, 977, doi: 10.1126/science.1185402

Bouvier, J. 2013, in EAS Publications Series, Vol. 62, EAS Publications Series, ed. P. Hennebelle & C. Charbonnel, 143–168, doi: 10.1051/eas/1362005

Brown, B. P., Browning, M. K., Brun, A. S., Miesch, M. S., & Toomre, J. 2010, ApJ, 711, 424, doi: 10.1088/0004-637X/711/1/424

Brown, D. N., & Landstreet, J. D. 1981, ApJ, 246, 899, doi: 10.1086/158982

Brown, S. F., Donati, J. F., Rees, D. E., & Semel, M. 1991, A&A, 250, 463

Brun, A. S., & Browning, M. K. 2017, Living Reviews in Solar Physics, 14, 4, doi: 10.1007/s41116-017-0007-8

Brun, A. S., Strugarek, A., Varela, J., et al. 2017, ApJ, 836, 192, doi: 10.3847/1538-4357/aa5c40

Budding, E., Bembrick, C., Carter, B. D., et al. 2006, Ap&SS, 304, 13, doi: 10.1007/s10509-006-9086-z

Byrne, P. B., Eibe, M. T., & Rolleston, W. R. J. 1996, A&A, 311, 651

Caligari, P., Moreno-Insertis, F., & Schussler, M. 1995, ApJ, 441, 886, doi: 10.1086/175410

Cang, T. Q., Petit, P., Donati, J. F., et al. 2020, A&A, 643, A39, doi: 10.1051/0004-6361/202037693

Carroll, T. A., Strassmeier, K. G., Rice, J. B., & Künstler, A. 2012, A&A, 548, A95, doi: 10.1051/0004-6361/201220215

Chabrier, G., & Küker, M. 2006, A&A, 446, 1027, doi: 10.1051/0004-6361:20042475

Charbonneau, D., Brown, T. M., Burrows, A., & Laughlin, G. 2007, in Protostars and Planets V, ed. B. Reipurth, D. Jewitt, & K. Keil, 701. https://arxiv.org/abs/astro-ph/0603376

Charbonneau, D., Brown, T. M., Latham, D. W., & Mayor, M. 2000, ApJ, 529, L45, doi: 10.1086/312457

Charbonneau, P. 2005, Living Reviews in Solar Physics, 2, 2, doi: 10.12942/lrsp-2005-2

Che, X., Monnier, J. D., Zhao, M., et al. 2011, ApJ, 732, 68, doi: 10.1088/0004-637X/732/2/68

Claret, A. 1998, A&AS, 131, 395, doi: 10.1051/aas:1998278

Claret, A., & Bloemen, S. 2011, A&A, 529, A75, doi: 10.1051/0004-6361/201116451

Cole-Kodikara, E. M., Käpylä, M. J., Lehtinen, J. J., et al. 2019, A&A, 629, A120, doi: 10.1051/0004-6361/201935729

Collier Cameron, A. 1999, Astronomical Society of the Pacific Conference Series, Vol. 158, Stellar Prominences, ed. C. J. Butler & J. G. Doyle, 146

Collier Cameron, A., & Donati, J. F. 2002, MNRAS, 329, L23, doi: 10.1046/j.1365-8711.2002.05147.x

Collier Cameron, A., & Robinson, R. D. 1989a, MNRAS, 236, 57, doi: 10.1093/mnras/236.1.57

—. 1989b, MNRAS, 238, 657, doi: 10.1093/mnras/238.2.657

Collins, George W., I., & Harrington, J. P. 1966, ApJ, 146, 152, doi: 10.1086/148866

Collins, Geroge W., I. 1965, ApJ, 142, 265, doi: 10.1086/148282

Cranmer, S. R. 1996, PhD thesis, Bartol Research Institute, University of Delaware

Cutri, R. M., Skrutskie, M. F., van Dyk, S., et al. 2003a, 2MASS All Sky Catalog of point sources.

—. 2003b, VizieR Online Data Catalog, II/246

Davenport, J. R. A. 2016, ApJ, 829, 23, doi: 10.3847/0004-637X/829/1/23

Deutsch, A. J. 1958, in Electromagnetic Phenomena in Cosmical Physics, ed. B. Lehnert, Vol. 6, 209

Donati, J. F., Brown, S. F., Semel, M., et al. 1992, A&A, 265, 682

Donati, J. F., Catala, C., Landstreet, J. D., & Petit, P. 2006a, Astronomical Society of the Pacific Conference Series, Vol. 358, ESPaDOnS: The New Generation Stellar Spectro-Polarimeter. Performances and First Results, ed. R. Casini & B. W. Lites, 362

Donati, J. F., & Collier Cameron, A. 1997, MNRAS, 291, 1, doi: 10.1093/mnras/291.1.1

Donati, J. F., Collier Cameron, A., Hussain, G. A. J., & Semel, M. 1999, MNRAS, 302, 437, doi: 10.1046/j.1365-8711.1999.02095.x

Donati, J. F., Collier Cameron, A., & Petit, P. 2003a, MNRAS, 345, 1187, doi: 10.1046/j.1365-2966.2003.07101.x

Donati, J. F., Mengel, M., Carter, B. D., et al. 2000, MNRAS, 316, 699, doi: 10.1046/j.1365-8711.2000.03570.x

Donati, J. F., Semel, M., Carter, B. D., Rees, D. E., & Collier Cameron, A. 1997, MNRAS, 291, 658, doi: 10.1093/mnras/291.4.658

Donati, J. F., Collier Cameron, A., Semel, M., et al. 2003b, MNRAS, 345, 1145, doi: 10.1046/j.1365-2966.2003.07031.x

Donati, J. F., Howarth, I. D., Jardine, M. M., et al. 2006b, MNRAS, 370, 629, doi: 10.1111/j.1365-2966.2006.10558.x

Donati, J. F., Hébrard, E., Hussain, G., et al. 2014, MNRAS, 444, 3220, doi: 10.1093/mnras/stu1679

Donati, J. F., Moutou, C., Malo, L., et al. 2016, Nature, 534, 662, doi: 10.1038/nature18305

Donati, J. F., Kouach, D., Moutou, C., et al. 2020, MNRAS, doi: 10.1093/mnras/staa2569

Dumusque, X., Borsa, F., Damasso, M., et al. 2017, A&A, 598, A133, doi: 10.1051/0004-6361/201628671

Dunstone, N. J., Barnes, J. R., Collier Cameron, A., & Jardine, M. 2006a, MNRAS, 365, 530, doi: 10.1111/j.1365-2966.2005.09729.x

Dunstone, N. J., Collier Cameron, A., Barnes, J. R., & Jardine, M. 2006b, MNRAS, 373, 1308, doi: 10.1111/j.1365-2966.2006.11128.x

Eaton, J. A., & Hall, D. S. 1979, ApJ, 227, 907, doi: 10.1086/156800

Eibe, M. T. 1998, A&A, 337, 757

Ekström, S., Georgy, C., Eggenberger, P., et al. 2012, A&A, 537, A146, doi: 10.1051/0004-6361/201117751

Fang, X.-S., Gu, S.-H., Cheung, S.-L., et al. 2010, Research in Astronomy and Astrophysics, 10, 253, doi: 10.1088/1674-4527/10/3/007

Folsom, C. P., Petit, P., Bouvier, J., et al. 2016, MNRAS, 457, 580, doi: 10.1093/mnras/stv2924

Folsom, C. P., Bouvier, J., Petit, P., et al. 2018a, MNRAS, 474, 4956, doi: 10.1093/mnras/stx3021

Folsom, C. P., Fossati, L., Wood, B. E., et al. 2018b, MNRAS, 481, 5286, doi: 10.1093/mnras/sty2494

Fukui, Y., & Kawamura, A. 2010, ARA&A, 48, 547, doi: 10.1146/annurev-astro-081309-130854

Gallet, F., & Bouvier, J. 2013, A&A, 556, A36, doi: 10.1051/0004-6361/201321302

Gray, D. F. 2005, The Observation and Analysis of Stellar Photospheres

Guerrero, G., Zaire, B., Smolarkiewicz, P. K., et al. 2019, ApJ, 880, 6, doi: 10.3847/1538-4357/ab224a

Gull, S. F., & Daniell, G. J. 1978, Nature, 272, 686, doi: 10.1038/272686a0

Gustafsson, B., Edvardsson, B., Eriksson, K., et al. 2008, A&A, 486, 951, doi: 10.1051/0004-6361:200809724

Hale, G. E. 1908, ApJ, 28, 315, doi: 10.1086/141602

Hall, J. C. 2008, Living Reviews in Solar Physics, 5, 2, doi: 10.12942/lrsp-2008-2

Hansen, C. J., Kawaler, S. D., & Trimble, V. 2004, Stellar Interiors: Physical Principles, Structure, and Evolution, second edition. edn., Astronomy and Astrophysics Library (New York, NY: Springer New York)

Hatzes, A. P. 2002, Astronomische Nachrichten, 323, 392, doi: 10.1002/1521-3994(200208)323:3/4\TU\textless{}392::AID-ASNA392\TU\textgreater{}3.0.CO;2-M

Henden, A. A., Levine, S., Terrell, D., & Welch, D. L. 2015, in American Astronomical Society Meeting Abstracts, Vol. 225, American Astronomical Society Meeting Abstracts #225, 336.16

Henry, T. J., Franz, O. G., Wasserman, L. H., et al. 1999, ApJ, 512, 864, doi: 10.1086/306793

Hill, C. A., Carmona, A., Donati, J. F., et al. 2017, MNRAS, 472, 1716, doi: 10.1093/mnras/stx2042

Hirayama, T., & Moriyama, F. 1979, Sol. Phys., 63, 251, doi: 10.1007/BF00174531

Hu, Z., Su, X., Li, X., Zhang, L., & Chen, F. 2019, Optical and Quantum Electronics, 51, 1

Hussain, G. A. J. 2002, Astronomische Nachrichten, 323, 349, doi: 10.1002/1521-3994(200208)323:3/4\TU\textless{}349::AID-ASNA349\TU\textgreater{}3.0.CO;2-E

Jackson, R. J., & Jeffries, R. D. 2010, MNRAS, 402, 1380, doi: 10.1111/j.1365-2966.2009.15983.x

Jardine, M. 2004, A&A, 414, L5, doi: 10.1051/0004-6361:20031723

Jardine, M., & Collier Cameron, A. 2019, MNRAS, 482, 2853, doi: 10.1093/mnras/sty2872

Jardine, M., Collier Cameron, A., Donati, J. F., & Hussain, G. A. J. 2020, MNRAS, 491, 4076, doi: 10.1093/mnras/stz3173

Jardine, M., Vidotto, A. A., van Ballegooijen, A., et al. 2013, MNRAS, 431, 528, doi: 10.1093/mnras/stt181

Järvinen, S. P., Strassmeier, K. G., Carroll, T. A., Ilyin, I., & Weber, M. 2018, A&A, 620, A162, doi: 10.1051/0004-6361/201833496

Jeans, J. H. 1902, Philosophical Transactions of the Royal Society of London Series A, 199, 1, doi: 10.1098/rsta.1902.0012

Jeffries, R. D., Jackson, R. J., Briggs, K. R., Evans, P. A., & Pye, J. P. 2011, MNRAS, 411, 2099, doi: 10.1111/j.1365-2966.2010.17848.x

Jensen, K. A., Swank, J. H., Petre, R., et al. 1986, ApJ, 309, L27, doi: 10.1086/184754

Johnston, C. D., Hood, A. W., Cargill, P. J., & De Moortel, I. 2017, A&A, 597, A81, doi: 10.1051/0004-6361/201629153

Johnstone, C. P., & Güdel, M. 2015, A&A, 578, A129, doi: 10.1051/0004-6361/201425283

Kővári, Z., Bartus, J., Strassmeier, K. G., et al. 2007, A&A, 463, 1071, doi: 10.1051/0004-6361:20065982

Kővári, Z., Strassmeier, K. G., Oláh, K., et al. 2019, A&A, 624, A83, doi: 10.1051/0004-6361/201834810

Klein, B., & Donati, J. F. 2019, MNRAS, 488, 5114, doi: 10.1093/mnras/stz1953

Knapp, M., Seager, S., Demory, B.-O., et al. 2020, AJ, 160, 23, doi: 10.3847/1538-3881/ab8bcc

Kochukhov, O., Makaganiuk, V., & Piskunov, N. 2010, A&A, 524, A5, doi: 10.1051/0004-6361/201015429

Kochukhov, O., Makaganiuk, V., Piskunov, N., et al. 2011, ApJ, 732, L19, doi: 10.1088/2041-8205/732/2/L19

Krause, F., & Raedler, K. H. 1980, Mean-field magnetohydrodynamics and dynamo theory

Kreidberg, L. 2015, PASP, 127, 1161, doi: 10.1086/683602

Kriskovics, L., Kővári, Z., Vida, K., et al. 2019, A&A, 627, A52, doi: 10.1051/0004-6361/201834927

Kuiper, G. P. 1938, ApJ, 88, 472, doi: 10.1086/143999

Kuperus, M. 1969, Space Sci. Rev., 9, 713, doi: 10.1007/BF00174033

Kupka, F., Piskunov, N., Ryabchikova, T. A., Stempels, H. C., & Weiss, W. W. 1999, A&AS, 138, 119, doi: 10.1051/aas:1999267

Kurucz, R. 1993, ATLAS9 Stellar Atmosphere Programs and 2 km/s grid. Kurucz CD-ROM No. 13. Cambridge, 13

Labrosse, N., Heinzel, P., Vial, J. C., et al. 2010, Space Sci. Rev., 151, 243, doi: 10.1007/s11214-010-9630-6

Lada, C. J., & Kylafis, N. D. 1999, NATO Advanced Study Institute (ASI) Series C, Vol. 540, The Origin of Stars and Planetary Systems

Landi Degl'Innocenti, E. 1992, Magnetic field measurements., ed. F. Sanchez, M. Collados, & M. Vazquez, 71

Landstreet, J. D. 1988, ApJ, 326, 967, doi: 10.1086/166155

Lanza, A. F., Rodonò, M., & Pagano, I. 2004, A&A, 425, 707, doi: 10.1051/0004-6361:20047028

Lanza, A. F., Rodonò, M., Pagano, I., Barge, P., & Llebaria, A. 2003, A&A, 403, 1135, doi: 10.1051/0004-6361:20030401

Leroy, J. L., & Le Borgne, J. F. 1989, A&A, 223, 336

Lucy, L. B. 1967, ZAp, 65, 89

Magic, Z., Chiavassa, A., Collet, R., & Asplund, M. 2015, A&A, 573, A90, doi: 10.1051/0004-6361/201423804

Malkov, O. Y. 2007, MNRAS, 382, 1073, doi: 10.1111/j.1365-2966.2007.12086.x

Marsden, S. C., Jardine, M. M., Ramírez Vélez, J. C., et al. 2011, MNRAS, 413, 1939, doi: 10.1111/j.1365-2966.2011.18272.x

Marsden, S. C., Petit, P., Jeffers, S. V., et al. 2014, MNRAS, 444, 3517, doi: 10.1093/mnras/stu1663

Marsh, T. R., & Horne, K. 1988, MNRAS, 235, 269, doi: 10.1093/mnras/235.1.269

Masana, E., Jordi, C., & Ribas, I. 2006, A&A, 450, 735, doi: 10.1051/0004-6361:20054021

Mayor, M., & Queloz, D. 1995, Nature, 378, 355, doi: 10.1038/378355a0

Monnier, J. D., Zhao, M., Pedretti, E., et al. 2007, Science, 317, 342, doi: 10.1126/science.1143205

Morin, J., Donati, J. F., Petit, P., et al. 2008, MNRAS, 390, 567, doi: 10.1111/j.1365-2966.2008.13809.x

Mossman, J. E. 1989, QJRAS, 30, 59

Noyes, R. W., Hartmann, L. W., Baliunas, S. L., Duncan, D. K., & Vaughan, A. H. 1984, ApJ, 279, 763, doi: 10.1086/161945

O'dell, M. A., & Collier Cameron, A. 1993, MNRAS, 262, 521, doi: 10.1093/mnras/262.2.521

O'dell, M. A., Hendry, M. A., & Collier Cameron, A. 1994, MNRAS, 268, 181, doi: 10.1093/mnras/268.1.181

O'Gorman, E., Kervella, P., Harper, G. M., et al. 2017, A&A, 602, L10, doi: 10.1051/0004-6361/201731171

Osterbrock, D. E. 1989, Astrophysics of gaseous nebulae and active galactic nuclei

Oswalt, T. D., & Barstow, M. A. 2013, Planets, Stars and Stellar Systems Vol. 4, doi: 10.1007/978-94-007-5615-1

Pagano, I. 2013, Stellar Activity, ed. T. D. Oswalt & M. A. Barstow, Vol. 4, 485, doi: 10.1007/978-94-007-5615-1_10

Pallavicini, R., Golub, L., Rosner, R., et al. 1981, ApJ, 248, 279, doi: 10.1086/159152

Parenti, S. 2014, Living Reviews in Solar Physics, 11, 1, doi: 10.12942/lrsp-2014-1

Pecaut, M. J., & Mamajek, E. E. 2013, ApJS, 208, 9, doi: 10.1088/0067-0049/208/1/9

Petit, P., Donati, J. F., & Collier Cameron, A. 2002, MNRAS, 334, 374, doi: 10.1046/j.1365-8711.2002.05529.x

Petit, P., Louge, T., Théado, S., et al. 2014, PASP, 126, 469, doi: 10.1086/676976

Petit, P., Donati, J. F., Wade, G. A., et al. 2004, MNRAS, 348, 1175, doi: 10.1111/j.1365-2966.2004.07420.x

Petit, P., Dintrans, B., Solanki, S. K., et al. 2008, MNRAS, 388, 80, doi: 10.1111/j.1365-2966.2008.13411.x

Petit, P., Folsom, C. P., Donati, J. F., et al. 2021, A&A, 648, A55, doi: 10.1051/0004-6361/202040027

Pillitteri, I., Remage Evans, N., Wolk, S. J., & Bruck Syal, M. 2013, AJ, 145, 143, doi: 10.1088/0004-6256/145/5/143

Pinsonneault, M. H., Stauffer, J., Soderblom, D. R., King, J. R., & Hanson, R. B. 1998, ApJ, 504, 170, doi: 10.1086/306077

Plavchan, P., Barclay, T., Gagné, J., et al. 2020, Nature, 582, 497, doi: 10.1038/s41586-020-2400-z

Prosser, C. F. 1992, AJ, 103, 488, doi: 10.1086/116077

Prosser, C. F., Randich, S., Stauffer, J. R., Schmitt, J. H. M. M., & Simon, T. 1996, AJ, 112, 1570, doi: 10.1086/118124

Randich, S. 2000, in Astronomical Society of the Pacific Conference Series, Vol. 198, Stellar Clusters and Associations: Convection, Rotation, and Dynamos, ed. R. Pallavicini, G. Micela, & S. Sciortino, 401. https://arxiv.org/abs/astro-ph/9909139

Rauer, H., Catala, C., Aerts, C., et al. 2014, Experimental Astronomy, 38, 249, doi: 10.1007/s10686-014-9383-4

Reiners, A. 2012, Living Reviews in Solar Physics, 9, 1, doi: 10.12942/lrsp-2012-1

Rice, J. B., & Strassmeier, K. G. 2000, A&AS, 147, 151, doi: 10.1051/aas:2000366

—. 2001, A&A, 377, 264, doi: 10.1051/0004-6361:20011002

Ricker, G. R., Winn, J. N., Vanderspek, R., et al. 2014, in Society of Photo-Optical Instrumentation Engineers (SPIE) Conference Series, Vol. 9143, Space Telescopes and Instrumentation 2014: Optical, Infrared, and Millimeter Wave, 914320, doi: 10.1117/12.2063489

Rodono, M., Lanza, A. F., & Catalano, S. 1995, A&A, 301, 75

Roettenbacher, R. M., Monnier, J. D., Korhonen, H., et al. 2016, Nature, 533, 217, doi: 10.1038/nature17444

Ryabchikova, T., Piskunov, N., Kurucz, R. L., et al. 2015, Phys. Scr, 90, 054005, doi: 10.1088/0031-8949/90/5/054005

Ryabchikova, T. A., Piskunov, N. E., Kupka, F., & Weiss, W. W. 1997, Baltic Astronomy, 6, 244, doi: 10.1515/astro-1997-0216

Salaris, M., & Cassisi, S. 2005, Evolution of Stars and Stellar Populations

Schrijver, C. J., De Rosa, M. L., & Title, A. M. 2003, ApJ, 590, 493, doi: 10.1086/374982

Schrijver, C. J., & Zwaan, C. 2000, Solar and Stellar Magnetic Activity

Schroeder, K. P. 1983, A&A, 124, L16

Schuessler, M., Caligari, P., Ferriz-Mas, A., Solanki, S. K., & Stix, M. 1996, A&A, 314, 503

See, V., Jardine, M., Vidotto, A. A., et al. 2015, MNRAS, 453, 4301, doi: 10.1093/mnras/stv1925

—. 2017, MNRAS, 466, 1542, doi: 10.1093/mnras/stw3094

See, V., Matt, S. P., Folsom, C. P., et al. 2019, ApJ, 876, 118, doi: 10.3847/1538-4357/ab1096

Semel, M., Donati, J. F., & Rees, D. E. 1993, A&A, 278, 231

Shore, J. E., & Johnson, R. W. 1980, IEEE Transactions on Information Theory, 26, 26

Skelly, M. B., Unruh, Y. C., Barnes, J. R., et al. 2009, MNRAS, 399, 1829, doi: 10.1111/j.1365-2966.2009.15411.x

Skelly, M. B., Unruh, Y. C., Collier Cameron, A., et al. 2008, MNRAS, 385, 708, doi: 10.1111/j.1365-2966.2008.12917.x

Skilling, J., & Bryan, R. K. 1984, MNRAS, 211, 111, doi: 10.1093/mnras/211.1.111

Skumanich, A. 1972, ApJ, 171, 565, doi: 10.1086/151310

Spiegel, E. A., & Zahn, J. P. 1992, A&A, 265, 106

Stauffer, J. R., Barrado y Navascués, D., Bouvier, J., et al. 1999, ApJ, 527, 219, doi: 10.1086/308069

Steeghs, D. 2003, MNRAS, 344, 448, doi: 10.1046/j.1365-8711.2003.06917.x

Steeghs, D., Horne, K., Marsh, T. R., & Donati, J. F. 1996, MNRAS, 281, 626, doi: 10.1093/mnras/281.2.626

Stix, M. 2004, The sun : an introduction

Strassmeier, K. G. 2009, A&A Rev., 17, 251, doi: 10.1007/s00159-009-0020-6

Strassmeier, K. G., Pichler, T., Weber, M., & Granzer, T. 2003, A&A, 411, 595, doi: 10.1051/0004-6361:20031538

Strassmeier, K. G., & Rice, J. B. 1998, A&A, 330, 685

Tassoul, J.-L. 1978, Theory of rotating stars

Tatebe, K., Chandler, A. A., Wishnow, E. H., Hale, D. D. S., & Townes, C. H. 2007, ApJ, 670, L21, doi: 10.1086/524108

Tinbergen, J. 1996, Astronomical Polarimetry

Ud-Doula, A., Owocki, S. P., & Townsend, R. H. D. 2008, MNRAS, 385, 97, doi: 10.1111/j.1365-2966.2008.12840.x

van Belle, G. T. 2012, A&A Rev., 20, 51, doi: 10.1007/s00159-012-0051-2

van Leeuwen, F. 2009, A&A, 497, 209, doi: 10.1051/0004-6361/200811382

Vidotto, A. A. 2016, MNRAS, 459, 1533, doi: 10.1093/mnras/stw758

—. 2021, Living Reviews in Solar Physics, 18, 3, doi: 10.1007/s41116-021-00029-w

Vidotto, A. A., Gregory, S. G., Jardine, M., et al. 2014, MNRAS, 441, 2361, doi: 10.1093/mnras/stu728

Villarreal D'Angelo, C., Jardine, M., Johnstone, C. P., & See, V. 2019, MNRAS, 485, 1448, doi: 10.1093/mnras/stz477

Villarreal D'Angelo, C., Jardine, M., & See, V. 2018, MNRAS, 475, L25, doi: 10.1093/mnrasl/slx206

Vogt, S. S., Hatzes, A. P., Misch, A. A., & Kürster, M. 1999, ApJS, 121, 547, doi: 10.1086/313195

Vogt, S. S., & Penrod, G. D. 1983, PASP, 95, 565, doi: 10.1086/131208

Vogt, S. S., Penrod, G. D., & Hatzes, A. P. 1987, ApJ, 321, 496, doi: 10.1086/165647

von Zeipel, H. 1924, MNRAS, 84, 665, doi: 10.1093/mnras/84.9.665

Wade, G. A., Bagnulo, S., Kochukhov, O., et al. 2001, A&A, 374, 265, doi: 10.1051/0004-6361:20010735

Wade, G. A., Donati, J. F., & Landstreet, J. D. 2000, New A, 5, 455, doi: 10.1016/S1384-1076(00)00041-5

Waite, I. A., Marsden, S. C., Carter, B. D., et al. 2017, MNRAS, 465, 2076, doi: 10.1093/mnras/stw2731

Walkowicz, L. M., & Basri, G. S. 2013, MNRAS, 436, 1883, doi: 10.1093/mnras/stt1700

Watson, C. A., de Mooij, E. J. W., Steeghs, D., et al. 2019, MNRAS, 490, 1991, doi: 10.1093/mnras/stz2679

Weber, E. J., & Davis, Leverett, J. 1967, ApJ, 148, 217, doi: 10.1086/149138

Winn, J. N. 2009, in Transiting Planets, ed. F. Pont, D. Sasselov, & M. J. Holman, Vol. 253, 99–109, doi: 10.1017/S174392130802629X

Wolszczan, A., & Frail, D. A. 1992, Nature, 355, 145, doi: 10.1038/355145a0

Wright, N. J., Drake, J. J., Mamajek, E. E., & Henry, G. W. 2011, ApJ, 743, 48, doi: 10.1088/0004-637X/743/1/48

Yen, S. X., Reffert, S., Schilbach, E., et al. 2018, A&A, 615, A12, doi: 10.1051/0004-6361/201731905

Yu, K. C. 2000, PhD thesis, CASA, Campus Box 389, Boulder, CO 80309

Yu, L., Donati, J. F., Hébrard, E. M., et al. 2017, MNRAS, 467, 1342, doi: 10.1093/mnras/stx009

Yu, L., Donati, J. F., Grankin, K., et al. 2019, MNRAS, 489, 5556, doi: 10.1093/mnras/stz2481

Zacharias, N., Finch, C. T., Girard, T. M., et al. 2013, AJ, 145, 44, doi: 10.1088/0004-6256/145/2/44

Zaire, B., Donati, J. F., & Klein, B. 2021, MNRAS, 504, 1969, doi: 10.1093/mnras/stab1019

Zeeman, P. 1897, ApJ, 5, 332, doi: 10.1086/140355

Zhao, M., Monnier, J. D., Pedretti, E., et al. 2009, ApJ, 701, 209, doi: 10.1088/0004-637X/701/1/209